Numerical investigations on the uniaxial tensile behaviour of Textile Reinforced Concrete

Numerische Untersuchungen zum einaxialen Zugtragverhalten von Textilbeton

Von der Fakultät Bauingenieurwesen
der Technischen Universität Dresden
zur Erlangung der Würde eines
Doktor-Ingenieurs (Dr.-Ing.)
genehmigte

Dissertation

vorgelegt von
Dipl.-Ing. Jens Uwe Hartig
geboren am 6. Dezember 1979 in Riesa

Gutachter:
Prof. Dr.-Ing. habil. Ulrich Häußler-Combe
Prof. Dr.-Ing. Dr.-Ing. E.h. Dr. h.c. Ekkehard Ramm

Tag der Verteidigung: 27.01.2011

Abstract

In the present work, the load-bearing behaviour of Textile Reinforced Concrete (TRC), which is a composite of a fine-grained concrete matrix and a reinforcement of high-performance fibres processed to textiles, exposed to uniaxial tensile loading was investigated based on numerical simulations. The investigations are focussed on reinforcement of multi-filament yarns of alkali-resistant glass. When embedded in concrete, these yarns are not entirely penetrated with cementitious matrix, which leads associated with the heterogeneity of the concrete and the yarns to a complex load-bearing and failure behaviour of the composite. The main objective of the work was the theoretical investigation of effects in the load-bearing behaviour of TRC, which cannot be explained solely by available experimental results. Therefore, a model was developed, which can describe the tensile behaviour of TRC in different experimental test setups with a unified approach.

Neglecting effects resulting from Poisson's effect, a one-dimensional model implemented within the framework of the Finite Element Method was established. Nevertheless, the model takes also transverse effects into account by a subdivision of the reinforcement yarns into so-called segments. The model incorporates two types of finite elements: bar and bond elements. In longitudinal direction, the bar elements are arranged in series to represent the load-bearing behaviour of matrix or reinforcement. In transverse direction these bar element chains are connected with bond elements. The model gains most of its complexity from non-linearities arising from the constitutive relations, e. g., limited tensile strength of concrete and reinforcement, tension softening of the concrete, waviness of the reinforcement and non-linear bond laws. Besides a deterministic description of the material behaviour, also a stochastic formulation based on a random field approach was introduced in the model. The model has a number of advantageous features, which are provided in this combination only in a few of the existing models concerning TRC. It provides stress distributions in the reinforcement and the concrete as well as properties of concrete crack development like crack spacing and crack widths, which are in some of the existing models input parameters and not a result of the simulations. Moreover, the successive failure of the reinforcement can be studied with the model. The model was applied to three types of tests, the filament pull-out test, the yarn pull-out test and tensile tests with multiple concrete cracking.

The results of the simulations regarding the filament pull-out tests showed good correspondence with experimental data. Parametric studies were performed to investigate the influence of geometrical properties in these tests like embedding and free lengths of the filament as well as bond properties between filament and matrix. The presented results of simulations of yarn pull-out tests demonstrated the applicability of the model to this type of test. It has been shown that a relatively fine subdivision of the reinforcement is necessary to represent the successive failure of the reinforcement yarns appropriately. The presented results showed that the model can provide the distribution of failure positions in the reinforcement and the degradation development of yarns during loading. One of the main objectives of

the work was to investigate effects concerning the tensile material behaviour of TRC, which could not be explained, hitherto, based solely on experimental results. Hence, a large number of parametric studies was performed concerning tensile tests with multiple concrete cracking, which reflect the tensile behaviour of TRC as occurring in practice. The results of the simulations showed that the model is able to reproduce the typical tripartite stress-strain response of TRC consisting of the uncracked state, the state of multiple matrix cracking and the post-cracking state as known from experimental investigations. The best agreement between simulated and experimental results was achieved considering scatter in the material properties of concrete as well as concrete tension softening and reinforcement waviness.

Kurzfassung

Die vorliegende Arbeit beschäftigt sich mit Untersuchungen zum einaxialen Zugtragverhalten von Textilbeton. Textilbeton ist ein Verbundwerkstoff bestehend aus einer Matrix aus Feinbeton und einer Bewehrung aus Multifilamentgarnen aus Hochleistungsfasern, welche zu textilen Strukturen verarbeitet sind. Die Untersuchungen konzentrieren sich auf Bewehrungen aus alkali-resistentem Glas. Das Tragverhalten des Verbundwerkstoffs ist komplex, was aus der Heterogenität der Matrix und der Garne sowie der unvollständigen Durchdringung der Garne mit Matrix resultiert. Das Hauptziel der Arbeit ist die theoretische Untersuchung von Effekten und Mechanismen innerhalb des Lastabtragverhaltens von Textilbeton, welche nicht vollständig anhand verfügbarer experimenteller Ergebnisse erklärt werden können. Das entsprechende Modell zur Beschreibung des Zugtragverhaltens von Textilbeton soll verschiedene experimentelle Versuchstypen mit einem einheitlichen Modell abbilden können.

Unter Vernachlässigung von Querdehneffekten wurde ein eindimensionales Modell entwickelt und im Rahmen der Finite-Elemente-Methode numerisch implementiert. Es werden jedoch auch Lastabtragmechanismen in Querrichtung durch eine Unterteilung der Bewehrungsgarne in sogenannte Segmente berücksichtigt. Das Modell enthält zwei Typen von finiten Elementen: Stabelemente und Verbundelemente. In Längsrichtung werden Stabelemente kettenförmig angeordnet, um das Tragverhalten von Matrix und Bewehrung abzubilden. In Querrichtung sind die Stabelementketten mit Verbundelementen gekoppelt. Das Modell erhält seine Komplexität hauptsächlich aus Nichtlinearitäten in der Materialbeschreibung, z.B. durch begrenzte Zugfestigkeiten von Matrix und Bewehrung, Zugentfestigung der Matrix, Welligkeit der Bewehrung und nichtlineare Verbundgesetze. Neben einer deterministischen Beschreibung des Materialverhaltens beinhaltet das Modell auch eine stochastische Beschreibung auf Grundlage eines Zufallsfeldansatzes. Mit dem Modell können Spannungsverteilungen im Verbundwerkstoff und Eigenschaften der Betonrissentwicklung, z.B. in Form von Rissbreiten und Rissabständen untersucht werden, was in dieser Kombination nur mit wenigen der existierenden Modelle für Textilbeton möglich ist. In vielen der vorhandenen Modelle sind diese Eigenschaften Eingangsgrößen für die Berechnungen und keine Ergebnisse. Darüber hinaus kann anhand des Modells auch das sukzessive Versagen der Bewehrungsgarne studiert werden. Das Modell wurde auf drei verschiedene Versuchstypen angewendet: den Filamentauszugversuch, den Garnauszugversuch und Dehnkörperversuche.

Die Berechnungsergebnisse zu den Filamentauszugversuchen zeigten eine gute Übereinstimmung mit experimentellen Resultaten. Zudem wurden Parameterstudien durchgeführt, um Einflüsse aus Geometrieeigenschaften wie der eingebetteten und freien Filamentlänge sowie Materialeigenschaften wie dem Verbund zwischen Matrix und Filament zu untersuchen. Die Berechnungsergebnisse zum Garnauszugversuch demonstrierten die Anwendbarkeit des Modells auf diesen Versuchstyp. Es wurde gezeigt, dass für eine realitätsnahe Abbildung des Versagensverhaltens der Bewehrungsgarne eine relativ feine Auflösung der Bewehrung notwendig ist. Die Berechnungen lieferten die Verteilung von Versagenspositionen

in der Bewehrung und die Entwicklung der Degradation der Garne im Belastungsverlauf. Ein Hauptziel der Arbeit war die Untersuchung von Effekten im Zugtragverhalten von Textilbeton, die bisher nicht durch experimentelle Untersuchungen erklärt werden konnten. Daher wurde eine Vielzahl von Parameterstudien zu Dehnkörpern mit mehrfacher Matrixrissbildung, welche das Zugtragverhalten von Textilbeton ähnlich praktischen Anwendungen abbilden, durchgeführt. Die Berechnungsergebnisse zeigten, dass der experimentell beobachtete dreigeteilte Verlauf der Spannungs-Dehnungs-Beziehung von Textilbeton bestehend aus dem ungerissenen Zustand, dem Zustand der Matrixrissbildung und dem Zustand der abgeschlossenen Rissbildung vom Modell wiedergegeben wird. Die beste Übereinstimmung zwischen berechneten und experimentellen Ergebnissen ergab sich unter Einbeziehung von Streuungen in den Materialeigenschaften der Matrix, der Zugentfestigung der Matrix und der Welligkeit der Bewehrung.

Preface

This dissertation was prepared during my activity as a research associate at the Institute of Concrete Structures of the Faculty of Civil Engineering at Technische Universität Dresden. The topic of this thesis corresponds to one of the research projects within Sonderforschungsbereich 528 (collaborative research centre 528) funded by Deutsche Forschungsgemeinschaft (DFG, German Research Foundation).

At this exposed position I want to express sincere thanks and acknowledgement to several persons. As their and also my mother tongue is German I will proceed on the next two pages in German language as well.

An erster Stelle möchte ich meinem Doktorvater Herrn Prof. Dr.-Ing. habil. Ulrich Häußler-Combe danken. Er hat es mir durch meine Anstellung am Lehrstuhl für Spezielle Massivbauwerke erst ermöglicht, die Schritte zur Promotion gehen zu können. Während meiner Tätigkeit am Lehrstuhl stand er mir zudem stets mit Rat und Tat zur Seite und trug durch eine wohl dosierte Erhöhung des "Promotionsdrucks" zur Vollendung der Arbeit bei.

Herrn Prof. Dr.-Ing. Dr.-Ing. E.h. Dr. h.c. Ekkehard Ramm von der Universität Stuttgart danke ich für die Übernahme des Gutachtens und die wertvollen Hinweise zu dieser Arbeit.

Des Weiteren danke ich Herrn Prof. Dr.-Ing. habil. Bernd W. Zastrau für die Übernahme des Vorsitzes und Herrn Prof. Dr.-Ing. Peer Haller für die Mitwirkung in der Promotionskommission. Nicht unerwähnt soll hier auch die wohlwollende Förderung beider während meiner Zeit als studentische und wissenschaftliche Hilfskraft sowie als Diplomand an ihren Lehrstühlen bleiben, die sicherlich auch zum Wunsch zur Promotion beigetragen hat.

Herrn Prof. Dr.-Ing. Viktor Mechtcherine und Herrn Prof. Dr.-Ing. Manfred Curbach danke ich ebenfalls für die Mitwirkung in der Promotionskommission. Herrn Prof. Curbachs Wirken als treibende Kraft hinter dem Sonderforschungsbereich 528 "Textile Bewehrungen zur bautechnischen Verstärkung und Instandsetzung" sei hier zudem hervorgehoben. Da diese Arbeit innerhalb eines Teilprojekts des Sonderforschungsbereichs entstand, möchte ich auch dafür meine Anerkennung ausdrücken.

Mein Dank gilt außerdem den Mitarbeitern und Mitarbeiterinnen des Instituts für Massivbau und den Mitgliedern des Sonderforschungsbereichs 528 für die gute Zusammenarbeit. Herausheben möchte ich an dieser Stelle die "Besatzung des Raums Bey85", insbesondere die Herren Dipl.-Ing. Mirko Kitzig, Dipl.-Ing. Dipl.-Inf. Kai Schicktanz, Dr.-Ing. Patrick Pröchtel, M.Sc. Henry Schäfer und M.Sc. Joachim Finzel. Die Gespräche und Diskussionen über die Jahre haben sicherlich zu meiner Entwicklung beigetragen. Mirko und Kai sei noch einmal besonders für die Opferung vieler Sommerabend- und Wochenendstunden für das Korrekturlesen der Arbeit gedankt.

Bei der Erstellung der zahlreichen Abbildungen für diese Arbeit waren mir meine studentischen Hilfskräfte Herr Maximilian Weidner und Herr Eric Teichmann eine große Hilfe. Beim Erkenntnisgewinn in der Welt der Stochastik hat mich Frau Daniela Wolf sehr unterstützt.

Nicht zuletzt möchte ich meinen Eltern und meiner Familie für die stete bewusste und unbewusste Unterstützung in den letzten Jahren danken, ohne die der erfolgreiche Abschluss der Promotion zumindest wesentlich schwieriger gewesen wäre.

Selbstverständlich haben mich noch wesentlich mehr Personen auf ihre Weise unterstützt. Ein Aufzählung all jener birgt immer die Gefahr jemanden zu vergessen. Ich mache es daher kurz und sage herzlichst: “You know who you are!” Danke!

Riesa, im März 2011

Jens Hartig

Contents

List of Figures

List of Tables

1. Introduction

1.1. Historical development and selected properties of textile reinforced concrete

Composite materials or composites, which are combinations of different materials leading to a new material, are often used in civil engineering. The reason is that the optimal plain material with regard to structural and economical performance does often not exist. Thus, it is necessary to combine the advantageous properties of single materials for instance regarding load-bearing capacity, durability, weight and costs to eliminate mutually their drawbacks. The structural materials most often used in civil engineering are concrete and steel. Concrete is quite cheap and has relatively large compressive load-bearing capacity, but the tensile load-bearing capacity is very low. Thus, plain concrete is not applicable if significant tensile loading cannot be ruled out in advance, as it is the case in arch structures or short columns where predominantly compressive loading occurs. In contrast, steel has relatively high tensile load-bearing capacity but it is quite expensive.

This led in the middle of the 19^{th} century to the idea to strengthen combined loaded structural elements of concrete as e. g. slabs, which are exposed to bending, with steel bars arranged in the tensile loaded zones of the concrete, see e. g. [Ramm 2007] for a historical review. One of the preceding developments, which has already strong similarity to the material under consideration in this work, was the application of thin steel wire meshes in cementitious matrices, which was called "*Fer-Ciment*" and is known as well as used today as *Ferrocement*, see [Naaman 2000]. A big advantage of the embedding of the steel bars in concrete results from the alkalinity of the concrete, which automatically protects the steel from corrosion resulting from oxidation over long time periods. This protection is also referred to as passivation. Nevertheless, the alkalinity of the concrete reduces successively due to chemical reactions in the concrete with carbon dioxide. This process, also known as carbonation of the concrete, initiates at the concrete surfaces and moves towards the inner parts of the concrete where it enables steel corrosion due to the lost passivation. In order to delay the steel corrosion, an additional concrete cover over the steel bars has to be arranged, which is not necessarily needed for a sufficient stress transfer between concrete and reinforcement by means of bond mechanisms. The additional concrete cover increases the dead weight of the structure and also often prevents the construction of filigree structures. Despite these issues, steel bar reinforced concrete was the most successful building material during the last century and still is.

The durability problem led to the idea to use reinforcement materials instead of steel, which do not suffer from corrosion due to oxidation but also not from the alkalinity of the concrete. Also other considerations as e. g. the desire to optimise the composite material regarding its application or to increase the load-bearing capacity contributed to this development.

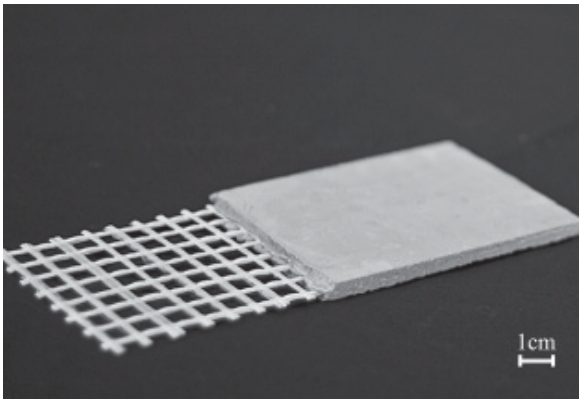

(a) Coated biaxial textile of AR glass embedded in fine-grained concrete; photo: *SFB 528*

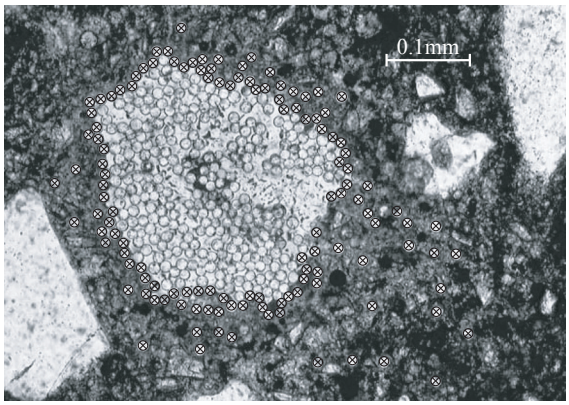

(b) Multi-filament AR glass yarn in fine-grained concrete (⊗ = filament with matrix contact); from [Häussler-Combe & Hartig 2007]

Figure 1.1.: Textile reinforced concrete (TRC)

Examples for reinforcement materials, which offer high stiffness and tensile strength if produced to tiny fibres and exhibit corrosion-resistance in concrete, are for instance carbon, special glass or aramid. Apart from civil engineering, composites of such high-strength fibres and polymeric matrices have been used successfully since the middle of the 20$^{\text{th}}$ century in highly loaded structural elements, as for instance in aerospace or automobile technologies. In civil engineering, this concept is also applied in reinforcement bars of fibre reinforced polymers. However, the costs of this technology, which are considerably higher than those of conventional steel reinforced concrete, limit often an application in practice, so far. A parallel development was the direct addition of short fibres to the concrete. Due to the random distribution of the fibres in the concrete, the main disadvantage of this technology is that the fibres cannot be oriented according to the principal stress directions and, thus, a large amount of fibres remains unloaded. However, also this technology is occasionally applied and still under investigation, e. g. as *Engineered Cementitious Composite* (ECC, see e. g. [Li 2003]), *Ultra-High-Performance Concrete* (UHPC, see e. g. [Fehling et al. 2008]) or *Strain-Hardening Cement-Based Composite* (SHCC, see e. g. [Mechtcherine & Jun 2007]).

Due to the disadvantages of the short-fibre composites, it was somewhat consequential to recollect the way the reinforcement is arranged in conventional reinforced concrete where continuous reinforcement bars or mats of bars are used. In textile technology, which is used to process fibre materials, the single steel bar has its counterpart with fibres while steel reinforcement mats correspond to fabrics or textiles. The textile structures are usually produced from bundles of endless fibres, so-called filaments. These bundles are also named multi-filament yarns or rovings. Depending on the type of the yarn and the used fibre materials such yarns consist of hundreds up to thousands of filaments, which have diameters of usually a few micrometers. As already mentioned, a multitude of suitable fibre materials as e. g. alkali-resistant glass, carbon, aramid or polymeric fibres exists, which might be chosen corresponding to the intended application of the composite. The investigations in this work focus on alkali-resistant glass as reinforcement, which provides sufficiently high Young's modulus and tensile strength as well as corrosion resistance when embedded in concrete. Furthermore, alkali-resistant glass fibres are relatively cheap compared, e. g., to carbon fibres.

(a) Installation of the pedestrian bridge made of TRC (span 16 m) in Kempten (Germany)

(b) Retrofitting of a barrel-shaped roof in Zwickau (Germany)

Figure 1.2.: Applications of TRC; photos: *SFB 528*

Corresponding to the filigree reinforcement, fine cementitious matrices are often used, which have maximum aggregate sizes of only a few millimetres and resemble mortars. Nevertheless, these matrices exhibit strength properties similar to high-strength concretes. Thus, they are referred to as fine-grained concrete. The resulting composite of a fine-grained concrete and a textile reinforcement is called textile reinforced concrete (TRC), see Fig. 1.1(a), and is the subject of this work. TRC has special properties, which result from the heterogeneities of the matrix and the reinforcement. It is for instance observable that reinforcement yarns are usually not completely penetrated by concrete matrix, see Fig. 1.1(b), which leads to complex load transfer mechanisms. This complicates also the modelling of the material behaviour of TRC, e. g., compared to conventional steel reinforced concrete considerably. Early experimental investigations concerning TRC are summarised for instance in [Bentur & Mindess 1990] and [Curbach & et al. 1998]. Meanwhile, a large number of experimental and theoretical investigations on TRC exists, see e. g. [Curbach 2003], [Hegger et al. 2006a], [Brameshuber 2006] and [Curbach & Jesse 2009]. A major part of these investigations was carried out within two collaborative research centres in Aachen (Germany) and Dresden (Germany) focussing on the development of TRC. The present work was carried out in the collaborative research centre in Dresden, which is also referred to as *SFB 528*.

The main advantage of this new material is the slenderness of the resulting structures since the concrete cover, which is necessary to ensure bond between concrete and reinforcement, is also sufficient for the protection of the reinforcement against degradation, e. g. due to abrasion. Typically, the cross-sectional thickness of TRC elements is between some millimetres and a few centimetres, see Fig. 1.1(a). However, TRC is not intended to replace conventional reinforced concrete in its major fields of application but to serve as an alternative if slim structures are demanded. Furthermore, it is excellently suitable for the retrofitting and strengthening of existing concrete structures because only few additional dead weight is applied while increasing the resistance of the structure significantly. For both fields of application, thin new structures and strengthening of existing structures, the applicability has been already demonstrated. Examples for new structures are given with pedestrian bridges of TRC in Oschatz (Germany) and Kempten (Germany), see [Curbach et al. 2007] and Fig. 1.2(a). Structural retrofitting and strengthening were applied at a hypar shell in Schweinfurt (Germany), see [Weiland et al. 2008], and at a barrel-shaped roof in Zwickau

(Germany), see [Schladitz et al. 2009] and Fig. 1.2(b). In the latter cases, it was important to realise thin additional layers to keep the increase of dead weight as low as possible and to preserve the existing shape and dimensions. Besides the mentioned applications with predominantly static loading, TRC has been also found useful to increase the structural resistance under dynamic loading. For the case of seismic loading, conventional reinforced concrete columns retrofitted with TRC were successfully tested by [Bournas et al. 2007]. For the case of impact loading, promising results for conventional reinforced concrete slabs strengthened with TRC were carried out by [Beckmann et al. 2010].

In the mentioned applications, dimensioning was performed mostly based on adapted design rules for conventional reinforced concrete with conservative estimations of the material parameters and experiential knowledge. A prerequisite for appropriate design models is an accurate description of the material behaviour over the entire range of application. To collect this knowledge, a lot of experiments were performed so far. Similar to the behaviour of conventional reinforced concrete, also TRC shows relatively large scatter in the experimental results because of the heterogeneity of matrix and reinforcement. Moreover, most of the effects of the load-bearing mechanisms interact in the experiments, which complicates a clear identification of the extent of a single influence also because the material parameters cannot be modified arbitrarily in the experiments. For the comprehension of the material behaviour of the composite TRC, which results from these effects, mechanical models are useful and important to investigate the influence of single mechanisms on the material behaviour. This is also crucial for a reliable design and dimensioning of structures or structural elements of TRC as the used reinforcement yarns and fine-grained concrete usually fail in a quasi-brittle manner but on different load levels.

1.2. Objective, structure and scope of the work

The investigations in this work are restricted to predominantly tensile loading, while other types of loading as compression, shear, torsion or bending as well as multiaxial loadings are not considered. Therefor, a mechanical model for the uniaxial behaviour of TRC shall be developed, which is able to determine the system response for a broad range of uniaxial tensile tests including single fibre pull-out tests and yarn pull-out tests as well as tensile tests with multiple cracking of the matrix. Although applicable models exist for single tests, a “unified model” is still missing. Of course, the model shall not be developed to serve as an end in itself but to help to shed some light on the influence of single load-bearing mechanisms on the tensile behaviour of TRC.

In order to develop an appropriate model, the material behaviour of the single components of the composite as well as their interaction have to be known as far as possible. For this purpose, Chapter 2 is devoted to the description of the structural properties of the fine-grained concrete and the reinforcement material as well as of the composite. In this context, it is also given attention to the constitutive and failure behaviour of the composite and its constituents under tensile loading. If it seems necessary for the modelling, as in the case of the composite, also the test setups leading to the experimental results are described.

In Chapter 3, existing models concerning the uniaxial tensile behaviour of TRC are briefly reviewed. Meanwhile, a number of models has been developed. Some of them, like the class of fibre bundle models mainly focus on the determination of the constitutive and failure behaviour of plain multi-filament yarns with different load sharing mechanisms, geometrical configurations and statistical distributions of the material properties. Other models, which are called crack bridge models, are developed to investigate the load transfer mechanisms at single cracks. Furthermore, models exist which represent the material behaviour of the composite in a homogenised manner with effective constitutive behaviour without a subdivision into matrix and reinforcement. Based on this review, requirements for an improved, "unified" model are derived.

Chapter 4 includes the derivation and description of the developed model. The model is from the geometrical point of view quite basic as it consists of one-dimensional bar elements and bond-link elements arranged in a lattice scheme. However, it gains complexity from the incorporated material non-linearities, which e. g. include concrete cracking and reinforcement failure as well as degradation of bond between concrete and reinforcement. Furthermore, tension softening of the concrete and waviness of the reinforcement are considered. At first, the material parameters are modelled deterministically, which means that stochastic spatial fluctuations do not exist. In a second step, an approach to introduce scatter to the material properties is applied by means of random fields. The model is implemented in the Finite Element Method. As the computation time for the solution increases with increasing size of the system of equations associated with the finite element model, some effort has been also spent to use efficient solution methods.

In Chapter 5, the results of the computations are presented and evaluated. Therefor, the analytical technique of parametric studies is used. As mentioned previously, three types of experiments are simulated: the filament pull-out test, the yarn pull-out test and the tensile test with multiple matrix cracking. Corresponding to the increasing complexity of these tests also the complexity of the respective model configurations increases from the first to the last of these tests. Thus, especially regarding the tensile test with multiple matrix cracking a large number of parametric studies is carried out to investigate for instance the influence of the non-linearities introduced in the model on the tensile behaviour of the composite. In this context, a perfect reproduction of experimental results is not of primary interest. It is rather intended to find explanations for characteristics in the load-bearing behaviour of TRC, which cannot be explained based solely on experimental results.

At the end, the results of this work are summarised and a number of conclusions are drawn.

2. Material properties and their experimental determination

Before developing models for a material behaviour, it is advantageous to collect already existing knowledge about it, at first. Therefore, the known structural characteristics and properties of TRC are summarised in this chapter. It is started with the composite's constituents, namely the reinforcement of multi-filament yarns and the matrix of fine-grained concrete, and ended with the composite TRC itself. In this context, also experimental methods and respective results for the determination of the load-bearing behaviour of the particular materials and material combinations are addressed and assessed regarding their significance for a subsequent modelling.

2.1. Reinforcement

2.1.1. Reinforcement composition

For TRC, textiles produced of multi-filament yarns of high-performance fibres are used as reinforcement. As it was already mentioned, different fibre materials are applicable as for instance special glass, carbon or aramid. In this work, only alkali-resistant (AR) glass is considered because it exists a large variety of experimental results regarding this reinforcement material in combination with cementitious matrices. Common (quartz) glass is mainly composed of silicon dioxide SiO_2 (silica) and has an amorphous structure built from tetrahedrons of four oxygen atoms with a silicon atom in the centre, see the 2D projections of the atomic structure in Fig. 2.1(b). The amorphous structure results from fast cooling of the molten glass, which suppresses the crystallisation, compare Fig. 2.1(a) and 2.1(b). This is also the reason why glass is often referred to as frozen liquid. Glass usually consists of further constituents as for instance sodium oxide Na_2O (soda) and in the case of alkali-resistant glass an amount of about 20 % zirconium dioxide ZrO_2. Na_2O weakens the structure because the Na atoms separate binding oxygens, see Fig. 2.1(c). In contrast, ZrO_2 might be build in the atomic structure of SiO_2 (or vice versa) because of the similiar chemical configuration of SiO_2 and ZrO_2, which strengthens the atomic structure due to a higher binding energy in ZrO_2 compared to SiO_2.

Quartz glasses have a relatively low resistance against alkaline solutions because OH^- (hydroxide) ions react with the silicon ions, which destroys the tetrahedral configuration, see e. g. [Spauszus 1974]. As it will be shown in Section 2.2.1, hydrated cement has a high alkalinity due to a large amount of $Ca(OH)_2$ (calcium hydroxid). This results in a poor durability of common quartz glasses in cementitious matrices. The higher binding energy provided by

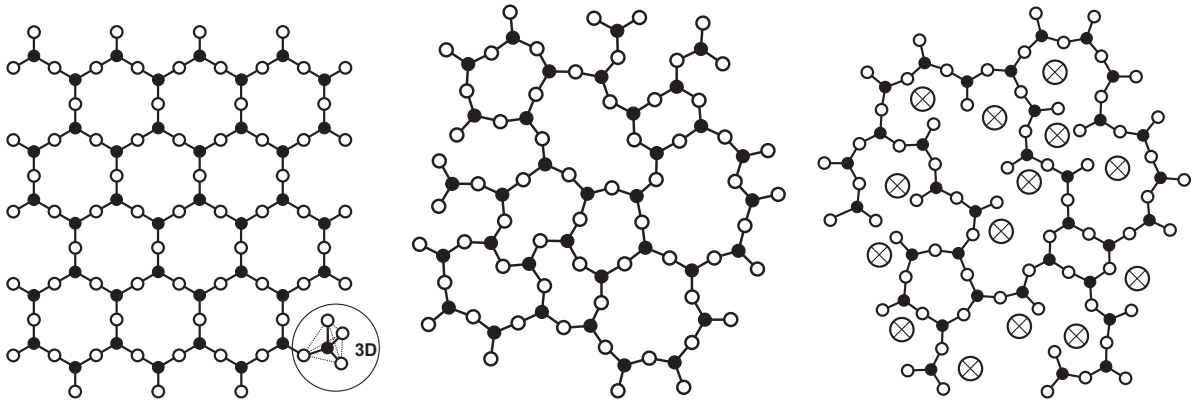

(a) SiO_2 in crystalline configuration, according to [Zachariasen 1932]

(b) SiO_2 in amorphous configuration, according to [Warren 1934]

(c) Structure of soda-silica glass, according to [Warren & Biscoe 1938]

Figure 2.1.: 2D projection of the atomic structure (Si = •, O = ∘, Na = ⊗) of SiO_2 (the fourth O atoms of the tetrahedrons are situated above or below the Si atom)

ZrO_2 leads also to much slower reactions of hydroxide ions with silicon ions and is the main reason for the considerably increased alkali-resistance of such glasses compared to quartz glass. This enables a good durability of such glasses in the alkaline concrete matrix. Detailed compilations of the chemical composition of typical AR glasses can be found in [Abdkader 2004] and [Butler 2009], where also the atomic structure of glass is described in more detail.

The production of the textiles occurs in two main steps. In the first step, the multi-filament yarns are produced, which are used in the second step to produce the textiles. The different production processes and yarn types are described concerning AR glass, e. g., in [Zorn 2003]. For the yarns used in TRC, the so-called nozzle pulling procedure is used, where all filaments of the yarn are pulled simultaneously from the glass melt, which minimises length differences between the filaments and reduces initially non-uniform loading of the filaments in the composite, see Fig. 2.2. The filament diameter, which is for the used fibres in a range of 10 up to 20 μm, can be controlled with the pulling speed. Instead of a diameter specification a fineness is usually given in the unit [tex], which specifies the weight of the fibres per unit length where 1 tex=1 g/km. Subsequently to the pulling-off, a sizing is applied to the filaments, which facilitates further processing and enhances the alkali-resistance of the fibres. Finally, the yarns are wounded on coils where the yarns also receive a so-called protection twist, which prevents the yarns from fanning out, to improve the processability as [Lepenies 2007] points out. At this stage, the multi-filament yarns are ready to be processed to textile structures, which is the second step.

There exist various techniques to produce fabrics from the multi-filament yarns, which lead to different properties. For the application in TRC, the fabrics need special properties as it is pointed out in [Brameshuber 2006]. It is important that the fabrics are open-structured to ensure a good permeability and complete envelope with concrete. Furthermore, it is advantageous for the handling that the fabrics have a sufficient structural stability. Another important property concerns the load-bearing behaviour where usually a direct resistance to loading is necessary, which necessitates a straight alignment of the multi-filament yarns

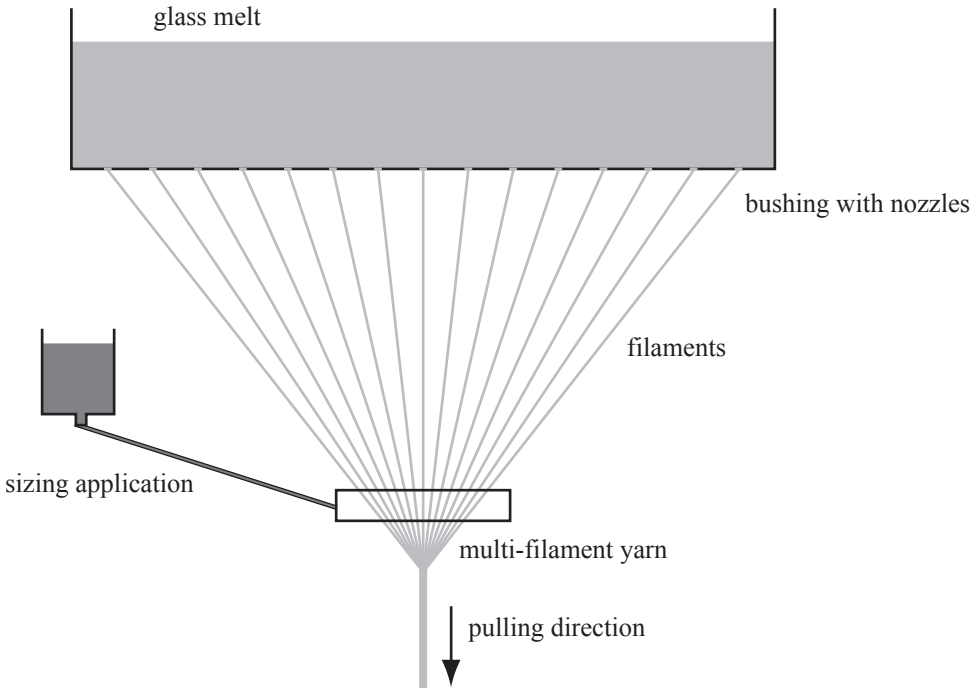

Figure 2.2.: Production process for glass multi-filament yarns; according to [Butler 2009]

in the fabric. Thus, weaved and braided fabrics are disadvantageous for the application in TRC. Better suited are fabrics where the yarn layers of the different directions are stacked, which leads to a straight and parallel alignment of the yarns in the respective layers and facilitates almost arbitrary distances between the yarns. The displacement stability is reached with different fixing techniques, for instance scrims where the crossing points of the yarns are fixed or warp-knits where the fixation is realised along the so-called warp threads, see e. g. [Brameshuber 2006] for more details. Additional displacement stability can be reached with an additional coating, which can be used simultaneously to improve the protection of the glass against the alkalinity of the concrete and to improve the bond between concrete and reinforcement, see [Köckritz 2007]. The coatings are often polymer-based and have to be adapted to the matrix and the reinforcement, see e. g. [Mäder et al. 2004, Gao et al. 2004, Gao et al. 2007, Scheffler et al. 2009a, Scheffler et al. 2009b].

2.1.2. Tensile properties of alkali-resistant glass

In the commonly applicable loading range, glass shows almost linear elastic tensile behaviour up to failure, which occurs in a brittle manner. Thus, the tensile stress-strain (σ-ε) behaviour of glass until failure can be described with Hooke's law:

$$\sigma = \begin{cases} E_g \varepsilon & \text{for} \quad 0 \leq \varepsilon \leq \frac{f_{gt}}{E_g} \\ 0 & \text{for} \quad \varepsilon > \frac{f_{gt}}{E_g} \end{cases} \tag{2.1}$$

with the Young's modulus E_g and the tensile strength f_{gt} of the glass, see Fig. 2.3(a). Both, Young's modulus and tensile strength depend on the composition of the glass as indicated previously. Plain SiO_2-glass has a Young's modulus of about $73\,000\,\mathrm{N/mm^2}$, see

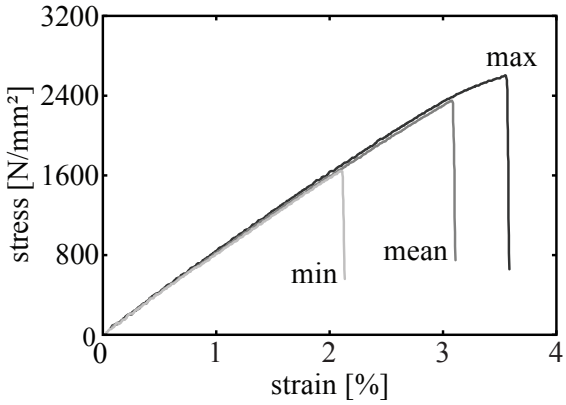

(a) Filaments of NEG-ARG 620-01; data from [Abdkader 2004]

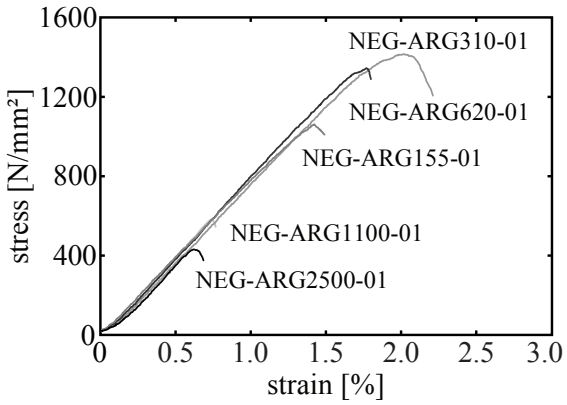

(b) Multi-filament yarns; data from [Abdkader 2004]

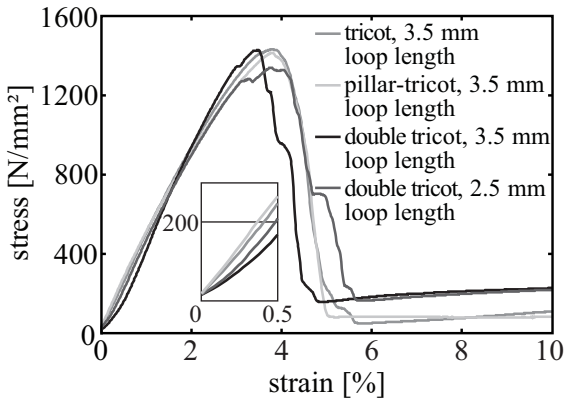

(c) Warp-knitted textiles of NEG-ARG 310-01 with different binding techniques; data from [SFB528 2001]

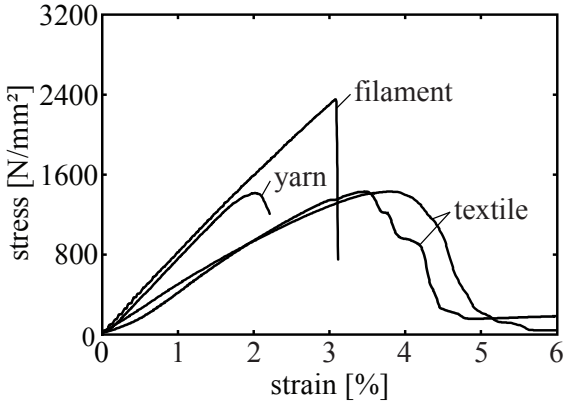

(d) Comparison of filaments, multi-filament yarns and textiles

Figure 2.3.: Stress-strain relations of AR glass (Abbreviated notations refer to alkali-resistant glass (ARG) produced by "Nippon Electric Glass" (NEG) with a fineness of, e. g., 310 tex with different sizings (01), see [Abdkader 2004] for details)

[Le Bourhis 2008]. It is known that the addition of alkalis, e. g. NaO_2, reduces E_g because of the disturbance of the atomic structure while other additions, e. g. ZrO_2, can increase E_g, see [Kühne 1984]. The AR glass filaments used in the context of this work have according to [Abdkader 2004] Young's moduli in the range of 73 000-80 500 N/mm^2 depending on the filament type and the sizing. These values were determined by [Abdkader 2004] in a testing machine of type Fafegraph ME. The filament was attached to the testing machine by means of two clamps where one is fixed and the other is movable. The applied force and the displacement of the movable clamp were measured with internal devices. To gain the mean stress in the filament, the applied force was related to the cross-sectional area of the filament, which was measured by [Abdkader 2004] with a device of type Vibromat ME. The mean strain resulted from the measured displacement related to the free length of the filament. The mean Young's modulus of the filament can then be determined as slope of the resulting stress-strain relation, see e. g. Fig. 2.3(a). The indirect displacement measurement by means of displacements of the testing machine instead of a direct measurement on the specimen leads always to errors concerning the determination of the response of the specimen, which

have to be reduced as far as possible. In this case, sources of error are e. g. a slipping of the filaments in the clamp and deformations of parts of the testing machine itself, which can lead to an overestimation of the deformations of the specimen and thus to a reduction of the determined Young's modulus. However, [Abdkader 2004] spent a lot of effort in reducing these errors. Furthermore, [Abdkader 2004] experienced no dependence of the Young's modulus on the geometry, i. e. on the filament diameter or free length.

While the Young's modulus of glass mainly depends on the atomic structure but not on geometrical properties of the investigated glass body, things are different concerning failure or tensile strength, respectively. For instance [Le Bourhis 2008] points out that "fracture depends on intrinsic properties but more importantly on extrinsic ones (process-induced and damage-induced flaws) that make the problem very complex." The theoretical tensile strength of plain SiO_2-glass only considering the atomic structure is as high as $16\,000\,\mathrm{N/mm^2}$, see [Le Bourhis 2008]. Unfortunately, this value is far above those values, which filaments possess in practice, not to mention bulky glass bodies. Tensile tests by [Abdkader 2004] revealed mean tensile strengths of AR glass filaments in a range of about $1500\,\mathrm{N/mm^2}$ up to $2300\,\mathrm{N/mm^2}$ depending on the type and the sizing of the filament, see Fig. 2.3(a). Regarding the used AR glass, the influence of the modified atomic structure compared to plain SiO_2-glass is not entirely clear but seems to have also less importance compared to the extrinsic properties as mentioned previously. The starting points of glass failure are usually defects or flaws on the surface of the glass body, which lead to stress concentrations and unstable crack growth if failure once is initiated. In [Butler et al. 2009] several reasons for the relatively high tensile strength of glass fibres compared to bulky glass bodies are summarised:

- high cooling rate in the production process, which leads to a homogeneous glass structure without separation of single ingredients and crystallisation
- development of internal stress states during cooling leading to compressive stresses near the surface and tensile stresses inside the fibres, which act as a pre-stressing and extenuate the stress concentrations at the flaws
- because of the small dimensions a size effect occurs, which leads to a lower probability of critical flaws compared to the bulky glass bodies.

Furthermore, it is observable that the tensile strength of the filaments depends also on the free length of the tested specimens. The free length is the length between the fixation positions of the specimen in the test setup, see Fig. 2.4. The highest tensile strength can be achieved with short free length, while the mean tensile strength decreases with increasing specimen lengths. This can be explained by means of statistics according to Weibull theory [Weibull 1939], which states for instance that the probability of critical flaws increases with increasing specimen lengths. This effect is also referred to as statistical size effect. Another size effect, which is, however, not completely independent from the statistical size effect is the energetic size effect, which results from an increasing stored elastic energy in the filament with increasing filament length. Due to the increased stored energy, flaws start to grow unstable at lower load levels, which leads to lower tensile strength. A more detailed discussion of sources and effects of size effects can be found, e. g., in [Curbach et al. 2006].

The constitutive behaviour of the yarns under tensile loading is determined in similar tests as for filaments. However, more attention needs to be paid to the load application to the

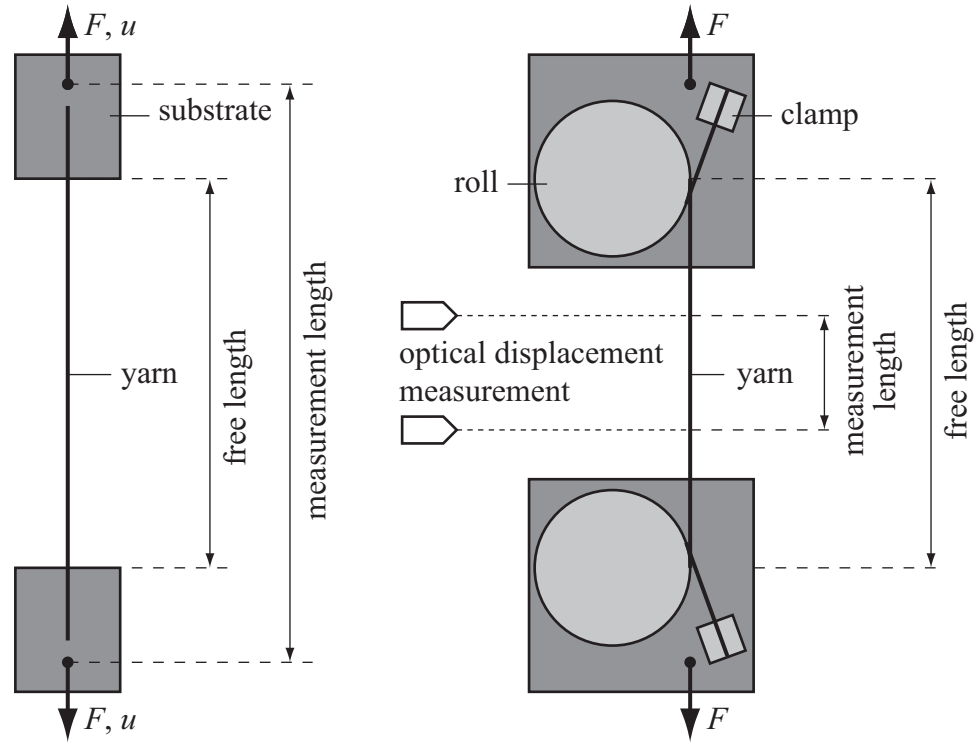

(a) Yarn fixation via glueing, according to [Al-Masri & Wulfhorst 2001]

(b) Test setup by [Abdkader 2004]

Figure 2.4.: Test setups for tensile tests of multi-filament yarns

fibres as a bundle of filaments needs to be fixed in the testing machine. Clamping seems disadvantageous in this context as it leads to lateral pressure, which might lead to artificially earlier failure of the filaments compared to embedded filaments. Glueing on or in a suitable substrate as e. g. paper or epoxy resin seems to be appropriate but increases the effort of specimen preparation, see Fig. 2.4(a). A novel technique was developed by [Abdkader 2004] with adding interposed rolls before the clamps to homogenise the loading of the filaments, see Fig. 2.4(b). As in the case of the filament tests, the deformation measurement is of importance for the determination of the Young's modulus. In order to avoid influences of the machine deformation on the measured yarn deformation, [Abdkader 2004] applied optical displacement measurement within the free length of the yarn, see Fig. 2.4(b). In contrast, [Al-Masri & Wulfhorst 2001] used the displacement of the traverse of the testing machine as indicated in Fig. 2.4(a), which leads to an overestimation of the deformations of the specimen and to an underestimation of the Young's modulus of about 15 up to 30 % compared to the values determined by [Abdkader 2004] as it is also pointed out in [Jesse 2004].

In the yarn tests, often an initially reduced Young's modulus is observable, which merges towards the mean Young's modulus of the filaments with increased loading, see [Abdkader 2004]. Fig. 2.3(b) shows respective stress-strain relations where the stress corresponds to the measured force related to cross-sectional area of the yarn and the strain is the measured relative displacement related to the measurement length. The explanation for the delayed activation of the yarn is an initially imperfect alignment of the filaments, a so-called waviness,

e. g. due to the coiling of the yarns. Thus, it is not a material property but results from a geometrical effect on small scale. It leads to a successively increasing participation of the filaments in load-bearing with increasing loading. As a yarn consists of a number of filaments also the mean tensile strength of the yarn differs compared to filaments. In general, it is observable that the mean tensile strengths of the yarns are with values in a range of about 400-1600 $\mathrm{N/mm^2}$ considerably lower compared to those of respective filaments [Abdkader 2004], which can be explained again with the larger probability of critical defects due to a larger number of filaments, see also [Daniels 1945, Curbach et al. 2006, Chudoba et al. 2006, Vořechovský & Chudoba 2006]. Concerning the failure mechanisms, it can be noticed that the ductility increases with the number of fibres simultaneously loaded. This means while a single filament behaves linear elastic up to the brittle failure, a yarn shows a distinct reduction of the stiffness before failure due to the failure of the weakest filaments, which does not lead to global failure, and could show post-strength resistance depending on the specimen length and the scatter of the filament tensile strengths, see [Abdkader 2004, Curbach et al. 2006, Vořechovský & Chudoba 2006] and Fig. 2.3(b).

The tensile behaviour becomes even more complex for textiles where several yarns are loaded in parallel. Experimental results of tensile tests with textiles for TRC are rare, see e. g. [SFB528 2001, Stockmann 2002]. However, those applicable are performed similar to the yarn tensile tests with simple clamping constructions at the ends of the textiles. The effect of an initially reduced mean Young's modulus is more pronounced compared to one yarn because the textile processing introduces further waviness to the yarns, which mainly depends on the binding technique. Respective, stress-strain relations where the stress is the applied force divided by the sum of the cross-sectional areas of the yarns and the strain is the measured displacement of the traverse of the testing machine related to the free length of the specimen are shown in Fig. 2.3(c). As for the single yarn, the Young's modulus of the textile merges theoretically towards the mean Young's modulus of the filaments. However, this does not coincide with Figs. 2.3 (c,d) where the Young's modulus after fibre alignment is clearly lower compared to filament and yarn. This can be explained, see also [Jesse 2004], with an insufficient determination of the strain based on the displacement of the traverse of the testing machine instead of a more exact measurement directly on the specimen as discussed previously regarding the yarn tensile tests. However, a certain reduction of the Young's modulus might occur, because of pre-existing failed filaments or weak, pre-damaged filaments already failing before all filaments are activated. If the measured force is related to the cross-sectional area of the fibre material, an additional coating of the textile might also apparently increase the stiffness of the textiles and the Young's modulus, respectively. Concerning the mean tensile strengths of the textiles, a further reduction compared to those of respective yarns can be noticed. This can be again explained with stochastic effects but also with the degradation, up to the failure, of single filaments due to the production and processing, see Fig. 2.3(d). To a certain extent this effect can be reduced with the application of coatings, which leads to a homogenisation of the normal stresses over the cross section and, thus, a delayed failure of the reinforcement. The failure mechanism becomes more ductile compared to the single yarns, as more filaments are loaded in parallel and a load redistribution is possible to some extent, see Fig. 2.3(d). Moreover, also the delayed activation of a fraction of filaments due to waviness might increase the ductility.

2.2. Matrix

2.2.1. Matrix composition

Besides the reinforcement, TRC consists also of a matrix where the reinforcement is embedded. While for fibre-reinforced polymers (FRP) resins, e. g. epoxy resins, are used, concrete or cementitious matrices are applied for TRC. Concrete matrices are themselves compound materials consisting essentially of hardened cement paste, aggregates and pores. This subdivision corresponds to the mesoscopic observation level regarding concrete and is only one of the possible observation levels. For larger structures it might be more useful to consider concrete as a homogeneous material with mean properties of its constituents, which is also known as macroscopic observation level. Vice versa, one can also describe the constituents more detailed, e. g. on the microscopic observation level, in order to gain more information about the material behaviour. This will be done in the following for the hardened cement paste. A further refinement up to the atomistic or nanoscopic level is possible but is omitted here except for some chemical considerations.

Concerning the composition, the matrix used for TRC differs considerably from conventional concrete. One reason are the small distances of only a few millimetres between the layers of the reinforcement textiles, which necessitates the application of relatively small aggregates. In the used TRC, the maximum aggregate size is about 1 mm. This enables also the penetration of the matrix into the textiles, which usually have yarn spacings of a few millimetres, i. e. approximately 10 mm. Thus, the matrix appears more as a mortar but some of the mechanical properties, which are discussed in the next section, rather correspond to high-strength concretes. Comparing the artificial stone concrete to natural stones, the used fine-grained concrete resembles a sandstone while normal concretes are more like conglomerates or breccias depending on the shape of the aggregates.

Since the force transmission between matrix and reinforcement is in contrast to steel bars only possible via adhesion and friction, because of the missing ribs at the reinforcement, the matrices also have to be adapted to the reinforcement material in order to achieve good structural performance and durability. Especially the alkalinity of the matrix is at least in combination with glass reinforcement an important factor because a high alkalinity can lead to degradation of the glass filaments despite the improved alkali-resistance of the used AR glass, see for instance [Butler et al. 2009]. Therefore, matrices with binders with low Portland cement content are preferred in general. Nevertheless, also the binders usually used for TRC, e. g. blast furnace cements, contain a considerable amount of Portland cement.

The major ingredients of Portland cement are calcium oxide (lime) CaO (≈65 %), silicium dioxide (silica) SiO_2 (≈20 %), aluminium oxide (alumina) Al_2O_3 (≈6 %) and ferric oxide (rust) Fe_2O_3 (≈3 %), see e. g. [Barthold et al. 1997]. Additionally, it usually contains certain amounts of MgO, SO_3, Na_2O and K_2O. These ingredients are burned in a so-called rotary killn where the materials are sintered, which produces the so-called Portland cement clinkers. Through a grinding process the well-known powder of cement grains is achieved, where gypsum $CaSO_4{\cdot}2H_2O$ (≈4 %) is added, see e. g. [van Mier 1996] for more details concerning the production process. The main clinkers that develop in this process are given in Table 2.1.

Table 2.1.: Portland cement clinkers; from [van Mier 1996]

name	**chemical composition**	**abbrevation**
tricalcium silicate	$3CaO{\cdot}SiO_2$	C_3S
dicalcium silicate	$2CaO{\cdot}SiO_2$	C_2S
tricalcium aluminate	$3CaO{\cdot}Al_2O_3$	C_3A
tetracalcium aluminoferrite	$4CaO{\cdot}Al_2O_3{\cdot}Fe_2O_3$	C_4AF

During the hydration process, which is described in detail e. g. in [van Mier 1996] and [Barthold et al. 1997], the cement reacts with added water denoted with H. At first, the water reacts with C_3A and gypsum:

$$C_3A + 3(\underbrace{CaSO_4 \cdot 2H}_{\text{gypsum}}) + 26H \rightarrow \underbrace{C_6A(SO_4)_3 \cdot 32H}_{\text{ettringite}}$$

leading to the development of hard shells of so-called ettringite crystals around the cement grains. The ettringite layer hampers the water to penetrate into the cement grains, which delays the hydration. Due to increasing pressure in the shells caused by further reactions, the ettringite layer breaks after a certain time (≈1-2 hours) and the hydration can proceed with the C_3S and C_2S clinkers. In both reactions the same reaction products develop:

$$2C_3S + 6H \rightarrow C_3S_2H_3 + 3CH$$

$$2C_2S + 4H \rightarrow C_3S_2H_3 + CH,$$

which are calcium silicate hydrates (CSH) and calcium hydroxide (CH), where CH strongly influences the alkalinity of the concrete. The calcium silicate hydrates constitute as needles growing from the cement particles, where the needles from the C_3S reaction are known to be longer and to develop earlier than the needles from the C_2S reaction, which backfill the remaining space. The CH crystals are hexagonal shaped and develop between the CSH needles, see Fig. 2.5. It is known that CH has relatively low strength, which reduces the strength of the hardened cement paste and should be limited in normal concrete. On the other hand, CH is a prerequisite for the initiation of the hydration of blast furnace slag and fly-ash. Furthermore, CH is one of the substances in the concrete, which are responsible for the high alkalinity.

Blast furnace cements and fly-ash cements have compared to Portland cement reduced contents of CaO (≈50 %) and increased contents of SiO_2 (≈30 %) as well as Al_2O_3, see [van Mier 1996]. Furthermore, blast furnace cement consists of more MgO. For the hydration of blast furnace and fly-ash cements, which occur much slower compared to Portland cement, the CH is the activator while the reaction products are the same as for Portland cement [Barthold et al. 1997]. Because of the reactions with CH the alkalinity of the concrete is reduced if blast furnace cements or fly-ash cements are used, see [Butler et al. 2009] for a detailed description. Moreover, due to the secondary hydration of blast furnace and fly-ash cements, which consumes weak CH, the strength develops quite slowly while the final strength is potentially higher compared to plain Portland cement.

[1]Environmental Scanning Electron Microscope

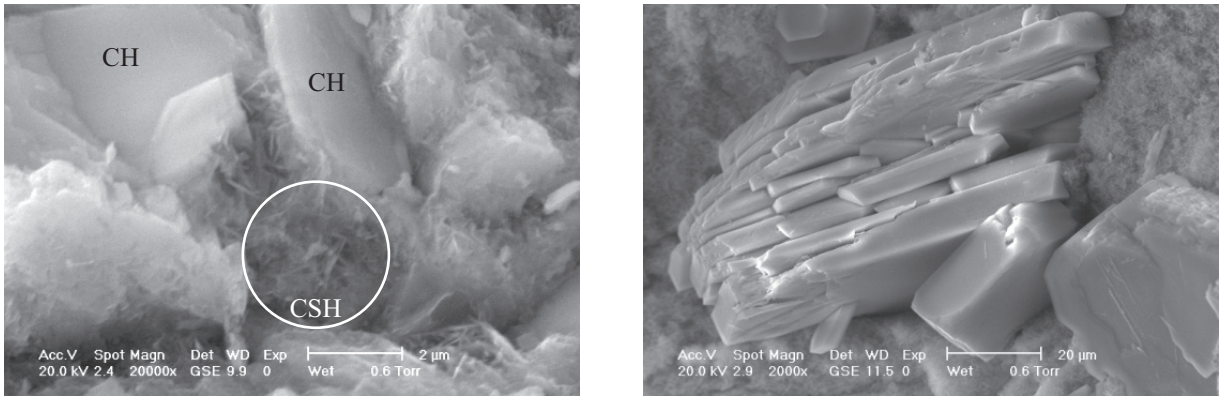

(a) CH and CSH phases

(b) CH phase

Figure 2.5.: ESEM[1]-images of cement paste micro-structure; from [Butler 2009]

The hardened cement paste is not a compact medium but includes more or less smaller and larger pores. These pores may result from imperfect compaction leading to air inclusions. Other pores result from initially free water, which is not used in the hydration process of the cement. Furthermore, so-called micro-cracks exist, which develop in the hardening process of the concrete because of differential shrinkage and thermal gradients between aggregates and hardened cement past, see [van Mier 1996]. These pores or voids weaken the material structure of the concrete.

Hitherto, only the hardened cement paste was characterised despite normal concretes consist to about 75 vol.-% of aggregates. Although, in the used fine-grained concrete this portion is redued to about 50 %, the aggregate and the bond between hardened cement paste and aggregate influence the material behaviour of the concrete decisively. It is known that the structure of the hardened cement paste in the vicinity of the grains ($<100\,\mu$m thickness) is different compared to the hardened cement paste distant to the grains. This so-called interfacial transition zone (ITZ) has a porous structure and consists of ettringite, CH and CSH. It is considered to be the weakest link in normal concretes, which is also experimentally proved, see e. g. [van Mier 1996] for a detailed description of the structure and properties of the interfacial transition zone.

Based on the composition of the matrix, a number of predictions concerning the material properties and the respective development are possible. This might be helpful in the case that these properties were not determined for the special material and, thus, have to be estimated based on properties of similar materials. For the experiments, presented in Section 2.3 matrices with binders of blast furnace cement, fly ash and microsilica are used. The detailed compositions of these matrices can be found in Table 2.2. Besides, the matrix compositions used for the specimens by [Jesse 2004] and [Butler et al. 2009] also a quite different matrix containing a high amount of Portland cement is included because [Brockmann 2005] studied the post-cracking behaviour of this matrix, which was not performed for the other two matrices.

Table 2.2.: Compositions of fine-grained concretes for reinforcement of AR-glass (content of superplasticiser not considered)

component	Jesse* [kg/m³]	Butler** [kg/m³]	Brockmann*** [kg/m³]
Portland cement (CEM I 52.5)			490
blast furnace cement (CEM III/B 32.5 NW/HS/HA)	628	550	
fly ash	266	248	175
microsilica suspension (50 mass-% powder, 50 mass-% water)	101	55	35
sand 0-1 mm	942	1101	
sand 0-0.6 mm			1214
water	215	248	280

* from [Jesse 2004]

** matrix M1 from [Butler et al. 2009]

*** matrix PZ-0899-01 from [Brockmann 2005]

2.2.2. Tensile pre- and post-cracking behaviour

The constitutive behaviour of concrete is characterised by far-reaching differences between tensile and compressive loading. As only predominantly tensile loading is considered in this work, the following description is limited to this case. However, in order to proof the statement that the used matrix has properties similar to high-strength concrete also the direct compressive strength is given in Tab. 2.3.

There exist different techniques to determine the tensile behaviour of concrete where the uniaxial tensile test seems to be the most appropriate. In this type of test, usually waisted or notched specimens are exposed to uniaxial tension applied with displacement control and the stress-strain response is recorded. Due to the brittleness and the heterogeneity of the material, difficulties occur concerning the correct determination of the tensile strength in these tests. Yet the correct experimental determination of the tensile strength is difficult, more problematic is still the situation regarding the correct determination of the post-cracking behaviour. A good review of respective experimental methods and associated problems is given by [van Mier & van Vliet 2002]. Probably due to the problems summarised in [van Mier & van Vliet 2002] and relatively strong autogeneous shrinkage of the matrix leading to cracks in unreinforced specimens as [Jesse 2004] reports, no experimental data of the direct tensile strength and the post-cracking behaviour is available for the used fine-grained concrete. Only flexural tests were performed to determine the tensile strength, see [Jesse 2004].

In general, concrete shows initially almost linear elastic behaviour under tensile loading, see Fig. 2.6. With increasing loading, the exisiting micro-cracks, which are initially distributed mostly in the interfacial transition zones between the hardened cement paste and the aggregates, successively open and propagate when the load is further increased. In normal concretes, the micro-cracks propagate into the hardened cement paste because of its lower

Table 2.3.: Experimentally determined material properties of the matrix

property	**symbol**	**unit**	**value**
Young's modulus*	E_c	N/mm^2	28 500
flexural tensile strength	$f_{ct,f}$		
mean value*		N/mm^2	7.11
standard deviation*		N/mm^2	0.76
empirical 5 %-percentile*		N/mm^2	5.84
empirical 95 %-percentile*		N/mm^2	8.41
approx. fracture energy**	G_f	N/m	40
approx. maximum stress-transferring crack width**	w_c	mm	0.2
direct compressive strength*	f_{cc}	N/mm^2	76.3
density*	ϱ_c	g/cm^3	2.17

* from [Jesse 2004]

** according to [Brockmann 2005]

strength compared to the aggregate while in high-strength concretes also the aggregates might be involved, see e. g. [Remmel 1994]. As the strength properties of the fine-grained concrete indicate a high-strength concrete, it can be assumed that cracks also propagate through the grains in TRC. Furthermore, new micro-cracks might develop at positions with local stress concentrations and low local strength, for instance at pores or voids. At a certain load, which is usually estimated with about 70 % of the ultimate load, see e. g. [Barthold et al. 1997], the development of further micro-cracks localises in a narrow band called the fracture process zone. In a uniformly loaded specimen without sectional weakening, the position of this zone cannot be forecast in reality because of the heterogeneity of the material. It develops at the zone with the largest defects and/or highest local loading. While the deformations u increase in the fracture process zone, the deformations decrease in the other parts of the specimen, compare curves for ranges "A" and "B" in Fig. 2.6. The crack development leads to a reduction of intact cross-sectional area and, consequently, to a reduction of the stiffness, which is reflected in the stress-strain relation with a decreasing slope or tangential modulus, respectively. The tensile strength f_{ct} is then defined as the stress value where the tangential modulus is equal to zero. The used fine-grained concrete has a relatively large tensile strength, see Tab. 2.3, which corresponds to a high-strength concrete.

After reaching f_{ct} often brittle failure is assumed in practice. However as it is indicated in Fig. 2.6, cementitious matrices as for instance concrete or mortar show post-strength resistance. Reaching f_{ct}, the spatially distributed micro-cracks in the fracture process zone start to coalesce leading to the development of macro-cracks. In the case of macro-crack development, a stress-strain relation for the entire specimen as appropriate for the description of the pre-cracking behaviour cannot describe the inhomogeneous deformations, which start to increase in the vicinity of the localisation. Instead, usually a stress-crack width (σ-w) relation is established. Therefore, the deformations u are usually determined over a small length over the crack, e. g. range "A" in Fig. 2.6, which is often forced by notches to develop at a predefined position in the specimen. The measured deformation contains elastic deformations and inelastic deformations due to crack growth. To establish the σ-w relation, it is assumed

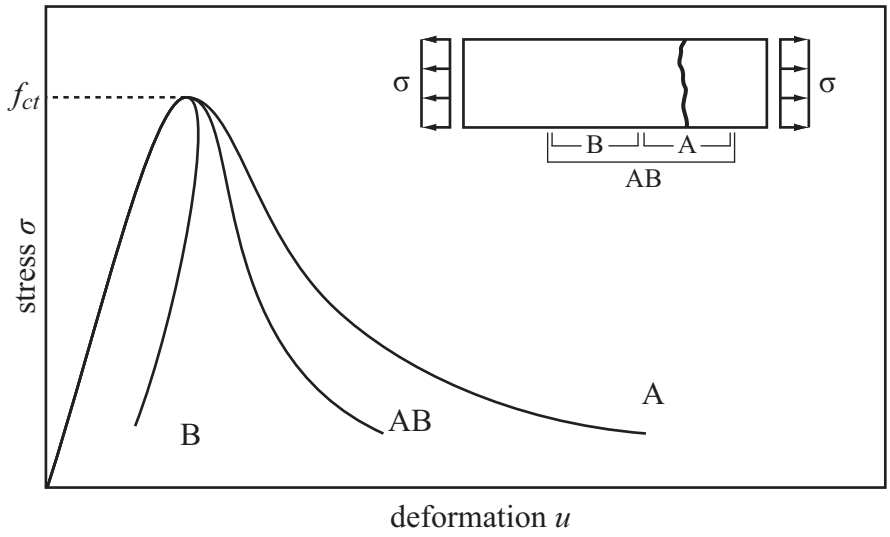

Figure 2.6.: Schematic stress-deformation diagrams for measuring devices placed at different positions on a tensile bar, according to [van Mier 1996]

that the inelastic deformations correspond to the crack width w, i. e. the fracture process zone is replaced virtually by a fictious crack, see [Petersson 1981]. This corresponds also to the assumption of the fictious crack model by [Hillerborg et al. 1976], see also Fig. 3.6. Because of the heterogeneity of the concrete the development of macro-cracks is not a continuous process. It is rather characterised by different mechanisms as crack propagation and stopping if e. g. a crack runs from the cement paste against an aggregate grain. Furthermore, the macro-cracks might also show coalescence, branching, bridging and overlapping, as [van Mier 1996] points out in detail. Schematically, the crack development in a cross section is shown in Fig. 2.7. In Fig. 2.16, typical matrix crack patterns of TRC specimens are shown, which indicate that the described mechanisms also occur in the matrix used for TRC. Even if the crack has completely separated the entire cross section, some residual stresses might be transferable over the crack by means of friction or interlocking between the crack faces. These effects are especially pronounced with large and rough aggregates and low tensile strength of the hardened cement paste, where the macro-cracks flank the aggregates. As the fine-grained concrete has small aggregates and a relatively high tensile strength, the effects of friction and interlocking can be expected rather small, see also [Remmel 1994].

For mechanical models, the energy which is needed to separate the cracked cross section is of importance. It is also referred to as fracture energy G_f and is defined as area under the σ-w curve or respectively the integral

$$G_f = \int_0^{w_c} \sigma \mathrm{d}w. \tag{2.2}$$

where w_c is the crack width where no further stress is transferred over the crack any more. This concept has some deficiencies. One deficiency is that not the entire energy applied to the specimen is dissipated in the fracture process of the final crack. Energy might be also dissipated e. g. as heat or for inelastic deformations distant to the macro-crack. Moreover, the crack width w is usually not directly measured in the experiments as previously pointed out. It represents rather the integral of the inelastic deformations in the fracture process

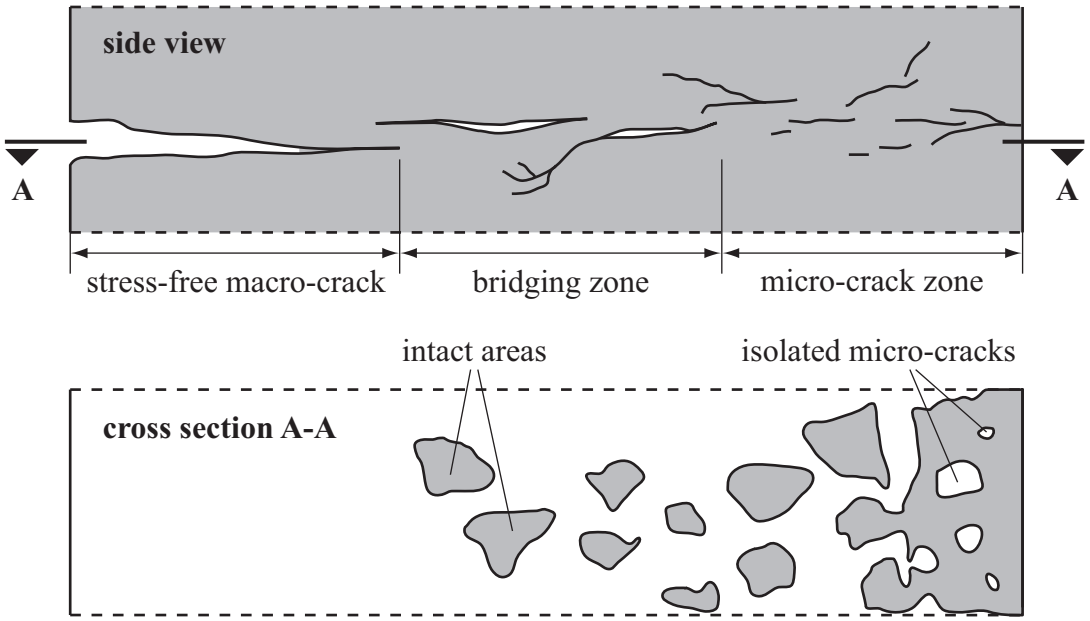

Figure 2.7.: Schematic cracking mechanisms of concrete in mode I fracture, according to [van Mier 1996]

zone. Thus, respective models will usually overestimate crack widths in a macroscopic point of view.

The name fracture energy might be also misleading as the unit of G_f is [N/m]. It is in fact an energy related to an area. Often the cross-sectional area of the specimen is used, which is an assumption neglecting e. g. the roughness of the crack faces and surfaces of other micro-cracks in the fracture process zone. Thus, G_f is only a useful estimate. The total fracture energy, which is needed for the specific specimen under consideration for a complete rupture, can be determined by means of a force-crack width relation. However, this measure does not represent a material property as it depends also on the size of the specimen. It should be further pointed out that the post-cracking behaviour of the concrete can be only observed if the specimens are sufficiently small. The reason is that the elastic energy stored in the specimen increases with increasing specimen size and in the case of crack initiation the increasing stored elastic energy leads to a sudden rupture of the specimen. This effect is also known as energetic size effect, see e. g. [Bažant 2002] and [van Mier & van Vliet 2002].

Besides the post-cracking tensile behaviour of concrete in the loading regime, it is also of vital interest how the material responds to unloading and reloading in the post-cracking state. Corresponding experimental results are presented e. g. in [Gopalaratnam & Shah 1985] and [Cornelissen et al. 1986]. In Fig. 2.8, experimental results of concrete exposed to different cyclic loading regimes by [Cornelissen et al. 1986] are shown. The courses of the stress-crack opening (σ-w) relations in unloading and reloading show significantly non-linear courses. A problem regarding the interpretation of these test results is that the measured deformations include elastic deformations in the undamaged parts in the vicinity of the cracks and the crack opening itself, which is most often not uniform over the cross section, see Fig. 2.7. A detailed explanation of the cyclic tensile post-cracking behaviour is a topic on its own and not attempted within this work. However, some interesting observa-

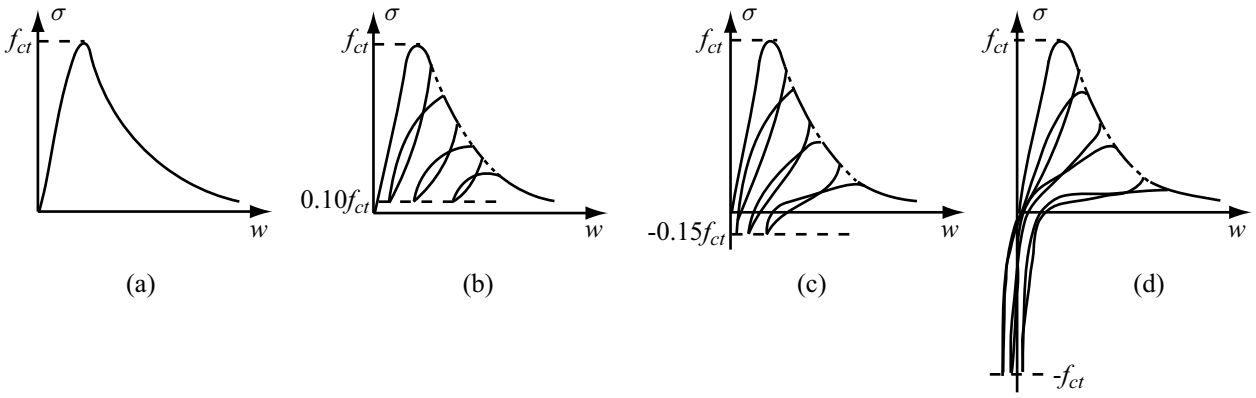

Figure 2.8.: Uniaxial stress-crack opening response of concrete to predominantly cyclic tensile loading for different loading regimes (a-d); according to [Cornelissen et al. 1986]

tions in these tests are summarised briefly in the following. For instance, it can be seen in the σ-w relations in Fig. 2.8 that also in the case of complete unloading ($\sigma = 0$) inelastic deformations remain. These remaining deformations in concrete do not result from plasticity as in the case of metals. They are rather an outcome of incompatibilities of the crack faces e. g. due to small transverse motions, which need additional energy to be closed in the unloading regime. An argument for this explanation is that the remaining deformations are smaller under repeated unloading and reloading if the loading regime covers also the compression range, see Fig. 2.8(c,d) where the cracks are forced to close. This corresponds also to the previous brief discussion of frictional forces and interlocking of grains as well as crack branching and coalescence associated with concrete cracking. Furthermore, experimental results in [Gopalaratnam & Shah 1985] indicate that larger elastic back-deformations occur in mortars than in concrete. The reason seems to be that large aggregates are missing in mortars and consequently the fracture surface is smoother. Moreover, the experimental results presented in [Gopalaratnam & Shah 1985] and [Cornelissen et al. 1986] indicate that the envelope of the cyclic stress-strain response is just the stress-strain relation for monotonic loading. This is important for the subsequent modelling when only monotonic stress-strain relations are at hand (if they are) to determine material properties and to estimate missing ones.

The post-cracking behaviour was not determined experimentally for the used fine-grained concrete. Thus, these material characteristics have to be estimated based on experimental results on different but related matrices. In [Brockmann 2005], the fracture behaviour of matrices close-related to the matrix used here are investigated. However, three-point-bending tests were carried out where the determination of the tensile strength and with it the fracture energy is problematic, because of the non-uniform state of stress as it is pointed out in [van Mier & van Vliet 2002]. Nevertheless, as a reference for the fracture energy G_f a value of 40 N/m is used corresponding to mixture PZ-0899-01 in [Brockmann 2005]. In order to establish a $\sigma - w$ relation, see Section 4.2.1 and Fig. 5.46, the crack width at which no further stress can be transferred over the crack w_c has to be known. Based on the results by [Brockmann 2005] a value of 0.2 mm was estimated for w_c.

2.3. Composite

2.3.1. Mechanical and structural properties

The composite TRC is given with the reinforcement yarns or textiles embedded in the cementitious matrix. As pointed out in Section 2.1, the reinforcement yarns are composed of a large number of filaments, which are densely packed. Thus, the question arises how the yarns are penetrated with matrix. Of course, a penetration is a priori only possible if no additional coating is applied to the yarns, which prevents an intruding of matrix particles. However also without additional coating, the small dimensions of the filaments with diameters of about 10-20 μm and the distances between the filaments in the same magnitude lead to filtration effects. It can be expected that aggregates are completely prevented from intrusion and also the cement paste only reaches into an outer layer of the yarns because of its relatively high viscosity. The yarn core might be only reached by cement grains dissolved in water, which might not build stable connections between filaments. Also in the case of polymer-based coatings as mentioned in Section 2.1.1, the polymer chains are dissolved in water when applied to the textiles. Consequently, this leads also to discontinuous cross-linkages between the filaments when the water has dissolved after thermal curing, and supposedly to a decreasing number of cross-linkages towards the yarn core.

Thus, within a yarn two major bond zones exist in general, see Fig. 1.1(b). In the outer ring zone of a yarn, the so-called fill-in zone, where the matrix has continuous contact to the filaments, a relatively strong adhesive bond between the matrix and the filaments exists. Optionally, coatings constitute bond intermediators between matrix and filaments. The adhesion is mainly caused by chemical bonds between the cement paste and the filaments but might also result from mechanical interlocking. Towards the core of the yarns less matrix intrudes. This results in a primarily frictional load transfer between the filaments after the initial resistance of the weak adhesive cross-linkages is exceeded. However, if additional coatings are applied, which intrude to the core of the yarns, the bond can be assessed substantially stronger due to a larger number of adhesive cross-linkages and adapted bond properties between coating, filament and matrix. The frictional load transfer depends on the surface roughness and the lateral pressure acting at the contact area. In the frictional load transfer mechanisms, the transferable forces are substantially lower compared to the case of adhesion in the fill-in zone. Contrary to steel reinforcement bars with ribs, a shear bond because of mechanical interlocking between reinforcement and concrete does not exist in fibre direction. However, in textiles the transverse yarns, which are connected to the longitudinal yarns might cause also shear bond.

The size and the ratio between the fill-in and the core zones depend on different properties. The shape of the yarn or the ratio between circumference and cross-sectional area of the yarn, respectively, is one of these factors. For instance a circular shaped yarn, which has a small circumference related to the cross-sectional area, has a small number of filaments in the fill-in zone and a large number of filaments in the core. In contrast, a very flat yarn, for instance with an elliptical shape, might have almost all filaments in the fill-in zone and might have essentially no core zone. Nevertheless, the yarn geometries are in reality usually more complex than these special cases. Another aspect, which influences the penetrability, is the packing density of the yarns, which in turn depends on the production technique of

the yarn and the binding technique of the textile. While a low packing density enables a better penetrability of the yarns, a high packing density might enhance the frictional load transfer because of an increased lateral pressure. To some extent also the viscosity of the fresh matrix or the coating influences the penetration into the yarns.

As the embedding of the reinforcement is performed before the concrete is hardened, similar effects occur at the interfaces between the reinforcement and the cement paste as between the aggregates and the cement paste during hardening. It is known that the cementitious matrix has a different structure in the closer vicinity of the reinforcement yarns than the bulk matrix similar to the interfacial transition zone between aggregates and hardened cement paste, see e. g. [Banholzer 2004], [Jesse 2004], [Lepenies 2007] and [Konrad 2008] regarding TRC. In [Banholzer 2004] and [Jesse 2004], photographs are presented showing these different matrix structures of the bulk matrix and in the interfacial transition zone in the vicinity of a filament and a multi-filament yarn, respectively. There are various mechanisms and processes leading to this effect. For instance, the crystallisation process during the hydration of the cement is disturbed in the vicinity of the reinforcement yarns. Furthermore, the yarns might provide or withdraw water to or from the surrounding matrix depending on their water content. This leads to additional pores in the matrix or to incomplete hydration of the cement, which both will reduce stiffness and strength of this zone. Furthermore, water soluble sizings and coatings will influence the hydration process of the cement. Thus, an important factor for the performance of the composite are the sizings and coatings on the reinforcement, which have to be adapted to reinforcement and matrix and vice versa, as it was already pointed out in the Sections 2.1 and 2.2.

The quantification of the differences between the material properties of the bulk matrix and the interfacial transition zone, which primarily influence the bond to the filaments, is difficult because of the heterogeneity of the matrix and the small scale. Nevertheless, micro-strength tests by [Zhu & Bartos 1997] where also the width of interfacial transition zone was estimated with about 50 μm showed that the micro-strength in the interfacial transition zone is considerably lower than in the surrounding matrix. However, these investigations also showed that during ageing these differences reduce, which is also pointed out in [Butler et al. 2009]. For the stiffness of the interfacial transition zone experimental investigations seem to be missing, at least for TRC. Investigations by [Zhu & Bartos 2000] with steel reinforcement indicate that also the stiffness is reduced.

2.3.2. Tensile tests without matrix cracks - Filament pull-out tests

An important property for the description of the load-bearing behaviour of TRC is the bond behaviour between the filaments and the matrix. Experimentally, the bond behaviour of single filaments to the matrix can be determined by means of pull-out tests. Respective investigations where performed for AR-glass and cementitious matrices for instance by [Banholzer 2004] and [Zhandarov & Mäder 2003, Zhandarov & Mäder 2005]. The advantage of these tests is that at least the geometrical setup, for instance bond length and contact area, is well defined and based on the resulting load-deformation relations unique bond laws for these systems can be determined, see e. g. [Banholzer 2004, Lepenies 2007]. The disadvantage of this type of tests is, however, that it does not reflect the conditions in

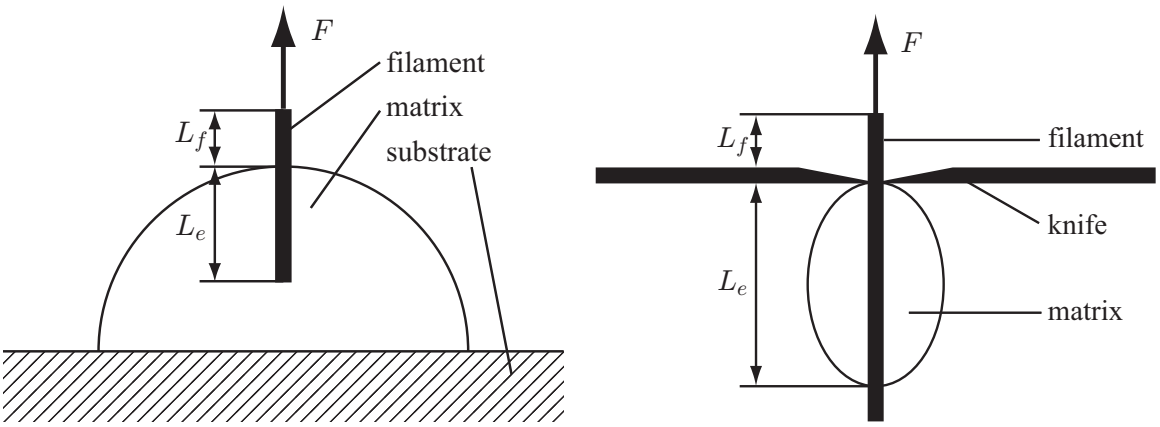

(a) Filament pull-out test (b) Microbond test

Figure 2.9.: Micromechanical tests for the determination of the bond behaviour between matrix and filaments; according to [Zhandarov & Mäder 2005]

TRC. As it was pointed out in the previous section, the composition of the yarns of hundreds of filaments leads to complex configurations concerning the embedding and, thus, also concerning the force transmission between matrix and reinforcement. Another reason is that usually only cement slurry without aggregates is used as matrix. As a consequence, in a filament pull-out test almost ideal conditions concerning the embedding of the filament in the matrix are established, which cannot be achieved in TRC. Thus, the resulting bond stresses can only be seen as upper limits for the application to TRC. However, these tests are useful to get information about the load transfer behaviour between matrix and reinforcement in principle.

In Fig. 2.9, common experimental setups for the determination of the bond behaviour between single filaments and matrix are illustrated, see also [Zhandarov & Mäder 2005]. Originally, these setups were developed for pull-out tests of fibre reinforced polymers. The force is applied in these experiments directly to the filament. The tests shown in Fig. 2.9 differ concerning the boundary conditions and, thus, the stress state of the matrix. While in the pull-out test in Fig. 2.9(a) the matrix adheres on a substrate and is tensile loaded, it is fixed by means of knives in the microbond test, which leads to a compressive loading of the matrix, see Fig. 2.9(b). Besides the embedding length L_e of the filament in the matrix also the free length L_f affects the results of these tests. In the free part, elastic energy is stored, which is the larger the longer L_f is. If debonding starts it might happen with long L_f that the filament relaxes suddenly and no distinct pull-out curve might be observable. This represents an energetic size effect. Thus, L_f should be chosen as short as possible in experiments.

In Fig. 2.10, a force-displacement relation corresponding to investigations by [Zhandarov & Mäder 2005] is shown. In the test, an AR-glass filament with a diameter of 15.6 μm was embedded on a length L_e of about 1 mm in cementitious matrix. In Fig. 2.10(b), it can be seen that no distinct linear part exists, which indicates that bond degradation starts short after load application. However, in [Zhandarov & Mäder 2005] also corresponding results with an initial linear elastic part of the load-displacement relation were presented, which reveals that cases with initially stable bond exist. The successive debonding is associated with

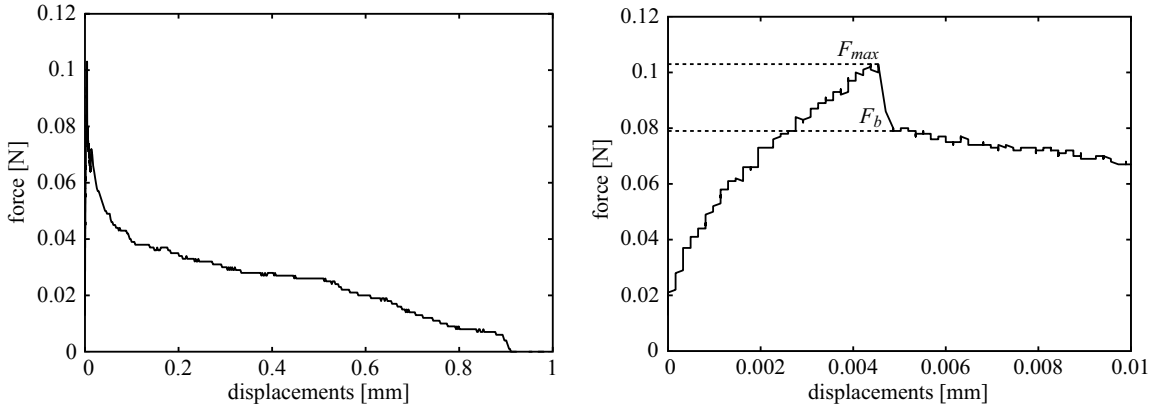

(a) Force-displacement relation of filament pull-out test

(b) Detail of force-displacement relation

Figure 2.10.: Force-displacement relation of a filament pull-out test of an AR-glass filament embedded in cementitious matrix (Experimental data provided by subproject A5 of SFB 528)

a decreasing slope of the force-displacement relation. Nevertheless, the force-displacement relation still increases because additionally to the adhesive forces in the intact regions, frictional forces in the debonded regions are activated. The maximum value of the pull-out load F_{max} is reached when the applied load cannot be resisted by the interface and a sudden elastic relaxation of the filament occurs. This leads in the force-displacement relation to a force drop until a value F_b. Subsequently, the force decreases further until the full pull-out of the filament. In this state, only frictional forces are transferred between the filament and the matrix, which decrease in sum due to the reducing embedding length. As the course of the decreasing curve is non-linear it has to be expected that also the transferable forces decrease due to bond degradation.

2.3.3. Tensile tests with a single matrix crack - Yarn pull-out tests

As pointed out in the previous sections, the bond behaviour between a yarn and the matrix cannot be determined sufficiently with filament pull-out tests because different bond zones with different force transfer mechanisms exist inside a yarn. In order to investigate the bond behaviour of entire yarns, so-called yarn pull-out out tests are usually carried out. Such tests were performed regarding TRC materials e. g. by [Banholzer 2004], [Krüger 2004, Xu et al. 2004] and [Butler 2009].

In [Banholzer 2004], a one-sided pull-out test similar to the filament pull-out test described in the previous section is used. Therefor, a yarn is embedded at one end in a block of epoxy resin and at the other end in a block of cementitious matrix. A shortcoming of this test is that the resin might also penetrate parts of the yarns, which are embedded in the cementitious matrix. Furthermore, the embedding in the resin leads to almost uniform bond conditions in this part of the yarn resulting in equal displacements of the filaments at the boundary layer between resin and cementitious matrix. This does not coincide with the situation in TRC where the filaments in the core might be pulled out from both crack faces.

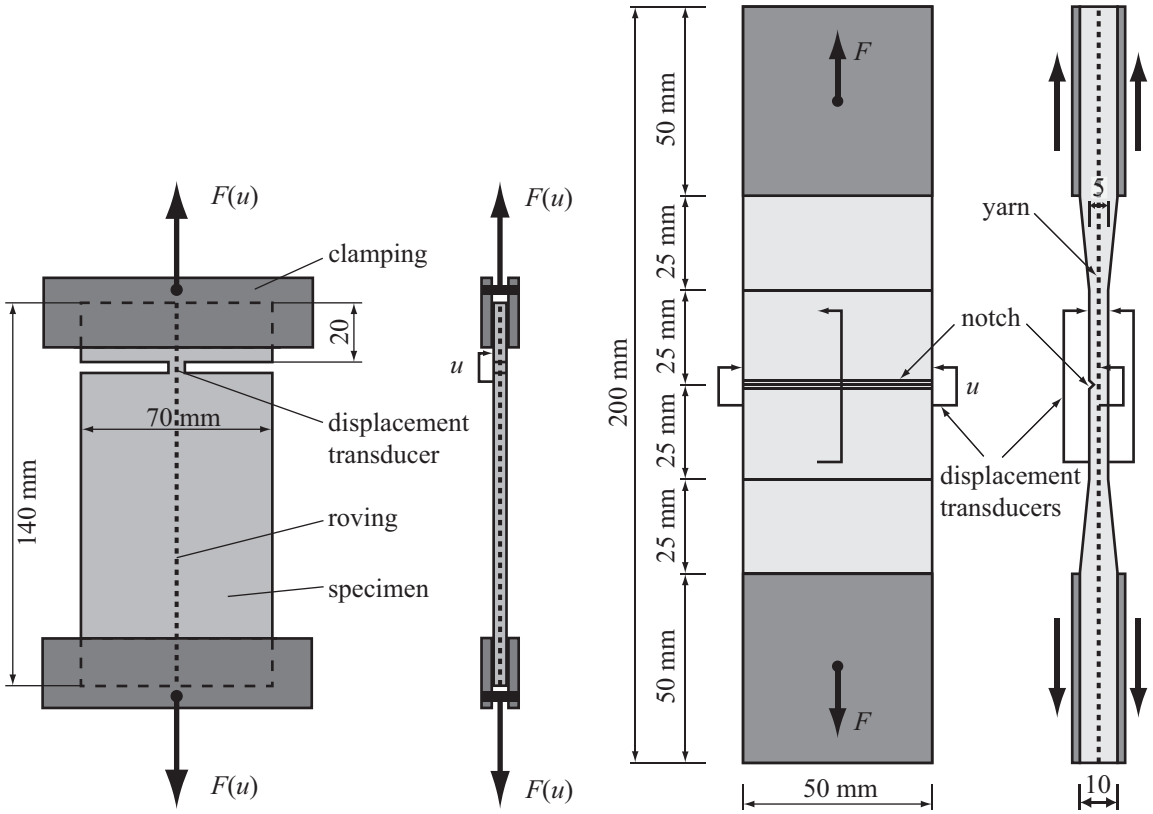

(a) Test setup by [Krüger 2004] (b) Test setup by [Butler 2009]

Figure 2.11.: Setups for two-sided yarn pull-out test

However, a nice feature of the test by [Banholzer 2004] is the "Failure Investigation using Light Transmission properties" (FILT), which can locate the cross-sectional position of failed filaments within some bounds. It uses the property of glass fibres to transmit light if they are intact. Since the position of filament failure in longitudinal direction cannot be determined with this test, the observed position of the failed filaments at the end of the specimen might not coincide with the position where the filament failed if the filaments change their position in the yarn in longitudinal direction. Assuming that these position changes are negligible, the FILT test gives evidence that yarn failure starts with the failure of the filaments in the fill-in zone while the core filaments are intact for the largest pull-out displacements if they fail at all and are not simply pulled out. This behaviour is also often called telescopic failure behaviour. Furthermore, it is also possible to assign the filament failure event to a specific state in the force-displacement relation.

In subsequent experimental investigations, [Kang et al. 2009] used acoustic emission analysis to determine filament failure events and their spatial location in the specimen. Conclusions of this work were that most of the filament failure events occur after reaching the ultimate load and are responsible for the load decrease. Furthermore, almost only the filaments in the fill-in zone failed. The core filaments were pulled out in these tests and did not fail because uncoated yarns were used in these tests. Moreover, a tendency that the locations of early filament failure were close to the load application while later failure was located farther in the concrete part, is reported. This corresponds to the observations of telescopic failure of the yarns in the FILT test.

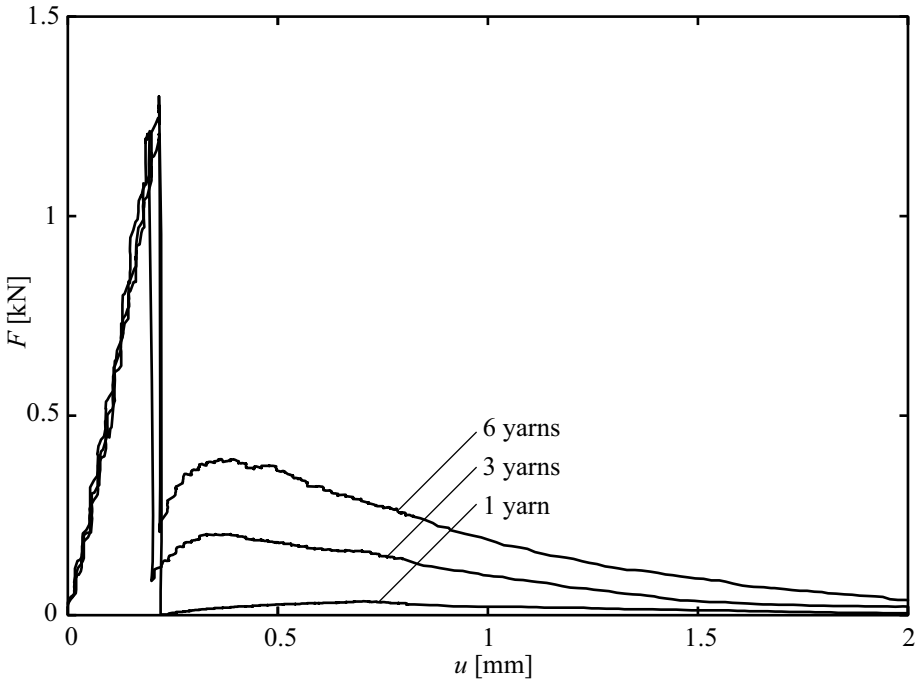

Figure 2.12.: Test results of two-sided yarn pull-out test (Experimental data provided by subproject A5 of SFB 528)

Two-sided yarn pull-out tests are used by [Krüger 2004], see Fig. 2.11(a), and [Butler 2009], see Fig. 2.11(b). In the following, only the results by [Butler 2009] are treated in some detail, as the applied materials correspond to other experimental investigations considered in this work. In Fig. 2.11(b), a typical specimen used by [Butler 2009] is shown. It has a waisted shape and a notch at the centre of the specimen to ensure a matrix crack at a pre-defined position. The specimens are usually reinforced with one up to six yarns. These reinforcement ratios can be classified as undercritical amounts of reinforcement, and prevent further matrix cracks. In this regard, "undercritical" means that an insufficient amount of reinforcement is available to retransfer sufficient stresses back to the matrix via bond mechanisms to reach the tensile strength of the matrix again at a different position. The opposite is an "overcritical" reinforcement ratio, which leads to multiple cracking of the matrix and further stress increase in the composite after the final crack pattern is reached. The "critical" reinforcement ratio, which is a rather theoretical case, can be characterised with multiple matrix cracking but no further load increase after multiple cracking.

The tests are performed with displacement control and the force as well as the crack opening displacement are recorded, see Fig. 2.11. Starting with an intact specimen, a typical force-displacement (F-u) relation, see Fig. 2.12, starts linearly increasing according to the stiffness of the matrix. If the tensile strength of the matrix is reached, the F-u relation drops relatively abrupt to a lower force value. It can be assumed that simultaneously to the matrix crack also filaments fail. Preferred candidates are filaments with low local tensile strength in the fill-in zone where also strong bond exists. Subsequently, the reinforcement is activated via bond mechanisms between matrix and reinforcement, which leads to a second non-linear increase of the F-u relation. The non-linearity might result from several mechanisms as e. g. the non-linear bond characteristics and successive failure of further filaments. The successive failure of filaments was determined by [Butler 2009] by means of acoustic emission analysis. The

slope of the F-u relation decreases with increased loading and reaches a second maximum, which depends on the amount of reinforcement as observable in Fig. 2.12. After reaching the maximum value, the F-u relation decreases slowly as a consequence of failing filaments and bond degradation. The acoustic emission analysis revealed that most of the filaments fail in the decreasing part of the F-u relation. Failure of the filaments in the yarn core depends on the bond quality and force transmission length, which can lead also to filament pull-out instead of failure. Thus, the load-bearing behaviour in the pull-out test is substantially influenced by the strength distribution in the filaments and the load transfer mechanisms in the yarns.

2.3.4. Tensile tests with multiple matrix cracking

The previously described filament and yarn pull-out tests are primarily intended to gain some information about the load transfer mechanisms between the matrix and the reinforcement yarns. However, these tests do not reflect the load-bearing mechanisms in practical applications where multiple matrix cracking and strain-hardening behaviour of the composite is desired. Hence, another type of test is usually performed, which meets these requirements. Typically plate-shaped specimens with an overcritical amount of reinforcement are used, which allows for multiple cracking of the matrix. Various specimen shapes and load transmission constructions were developed by different experimenters, e. g. [Jesse 2004] or [Molter 2005]. In Fig. 2.13, two exemplary test setups are shown. The specimens used by [Molter 2005], see Fig. 2.13(a) have a waisted shape to reduce disturbances of the stress field by the load transmission construction, which is realised with a perforated steel plate encased in the matrix and a steel bolt for load transmission. The production of such specimens is obviously associated with a lot of effort. The production effort is clearly reduced for the specimens by [Jesse 2004], see Fig. 2.13(b), where plane plates are used. Stress concentrations at the transition from the load transmission zone to the free zone are tried to be reduced by means of clamping constructions with elastomer interlayers. With both specimens similar experimental results are reported. The following description is limited to the summary of the results by [Jesse 2004], because the applied materials correspond to the previously described experimental investigations by [Zhandarov & Mäder 2005] and [Butler 2009]. Moreover, the quality of the experimental results seems to be better in [Jesse 2004] compared to [Molter 2005] as theoretical investigations, e. g. in Section 5.3.5.3, indicate.

The tensile specimens used by [Jesse 2004] have reinforcement ratios in the range of approximately 1 % up to 3 %. The reinforcement ratio, also referred to as fibre volume content, is defined as

$$V_f = \frac{A_r}{A_c} \tag{2.3}$$

where A_r and A_c are the cross-sectional areas of reinforcement and matrix, respectively. In A_c, the reduction due to the embedded yarns consisting of the cross-sectional areas of the filaments and voids is neglected. The reinforcement was applied in two ways: as unidirectional yarns and as biaxial textiles. The reinforcement with unidirectional yarns was performed to study the material behaviour of TRC independent of the transverse reinforcement. Therefor, the yarns had to be stretched before embedding in the matrix to ensure a sufficient alignment.

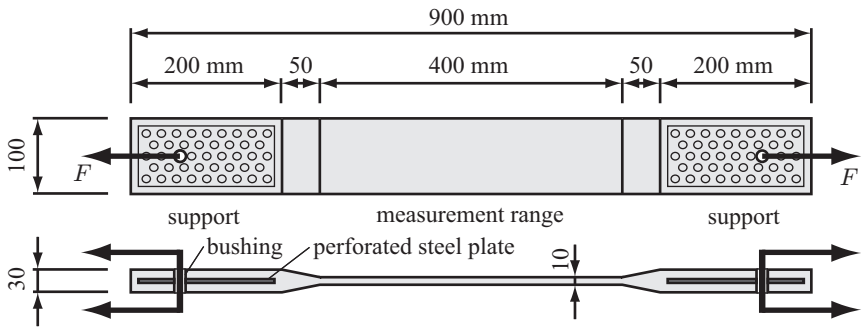

(a) Tensile specimen of [Molter 2005]

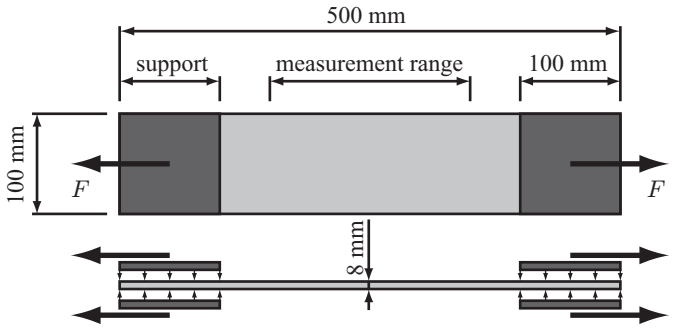

(b) Tensile specimen of [Jesse 2004]

Figure 2.13.: Test setups for the determination of the tensile behaviour of TRC with multiple cracking

However, the prestressing of the fibres is negligible regarding the influence on the stress-strain response of TRC. In the case of textiles, a stretching of the yarns to ensure alignment is not necessary because of the structural stability of the yarns due to the textile processing. The tests were carried out with displacement control in a standard hydraulic testing machine. During the tests, the applied forces F are measured with a load cell and displacements are measured with clip-on extensometers on a measurement range of 200 mm in the centre part of the specimen, see Fig. 2.13(b). From the measured forces F_m, mean stresses $\overline{\sigma}$ are calculated by relating F_m to A_c:

$$\overline{\sigma} = \frac{F_m}{A_c}. \tag{2.4}$$

The measured displacements Δu are related to the measurement range L_m ($= 200\,\text{mm}$) resulting in a mean strain $\overline{\varepsilon}$:

$$\overline{\varepsilon} = \frac{\Delta u}{L_m}. \tag{2.5}$$

The mean stress-mean strain ($\overline{\sigma}$-$\overline{\varepsilon}$) behaviour of uniaxial tensile loaded TRC specimens is similar to concrete reinforced with steel bars. For the following description of the main characteristics of the load-bearing behaviour, it is insignificant in the first instance if yarns or textiles were applied as reinforcement. The $\overline{\sigma}$-$\overline{\varepsilon}$ relation, see Fig. 2.14, starts with the uncracked state with an almost linear slope, which essentially reflects the Young's modulus of the matrix as the reinforcement ratio is usually about 1 up to 3 % and the Young's modulus of the AR glass has only about the double value of those of the matrix. As the

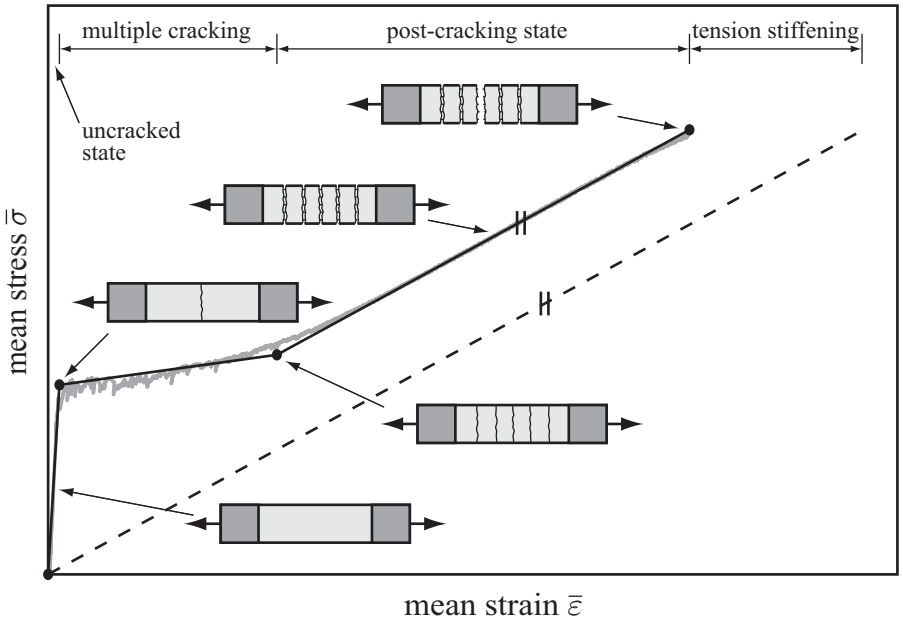

Figure 2.14.: Typical stress-strain behaviour of TRC under uniaxial tensile loading

load is applied to the matrix and the reinforcement is not pre-tensioned the reinforcement is initially unloaded. Only when the matrix is deformed sufficiently, the reinforcement is activated and participates somewhat on the load-bearing. Nevertheless, the reinforcement yarns might hamper the growth of macroscopic cracks, which develop perpendicular to the loading direction and run successively against the reinforcement yarns placed in loading direction. This leads to the effect that the first macroscopic matrix crack often occurs at stress values in the $\overline{\sigma}$-$\overline{\varepsilon}$ relation corresponding to Fig. 2.14, which are higher than the nominal matrix tensile strength. This effect is also referred to as suppression of cracks and is the larger the higher the reinforcement ratio is, see Fig. 2.15. Furthermore, also improved bond properties might increase the suppression of cracks.

The development of the first macro-crack is associated with the redistribution of stresses to the reinforcement yarns via bond mechanisms, compare Section 2.3.1. This is the start of the so-called state of multiple cracking, see Fig. 2.14. After the first matrix crack occurred, the reinforcement has to bridge the crack. However, to some extent also the matrix might still participate in crack-bridging with its post-cracking resistance, compare Section 2.2.2. As in tests under consideration overcritical amounts of reinforcement are applied, further matrix macro-cracks can develop when the load is increased. Therefor, forces have to be transferred from the reinforcement to the matrix along the force transmission lengths starting at the crack faces. If the force transmission length is sufficiently long and the transferable bond stresses are sufficiently large, the stress in the matrix can reach the tensile strength again leading to a new crack. The distance between two adjacent cracks is called crack spacing. The first developing cracks show usually large crack spacing. However, at higher load levels often further matrix cracks develop between existing cracks. If biaxial textiles are used the positions of the transverse yarns are preferential locations for cracking because the cross-sectional area of the matrix is reduced at these locations. Often the positions of the transverse yarns can be identified by means of the crack pattern, see [Jesse 2004] and Fig. 2.16. The mean slope of the $\overline{\sigma}$-$\overline{\varepsilon}$ relation in the state of multiple cracking is lower compared to the uncracked

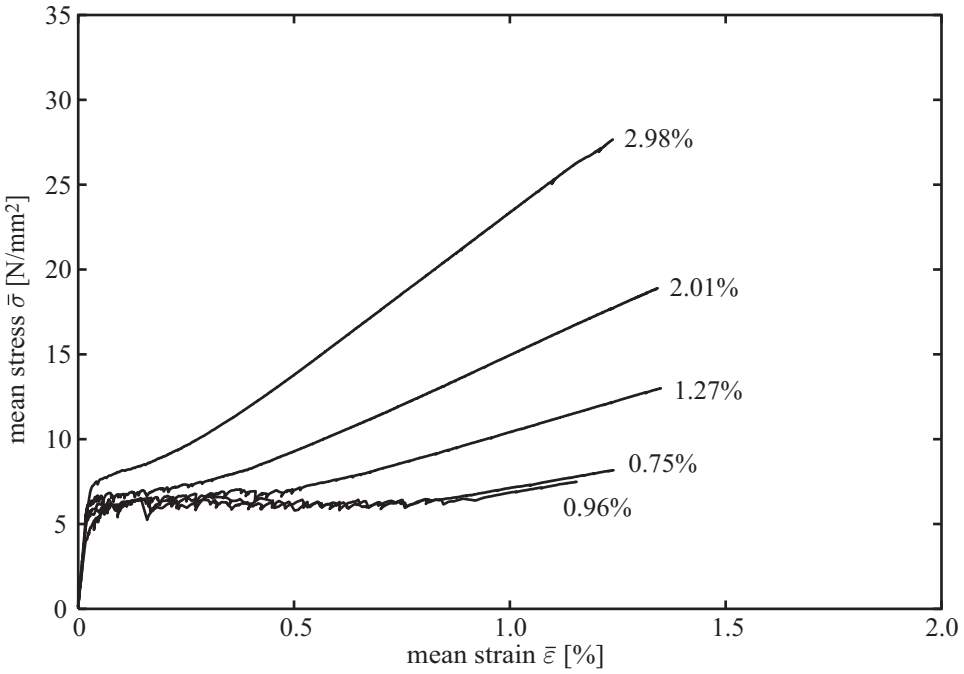

Figure 2.15.: Stress-strain relations of TRC with different reinforcement ratios (Experimental data provided by subproject B1 of SFB 528)

state and appears as a kind of saw tooth curve, see Fig. 2.14. Matrix cracking is finished when the remaining crack spacing is too small to transfer sufficiently forces back from the reinforcement to the matrix to reach the local matrix tensile strength again. Furthermore, with increasing loading also the bond between matrix and reinforcement is supposed to underlie degradation, which also reduces the transferable forces between matrix and reinforcement. The larger the reinforcement ratio is, the higher forces can be transferred and, thus, the crack spacing and the crack widths decrease with increasing reinforcement ratios, see Fig. 2.15. In Fig. 2.15, it can be also seen that the stress drops after matrix cracking decrease with increasing reinforcement ratios. Additionally, also the strain ranges where matrix cracks develop decrease with increasing reinforcement ratios, see Fig. 2.15. With low reinforcement ratios, it can only hardly be distinguished between the cracking and the post-cracking states, see Fig. 2.15.

After the final crack pattern is reached, the $\overline{\sigma}$-$\overline{\varepsilon}$ relation steepens again until the tensile strength of the reinforcement is reached as well, see Fig. 2.14. This so-called post-cracking state is mostly influenced by the material properties of the reinforcement. Thus, the slope of the $\overline{\sigma}$-$\overline{\varepsilon}$ relation increases with increasing reinforcement ratio. However, also the matrix participates in load-bearing between the cracks in the post-cracking state, which is also referred to as tension stiffening. Tension stiffening can be measured as a parallel shift of the linearised course of the $\overline{\sigma}$-$\overline{\varepsilon}$ relation in the post-cracking state through the origin of the coordinate system, see Fig. 2.14. Then tension stiffening is the strain shift between the measured and the translated $\overline{\sigma}$-$\overline{\varepsilon}$ relation (dashed line in Fig. 2.14). Especially in the case of textile reinforcement also "negative" tension stiffening can be observable, which can be explained with an initial waviness of the yarns depending on the production process of the textiles. This is observable in Figure 2.17, if the stress-strain relations for the loading in weft and warp direction of the fabrics are compared. The warp direction is less stretched

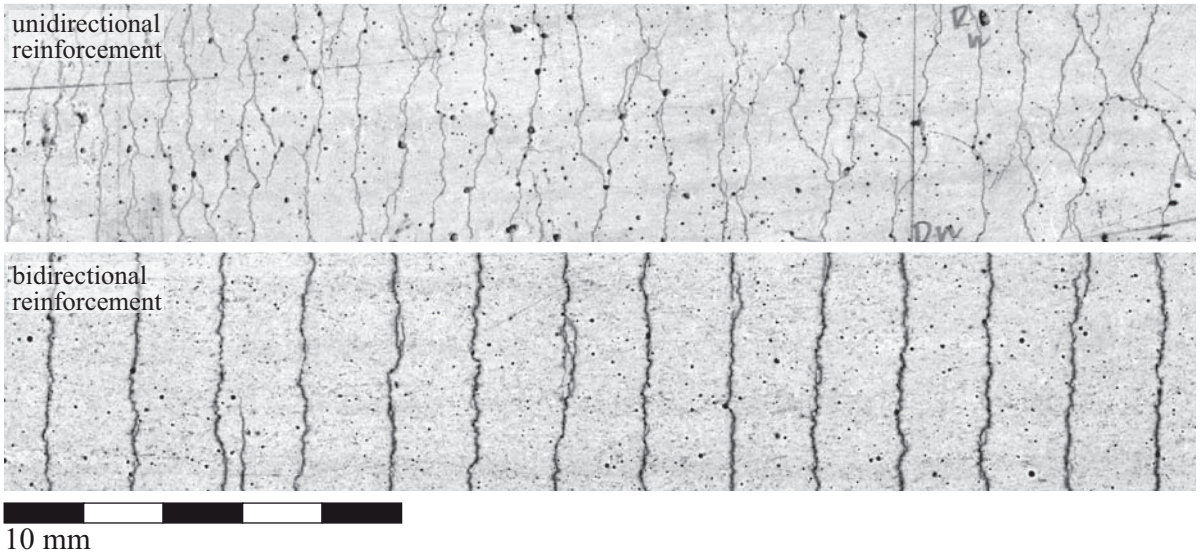

Figure 2.16.: Typical crack pattern for TRC with unidirectional and bidirectional AR glass reinforcements under tensile loading; from [Jesse 2004]

in the production process compared to the weft direction and shows relatively large initial waviness, which leads to larger deformations in case of matrix cracking and, thus, to a larger strain range of the cracking state as well as a $\overline{\sigma}$-$\overline{\varepsilon}$ response shifted to larger strains in the post-cracking state. The example of tension stiffening also points out the difficulties existing in the identification of the influences of competing mechanisms on the material response. In this case, the waviness of the reinforcement might completely mask the stiffening effect of the concrete in the post-cracking state.

As [Jesse 2004] points out, the slope in the post-cracking state m_{pc} should theoretically coincide with the stiffness of the plain reinforcement related to the cross-sectional area of the concrete matrix A_c

$$m_{pc} = \frac{E_r A_r}{A_c} \tag{2.6}$$

with the Young's modulus E_r and the cross-sectional area A_r of the reinforcement. However, it was noticed by [Jesse 2004] that the slope of the post-cracking state is usually lower than m_{pc}. Independent of the type of reinforcement (unidirectional yarns or textiles), the experiments by [Jesse 2004] revealed an upper limit of the slope in the post-cracking state of about 80 % of m_{pc}. Furthermore, these experimental results indicate a larger procentual decrease of the slope in the post-cracking state for low reinforcement ratios. Hitherto, a final explanation for these effects seems to be missing. Under the assumption of negligible errors in the measured results and in the determination of the particular material parameters, e. g. the Young's modulus of the reinforcement, a possible explanation is that a part of the reinforcement does not participate in load-bearing due to a premature failure of filaments in the fill-in zone during concrete cracking as [Jesse 2004] points out. However, this explanation contradicts with the fact that for increasing reinforcement ratios the stress in the reinforcement during matrix cracking decreases and might not reach the filament tensile strength. Additionally, the post-cracking resistance of the matrix reduces the stress in the reinforcement fibres right after matrix cracking. Thus, the assumption of simultaneous matrix cracking and

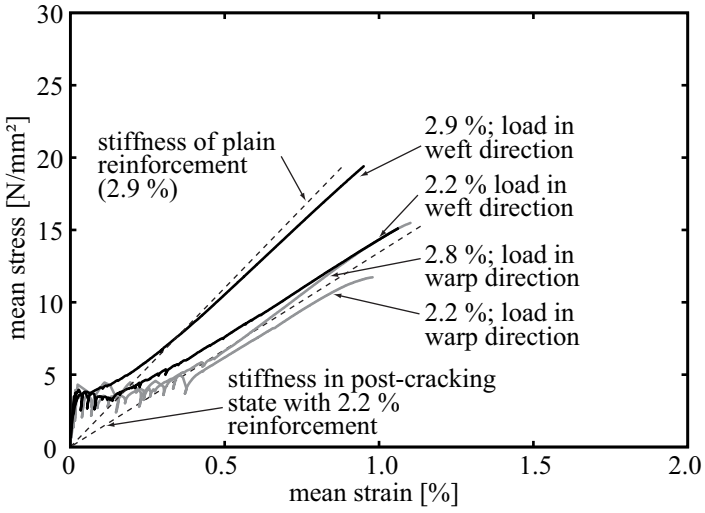

(a) Uncoated fabrics

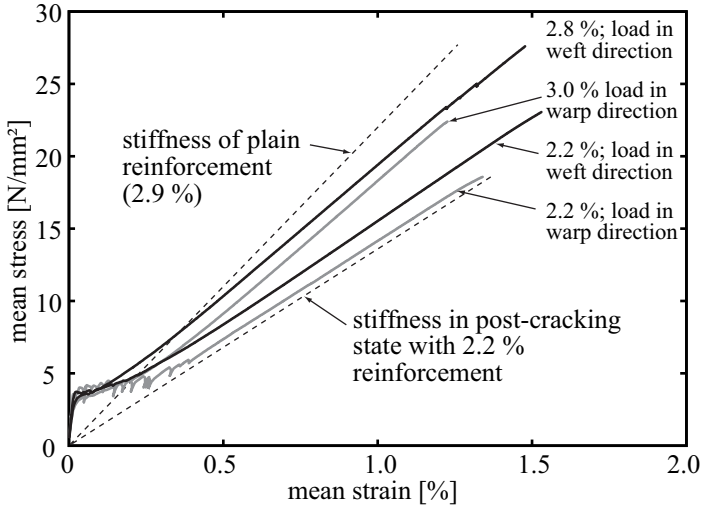

(b) Fabrics with polymer-coating based on Styrol-Butadien

Figure 2.17.: Experimental stress-strain relations with different reinforcement ratios, coatings and fabric orientations; from [Hartig et al. 2009]

filament failure in the fill-in zone seems plausible in case of low reinforcement ratios or for single pre-damaged filaments, but is not convincing for high fibre volume content. A different explanation is that inside the core of filament yarns a portion of filaments exists, which are weakly linked to their neighbours and, thus, do not significantly participate on the load transmission. In this case, the effect is independent of the reinforcement ratio but depends on the load transfer conditions in the yarn. Optical investigations on thin sections of yarns embedded in matrix by [Jesse 2004] seem to support this explanation, because especially circularly shaped yarns show a large amount of voids in the cross section. However, these local investigations are not sufficient for the estimation of the bond behaviour on a certain embedding length because it is quite improbable that all filaments, which are positioned in one cross section in the yarn core remain in this position over long distances in longitudinal direction. Moreover, if this weak stress transfer to the core would exist, the core filaments would be considerably pulled in the concrete at the ends of the specimen during loading, which is not reported from the experiments.

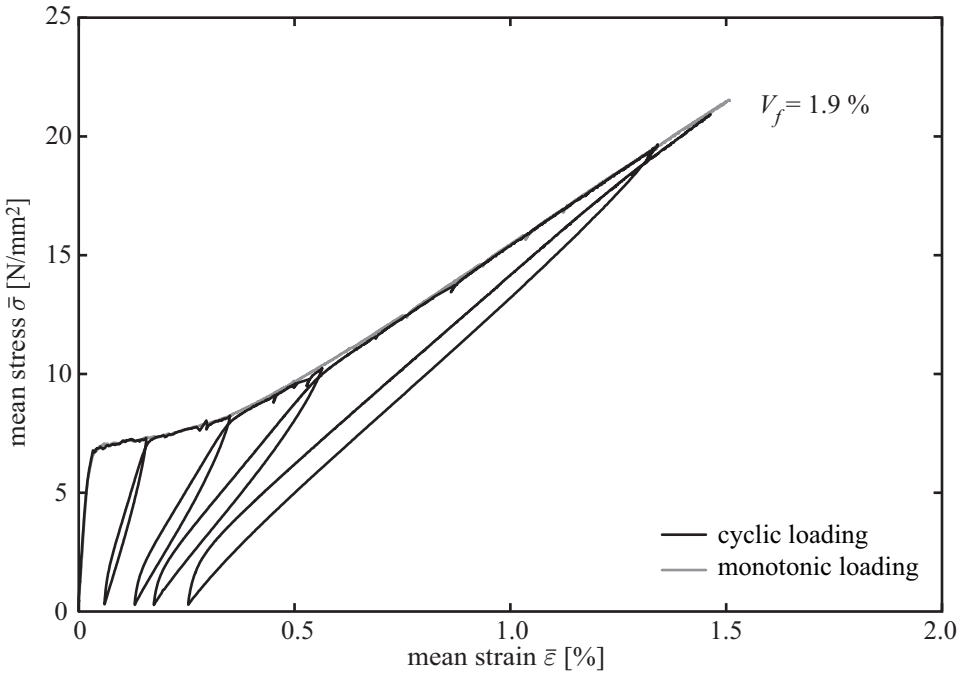

Figure 2.18.: Stress-strain relation of TRC exposed to cyclic loading (Experimental data provided by subproject B1 of SFB 528)

Reaching the ultimate state or the tensile strength of the reinforcement, respectively, the specimen fails in general suddenly. In some cases also a reduction of the slope of the stress-strain curve is observable right before ultimate failure indicating that the weakest filaments fail while the intact parts of the reinforcement can still resist the load. A state of yielding does not exist in TRC because the reinforcement material has no ability do deform plastically. The ultimate stress increases with increasing reinforcement ratios while the ultimate strain does not change significantly. Regarding the load-bearing capacity, it has been observed that with an appropriate additional coating on the fabrics a better exploitation of the reinforcement with higher strength and ultimate strains compared to uncoated fabrics is achieved. As an illustration of this effect in Figure 2.17 results of specimens reinforced with biaxial double tricot-bonded fabrics (7.2 mm yarn spacing in both directions) of AR-glass yarns (Vetrotex 1200 tex) with and without additional polymer-coating are shown. Reasons for this effect are for instance a certain protection of the filaments in the laminating process, which might prevent outer filaments from failure. The more important reason seems to be the homogenisation of stresses in the filament yarns due to the coating, which leads to a delayed failure initiation compared to uncoated fabrics, see also [Hartig et al. 2008].

Hitherto, only monotonic loading was taken into account. In the case of cyclic loading, the $\overline{\sigma}$-$\overline{\varepsilon}$ relation of the monotonic loading case can be seen as the envelope of the relation for cyclic loading, see Fig. 2.18. The observed unloading paths of the stress-strain relation are Z-shaped. This means that the stress-strain relation decreases with an initially steep slope, which merges to a flatter slope. In the middle part of the unloading path, the stress-strain relation decreases almost linearly while the slope increases again near the abscissa. The increase of stiffness near the abscissa might be explained with a compressional reloading of the concrete. It is also observable that during the unloading the origin of the stress-strain relation is not reached again, because some deformations remain. This effect can be consid-

ered as a macroscopic plastic deformation. However, it has to be pointed out that this is not an outcome of a yielding of the material as it is observable, e. g., for metals. It is rather a result of inelastic deformations between matrix and reinforcement due to bond degradation and frictional load transfer as well as incompatibilities of the fracture surfaces of the cracked concrete as already discussed in Section 2.2.2. The inelastic deformations increase with increasing loading. However, the largest portion of inelastic deformations occurs in the cracking state while unloading in the post-cracking state leads only to small additional inelastic deformations. This might indicate an initially elevated deformation of the reinforcement at the cracks due to waviness of the reinforcement. Furthermore, also increasing bond degradation and growing incompatibilities of the concrete crack faces might contribute to this effect. The mean slopes of the unloading paths are steeper at lower load levels than at higher ones. The reloading is characterised by a steep increase of the stress-strain relation, which passes into a flatter, almost linear slope and merges finally into the enveloping curve. The mean slopes of the reloading paths are also steeper at lower levels of unloading than at higher unloading levels, which is associated with the reduced increase of inelastic deformations with increasing unloading level as mentioned previously. Corresponding to the enveloping curve, also the cyclically loaded specimen finally fails reaching the tensile strength of the reinforcement.

2.4. Consequences for the modelling

The previous sections showed that the material structure of TRC is very complex because of the heterogeneities in the matrix, the reinforcement and the bond between both. A detailed model covering all presented aspects seems to be impossible to establish also because of the random character of the material structure. Thus, simplifications are necessary to develop a manageable model. Existing modelling approaches for the case of tensile loading are summarised in the next chapter while a novel model is presented in Chapter 4. Furthermore, the model has to incorporate material and geometrical properties at the microscopic scale as e. g. the bond properties or the filament arrangement. These properties are difficult to determine in experiments and show usually large scatter, which often requires appropriate assumptions. A model with predicting capabilities is hitherto only possible after a calibration of the material parameters based on known experimental results. The calibration of the parameters is itself an issue, because it is usually performed by means of a minimisation of the gap between calculated and experimental results. On the one hand, in the experiments usually only mean or smeared values as for instance forces, displacements or strains are measured, which on the other hand might depend simultaneously on different properties. Thus, a calibration of the parameters might not always have a unique solution. Additionally, the experimental results of concrete specimens show usually relatively large scatter, which complicates the determination of material parameters. Thus, the first step has to be a successful reproduction of experimental results within the bounds of accuracy given by the experimental results. Having a calibrated model, parametric studies can be performed, which can be seen as a prediction of the structural behaviour with varied material parameters.

3. Selected modelling approaches for the uniaxial tensile behaviour of TRC

Concerning the modelling of the tensile behaviour of cementitious composites a broad range of models exist. Especially, for steel-reinforced concrete great effort was spent in the past to develop models for a realistic description of the material behaviour. Nevertheless, the development is still proceeding. Often these existing approaches were starting points for the development of models for TRC. Other modelling approaches originate from the fields of fibre-reinforced polymers and ceramics. As a detailed description of the respective "historic" evolution is beyond the scope of this work only recently developed models for TRC are summarised in the following. Of course, such a condensed overview cannot be complete and is not able to point out every detail. The presentation is subdivided into three main parts, which seem to be also the necessary main ingredients of models concerning TRC, and are:

- the material and failure behaviour of the reinforcement
- the material and cracking behaviour of the matrix
- the load transfer between matrix and reinforcement as well as within the reinforcement.

The description includes both analytical and numerical approaches based on the Finite Element Method, which is described more detailed in Section 4.4. Often the models are distinguished by means of the scale, on which they cover characteristic effects and mechanisms. Typically, three scales are defined: the micro-scale, the meso-scale and and the macro-scale as well as sometimes a nano-scale, compare also Chapter 2. In the existing models for TRC, the concrete is usually modelled homogeneous, which clearly corresponds to the macro-scale. For the representation of the reinforcement, a number of approaches on different scales exist. In some models, the reinforcement of multi-filament yarns is considered in a detailed manner as single fibres, which corresponds to the micro-scale. In other models, filaments are summarised in groups or the multi-filament yarns are modelled as homogeneous bars, which corresponds to the meso-scale and the macro-scale, respectively. As a consequence, the models for TRC can often not be assigned uniquely to a scale. Thus, this scale distinction is not explicitly considered subsequently.

In the following, only such modelling approaches are regarded where the reinforcement is modelled discretely and is not smeared with the matrix resulting in a homogenised material description. Smearing of the reinforcement is often performed in models at the macroscopic scale, which are intended to offer efficient tools for the determination of the structural behaviour at this scale and are thus purposed for practical applications. Models with such smeared or homogenised material laws are not suitable to gain information about the material behaviour and the governing mechanisms. In fact, these smeared material models could and should be an outcome of more detailed models where one of this class of detailed models

shall be developed in the present work. Before describing in some more detail how particular geometrical and material properties are incorporated in existing models, the main characteristics of the models under consideration are described briefly in the next section.

3.1. Considered models

The most basic models to describe the stress-strain response of TRC with an overcritical amount of reinforcement to uniaxial tensile loading are given with the so-called *ACK Model* by [Aveston et al. 1971], the *AK Model* by [Aveston & Kelly 1973] and the *OH Model* by [Ohno & Hannant 1994], which are all analytical models. In Fig. 3.1, the predictions of the mean stress-strain ($\overline{\sigma}$-$\overline{\varepsilon}$) response by these models are shown qualitatively. The $\overline{\sigma}$-$\overline{\varepsilon}$ relation for the uncracked state can be established incorporating the Young's moduli and tensile strength of the matrix (E_m and σ_{mu}) and the reinforcement (E_f and σ_{fu}). For the cracking and the post-cracking state, assumptions for the stress distribution between the matrix and the reinforcement are made to derive a description for the $\overline{\sigma}$-$\overline{\varepsilon}$ behaviour. The stress distribution is always assumed symmetric to the crack, which does not necessarily correspond to reality and is thus a noticeable simplification. In the *ACK Model* and the *AK Model*, the reinforcement is assumed to be perfectly embedded in the brittle matrix and is consequently modelled as mono-filament. The main difference between both models are the assumptions for the bond between the matrix and the reinforcement. While the bond stresses are assumed constant in the *ACK Model* corresponding to frictional load transfer, it is considered linear elastic in the *AK Model* corresponding to the assumption of adhesive load transfer. In contrast, in the *OH Model* two interfaces are considered: one between the matrix and the so-called sleeve fibres embedded in the matrix and another one between the sleeve fibres and the core fibres where less or even no matrix intrudes. In both interfaces frictional load transfer, i. e. constant bond stress, is assumed while the bond stress is higher at the interface between the matrix and the sleeve fibres than in the inner interface. Assuming further a mean crack spacing, the strains ε_{mc} at the end of the cracking state in the *ACK Model* or the end of primary cracking ε_{mcI} and secondary cracking ε_{mcII} in the *OH Model* are derived, see Fig. 3.1. For the *AK Model*, such a strain threshold does not exist because of the unlimited linear elastic bond stress. Ultimate failure at a stress σ_u occurs in all models when the tensile strength of the fibres σ_{fu} is reached. The corresponding strain ε_u is always smaller compared to the respective failure strain of the reinforcement ε_{fu} due to the participation of the matrix on load-bearing between cracks, also known as tension stiffening. A more detailed evaluation and a comparison of these models was already given by [Jesse 2004], which makes another repetition of the formulae dispensable. In these models, the material parameters are described in a deterministic manner. However, in the *Stochastic Cracking Model* by [Cuypers & Wastiels 2006] the *ACK Model* is enhanced with a stochastic description of the concrete tensile strength.

Another analytical model is developed by [Richter 2005]. This model is based on the bond differential equation, compare Section 3.4.2, which supersedes the assumptions for the stress distributions between concrete and reinforcement. The model is able to reproduce appropriately the response of fibre pull-out tests, which is the most basic configuration of fibres embedded in matrix. Similar arguments also apply to the *Cohesive Interface Model* by [Banholzer 2004] for the simulation of filament pull-out tests. Furthermore, in [Richter

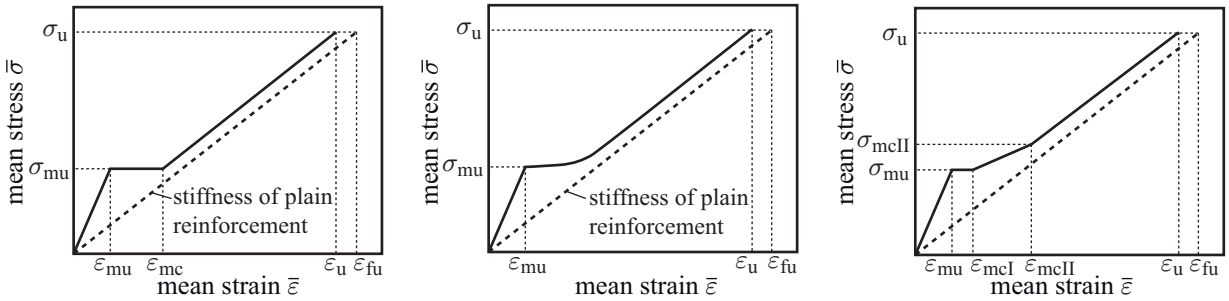

(a) *ACK Model* by [Aveston et al. 1971] (b) *AK Model* by [Aveston & Kelly 1973] (c) *OH Model* by [Ohno & Hannant 1994]

Figure 3.1.: Predictions of the tensile stress-strain behaviour by selected analytical models applied to TRC

2005] simulations of tensile specimens with multiple cracking corresponding to Section 2.3.4 were performed where the typical stress-strain response of the composite was relatively well reproduced. A nice feature of this model is that the anisotropy of the composite due to the inclusion of the multi-filament reinforcement can be taken into account by means of homogenisation methods. Some of the main drawbacks of this approach are that the positions of cracks are not covered, only symmetric stress distributions to the cracked cross sections are considered and the different bond zones in the reinforcement were only taken into account by means of neglecting the filaments in the core of the reinforcement. Moreover, due to the analytical nature of this model, a significant further subdivision of the reinforcement to cover effects resulting from the heterogeneity of the reinforcement and the load transfer mechanisms inside seems to be difficult if not impossible in practice.

A special class of models is given with the so-called *Fibre Bundle Models* as described briefly in Section 3.2.3. With these models the load-bearing and failure behaviour of multi-filament yarns is derived from the behaviour of all particular filaments. A drawback of these models in their present development state is that they only represent plain yarns but leave the interaction with the concrete unconsidered. However, as this class of models is an efficient means to study the load-bearing and failure behaviour of multi-filament yarns subjected to tensile loading resulting from its stochastic geometrical and material properties, it is also considered in the following.

One of the models, which combine a finer discretisation of the reinforcement and the consideration of the interaction with the concrete, is given with the *Strand Pull-Out Model* by [Banholzer 2004]. It is used to analyse the force-displacement response of yarn pull-out tests. Therefor, the yarn is represented with a layer model of an arbitrary number of layers. In the model, force-displacement relations for all particular layers are needed, which are established using the *Cohesive Interface Model* for the simulation of filament pull-out tests as mentioned previously. The failure state of every layer is fitted to an "active filaments"-displacement relation experimentally determined in the test under consideration. As the latter relation is unique for every specimen, the model has not really predictive capabilities. However, it might be useful to analyse the test under consideration. Another drawback of this model is that a realistic force-displacement response of the yarn pull-out test can only be achieved with a very large number of assumed layers. The *Strand Pull-Out Model* is described in some more detail in Section 3.2.3.

In [Konrad 2008], the so-called *Crack-Bridge Model*, which is a numerical model based on the Finite Element Method, is developed. It is primarily intended to analyse the behaviour of a matrix crack bridged by multi-filament yarns. Therefor, several sources of heterogeneity are introduced in the material law of the reinforcement showing usually a reduction of the load-bearing and failure performance compared to the assumption of homogeneity. In order to be able to simulate also multiple cracking of the matrix, as e. g. in tensile specimens corresponding to Section 2.3.4, the *Crack-Bridge Model* is combined with the *Stochastic Cracking Model* by [Cuypers & Wastiels 2006]. This approach overcomes also the deficiency of the *ACK Model* regarding TRC that the multi-filament reinforcement is modelled as a monofilament. In this context, the *Crack-Bridge Model* provides mean composite strains and mean crack spacings for certain load levels, which leads to a more realistic description of the stress strain response of the composite compared to the *ACK Model* and the *Stochastic Cracking Model*.

In [Lepenies 2007], an elaborate hierarchical multi-scale model framework with a number of analytical and numerical sub-models was developed, where the results at the lower scales, e. g. the micro-scale are used as input parameters for models at upper scales, e. g. meso-scale and macro-scale. To study the filament pull-out behaviour and to identify the bond law between matrix and filament, an analytical model corresponding to [Richter 2005] based on the bond differential equation is used. To investigate the failure behaviour of plain yarns, a *Fibre Bundle Model* is applied. The behaviour of a single crack bridge is investigated with analytical and numerical sub-models based on the *Adhesive-Cross-Linkage Model* by [Schorn 2003]. Furthermore, a so-called *Plug Model* is developed, which has similar considerations for the distributions of cross-linkages between filaments as the *Strand Pull-Out Model* by [Banholzer 2004], see also Fig. 3.5. However, both models follow up different solution strategies, see Section 3.2.3. For the simulation of the load-bearing behaviour of tensile specimens corresponding to Section 2.3.4, a combination of a *Fibre Bundle Model* and a model based on the bond differential equation for pull-out tests is used. The *Fibre Bundle Model* provides functions for the decrease of the cross-sectional area of the reinforcement and the bond quality between matrix and reinforcement with increasing loading. Multiple cracking is introduced with serial connections of pull-out test scenarios based on the bond differential equation. It has to be admitted that the global stress-strain or force-displacement responses of the various considered tests are in almost perfect agreement with respective experimental results. This might be explained with a good fitting of the various degradation functions to experimental results. Furthermore, it is worth to note that matrix cracks are prescribed and not an outcome of the simulation. Moreover, stress distributions in reinforcement and matrix are prescribed in a number of sub-models and not a result of the simulation. Additionally, the large number of sub-models makes the approach of [Lepenies 2007] quite complex and an application difficult.

A model, which is solely intended to represent the tensile behaviour of TRC corresponding to Section 2.3.4 is given with the *Two-Subroving Model* by [Hegger et al. 2006b, Bruckermann 2007]. It belongs to the class of finite element models. In this model, matrix and reinforcement are represented by one-dimensional bar elements, which are connected with zero-thickness bond elements. Furthermore, matrix cracks can develop discretely and are not prescribed, which facilitates a realistic representation of TRC specimens corresponding to Section 2.3.4. The reinforcement is subdivided into two parts: one representing the filaments in the fill-in zone and the other one to represent the filaments in the core. Obviously, this

rough discretisation of the reinforcement is not able to represent the telescopic behaviour of the multi-filament yarns. A speciality of this approach is that both parts of the reinforcement are directly linked to the matrix, which might be appropriate for the subdivision into two subrovings but cannot be extended physically meaningful for finer discretisations of the multi-filament yarns. Despite the coarse discretisation of the reinforcement, the model offers also the opportunity to analyse the stress distribution between the matrix and the reinforcement, which is an important feature of this model. In this context, it is also worth to mention that also asymmetric stress distributions between cracks in longitudinal direction can be represented with the model. This is an advantage compared to models in which symmetric stress distributions have to be assumed a priori to find a mathematical solution with acceptable effort.

In [Krüger 2004], a three-dimensional finite element model was established and applied to the simulation of yarn pull-out tests. With this model, it is possible to analyse the spatial stress distribution in the concrete. As the reinforcement is modelled as a compact bar, the stress distribution in the reinforcement over the cross section is inaccessible with this model. In the simulated force-displacement relations, the experimental maximum force and the corresponding displacement were accurately reproduced but in the subsequent pull-out regime the results of the model show insufficiencies compared to the experiments. Besides the realistic modelling of the concrete, the representation of the reinforcement is too simplified to gain information about the stress distribution in the reinforcement. Due to the spatial modelling large computational costs can be expected, which complicates a finer discretisation of the material structure.

After this brief survey over existing models regarding the tensile behaviour of TRC, the next sections will deal with particular approaches for the representation of geometrical and material properties.

3.2. Modelling of reinforcement of multi-filament yarns

3.2.1. Material behaviour of reinforcement

To establish appropriate laws for the material behaviour of the reinforcement it has to be noticed that the yarns are composed of a large number of filaments. As already mentioned in Section 2.1.2, the material behaviour of single filaments can be appropriately described with a linear elastic material law, see also Figs. 2.3(a) and 3.2(a). Thus, for the analysis of filament pull-out tests, e. g. in [Banholzer 2004] or [Richter 2005], usually stress-strain (σ-ε) relations of the form

$$\sigma = E_f \varepsilon \tag{3.1}$$

are used as material law for the filament where E_f is the Young's modulus of the filament. As failure of the filaments does usually not occur in filament pull-out tests, failure criteria are often missing. However, in [Konrad 2008] an inelastic material law is proposed for the reinforcement fibres considering a possible accumulation of additional notches due to contact of the filaments with sharp-edged matrix particles and the abrasion of fibre material when

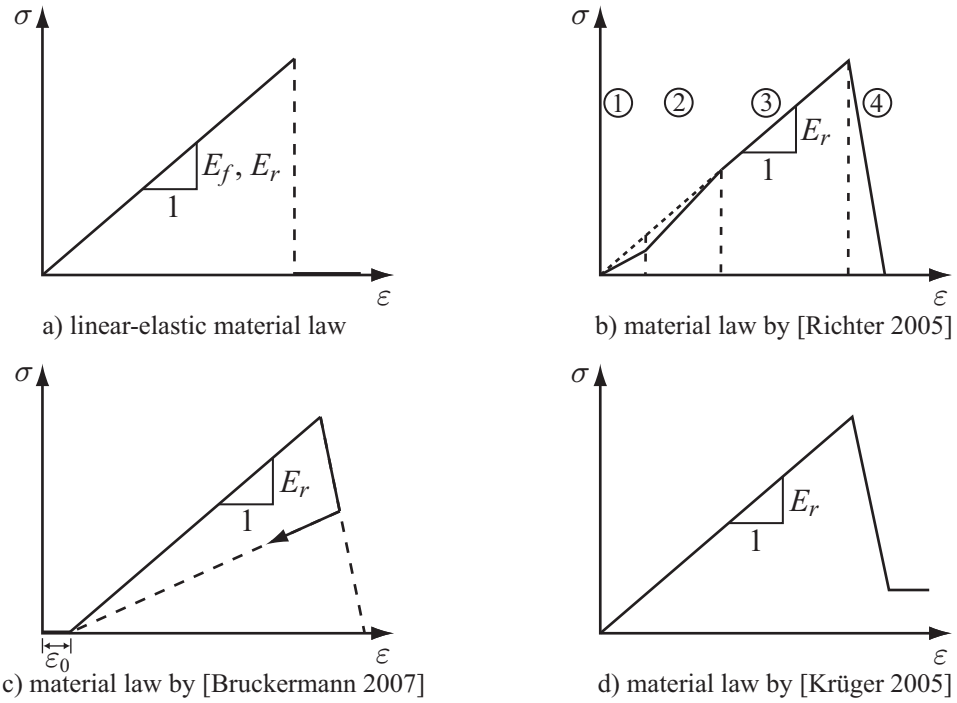

Figure 3.2.: Various constitutive laws for the reinforcement yarns

the filaments are moved over the rough matrix particles. The corresponding material law based on the concept of damage mechanics is given as

$$\sigma = (1 - D_f(\varepsilon_{max}, s_{inel}))\, E_f \varepsilon \quad \text{for} \quad 0 \leq D_f \leq 1 \tag{3.2}$$

with the damage of the fibre D_f depending on the maximum strain level reached by the fibre ε_{max} and the accumulated inelastic relative displacement (or slip) s_{inel}. For the determination of the evolution law for D_f it is referred to [Konrad 2008]. In the author's opinion, it is, however, questionable whether a significant amount of fibre material is abraded in typical loading scenarios, especially because usually a sizing or a coating is applied to the fibres.

The σ-ε behaviour of yarns might be also modelled with a linear elastic material law corresponding to Fig. 3.2(a) with the Young's modulus of the yarns E_r. This is done for instance in the *ACK Model* by [Aveston et al. 1971], the *AK Model* by [Aveston & Kelly 1973] and the *OH Model* by [Ohno & Hannant 1994]. However, experimental results show especially at low and high strains deviations from the linear course, see also Figs. 2.3(b) and 2.3(c). Therefor, [Richter 2005] proposed a subdivision of the material law for the yarns into four parts considering a delayed activation of the filaments due to waviness with an initially reduced Young's modulus and a decreasing part representing post-strength resistance based on the assumption of successive filament failure, see Fig. 3.2(b). A similar material law was proposed by [Bruckermann 2007] with an initial stress-free deformation ε_0 and a decreasing branch representing post-strength resistance, see Fig. 3.2(c). In [Krüger 2004] another constitutive law is proposed neglecting the delayed activation of the filaments but incorporating post-strength resistance and a constant residual stress, see Fig. 3.2(d). The constant residual stress might reflect unbroken filaments in the core of the yarn because the reinforcement is modelled in [Krüger 2004] as mono-filament without any subdivision as presented in the next section. In these models, a limited tensile strength is used to distinguish

between the pre- and the post-strength part of the relation. In [Lepenies 2007], a reduction of the cross-sectional area of the reinforcement A_r starting with the initial value A_0 based on the concept of damage mechanics is proposed to model the successive failure of filaments in the yarns:

$$A_r = (1 - D_A)A_0 \quad \text{with} \quad 0 \leq D_A \leq 1. \tag{3.3}$$

The evolution law for the damage-type variable D_A is non-linear and derived from a calibration based on experimental results of yarn pull-out tests corresponding to Section 2.3.3 or simulations with a fibre bundle model, see Section 3.2.3. In principle, this approach corresponds to Eq. (3.2), but with different values of the stiffness term EA manipulated. For this approach no failure criterion is necessary because the load-bearing capacity of the yarn automatically decreases with increasing D_A and is zero if $D_A = 1$.

In analytical models, e. g. by [Banholzer 2004] and [Richter 2005], the material law is included in the calculations via the stiffness term of the reinforcement $E_r A_r$. In numerical models based on the Finite Element Method, the reinforcement is often modelled with bar or truss elements, as e. g. in a numerical implementation of the *Adhesive-Cross-Linkage Model* by [Lepenies et al. 2007, Lepenies 2007] based on [Schorn 2003], in the *Two-Subroving Model* by [Bruckermann 2007] or in the *Crack-Bridge Model* by [Konrad 2008]. In the Finite Element Method, the stiffness term $E_r A_r$ is incorporated in the so-called element stiffness matrix, see Section 4.4.

3.2.2. Geometrical representation of reinforcement

As it was pointed out in Section 2.1.1, multi-filament yarns are highly heterogeneous. Furthermore, also different load transfer mechanisms exist over the cross section as described in Section 2.3.1. Thus, a model representing the yarns as a compact cross section without any subdivision similar to steel reinforcement bars might be not appropriate in most of the cases. However, [Krüger 2004] used such an approach to reduce the numerical effort in the finite element computations. In the *ACK Model* by [Aveston et al. 1971] and the *AK Model* by [Aveston & Kelly 1973], which were not primarily developed for TRC, a perfect embedding of the reinforcement fibres is assumed and, thus, a subdivision of the reinforcement remains unconsidered.

A number of approaches to subdivide the yarns exist, see [Zastrau et al. 2003b], [Brameshuber 2006] and Fig. 3.3. In every partition, several filaments are represented, which are assumed to have approximately constant properties. In the layer model, see Fig. 3.3(b), constant material and bond properties of the filaments in circumferential direction are assumed while varying material properties and/or imperfect bond are assumed in radial direction. A corresponding subdivision into two partitions is e. g. performed in the analytical model by [Richter 2005], the *OH-Model* by [Ohno & Hannant 1994] and the *Two-Subroving Model* by [Hegger et al. 2006b, Bruckermann 2007] to distinguish between the different bond conditions in the fill-in zone and the core zone of the yarns. In the *Strand Pull-Out Model* by [Banholzer 2004], the *Adhesive-Cross-Linkage Model* by [Schorn 2003] with respective implementations by [Lepenies et al. 2007, Lepenies 2007], the *Plug Model* by [Lepenies 2007] and the *Crack-Bridge Model* by [Konrad 2008], the yarn is represented by a layer model with more than two layers.

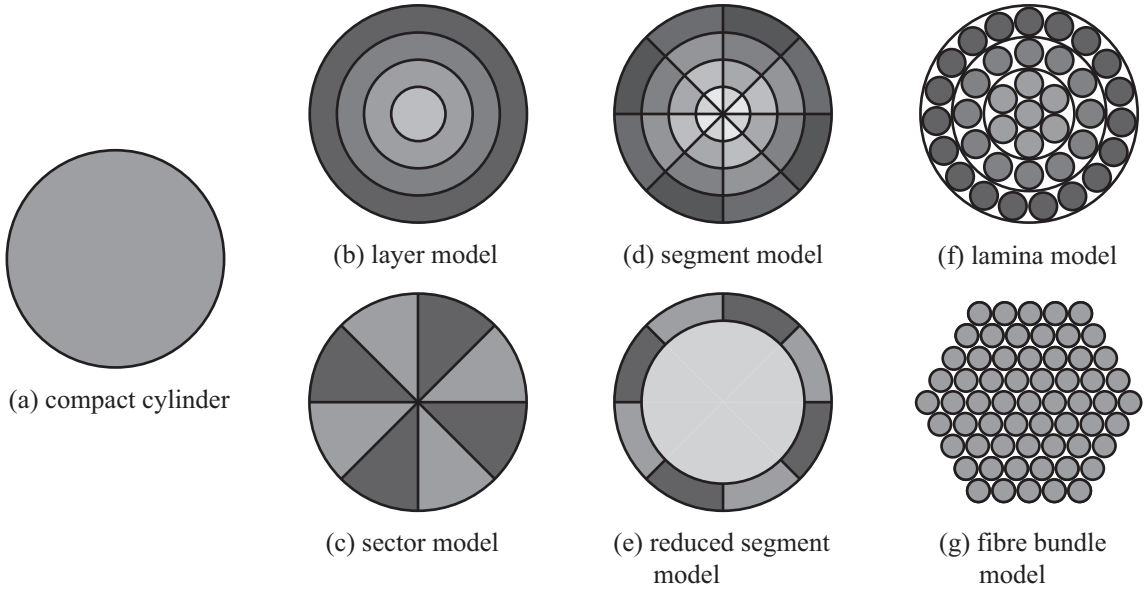

Figure 3.3.: Various schemes of the cross-sectional subdivisions of yarns

Vice versa, in the sector model, see Fig. 3.3(c), the material and bond properties are assumed constant in radial direction and varying in circumferential direction. For the modelling of varying bond conditions over the yarn cross section, a layer model seems to be more appropriate. For stochastic variations of material properties as e. g. Young's modulus or tensile strength both the layer and the sector model might be useful. This leads consequently, to a blending of both approaches resulting in the segment model, see e. g. [Hegger et al. 2002] and Fig. 3.3(d). With an increasing number of partitions also the effort to determine respective parameters and to solve the resulting mechanical problem increases. Thus, it might be useful to subdivide only some layers in circumferential direction while remaining compact parts as it is shown e. g. in Fig. 3.3(e) with a subdivision of only the outermost layer. The most realistic approach to model a yarn is to represent every filament separately, see Fig. 3.3(f,g). On the other hand, it is also the model where the greatest effort in the determination of the material parameters and the solution of the arising equations has to be spent. Thus, such a subdivision has been only used hitherto to analyse the behaviour of single yarns by means of so-called fibre bundle models, which are described briefly in the next section.

The shape of the yarns is not limited to circles as presented in Fig. 3.3. Often the yarns have more elliptical or completely irregular shapes. A nice way to represent also more complex cross-sectional shapes is given by means of superellipses as [Lepenies 2007] showed. The shape of the yarns also influences the number of filaments in contact with matrix as already mentioned in Section 2.3.1. Thus, for the modelling of the bond between the matrix and the reinforcement the contact area S is of importance. In a first approach, the contact area of a yarn S_{yarn} can be estimated simply as the circumference C of the assumed cross-sectional area of the yarn (circle, ellipsis, etc.) multiplied by the considered length (dx, ΔL) of the embedded yarn. Such kind of approach was used e. g. by [Richter 2005], [Lepenies 2007] and [Konrad 2008] optionally with a subdivision of the yarns into several layers corresponding to Fig. 3.3(b). This obviously underestimates the contact area as the yarns are composed of a large number of filaments, which have in sum a much larger surface area than the assumed compact body.

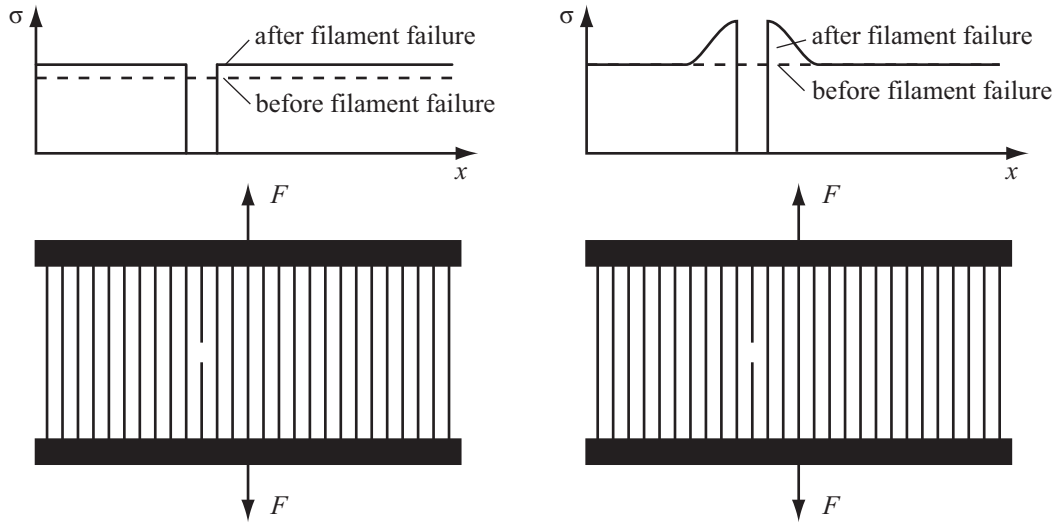

(a) Global load redistribution (b) Local load redistribution

Figure 3.4.: Global and local load redistribution in fibre bundle models

A step towards a more realistic estimation of S_{yarn} is made with a consideration of the surface roughness of the yarn due to composition of filaments. This still underestimates the real contact area, in general, because the matrix or the coating penetrate the yarns, which leads to larger bonded areas of the filaments than the parts at the surface of the yarn. In the *Two-Subroving Model* by [Bruckermann 2007], the contact area is estimated for the filaments in the fill-in zone and the core zone as the sum of the surface areas of the filaments assumed in these zones. While this approach is realistic for the fill-in zone, it overestimates the discontinuous contact areas between the filaments in the core of the yarns.

3.2.3. Fibre bundle models

An efficient class of models for the simulation of the load-bearing and failure behaviour of plain multi-filament yarns is given with fibre bundle models. The initial work on this topic was carried out by [Daniels 1945] based on the weakest-link model established by [Weibull 1939]. In this kind of model, a number of fibres with stochastically modelled material properties like tensile strength or Young's modulus, are loaded in parallel. If the tensile strength of a fibre is reached, the fibre is removed and the load is redistributed to the other fibres. Two major schemes exist concerning the load redistribution: global load sharing where the load is distributed uniformly to the other fibres and local load sharing where the load redistribution is limited to the fibres in the closer vicinity of the failed fibre, see Fig. 3.4. By means of these models the successive decrease of stiffness and failure mechanisms can be studied. Recently, special characteristics of TRC were applied to fibre bundle models, see [Chudoba et al. 2006], [Vořechovský & Chudoba 2006], [Curbach et al. 2006] and [Lepenies 2007].

Variations of fibre bundle models are given with the *Plug Model* by [Lepenies et al. 2007, Lepenies 2007] and the *Strand Pull-Out Model* by [Banholzer 2004], which are both analytical models. In these models, a number of filaments are summarised in discrete layers

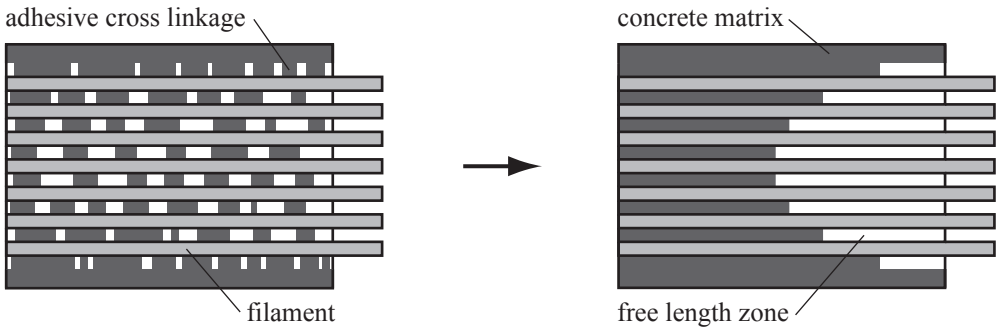

Figure 3.5.: Transformation of discontinuous adhesive cross linkages to free deformation length in the *Strand Pull-Out Model* and the *Plug Model*

corresponding to the layer model in Fig. 3.3(b) to represent the yarns. Furthermore, both models consider the reducing bond quality in the yarns towards the core with increasing free lengths of the layers. The rationale behind this approach is the assumption of a decreasing number of matrix "bridges", which can transfer adhesive forces between the filaments, towards the yarn core. This corresponds also to the assumptions in the *Adhesive-Cross-Linkage Model* by [Schorn 2003]. Accumulating all the matrix "bridges" at the embedded end of a pull-out test or the centre between two matrix cracks leads to increasing free length towards the core, see Fig. 3.5. Although the base model coincides in the *Strand Pull-Out Model* and the *Plug Model*, different ways of further analysis are followed.

In the *Plug Model*, the layers of the yarn are pulled equally at both the embedded and the free end of the yarn. The distribution of the free length leads to a stress distribution with usually large stresses in the outer layers and low stresses in the core. Applying a limited tensile strength leads to a successive failure of the yarn from the outer layers to the core. With this model the force-displacement response of the yarn at a single matrix crack is analysed depending on the distribution of the free length. This incorporates also information if the free length distribution leads to brittle or successive failure of the yarn.

In the *Strand Pull-Out Model*, it is assumed that the force-displacement response of a matrix-yarn system is determined by the superposition of the force-displacement responses of all filaments in the yarn. These force-displacement relations are determined by means of filament pull-out simulations based on bond differential equations corresponding to Section 3.4.2. The summary of a number of filaments in a certain layer necessitates mean force-displacement relations for every layer. The displacements where the layers are assumed to fail are determined based on results of the FILT test, compare Section 2.3.3. Furthermore, the innermost layers in the yarn core are assumed to be pulled out. With the model the simulated force-displacement response coincides well with corresponding experimental results. However, the model has not predictive capabilities as it is also stated in [Banholzer 2004]. The reason is that essential informations are used, which are unique for the test under consideration as for instance the active filaments-displacement relation and cannot be transferred easily to another test. Nevertheless, the model is helpful to understand the load-bearing and failure behaviour in pull-out tests.

3.3. Material and cracking behaviour of concrete matrix

Although concrete has a highly heterogeneous structure, it is assumed homogeneous in all models regarding TRC, i. e. the structural composition of cement paste, aggregates and pores as described in Section 2.2.1 is neglected. The pre-cracking uniaxial tensile behaviour of the matrix is usually assumed linear elastic:

$$\sigma = \begin{cases} E_c\varepsilon & \text{for} \quad 0 \leq \varepsilon \leq \frac{f_{ct}}{E_c} \\ 0 & \text{for} \quad \varepsilon > \frac{f_{ct}}{E_c} \end{cases} \tag{3.4}$$

where E_c is the Young's modulus of the matrix. Matrix cracking is usually detected with stress or strain criteria, i. e. reaching the assumed tensile strength f_{ct} or the corresponding strain $\varepsilon(\sigma = f_{ct})$. In [Bruckermann 2007], the tensile strength is modelled stochastically with a Gaussian distribution. From a physical point of view, this is not reasonable, because a tensile strength lower than zero is impossible but can occur at least theoretically with a Gaussian distribution, compare Fig. 4.9. This problem can be sorted out with a truncation of the Gaussian distribution function, which was not performed in [Bruckermann 2007]. In [Cuypers & Wastiels 2006], the *ACK Model* is enhanced with a stochastic description of matrix tensile strength by applying a two-parametric Weibull distribution, which can be assessed to be appropriate because the Weibull distribution yields only values larger than zero, see Appendix A.3. The resulting model is called *Stochastic Cracking Model*.

After a matrix crack has developed either brittle failure can be assumed, which means setting $\sigma = 0$ and $E_c = 0$ once the cracking criterion is reached, or post-cracking resistance can be considered. With respect to experimental observations as described in Section 2.2.2, the consideration of post-cracking resistance, also called tension softening, leads to a more realistic model. However, the incorporation of descriptions for tension softening usually increases the effort for the solution of the governing equations in both analytical and numerical models. As it is often assumed that tension softening has only a secondary influence on the load-bearing behaviour of the composite under uniaxial tensile loading, tension softening is often neglected and brittle failure is assumed instead. This is the case for instance in the *ACK Model* by [Aveston et al. 1971], the *AK Model* by [Aveston & Kelly 1973], the *OH Model* by [Ohno & Hannant 1994], the analytical model by [Richter 2005] and the numerical model by [Konrad 2008].

If tension softening is applied, the implementation is often based on the fictitious crack model by [Hillerborg et al. 1976], see Fig. 3.6. In this model, it is distinguished between uncracked zones with elastic deformations u_{el}, and a fracture process zone with a crack and a crack width w, which deforms inelastically. Superposing both types of deformation leads to the stress-displacement $(\sigma - u)$ relation of the entire specimen. In models based on the Finite Element Method applying continuum elements, a regularisation has to be applied to the softening elements to achieve mesh objectivity. For the one-dimensional case, w can be related to the length of the element, see Section 4.2.1. This is also known as crack band approach [Bažant & Oh 1983]. For the two-dimensional or the three-dimensional case, more complex considerations have to be carried out, see for instance [Pröchtel & Häussler-Combe 2008]. There exists a broad range of approaches for uniaxial softening laws of the fracture process zone, e. g. linear or exponential approaches. In [Bruckermann

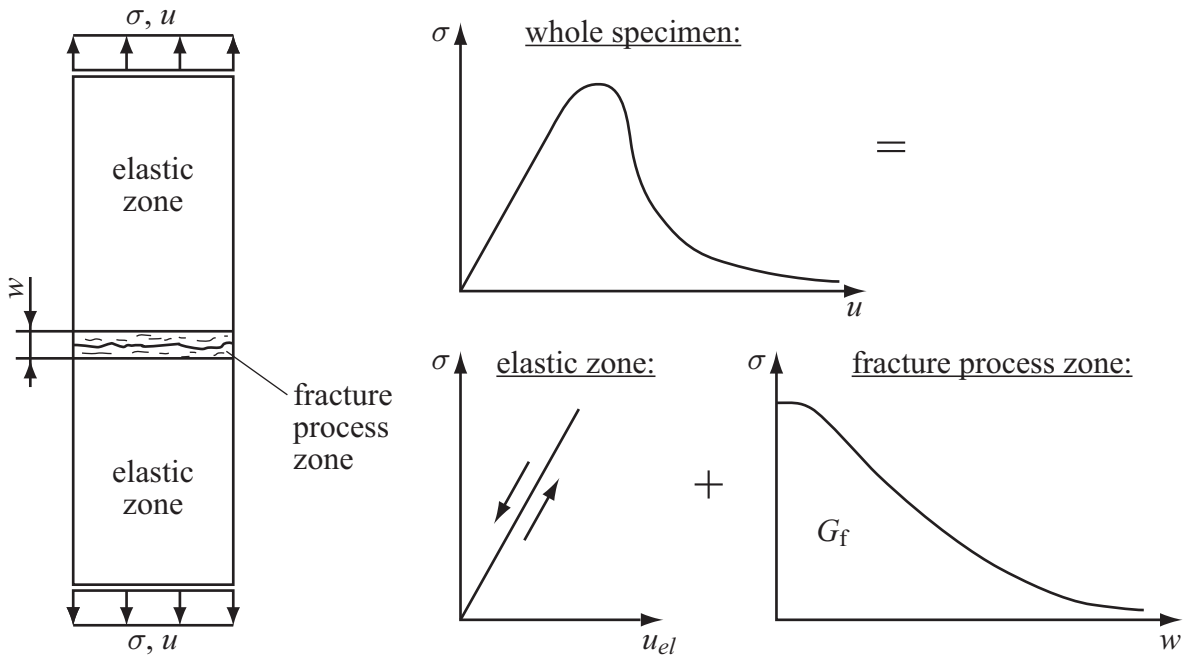

Figure 3.6.: Fictitious crack model; according to [Hillerborg et al. 1976]

2007], a bilinear softening law according to [Petersson 1981] and in [Lepenies 2007] an exponential softening law are used.

Besides the constitutive relation for the case of loading, also a respective material description for unloading and reloading has to be considered. Unloading obviously occurs if cyclic loading is applied. However, as reinforced concrete is considered, also local unloading due to stress redistribution during multiple cracking of the concrete as described in Section 2.3.4 can occur. As the concrete stiffness degrades in the tension softening regime, the constitutive relation is different to the loading case. Therefor two limit cases exist, which can be physically motivated. The first one is elastic unloading, i. e. a course back to the origin of the σ-ε relation, while the second one is plastic unloading according to the initial slope of the σ-ε relation. The assumption of plastic unloading incorporates inelastic deformations of the material where yielding of metals is an example. Contrary, elastic unloading goes out from the assumption that only the stiffness of the material decreases with increasing loading but no remaining deformations exist after complete unloading. This can be modelled based on the concept of damage mechanics. As mentioned previously, both cases are limit cases and, thus, the real behaviour will be situated in between as it was shown already in Section 2.2.2. However, it is worth to mention again that remaining deformations in concrete do not result from "real" plasticity as in the case of metals but rather from incompatibilities of the crack faces and grown micro-cracks, which need additional energy to be closed in the unloading regime. It was also shown in Section 2.2.2 that experimental stress-deformation relations show strong non-linearity and different courses for unloading and reloading as well as a dependence on the loading regime. An approach, which incorporates these complex properties is given e. g. by [Yankelevsky & Reinhardt 1989]. However regarding the matrices used in TRC, no corresponding data exists, which might be one reason why usually simplified approaches are used. For instance, in the model by [Bruckermann 2007] elastic damage is applied where the relation for unloading and reloading is identical.

In a number of models studying the behaviour of so-called crack bridges, the cracks are predefined and, thus, cracking and post-cracking of the matrix is not regarded. To this class of models belongs e. g. the *Adhesive-Cross-Linkage Model* by [Schorn 2003], the *Plug Model* by [Lepenies 2007] and the *Crack-Bridge Model* by [Konrad 2008]. Similar to the reinforcement, the material law is included in analytical models, e. g. by [Banholzer 2004] and [Richter 2005], in the calculations via the Young's modulus E_c in the stiffness term for the matrix $E_c A_c$. For the numerical models, the material law is included in the element stiffness matrix, see Section 4.4.

If multiaxial stress states are considered, an approach to model the constitutive behaviour is given with so-called microplane models, which are introduced as material law in the finite elements. For the foundations of this approach it is referred to [Bažant & Prat 1988]. In [Krüger 2004], a microplane model is used to describe the material behaviour of the matrix in 3D simulations of yarn pull-out tests according to Fig. 2.11(a) and for the simulation of four-point bending tests of TRC plates. Also [Bruckermann 2007] uses a microplane model reduced to the plane stress state in a model for the biaxial tensile behaviour of TRC plates. Alternatively, one of the multitude of multi-axial constitutive relations based on continuum mechanics might be applied to characterise the multi-axial behaviour of the matrix, see e. g. [Häussler-Combe & Hartig 2008].

3.4. Bond behaviour

3.4.1. Bond stress-slip relations

It is in general accepted that appropriate descriptions of the bond mechanisms are an essential part for the modelling of composites. Different approaches exist concerning TRC while most of them are based on so-called bond stress-slip (τ-s) relations. The bond stress τ is a tangential stress variable, which results from forces due to adhesive and frictional load transfer mechanisms acting at the interface between different materials or similar separated materials. The slip s is the relative displacement between the materials at the interface, e. g. between the matrix and the reinforcement or between parts of the reinforcement if the yarns are subdivided corresponding to Section 3.2.2.

In Fig. 3.7, a selection of possible bond laws is presented where the laws in Figs. 3.7(a)-(d) were analysed by [Lepenies et al. 2001, Zastrau et al. 2003a] for the usage in models concerning TRC. The most basic approach of a bond law is the assumption of a constant bond stress, see Fig. 3.7(a). This approach corresponds to the assumption of purely frictional load transfer and neglects existing adhesion. It is used e. g. in the *ACK Model* by [Aveston et al. 1971] and the *OH Model* by [Ohno & Hannant 1994]. Purely adhesive load transfer can be modelled with an elastic bond law, see also Fig. 3.7(a), which in turn neglects bond degradation. This approach is used e. g. in the *AK Model* by [Aveston & Kelly 1973]. Both bond law approaches oversimplify the real bond behaviour but might be helpful for efficient solutions e. g. in analytical models. For most bond laws used in numerical models more complex τ-s relations are applied. Usually the τ-s relation is modelled with an initial increase corresponding to the assumption of adhesive bond. With increasing loading a degradation

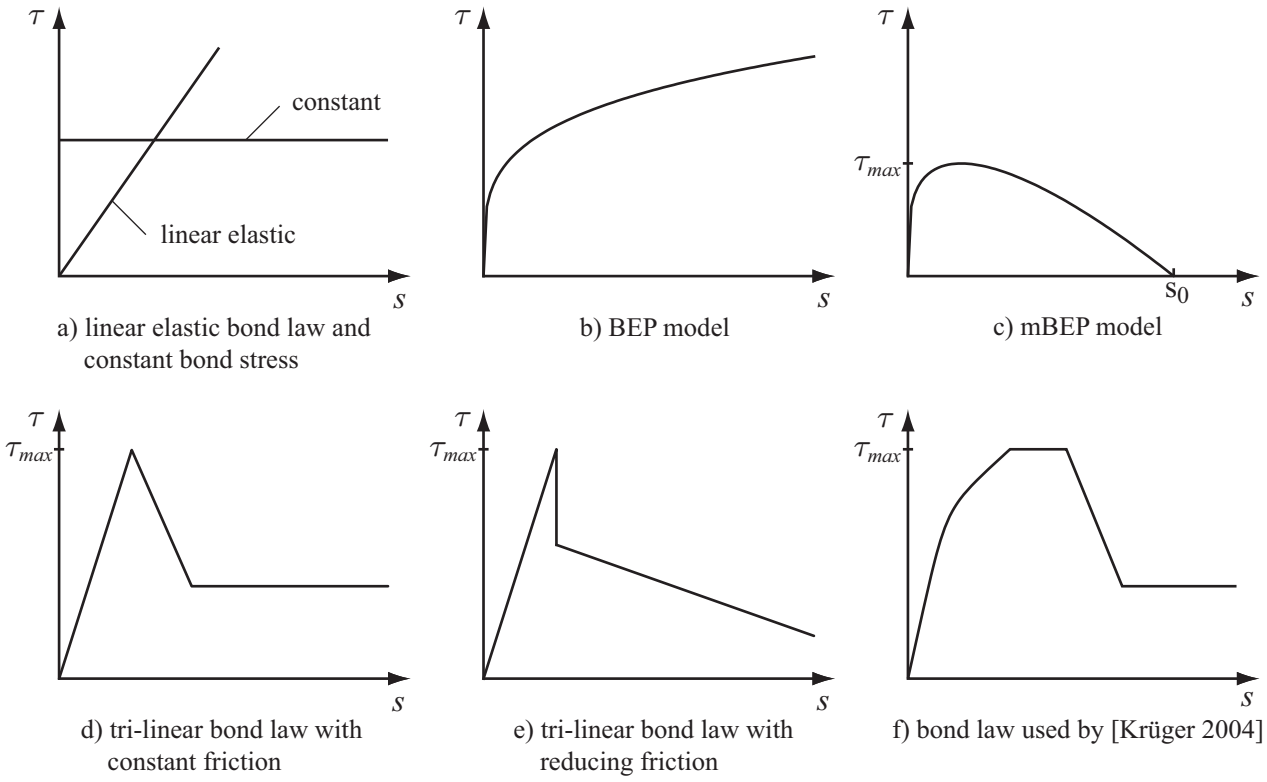

Figure 3.7.: Various bond laws

of the adhesive bond associated with a transition to friction can be assumed. An example for a τ-s relation possessing these characteristics is given with the so-called BEP model, see Fig. 3.7(b), proposed by [Eligehausen et al. 1983] for the bond between steel bars and concrete:

$$\tau(s) = C_{BEP} s^{\alpha_{BEP}} \quad \text{with} \quad 0 < \alpha_{BEP} < 1 \quad \text{and} \quad C_{BEP} > 0 \tag{3.5}$$

where C_{BEP} and α_{BEP} are shape parameters. In this approach, the transferable bond stress is not limited, but increases only less with increasing slip. This led [Focacci et al. 2000] to modify the BEP approach in order to introduce a bond stress limit and a subsequent reduction of the bond stress with further increasing slip, see Fig. 3.7(c). The corresponding τ-s relation is given as

$$\tau(s) = C_{mBEP} s^{\alpha_{mBEP}} \left(1 - \frac{s}{s_0}\right) \text{ with } 0 < \alpha_{mBEP} < 1,\ C_{mBEP} > 0 \text{ and } 0 \leq s \leq s_0 \tag{3.6}$$

with shape parameters C_{mBEP}, α_{mBEP} and the slip value s_0 where no further stress can be transferred over the interface. Both, the BEP and mBEP approach need only one equation to describe the load transfer behaviour of the interface, at least as long as the slip continuously increases, which make them quite attractive for both analytical and numerical models as no case distinctions are necessary. However, as the variability of the shape due to variations in the shape parameters is quite limited, bond laws are often defined as piecewise functions instead. While such an approach necessitates case distinction operations, almost arbitrary shapes of the τ-s relations are possible.

In the case of interfaces between filaments and matrix, usually tripartite piecewise functions with an initially elastic behaviour of the bond are used due to the adhesion between filaments and matrix. This is followed by a decreasing part corresponding to the assumption of degrading adhesion with the transition to friction after exceeding the bond strength τ_{max}. Finally, pure friction is assumed with a constant bond stress. A typical example for such a bond law is proposed by [Richter 2005] for TRC with a trilinear course based on the bond law by [Abrishami & Mitchell 1996] developed for the bond between deformed steel bars and concrete, see Fig. 3.7(d). Furthermore, this approach is enhanced in [Richter 2005] with a further subdivision of the decreasing part of the relation, which is interpreted as a state of completely degraded adhesion but with a relative high roughness of the interface successively reducing with increasing slip. There exist a number of variations of this approach. For instance in the bond law proposed by [Konrad 2008], which consists also of piecewise linear functions, it is assumed that the bond stress drops abruptly after the bond strength τ_{max} is reached, see Fig. 3.7(e). Additionally, reducing friction is assumed by [Konrad 2008], which is modelled with a decreasing course of the τ-s relation after the stress drop.

In [Bruckermann 2007], it is proposed to use τ-s relations based on filament pull-out tests, e. g. by [Banholzer 2004], approximated with multi-linear piecewise functions. In order to take into account a reduced bond quality in yarns compared to the perfectly embedded filament, as described in Section 2.3, scaling factors for the τ value resulting from the τ-s relation are introduced. Although multi-linear piecewise functions are proposed, [Bruckermann 2007] uses more simple bi-linear and tri-linear τ-s relations fitted to the τ-s relations determined based on filament pull-out tests. In [Lepenies 2007], a similar approach was applied. The τ-s relation was determined analytically based on the bond differential equation, see Section 3.4.2, assuming piecewise constant bond stresses along the embedded length. This leads to a step function for the τ-s relation, which can be arbitrarily shaped within the limits of the model. Furthermore, some damage-type function was introduced to reduce the contact area and associated the transferable force with increasing slip. As a last example of used τ-s relations, the approach by [Krüger 2004] shall be mentioned, which is based on the bond model for deformed steel bars provided in [ModelCode 1990], see Fig. 3.7(f). Specialities of this approach are the non-linear course of the initial part of the τ-s relation and the plastic deformations of the bond interface after reaching the maximum bond stress τ_{max}. Regarding the bond behaviour in TRC, it is, however, questionable whether considerable plastic deformations occur at this stage because ribs are missing on the yarns. Subsequently, a linear transition to the constant part of the τ-s relation is considered similar to the approach by [Richter 2005].

For a realistic description of the bond behaviour, an appropriate assumption for the case of unloading has to be included in the bond law. Apart from the case of cyclic loading also in the case of monotonically increasing uniaxial loading applied to the specimen, unloading might occur locally due to local stress redistributions e. g. in case of matrix cracking. This corresponds to the arguments for unloading and reloading of the matrix in the post-cracking regime given in Section 2.2.2. Thus, also in the τ-s relation a description for unloading (and reloading), i. e. a reduction of the maximum bond stress with decreasing slip at a certain load level, needs to be incorporated. In general, the course of the τ-s relation in the unloading regime has to deviate from the initial course for the case of loading. An exception is the initial stage where elastic deformation of the bond interface can be assumed, which justifies a modelling of the τ-s relation for unloading identical to the case of loading. However,

after reaching the bond strength τ_{max} bond degradation can be assumed, which necessitates a reduction of maximum reachable bond stress. Often a linear course of the τ-s relation describing unloading is chosen. Limit cases for the unloading course, which can be physically motivated, are elastic unloading, i. e. a course back to the origin of the τ-s relation, and plastic unloading according to the initial slope of the τ-s relation. A physical interpretation of both limit cases, which applies also to the bond laws was already given in Section 3.3 regarding the unloading behaviour of concrete in the post-cracking regime. It can be supposed that under a monotonic tensile loading, the differences between both limit cases are insignificant as the local slip reduction is usually relatively small. However, the system response will be supposedly significantly different if cyclic loading is applied. In most of the existing models, one of the limit cases is used although it is in general accepted that a mixture of both would lead to a more realistic description. Elastic unloading is used for instance by [Bruckermann 2007]. In contrast, in the *ACK Model* and the model by [Krüger 2004] plastic unloading is applied. In the bond models by [Lepenies 2007] and [Konrad 2008], both elastic and plastic unloading as well as intermediate states are implemented. However, in [Lepenies 2007] the differences and effects with varied unloading regimes in the τ-s relation were not investigated. Similarly, in [Konrad 2008] only the behaviour of a single crack bridge was analysed with varying unloading slopes. In the analytical model by [Richter 2005], the *AK Model* and the *OH Model* unloading remains unconsidered.

As it was mentioned previously, the bond conditions inside a yarn are not constant but the transferable bond stress reduces towards the core of the yarns. The reason is that the matrix or the coatings usually penetrate only the outer parts of the yarns continuously. Consequently, only lower adhesive or frictional load transfer occurs between the filaments in the yarn core. Thus, for the inner interfaces, if modelled at all, different τ-s relation compared to the fill-in zone have to be established. In [Bruckermann 2007], the τ value resulting from the τ-s relation based on filament pull-out tests is simply scaled with a scalar factor representing the bond quality, which is larger than 0 and lower than 1. Although this scaling factor is chosen much lower compared to the bond law for the fill-in zone, it is questionable if this approach takes into account appropriately the different load transfer mechanisms in both zones. A similar approach incorporating scaling parameters is followed by [Konrad 2008] in the *Crack-Bridge Model* where the yarns are subdivided into a number of layers. Additionally, a so-called bond-free length is introduced to model the reduction of the contact area between matrix and reinforcement towards the core of the yarn. In the implementations of the *Adhesive-Cross-Linkage Model* by [Lepenies 2007], the reduction of bond quality towards the core is represented in two versions. In a discontinuous description of the bond, the bond quality is reduced by a reduction of bond elements towards the core resulting in a decrease of the contact area. In a continuous description, the bond strength is reduced linearly towards the core, which corresponds to the scaling parameters by [Bruckermann 2007] and [Konrad 2008]. In the *Plug Model* by [Lepenies 2007], bond is not explicitly modelled but the bond variations in the yarns are represented by increasing bond-free length towards the yarn core. The same applies also for the *Strand Pull-Out Model* by [Banholzer 2004]. The analytical model by [Richter 2005] contains a description of the inner interface, which is however not used in exemplary simulations. In the model by [Krüger 2004] it is not distinguished between fill-in zone and core of the yarns as already mentioned.

3.4.2. Analytical models based on bond differential equation

In analytical models, the distribution of the forces between the matrix and the reinforcement is often determined by means of solutions of the bond differential equation. A candidate of such an analytical model for the tensile behaviour of TRC is the one-dimensional model developed by [Richter 2005]. Similar models are given in [Lepenies 2007] and [Banholzer 2004, Banholzer et al. 2005]. To establish the bond differential equation for an arbitrary two-phase composite where both phases are homogeneous materials, see Fig. 3.8, equilibrium considerations at a differential element of length $\mathrm{d}x$ lead to the balance of forces

$$N_r(x) + N_c(x) = N_r(x) + \mathrm{d}N_r(x) + N_c(x) + \mathrm{d}N_c(x) \tag{3.7}$$

with the normal forces in the reinforcement $N_r(x)$ and the matrix $N_c(x)$ as well as respective differential increments $\mathrm{d}N_r(x)$ and $\mathrm{d}N_c(x)$ depending on the position x. From Eq. (3.7) it follows that

$$\mathrm{d}N_c(x) = -\mathrm{d}N_r(x), \tag{3.8}$$

which can be quantified with

$$\mathrm{d}N_c(x) = -\tau(x)C\mathrm{d}x \quad \text{and} \quad \mathrm{d}N_r(x) = \tau(x)C\mathrm{d}x \tag{3.9}$$

where C is the circumference of the contact area and τ the bond stress. The slip s is defined as relative displacement between the displacements of the matrix u_c and reinforcement u_r

$$s(x) = u_r(x) - u_c(x). \tag{3.10}$$

A differentiation of Eq. (3.10) with respect to x leads to the strains of matrix ε_c and reinforcement ε_r

$$\frac{\mathrm{d}s(x)}{\mathrm{d}x} = \frac{\mathrm{d}u_r(x)}{\mathrm{d}x} - \frac{\mathrm{d}u_c(x)}{\mathrm{d}x} = \varepsilon_r(x) - \varepsilon_c(x). \tag{3.11}$$

A second differentiation with respect to x gives the respective strain variations

$$\frac{\mathrm{d}s^2(x)}{\mathrm{d}x^2} = \frac{\mathrm{d}\varepsilon_r(x)}{\mathrm{d}x} - \frac{\mathrm{d}\varepsilon_c(x)}{\mathrm{d}x}. \tag{3.12}$$

Under the assumption of a linear elastic behaviour of matrix and reinforcement, the strains can be formulated as

$$\varepsilon_r(x) = \frac{N_r}{E_r A_r} \quad \text{and} \quad \varepsilon_c(x) = \frac{N_c}{E_c A_c} \tag{3.13}$$

with the Young's moduli E_c, E_r and the cross-sectional areas A_c, A_r of matrix and reinforcement. Inserting Eqs. (3.13) and (3.9) into Eq. (3.12) leads with a slip-based bond law $\tau[s(x)]$ to the bond differential equation

$$\frac{\mathrm{d}s^2(x)}{\mathrm{d}x^2} = \left(\frac{1}{E_r A_r} + \frac{1}{E_c A_c}\right) C\tau[s(x)]. \tag{3.14}$$

With a double integration of Eq. (3.14) and the application of appropriate boundary con-

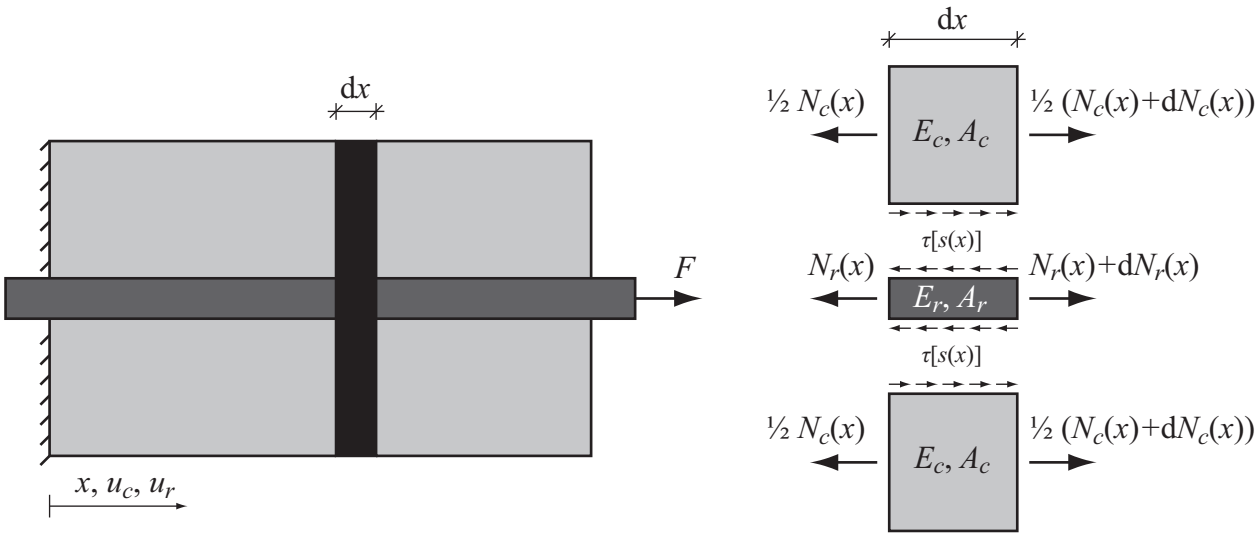

Figure 3.8.: Equilibrium of forces at a differential element of a fibre embedded in cementitious matrix

ditions, a solution for $s(x)$ can be established. For the case of constant $\tau[s(x)]$ a solution is presented e. g. by [Lepenies 2007]. Furthermore, [Richter 2005] gave piecewise closed solutions for a multi-linear τ-s relation. The advantage of such an approach is an efficient analysis if the problem is once solved. However, for more complex systems the effort to establish a closed solution can increase considerably. For instance if one considers more than one interface, as for instance [Richter 2005] does with an additional inner interface between the fill-in zone and the core zone of a yarn besides the outer interface between the matrix and the yarn, a system of second-order differential equations has to be solved. Nevertheless, models of this kind can be efficiently applied to the analysis of relatively simple tests as e. g. filament pull-out tests, where only one interface exists and the material behaviour of matrix and filament can be assumed linear elastic, see e. g. [Banholzer 2004, Banholzer et al. 2005], [Richter 2005] or [Lepenies 2007].

3.4.3. Numerical modelling of bond

For the numerical modelling of the load transfer mechanisms in TRC three major approaches exist. The first and most basic approach is given with a direct coupling of matrix and reinforcement neglecting any relative displacement, limited bond stresses and bond degradation between the matrix and the reinforcement. This approach is of course not very realistic and, thus, also the results of respective calculations often reflect the structural response only in a rough manner.

The second approach is based on the concept of contact mechanics and the third approach is based on bond stress-slip relations similar to the previous section. To the knowledge of the author, the contact mechanics approach is only applied regarding TRC to model delamination processes between the material layers of TRC, see [Matheas 2006]. Concerning the bond between matrix and reinforcement, hitherto, contact elements were not applied, probably due to the great numerical effort one faces with the contact detection.

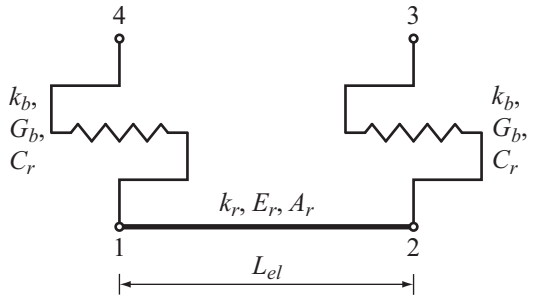

Figure 3.9.: Bond element used in [Bruckermann 2007] and [Konrad 2008]

The common approach is to use so-called bond elements where a broad variety exists. In [Konrad 2008] some kind of macro-element called *Fibre Interface Model* is used, which represents the axial rigidity of the reinforcement fibres and the bond to the matrix or subsequent fibres. Four different approaches for the bond representation are tested in [Konrad 2008] regarding numerical efficiency and robustness. Finally, a zero-thickness bond element corresponding to [Herrmann 1978] is chosen and used in the subsequent computations, see Fig. 3.9. This element has four nodes and a linear displacement approach. Deviating from the approach by [Herrmann 1978], deformations perpendicular to the axis of the bar element are not taken into account. The element stiffness matrix $\mathbf{K}_{el}$ of this element type, which couples the vector of nodal displacements $\mathbf{u} = [u_1, u_2, u_3, u_4]^T$ of the element with the corresponding vector of nodal forces $\mathbf{f} = [f_1, f_2, f_3, f_4]^T$, compare Section 4.4, is given with

$$\mathbf{f} = \mathbf{K}_{el}\mathbf{u} = \begin{bmatrix} k_b + k_r & -k_r & 0 & -k_b \\ -k_r & k_b + k_r & -k_b & 0 \\ 0 & -k_b & k_b & 0 \\ -k_b & 0 & 0 & k_b \end{bmatrix} \mathbf{u} \text{ with } k_r = \frac{E_r A_r}{L_{el}},\ k_b = \frac{L_{el} G_b C_r}{2} \quad (3.15)$$

where k_r is the stiffness term of the reinforcement fibre resulting from the Young's modulus E_r and the cross-sectional area A_r of the reinforcement as well as the element length L_{el}. Furthermore, the stiffness term of bond k_b includes the circumference of the reinforcement C_r and the bond modulus G_b, which is called somewhat misleadingly bond stiffness in [Konrad 2008]. For the derivation of Eq. (3.15) and the properties of the element see [Herrmann 1978, Kaliakin & Li 1995, Konrad 2008]. The upper left 2×2-submatrix in Eq. (3.15) contains the element stiffness matrix of a simple two-node bar element, compare Section 4.4.4.1. Moreover, it can be seen from the allocation of the matrix in Eq. (3.15) that the displacement fields of both bond sub-elements are decoupled. The advantage of summarising the properties of the reinforcement and the bond in one element is that degradation and failure mechanisms of both can be treated simultaneously on the element level. This may slightly reduce numerical costs. However, if unbonded reinforcement parts have to be modelled, i. e. no corresponding matrix elements or other reinforcement elements exist, the deformation state of the free nodes remains undetermined. This leads to numerical problems, which can be circumvented by omitting the free nodes leading to a simple bar element. The same element type is also used by [Bruckermann 2007] in the *Two-Subroving-Model*.

In [Krüger 2004], a zero-thickness bond element developed by [Ožbolt et al. 2002] is used. Also in this approach only degrees of freedom in the axial direction of the reinforcement bar elements are considered while degrees of freedom in transverse direction remain unconsidered. However, a degradation of bond due to radial concrete stresses is incorporated in the bond

law. Bond elements are also used in the implementation of the Adhesive Cross-Linkage model by [Lepenies 2007] where it is however not documented how the bond elements are implemented.

3.5. Requirements to an improved model

In the previous sections, modelling approaches for various geometrical and material parameters typical for TRC were presented. In this section, requirements to an improved model shall be briefly discussed. As it was already mentioned in the introduction, the aim of this work is a model for the uniaxial tensile behaviour of TRC. Moreover, it would be desirable to have a unified model, which can reproduce or even better predict the behaviour of the composite starting from single fibre pull-out tests up to tensile tests with multiple concrete cracking without further sub-models. Besides the global responses of these systems, which are usually provided by experiments, a further insight in the stress distribution and redistribution, e. g. in case of matrix cracking, between the matrix and the reinforcement would be helpful for understanding the governing mechanisms.

Analytical models are not qualified to cover the entire range of these requirements with a reasonable effort. Especially if failure or cracking events have to be considered and complex kinematics have to be taken into account as it is the case for TRC, analytical models reach their limits usually quickly, as it was already indicated in the previous sections. Approaches, which can cover the entire range of these tests are given with the multi-scale model framework by [Lepenies 2007] and the framework by [Konrad 2008]. However, the stress distributions can only be determined for basic configurations as e. g. single crack bridges. Moreover, as both approaches consist of a number of sub-models, the desire of a unified model cannot be fulfilled with these approaches.

The most realistic approach would be a detailed three-dimensional model. However, as the conclusions from the model by [Krüger 2004] already showed, computational costs are an important issue, which circumvent the practical application of such a model. If it is taken into account that a main source of the complexity of the behaviour of TRC is the stochastic character of the material properties, these arguments are even amplified, because a stochastic analysis necessitates a series of simulations to gain results at a certain confidence level. This further increases the computational effort.

Thus, a certain reduction of detailedness has to be accepted for a conveniently usable model. The results of the *Two-Subroving Model* by [Hegger et al. 2006b, Bruckermann 2007] show a relatively good agreement with experimental observations at least for the applied tensile tests with multiple matrix cracking. Furthermore, scattering material properties can be incorporated in the model and it provides also stress distributions inside the composite. Thus, such kind of model is a candidate for further elaboration. However, a finer discretisation of the multi-filament yarns seems to be necessary to model also e. g. yarn pull-out tests where successive filament failure dominates the force-displacement response of the composite. Moreover, also the material description can be improved in particular as already pointed out.

4. A one-dimensional model for the uniaxial tensile behaviour of TRC

In the previous chapter, existing modelling approaches were presented. Furthermore, the properties and abilities of these models were evaluated and conclusions for an improved model were drawn. In this chapter, a novel modeling approach is presented. The model shall have the ability to cover a broad range of tensile tests regarding TRC, which are filament pull-out tests, yarn pull-out tests and tests with overcritically reinforced TRC specimens with multiple matrix cracking, with a unified approach. Additionally, the model shall provide the ability to analyse the stress distribution in the composite in order to investigate load-bearing and failure mechanisms, which often cannot be obtained, or are difficult to ascertain using experimental techniques.

4.1. Geometrical properties of the mechanical model

A main conclusion of the previous chapter was that a sufficiently fine discretisation of the reinforcement is necessary for a proper representation of the load-bearing response of TRC under tensile loading. On the other hand, computational costs still limit the conveniently usable detailedness of the discretisation. Thus, a fibre bundle model as represented in Figs. 3.3 (f,g) cannot be used in practice combined with a representation for the concrete which shows multiple cracking. However, a grouping of filaments with similar properties in segments as shown in Figs. 3.3 (d) might sufficiently reduce the problem size. Such a subdivision still offers the opportunity to model scattering material properties and varying bond conditions over the cross section. In many configurations, further simplifications might be appropriate as e. g. for a tensile test with multiple concrete cracking, where the scatter of the material parameters of the reinforcement is of minor importance because of the usually vast number of loaded filaments. In this case, also a layer model considering only varying bond conditions in radial direction might by sufficient. An even simpler model can be applied for filament pull-out tests where only a mono-filament needs to be modelled. However, as it is usually easier to simplify a complex model than to refine a coarse model, the geometrical framework for the reinforcement will be established in the following based on the most complex configuration, the segment model. Furthermore, such a configuration is also necessary for simulations of yarn pull-out tests. The concrete will be modelled homogeneously as comparable models confirmed the appropriateness of this approach.

Another conclusion in the previous chapter was that a numerical model based on the *Finite Element Method* would be advantageous due to its variability. An analytical model would establish too many restrictions in this respect. Although the implementation of the used finite elements is not presented before Section 4.4, it might be helpful for comprehension of

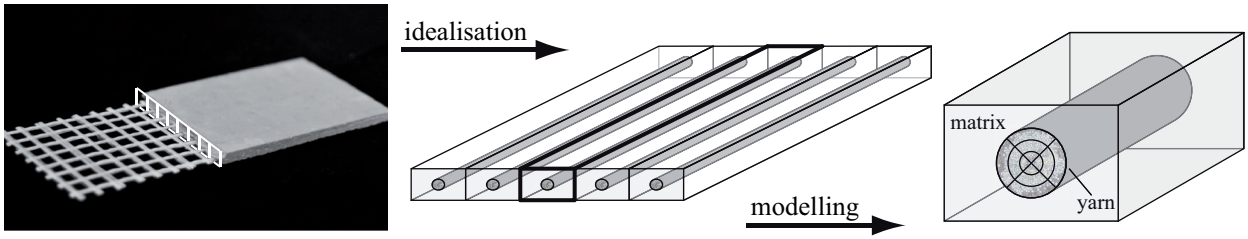

Figure 4.1.: Visualistion of idealisation for modelling of TRC

the following discussion to explain how the model is working, in general. It is emphasised once more that only predominantly uniaxial tensile loading is considered. For the modelling, the composite is subdivided into cells of matrix each with one embedded reinforcement yarn, see Fig. 4.1. Assuming that all of these cells possess approximately the same load-bearing behaviour due to the large number of yarns and uniaxial loading, the behaviour of the entire composite can be represented by a multiple of a single cell. Within this cell, the reinforcement yarn can be finer discretised to represent, e. g., bond gradients or varying material properties over the yarn cross section.

In the model, transverse strains due to Poisson's ratio are neglected. Furthermore, shear gradients in matrix and reinforcement, which occur especially in the case of matrix cracking where bond stresses are transferred at the interface between matrix and reinforcement, are supposed to be small due to a large number of reinforcement yarns relatively uniform distributed over the cross section and the reinforcement alignment corresponding to the loading direction. Thus, one-dimensional bar elements are sufficiently accurate to model the uniaxial properties of the components of the composite, i. e. the matrix and the reinforcement. Besides the bar elements, the model consists of bond elements to represent the load transfer between concrete and filaments as well as between filaments in a realistic manner. The bond elements represent also shear deformations of the vicinity of the interface between matrix and reinforcement. The model is shown schematically in Fig. 4.2. In longitudinal direction x, which is also the loading direction, the concrete and the reinforcement are modelled by serial connections of bar elements, called chains, see Fig. 4.2 (bottom centre). A sufficiently large number of bar elements is necessary to represent the stress distribution in longitudinal direction appropriately.

As pointed out in Section 2.3.1, the bond conditions in the multi-filament yarns usually vary over the cross section and the material properties of the filaments are subjected to scatter. Thus, a further subdivision of the reinforcement into several bar element chains is often necessary. Therefor, filaments with approximately equal properties are summarised in so-called segments, see Fig. 4.2 (top left). In longitudinal direction, each of these segments is represented by a bar element chain. Corresponding to the position in the segmentation scheme, these bar element chains are arranged in a lattice scheme in transverse direction, see Fig. 4.2 (bottom left). The force transfer between the concrete and the reinforcement segments is realised with bond elements arranged at corresponding nodes between the bar element chains. The bond elements are represented in Fig. 4.2 as springs for reasons of simplicity although their action is better represented by Fig. 4.19. It should be pointed out that similar models of bar element chains connected with bond elements were already used, e. g., by [Littwin 2001], [Häussler-Combe et al. 2004, Häussler-Combe & Jesse 2005], [Hegger et al. 2006b, Bruckermann 2007] and [Konrad 2008]. However, in all

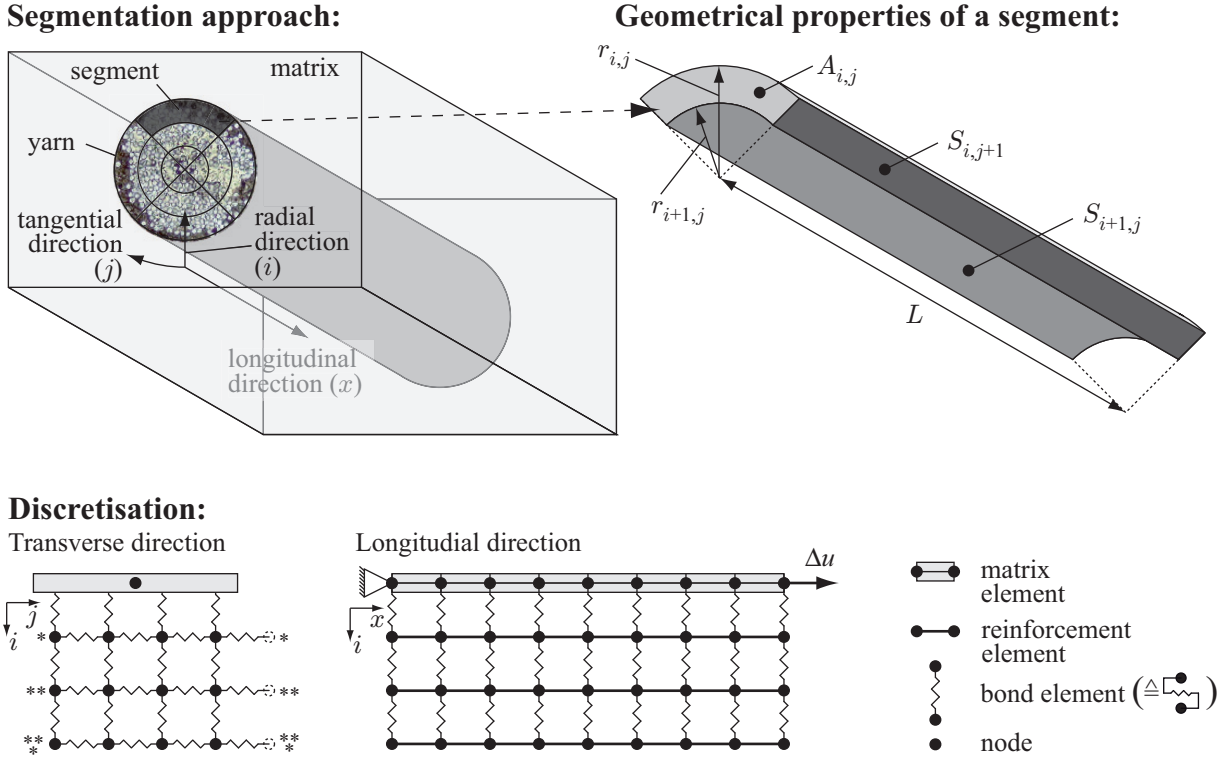

Figure 4.2.: Geometrical model (top) and lattice discretisation in the cross section (bottom left) and a longitudinal section (bottom right)

these models, the subdivision of the yarn was not performed in such detail as in the current model.

The geometrical arrangement of the bar elements and the bond elements in the model was introduced in principle in [Häussler-Combe & Hartig 2007]. The concrete is represented by a single chain of bar elements and, thus, it is assumed homogeneous in material and stress state in transverse direction. The cross-sectional area of the concrete is given by

$$A_c = a_c \cdot b_c \tag{4.1}$$

where a_c is the width and b_c is the height of the concrete or the specimen, respectively. The cross-sectional area of the reinforcement is small compared to that of the concrete. Therefore, the reduction of the cross-sectional area of the concrete due to the reinforcement is neglected.

Although, a one-dimensional model is used for the chains and, thus, there are only degrees of freedom in longitudinal direction, the heterogeneity of the reinforcement in transverse direction is considered. This is realised with the segmentation of the reinforcement using a lattice scheme. Therefor, a radial direction i ($i \in \mathbb{N} | 1 \leq i \leq m$) and tangential direction j ($j \in \mathbb{N} | 1 \leq j \leq n$) are defined as it is observable in Fig. 4.2 (top left). Every segment i, j is assumed as homogeneous with characteristic properties of the number of filaments, which it represents.

The cross-sectional area of a yarn A_{yarn} is approximated by the product of the mean cross-sectional area of the filaments $\bar{A}_{fil}$ and the number of filaments n_{fil} of a yarn:

$$A_{yarn} = n_{fil} \cdot \bar{A}_{fil}. \tag{4.2}$$

Assuming that the cross-sectional area A_{yarn} is a perfectly circular area, which might underestimate the dimensions of a yarn [JESSE 2004], leads with the radius r to $A_{yarn} = \pi \cdot r^2$. Hence, a certain segment i, j has a cross-sectional area $A_{i,j}$ of

$$A_{i,j} = \frac{1}{n}\pi \left(r_{i,j}^2 - r_{i+1,j}^2\right), \tag{4.3}$$

which is the segment of an annulus. As it can be seen, $r_{i,j}$ is the outer radius while $r_{i+1,j}$ is the inner radius of the segment i, j. If more than one yarn is considered, it is assumed that the cross-sectional area of a segment i, j can be determined with

$$A_{i,j} = n_{yarn}\frac{1}{n}\pi \left(r_{i,j}^2 - r_{i+1,j}^2\right) \tag{4.4}$$

where n_{yarn} is the number of yarns.

The interaction between the bar element chains is modelled with bond elements, which are controlled by bond laws formulated as bond stress-slip (τ-s) relation as described in Section 4.2.3. To calculate bond forces T resulting from the bond stresses τ, the estimation of the bond surface areas S is necessary. Therefor, the different bond characteristics in the fill-in zone and the core zone have to be considered. The bond surface areas in the fill-in zone can be assumed to be continuous because of the penetration with cementitious matrix. This is not the case in the core zone where, if at all, only discontinuous matrix cross-linkages as shown schematically in Fig. 3.5 (left) exist. It can be assumed that at least in the innermost parts of the core only frictional load transfer at the contact areas of the filaments is possible due to the warping and imperfect alignment of the filaments, which results also in discontinuous load transfer along the filaments. These arguments also apply for yarns with additional polymeric coating. These coatings are applied as suspensions and develop their strength not before they are hardened due to water removal and heat. This leads also to discontinuous bond between the filaments because the polymers do not fill the entire space between the filaments and, thus, only local cross-linkages develop. These effects cause the problem of the estimation of the bond surface areas in each segment. While in the fill-in zone a summation of the lateral surface areas of the filaments would be appropriate, for the core segments the contact areas between the filaments and the matrix cross-linkages would be needed to summed up. For the latter, unfortunately no experimental data exists. To solve this problem, the bond laws are varied while the bond surface areas are estimated according to the segmentation approach. This is possible because only the product of both is relevant when formulating the problem.

According to the lattice scheme, every segment interacts for $i < m$ with four surrounding segments: two in radial and two in tangential direction. For $i = m$, which means the innermost reinforcement segments, the segments interact only with three neighbours: one in radial and two in tangential direction. In tangential direction, which means between segments i, j and $i, j + 1$, the circumferential fraction is the difference between the inner and outer radius of the segment, which leads to the bond surface area

$$S_{i,j+1} = (r_{i,j} - r_{i+1,j}) \cdot L \tag{4.5}$$

where L is the length of the element in longitudinal direction, see also Fig. 4.2 (top right). The indices $i, j + 1$ of S refer to the interface between the segments i, j and $i, j + 1$, which is

under consideration. In radial direction, which means between two segments i, j and $i+1, j$, the bond surface area is given by the arc length of the respective segment and the length L in longitudinal direction

$$S_{i+1,j} = \frac{1}{n} \cdot L \cdot 2\pi r_{i+1,j}. \tag{4.6}$$

If more than one yarn is considered, the bond surface areas can be multiplied with the number of yarns n_{yarn} as all yarns are assumed to behave equally in the average. For one segment i, j, the total bond force $T_{i,j}$ is given for $i < m$ by the sum of the bond forces of the four interfaces

$$\begin{aligned} T_{i,j} &= T_{i+1,j} + T_{i-1,j} + T_{i,j+1} + T_{i,j-1} \\ &= \tau(s)_{i+1,j} \cdot S_{i+1,j} + \tau(s)_{i-1,j} \cdot S_{i-1,j} + \tau(s)_{i,j+1} \cdot S_{i,j+1} + \tau(s)_{i,j-1} \cdot S_{i,j-1} \end{aligned} \tag{4.7}$$

and for $i = m$ by the sum of the bond forces of the three interfaces

$$\begin{aligned} T_{i,j} &= T_{i-1,j} + T_{i,j+1} + T_{i,j-1} \\ &= \tau(s)_{i-1,j} \cdot S_{i-1,j} + \tau(s)_{i,j+1} \cdot S_{i,j+1} + \tau(s)_{i,j-1} \cdot S_{i,j-1}. \end{aligned} \tag{4.8}$$

Because of the lattice scheme, the bond surface areas in j-direction are equal. In contrast, the respective bond laws $\tau(s)$ can be different. Thus, besides the geometrical properties also the material properties are important in the model. Consequently, the next sections deal with the description of the material properties.

4.2. Deterministic constitutive models

4.2.1. Constitutive behaviour of concrete

As a starting point, the constitutive relations to describe the material behaviour of the concrete matrix are presented. The concrete is assumed to have up to a possible tensile failure linear elastic material behaviour according to Hooke's law

$$\sigma = \begin{cases} E_{c0}\varepsilon & \text{for} \quad 0 \leq \varepsilon \leq \frac{f_{ct}}{E_{c0}} \\ 0 & \text{for} \quad \varepsilon > \frac{f_{ct}}{E_{c0}} \end{cases} \tag{4.9}$$

where E_{c0} is the initial Young's modulus of the concrete, see Fig. 4.3 (a). This stress-strain (σ-ε) relation does not reflect the tensile behaviour of concrete entirely accurate as concrete shows some softening already before reaching the tensile strength f_{ct}, compare Fig. 2.6. However, the application of a corresponding constitutive law leads in the considered model in the deterministic case under tensile loading to a uniform softening of all concrete elements, which does not correspond to reality. The reason is that a priori no preferential position for strain localisation exists. This cannot be circumvented as long as no fluctuations in the material properties are introduced. On the other hand, the deviation of the $\sigma - \varepsilon$ relation from linear elasticity might be negligible with respect to the behaviour of the composite. Tensile failure or cracking, respectively, reaching the tensile strength f_{ct} is modelled with a stress criterion.

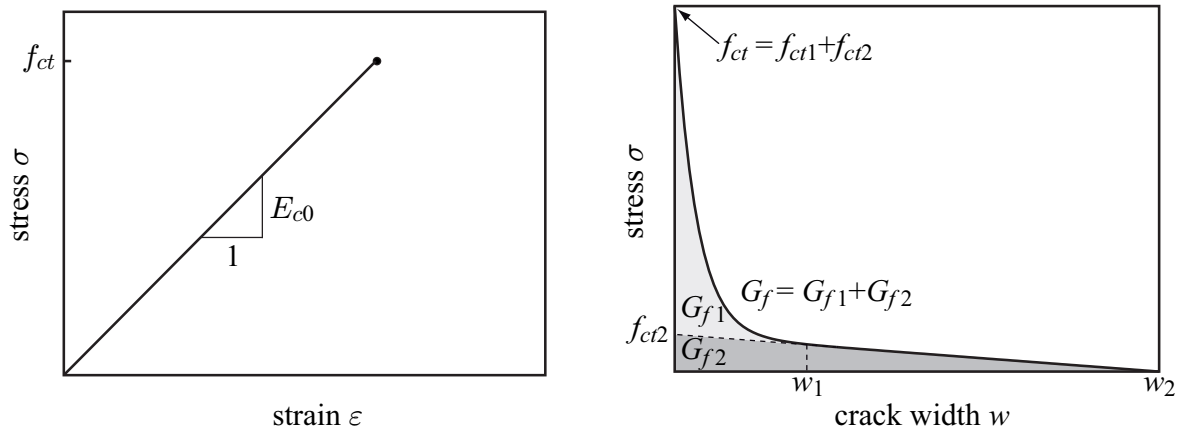

(a) Pre-cracking behaviour

(b) Post-cracking behaviour; according to [Remmel 1994]

Figure 4.3.: Constitutive relations of the concrete

When f_{ct} is exceeded brittle failure can be assumed in a first approach, i. e. setting $\sigma = 0$ and $E_{c0} = 0$. More realistic is considering post-cracking resistance also referred to as tension softening as described in Section 2.2.2. In the model, the respective σ-ε relation is implemented based on the tension softening law by [Remmel 1994], see Fig. 4.3 (b), which is formulated as stress-crack width ($\sigma - w$) relation for $0 < w \leq w_2$:

$$\sigma = f_{ct1} \exp\left(-\left(\frac{w}{w_1}\right)^c\right) + f_{ct2}\left(1 - \frac{w}{w_2}\right);\ f_{ct} = f_{ct1} + f_{ct2}. \tag{4.10}$$

The equation contains a form parameter c, two parameters f_{ct1} and f_{ct2} associated with the tensile strength f_{ct} as well as two characteristic crack widths w_1 and w_2. While the final crack width $w_2 (= w_c)$ and f_{ct} can be taken directly from experimental results, in the case of TRC e. g. from [Brockmann 2005], the parameters c, w_1 and the ratio between f_{ct1} and f_{ct2} have to be fitted to the experimental $\sigma - w$ relation under consideration of the fracture energy G_f [N/m]. Assuming that the ratio between f_{ct1} and f_{ct2} and the value of c are estimated, e. g. with a calibration at experimental results, the crack width w_1 can be determined with

$$G_f = G_{f1} + G_{f2} = f_{ct1} \int_0^\infty \exp\left(-\left(\frac{w}{w_1}\right)^c\right) \mathrm{d}w + \frac{1}{2} f_{ct2} w_2. \tag{4.11}$$

The solution of the integral equal to G_{f1} incorporates the Γ-function given in Eq. (A.14) leading to

$$G_{f1} = \frac{f_{ct1} w_1 \Gamma\left(\frac{1}{c}\right)}{c}. \tag{4.12}$$

Thus, w_1 can be determined with Eqs. (4.11) and (4.12) as

$$w_1 = \left(G_f - \frac{1}{2} f_{ct2} w_2\right) \frac{c}{f_{ct1} \Gamma\left(\frac{1}{c}\right)}. \tag{4.13}$$

Hitherto, Eq. (4.10) is related to the displacement w. To formulate σ depending on ε, the displacement w has to be related to a length L_{fpz}, which corresponds to the width of the

fracture process zone, compare Section 2.2.2. As tension softening starts after exceeding f_{ct}, ε has to be reduced by the respective strain value leading to

$$w = \left(\varepsilon - \frac{f_{ct}}{E_{c0}}\right) L_{fpz}. \tag{4.14}$$

In order to obtain mesh-objective results, L_{fpz} can be set conveniently equal to the bar element length L_{el} according to Section 4.4.4.1. This corresponds to a regularisation based on the crack band approach by [Bažant & Oh 1983]. The σ-ε relation for tension softening is then given with

$$\sigma = f_{ct1} \exp\left(-\left(\frac{L_{el}\left(\varepsilon - \frac{f_{ct}}{E_{c0}}\right)}{w_1}\right)^c\right) + f_{ct2}\left(1 - \frac{L_{el}\left(\varepsilon - \frac{f_{ct}}{E_{c0}}\right)}{w_2}\right)$$
$$\text{for } \frac{f_{ct}}{E_{c0}} < \varepsilon < \frac{f_{ct}}{E_{c0}} + \frac{w_2}{L_{el}}. \tag{4.15}$$

If $\varepsilon \geq f_{ct}/E_{c0} + w_2/L_{el}$, σ is assumed zero although it is not exactly zero due to the exponential term in Eq. (4.15). For the equilibrium iterations described later, the current Young's modulus has to be determined. For Newton-Raphson type solution methods, which will be presented in Section 4.4.3, the tangential value E_t might be necessary, which is the first derivative of the element's σ-ε relation. The first derivative of Eq. (4.15) with respect to ε is given, again for $f_{ct}/E_{c0} < \varepsilon < f_{ct}/E_{c0} + w_2/L_{el}$, with

$$\frac{\mathrm{d}\sigma}{\mathrm{d}\varepsilon} = E_t = -\frac{c\, f_{ct1}}{\left(\varepsilon - \frac{f_{ct}}{E_{c0}}\right)} \left(\frac{L_{el}\left(\varepsilon - \frac{f_{ct}}{E_{c0}}\right)}{w_1}\right)^c \exp\left(-\left(\frac{L_{el}\left(\varepsilon - \frac{f_{ct}}{E_{c0}}\right)}{w_1}\right)^c\right) - \frac{L_{el} f_{ct2}}{w_2}. \tag{4.16}$$

Corresponding to the restriction of Eq. (4.15), in the case of $\varepsilon \geq f_{ct}/E_{c0} + w_2/L_{el}$, the Young's modulus E_t is assumed equal to zero.

If unloading occurs in an element after exceeding f_{ct}, for example due to global unloading or local stress redistributions, σ reduces linearly in the element according to the function:

$$\sigma_{unload} = \frac{\sigma(\varepsilon = \varepsilon_{max})}{\varepsilon_{max}} \varepsilon. \tag{4.17}$$

The strain ε_{max} is the maximum value of ε reached so far and is hence a state variable. The tangential modulus for unloading is given with

$$\frac{\mathrm{d}\sigma_{unload}}{\mathrm{d}\varepsilon} = \frac{\sigma(\varepsilon = \varepsilon_{max})}{\varepsilon_{max}}, \tag{4.18}$$

which also corresponds to the concept of damage mechanics. The same relations are also used for reloading. The assumption of pure damage modelled with a linear function is a considerable simplification, as in Fig. 2.6 a non-linear unloading behaviour incorporating also inelastic deformations was identified for concrete in the post-cracking regime. However, as no experimental results regarding the cyclic post-cracking behaviour of the used concrete are available, the applied simplifications might be appropriate in a first approach.

From the computational point of view, the main advantage of the tension softening formulation by [Remmel 1994] is the almost linear decrease of the stress in the rear tail of the stress-strain relation, which is associated with an almost constant tangential element stiffness. This leads to better convergence compared to only exponential approaches as for instance given by [Gopalaratnam & Shah 1985] where the unfavourable case of tangential stiffnesses approaching asymptotically zero occurs. Nevertheless, problems with convergence can occur in the case of unloading, because the transition between the slopes in Eqs. (4.16) and (4.18) is not continuous.

4.2.2. Constitutive behaviour of reinforcement

In good agreement with experimental observations, compare Section 2.1.2, the tensile behaviour of glass can be modelled linear elastic with a limited tensile strength f_{rt}. However, due to the production process the reinforcement yarns often exhibit waviness, which leads to initial stress-reduced deformations. Therefor, the constitutive law for the reinforcement, see Fig. 4.4 (a), is implemented with a smooth exponential transition to the linear elastic relation (with a positive strain shift ε_{wav}):

$$\sigma = \begin{cases} (\exp(a_{wav}\varepsilon) - 1)b_{wav} & \text{for} \quad 0 \le \varepsilon \le \varepsilon_{ini} \\ E_r(\varepsilon - \varepsilon_{wav}) & \text{for} \quad \varepsilon_{ini} < \varepsilon < \varepsilon_{wav} + \frac{f_{rt}}{E_r} \\ 0 & \text{otherwise.} \end{cases} \tag{4.19}$$

The parameters a_{wav} and b_{wav} of the exponential function can be determined according to the condition that the exponential function is tangent to the linear function at a pre-defined point $(\varepsilon_{ini}, \sigma_{wav})$. Furthermore, Eq. (4.19) contains the Young's modulus E_r and the tensile strength f_{rt} of the reinforcement yarns. Both values can be determined in tension tests, see for instance [Abdkader 2004]. Again, the first derivatives of the $\sigma - \varepsilon$ relation, i. e. the tangent moduli, might be needed for the equilibrium iterations within the Finite Element Method, which are given with

$$\frac{\mathrm{d}\sigma}{\mathrm{d}\varepsilon} = \begin{cases} a_{wav}b_{wav}\exp(a_{wav}\varepsilon) & \text{for} \quad 0 \le \varepsilon \le \varepsilon_{ini} \\ E_r & \text{for} \quad \varepsilon_{ini} < \varepsilon < \varepsilon_{wav} + \frac{f_{rt}}{E_r} \\ 0 & \text{otherwise.} \end{cases} \tag{4.20}$$

In the case of negligible waviness, the material behaviour of the reinforcement can be assumed linear elastic according to Hooke's law with a limited tensile strength f_{rt}:

$$\sigma = \begin{cases} E_r\varepsilon & \text{for} \quad 0 \le \varepsilon \le \frac{f_{rt}}{E_r} \\ 0 & \text{for} \quad \varepsilon > \frac{f_{rt}}{E_r} \end{cases}, \tag{4.21}$$

see Fig. 4.4(b). According to Eq. (4.21), it is assumed that the reinforcement yarns fail in a brittle manner, which is supported by experimental observations by [Abdkader 2004]. Thus, in the case of failure of these elements, the Young's modulus E_r is set to zero. A certain post-failure resistance as observable in yarn tensile tests, compare Figs. 2.3 (b,c), is not incorporated in the constitutive relations. Vice versa, it can be a result in the simulations if the material properties of the reinforcement are modelled stochastically.

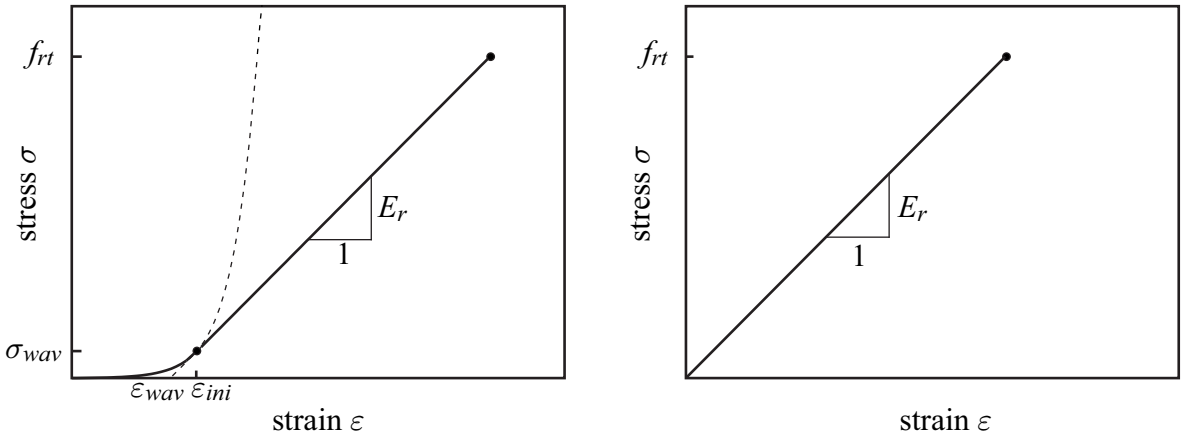

(a) With waviness (b) Linear elastic

Figure 4.4.: Constitutive relations for the reinforcement yarns

4.2.3. Interaction between constituents of the composite

The load transfer between the concrete and the reinforcement is described with bond stress-slip (τ-s) relations. In order to cover a broad range of possible τ-s relations, the bond laws are formulated as a set of i supporting points (s_i, τ_i), e. g. $(s^{ini}_{max}, \tau^{ini}_{max})$ or $(s^{ini}_{res}, \tau^{ini}_{res})$ in Fig. 4.5, with a suitable interpolation scheme. The interpolation between the supporting points is realised by means of the "Cubic Hermite Interpolating Polynomial Procedure" (PCHIP)[1] approach by [Fritsch & Carlson 1980]. A nice summary of the approach with an illustrative comparison to cubic splines, see [de Boor 1978], is given by [Moler 2004].

The PCHIP approach uses polynomials of cubic Hermite basis functions for each interval $s_i < s < s_{i+1}$. These polynomials show monotonicity and continuity in the first derivatives between consecutive intervals:

$$\begin{aligned}\tau(s) =& H_1(s)\tau_{i+1} + H_2(s)\tau_i + H_3(s)\tau'_{i+1} + H_4(s)\tau'_i \\ =& \frac{3h_k\tilde{s}^2 - 2\tilde{s}^3}{h_k^3}\tau_{i+1} + \frac{h_k^3 - 3h_k\tilde{s}^2 + 2\tilde{s}^3}{h_k^3}\tau_i + \frac{\tilde{s}^2(\tilde{s} - h_k)}{h_k^2}\tau'_{i+1} + \frac{\tilde{s}(\tilde{s} - h_k)^2}{h_k^2}\tau'_i \\ \text{with } h_k =& s_{i+1} - s_i,\ \tilde{s} = s - s_i \text{ and } \tau'_i = \frac{\mathrm{d}\tau(s_i)}{\mathrm{d}s}. \end{aligned} \tag{4.22}$$

The only unknowns in this equation are the slopes τ'_i at the supporting points, see Fig. 4.6. For the determination of these slopes, the slope of the straight line between the supporting points (s_i, τ_i) and (s_{i+1}, τ_{i+1}) is calculated with

$$\delta_k = \frac{\tau_{i+1} - \tau_i}{s_{i+1} - s_i}. \tag{4.23}$$

The idea of PCHIP is then to determine the slopes τ'_i in such a way that the values of the interpolating functions do locally not overshoot the values of the supporting points. Therefor, the approach takes advantage of the fact that if the values of the linear slopes δ_k and δ_{k+1}, left and right to the supporting point, have opposite signs or at least one of them is zero, the value s_i is a discrete local extremum. Thus, τ'_i is set equal to zero in this case.

[1] The hint by Dipl.-Ing. Dipl.-Inf. Kai Schicktanz to use this approach is appreciated.

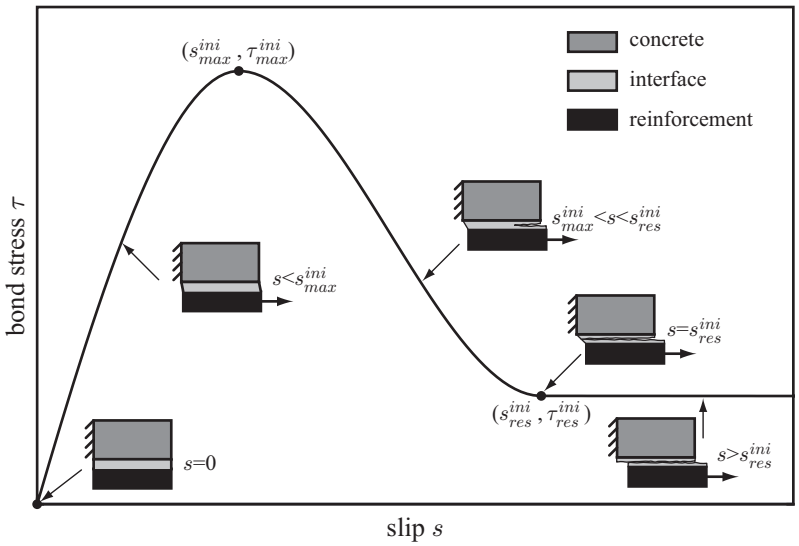

Figure 4.5.: Bond stress-slip relation

In the case that δ_k and δ_{k+1} have the same sign, the slope at s_i is calculated as the weighted harmonic mean between the linear slopes to the left and right according to

$$\begin{aligned} \frac{w_1 + w_2}{\tau_i'} =& \frac{w_1}{\delta_k} + \frac{w_2}{\delta_{k+1}} \text{ with } w_1 = 2h_{k+1} + h_k \text{ and } w_2 = h_{k+1} + 2h_k \\ \tau_i' =& \frac{w_1 + w_2}{\frac{w_1}{\delta_k} + \frac{w_2}{\delta_{k+1}}} \end{aligned} \tag{4.24}$$

where the weights w_1 and w_2 are determined by the interval lengths. These definitions are valid for interior points. At the first and the last supporting point, the slopes τ_i' have to be determined differently because only on one side δ_k values are available. Therefor, an estimation of the slope τ_1' at the first supporting point incorporating the information of the two first intervals is made:

$$\tau_1' = \frac{(2h_1 + h_2)\delta_1 - h_1\delta_2}{h_1 + h_2}. \tag{4.25}$$

If the values of τ_1' and δ_1 have opposite signs, τ_1' is set to zero. If the signs of δ_1 and δ_2 are different and if $|\tau_1'| > |3\delta_1|$ then τ_1' is set equal to $3\delta_1$. This condition is chosen somewhat arbitrarily but gives according to [Fritsch & Carlson 1980] "the most 'pleasing' results". In all other cases, τ_1' remains as estimated with Eq. (4.25). The slope at the last supporting point is estimated in the same way incorporating the two last intervals.

With a substitution of the coefficients of the quadratic and the cubic terms, Eq. (4.22) can be simplified as follows:

$$\begin{aligned} \tau(s) =& \tau_i + \tilde{s}\tau_i' + \tilde{s}^2 c_k + \tilde{s}^3 b_k \\ \text{with } b_k =& \frac{3\delta_k - 2\tau_i' - \tau_{i+1}'}{h_k} \text{ and } c_k = \frac{\tau_i' - 2\delta_k + \tau_{i+1}'}{h_k^2}. \end{aligned} \tag{4.26}$$

Thus, the coefficients h_k and δ_k as well as c_k and b_k have to be determined and stored once. Afterwards, τ can be calculated as a function of s, which is contained in $\tilde{s}$. A great advantage

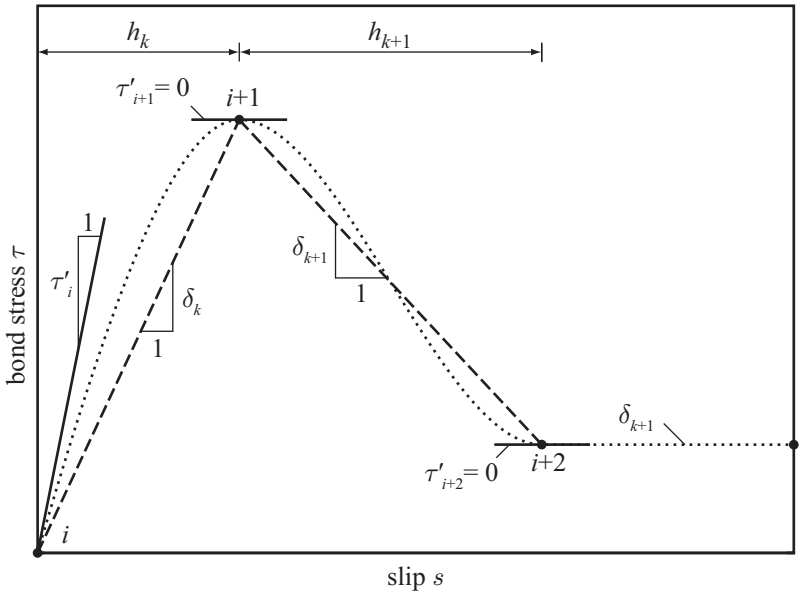

Figure 4.6.: Coefficients of bond law formulation based on PCHIP approach

of this approach compared to, e. g., a piecewise linear interpolation as shown in Fig. 3.7 is the smooth transition of the bond law at the supporting points, which at least reduces numerical problems during computations at these points.

Hitherto, only the interpolation approach between the supporting points of an arbitrary bond law has been specified while the choice of the positions of the supporting points will be given in the following based on the description in [Hartig et al. 2008]. The bond law for parts of the reinforcement, which interact directly with the concrete in the fill-in zone, as well as the supporting points for the interpolation are shown in Fig. 4.5. The first supporting point is the origin of the reference system, which is followed by a maximum value $(s^{ini}_{max}, \tau^{ini}_{max})$ according to the assumption of an initially adhesive bond. The slip s up to the value s^{ini}_{max}, where the interface is assumed intact, can be interpreted as a shear deformation of the interfacial transition zone between the concrete and the reinforcement, see Section 2.3.1. A similar explanation is also given in [Konrad 2008]. The bond stress increases with increasing slip values in this so-called state 0 according to the state diagram in the inset of Fig. 4.7. The black dot in the state diagram symbolises the initial state. The directions of the arrows show, which states of the bond law are accessible based on the current state. The state numbers are also incorporated in the τ-s diagram in Fig. 4.7.

After the maximum point, bond degradation combined with a transition to frictional load transfer is assumed, which is finished reaching the residual point $(s^{ini}_{res}, \tau^{ini}_{res})$. After this point, purely frictional load transfer is assumed, which is implemented in the bond law with a constant value τ^{ini}_{res}. It can be assumed that the bond degradation is irreversible. Therefor, in state 1 of the τ-s relation, see Fig. 4.7, an unloading path (state 3) differing from the loading path (state 1) is implemented.

It works as follows: if the absolute slip value reduces in the states 1 or 2, e. g. due to some unloading caused by local stress redistribution, the absolute value of the bond stress τ^{act}_{max} corresponding to the maximum reached slip s^{act}_{max} value is set as new maximum value. The unloading path is implemented as a linear function with a slope, which is chosen as the

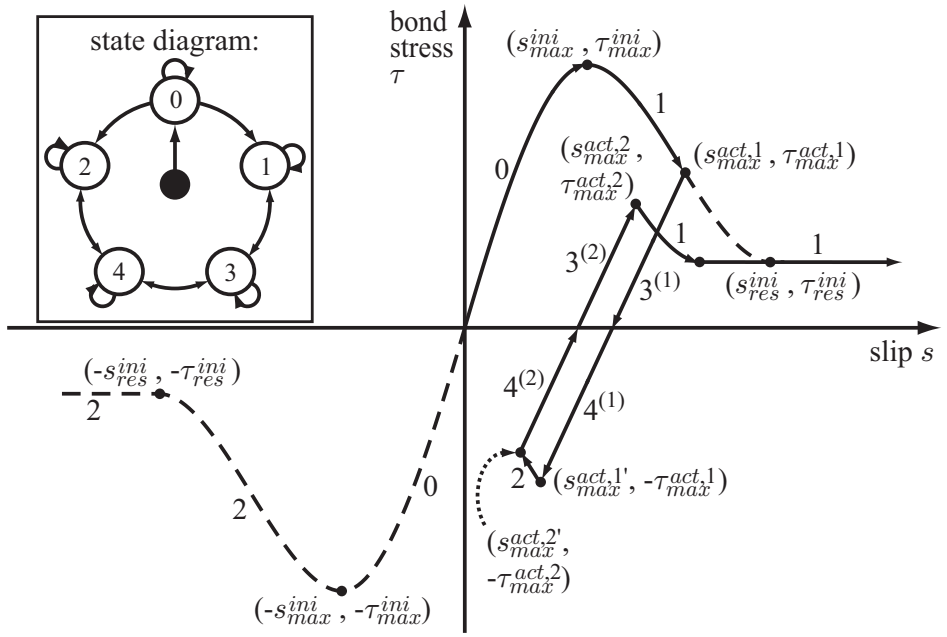

Figure 4.7.: Degradation algorithm in bond stress-slip relation exemplified with an arbitrarily chosen loading path

slope between the points (0,0) and $(s^{ini}_{max}, \tau^{ini}_{max})$. The bond stress changes according to the unloading path and the respective slip value as long as $-\tau^{act}_{max} \leq \tau(s) \leq \tau^{act}_{max}$ in the states 3 and 4, see Fig. 4.7. If $\tau(s)$ exceeds the value $-\tau^{act}_{max}$ in state 4, the bond law skips into state 2 with a course corresponding to state 1 but with reversed signs. Otherwise, if $\tau(s)$ exceeds τ^{act}_{max} in state 3, it skips into state 1 again. It shall be noted that the shape of the initial interpolation is maintained but the function is not reachable anymore for bond stress values $\tau(s) > \tau^{act}_{max}$ and $\tau(s) < -\tau^{act}_{max}$, respectively. The reduction of the maximum bond stress proceeds until one of the horizontal branches is reached. This approach corresponds to the concept of plasticity with a softening limit strength and progressing degradation of the material. As discussed in Section 3.4.1, other approaches for the slope of the unloading relations are possible, e. g. based on the concept of damage mechanics. However, as the force transfer is assumed to be dominated in the softening range by friction, the assumption of plasticity seems reasonable. Most realistic would be supposedly a combination of damage and plasticity while on the other hand corresponding experimental results for calibration are missing.

In order to model also fibre pull-out appropriately, the reduction of the contact area S_b when the fibres leave the surrounding concrete has to be taken into account. To incorporate this effect, the calculation of the force T transferable by a bond element i has to be modified. It can be calculated from the transferred bond stress $\tau(s)$ and the contact area S_b, which is assumed to be the lateral surface area of a cylinder, with

$$T(s,u) = \tau(s) S_b(u) \quad \text{where} \quad S_b(u) = L_b(u) C_b. \tag{4.27}$$

In Eq. (4.27), L_b is the length and C_b the circumference of S_b. Both τ and S_b depend on the displacement state u. As it can be seen from Eq. (4.27), the dependency of S_b on u results from the dependency of L_b on u while C_b is assumed constant. To give an idea how this is implemented in the model, the procedure of the determination of $L_b(u)$ is described in

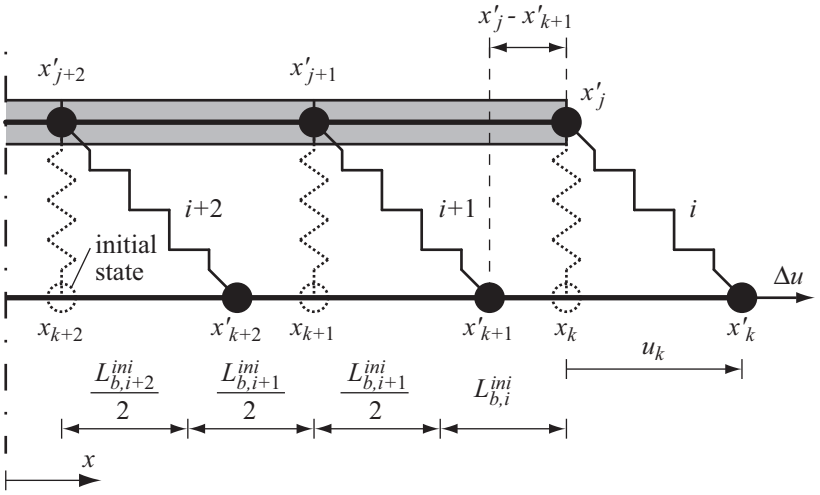

Figure 4.8.: Determination of element bond length

the following based on the example of a single fibre pull-out with a schematic discretisation corresponding to Fig. 4.8. It is assumed that the pull-out front has already reached bond element $i+1$, which has two nodes denoted with $j+1$ and $k+1$. The concrete end node j is used to determine the remaining bonded length of all bond elements. The coordinates of the nodes in the deformed state can be calculated with $x' = x + u$ where x is the coordinate in the undeformed state and u is the displacement of the node under consideration. In the initial state, bond element $i+1$ has a bonded length of $L^{ini}_{b,i+1}$ with half of this length assumed each to the right and the left of the element, compare Fig. 4.8. The variation of L_b due to a varying bar element length is neglected as it less than 2 % according to the failure strain of the used reinforcement. Based on these assumptions, the bonded length can be calculated for bond element $i+1$ with

$$L_{b,i+1}(u) = \begin{cases} L^{ini}_{b,i+1} & x'_j - x'_{k+1} \geq \frac{L^{ini}_{b,i+1}}{2} \\ \frac{L^{ini}_{b,i+1}}{2} + (x'_j - x'_{k+1}) & \text{for} \quad -\frac{L^{ini}_{b,i+1}}{2} < x'_j - x'_{k+1} < \frac{L^{ini}_{b,i+1}}{2} \\ 0 & x'_j - x'_{k+1} \leq -\frac{L^{ini}_{b,i+1}}{2} \end{cases} \tag{4.28}$$

This procedure applies similarly for the other bond elements. The situation becomes more complex when additional concrete cracks can occur. This is the case for instance in simulation of the double-sided yarn pull-out test, see Section 5.2, where the concrete cracks once at a prescribed position in the centre of the specimen. In this case, it turns out to be useful to define intact sections of concrete bar elements limited either by the end nodes of the concrete chain or the nodes of the cracked bar element and to apply the described procedure analogously. If the reinforcement is subdivided into several layers as it is case for yarn pull-out tests, this approach is used for the reinforcement elements in all layers although some frictional load transfer between the inner filaments is conceivable in reality.

4.3. Stochastic modelling of material properties

4.3.1. Stochastic representation of material properties

The material behaviour described in the previous section was assumed deterministic, i. e. no spatial fluctuations of the material parameters in a specimen exist. This is obviously not very realistic and calls for a better approximation, e. g. by means of statistical methods. At first, the concept of random variables and their mathematical description are treated to support the comprehension of the random field approach for introducing spatial fluctuations in the material properties described subsequently.

By means of stochastics, see e. g. [Bronstein et al. 2008], a material parameter (and also other variables) can be described with a random variable Y, which can be discrete or continuous. The discrete case is often associated with the evaluation of experimental test results, while the continuous approach is usually applied in modelling approaches.

Y describes all possible values of a material parameter. A realisation of Y is denoted with y and is assumed here to be a real-valued number. The distribution of Y is described with the cumulative distribution function (CDF) $F(y)$, which specifies the probability P that Y takes a value between $-\infty$ and y:

$$F(y) = P(Y \leq y); y \in \mathbb{R}; -\infty \leq y \leq \infty. \tag{4.29}$$

$F(y)$ is a non-decreasing function of y and takes the values 0 for $F(-\infty)$ and 1 for $F(\infty)$. In the discrete case, $F(y)$ is a step function defined as

$$F(y) = \sum_{y_i \leq y} p_i \tag{4.30}$$

with $p_i = P(Y = y_i)$ $(i = 1, 2, ..., N_{samples})$ and $N_{samples}$ being the number of samples. Examples for CDF's of discrete distributions are given e. g. in [Curbach et al. 2006] for experimentally determined distributions of filament tensile strengths. For continuous random variables, the CDF is defined as

$$F(y) = P(Y \leq y) = \int_{-\infty}^{y} f(t)\mathrm{d}t. \tag{4.31}$$

The integrand $f(t)$ in Eq. (4.31) is called probability density function (PDF). Thus, $F(y)$ can be interpreted as the area between $f(t)$ and the abscissa in the interval $-\infty \leq t \leq y$.

For the mechanical model, realisations of the random variable are needed. Therefor, the inverse function of the CDF has to be established, which is called quantile function or percent point function (PPF) and constitutes as:

$$F^{-1}(p) = \inf\{y : F(y) \geq p\};\ 0 < p < 1. \tag{4.32}$$

This means that $F^{-1}(p)$ is the minimum value of y for which the (input) probability p is smaller than $F(y)$. While for some kinds of functions $F(y)$ is explicitly invertible, e. g. the Weibull distribution, for other functions only a numerical approximation is possible.

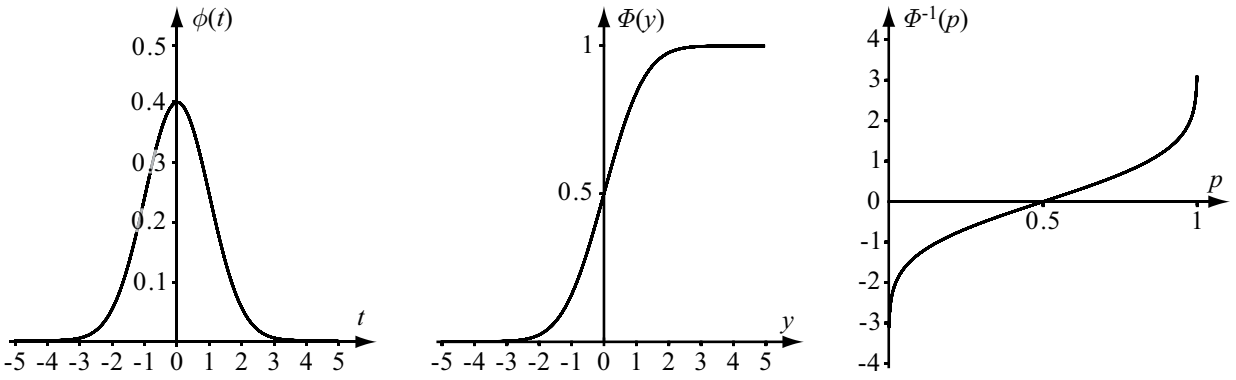

(a) Probability density function (b) Cumulative distribution function (c) Quantile function

Figure 4.9.: Standard Gaussian distribution function

An important example for a continuous distribution function, where also only a numerical approximation for $F^{-1}(p)$ is possible, is the standard Gaussian (normal) distribution where

$$\phi(t) = f(t) = \frac{1}{\sqrt{2\pi}} exp\left(-\frac{t^2}{2}\right),\ t \in \mathbb{R} \tag{4.33}$$

$$\Phi(y) = F(y) = \frac{1}{\sqrt{2\pi}} \int_{-\infty}^{y} f(t)\mathrm{d}t = \frac{1}{2}\left(1 + \mathrm{erf}\left(\frac{y}{\sqrt{2}}\right)\right),\ y \in \mathbb{R} \tag{4.34}$$

$$\Phi^{-1}(p) = F^{-1}(p) = \sqrt{2}\,\mathrm{erf}^{-1}\left(2p-1\right),\ p \in (0,1) \tag{4.35}$$

are the PDF, CDF and PPF, respectively, which are also shown in Fig. 4.9. erf(...) is the error function according to Eq. (A.3) and erf^{-1}(...) its inverse.

Results of experimental test series, i. e. discrete distributions, are often given by an expected value $E(Y)$ and a standard deviation $D(Y)$. For discrete distribution functions, $E(Y)$, which is also called first central moment of the distribution, is simply the arithmetic mean of i realisations y of a random variable Y given by

$$E(Y) = \frac{1}{N_{samples}} \sum_i y_i \tag{4.36}$$

For a series of $N_{samples}$ experimental tests, a y_i is the result of a single test.

For a continuous distribution function, $E(Y)$ can be determined with

$$E(Y) = \int_{-\infty}^{+\infty} y f(y)\mathrm{d}y. \tag{4.37}$$

The standard deviation $D(Y)$, which is a measure of variability around $E(Y)$, can be expressed in terms of the variance $D^2(Y)$, which is also referred to as second central moment of the distribution. In the discrete case, $D(Y)$ is given with

$$D(Y) = \sqrt{D^2(Y)} = \sqrt{\frac{1}{N_{samples}-1} \sum_i \left(y_i - E(Y)\right)^2}. \tag{4.38}$$

In case of a continuous distribution function, $D(Y)$ can be calculated with

$$D(Y) = \sqrt{D^2(Y)} = \sqrt{\int_{-\infty}^{+\infty} (y - E(Y))^2 \, f(y) \mathrm{d}y}. \tag{4.39}$$

As both $E(Y)$ and $D(Y)$ are integrals of the original PDF, a lot of information is hidden if experimental data is expressed only by these two values and the underlying distribution function is not given. It is for instance incomprehensible how the distribution function is shaped, e. g. if it is symmetric or if the co-domain is limited. Thus, for an appropriate modelling of fluctuating material properties also the corresponding distribution functions are necessary. For a number of material properties, theories for the distribution functions exist. For instance, the tensile strength is often modelled with a Weibull distribution, which is based on the "Weakest link theory", see [Weibull 1939].

4.3.2. Random fields

4.3.2.1. Motivation of application and general formulation of random fields

The microscopic structures of materials show more or less spatial random fluctuations. This leads also to spatial random fluctuations in the material properties. For instance Young's modulus and tensile strength of concrete depend on the respective properties of both the aggregates and the hardened cement paste, see Section 2.2.1, which are randomly distributed. In mechanical models on the mesoscopic and macroscopic scales, the material properties are often considered in a pointwise manner at spatial positions determined by the model. Thus, these points describe the behaviour of the material in their vicinity. As a consequence, the material properties of neighbouring points are mutually influenced as they share at least partly the same neighbourhood. This influencing is called correlation and smooths the spatial distribution of the values of the material parameters in mesoscopic and macroscopic models. A further homogenisation results in the current model from the condensation of the spatially distributed material properties to a one-dimensional description. Thus, a bar element has the characteristic properties of the original three-dimensional region, which it represents. Also between different material properties correlation might exist, which is called cross-correlation and can be interpreted as as measure of proportionality between different properties. A method to model smooth fluctuations of the material properties are random fields.

For the general formulation of random fields, the representation by [Sudret & Der Kiureghian 2000] is used in the following. It is assumed that a structure is discretised with a finite number of points having a number of random properties, e. g. Young's modulus and tensile strength. At each of those points i, a realisation of the random field $H(\mathbf{x}, \theta)$ exists where $\mathbf{x} \in \Omega$ is the coordinate vector in the open set Ω of the n-dimensional space $\mathbb{R}^n$ describing the geometry of the system. While $\mathbf{x}$ is deterministic, θ is a random coefficient. Every discretisation point i has a random variable (/property), which can be interpreted as point value or local average of the original field. These random variables $\chi^i(\theta)$ can be

expressed as weighted integrals of $H(\mathbf{x}, \theta)$ over the domain Ω:

$$\chi^i(\theta) = \int_\Omega H(\mathbf{x}, \theta) w(\mathbf{x}) \mathrm{d}\Omega \tag{4.40}$$

where $w(\mathbf{x})$ are weight functions corresponding to a specific discretisation method, see also [Sudret & Der Kiureghian 2000] for an overview. Hence, Eq. (4.40) represents a reduction of the continuous realisation of the random field $H(\mathbf{x}, \theta)$ to point values where the weight functions $w(\mathbf{x})$ control the influence of the vicinity on the point under consideration.

For a simulation with the presented model for TRC, rather a realisation of $H(.)$, i. e. a certain spatial distribution of a material property in the model, is of interest than the random variables $\chi^i(\theta)$, which shall be input parameters to establish the realisation. Thus, a formulation for determining $H(.)$ as a function of θ is needed. An approximation $\hat{H}(.)$ of the original random field $H(.)$ can be established by means of a finite summation

$$\hat{H}(\mathbf{x}, \theta) = \sum_{i=1}^{N_{var}} \chi^i(\theta) \varphi^i(\mathbf{x}). \tag{4.41}$$

over all N_{var} discretisation points i. In Eq. (4.41), $\chi^i(\theta)$ are still random variables but not necessarily with the same properties as in Eq. (4.40) and $\varphi^i(\mathbf{x})$ are deterministic basis functions. There exists a number of approaches for $\varphi^i(\mathbf{x})$ where one candidate based on the so-called Karhunen-Loève expansion is described in some detail in the next section.

4.3.2.2. Formulation and simulation of univariate non-Gaussian random fields

For every two random variables Y and Y' of a single random field representing one property at two discretisation points, the covariance $\sigma_{YY'}$ defined as

$$\sigma_{YY'} = E[(Y - E(Y))(Y' - E(Y'))] \tag{4.42}$$

can be determined. It is a measure for the interrelation of the random variables. Because variables of one random field are treated, it can be also called autocovariance. In order to make the interrelation comparable, it has to be normalised leading to the correlation coefficient $\rho_{YY'}$ defined as

$$\rho_{YY'} = \frac{\sigma_{YY'}}{D(Y) D(Y')}. \tag{4.43}$$

For the same reasons as discussed before, this variable is called autocorrelation coefficient in the context of random fields. In the case of two standard Gaussian variables Y and Y', $D(Y) = D(Y') = 1$ and, consequently, $\rho_{YY'} = \sigma_{YY'}$. For every two discretisation points of the random field, the autocorrelation can be determined. For the determination of the correlation coefficients usually an approach has to be established as most often information based on experimental data is missing. In the following, it is assumed that the expected value and the standard deviation of the underlying distribution function are constant in one random field as the characteristics of a single property are described. Nevertheless, the correlation coefficients might depend on distance and direction. Reasons for the directional

dependence might be for instance an anisotropy in the material properties. A convenient approach for the correlation coefficient is given according to [Vořechovský 2008] by

$$\rho_{YY'}(\mathbf{x},\mathbf{x}') = \prod_{j=1}^{dim} \exp\left(-\left(\frac{|x_j - x_j'|}{L_{corr,j}}\right)^2\right) \tag{4.44}$$

with the number of geometrical dimensions dim, the spatial coordinates x_j and x_j' of the random variables Y and Y', and the correlation lengths $L_{corr,j}$, which might depend on direction. In the one-dimensional model according to Section 4.1, dim=1 and $L_{corr,j} = L_{corr}$, which enables a simplification of Eq. (4.44). Also the coordinates x_j and x_j', which correspond in the mechanical model according to Section 4.1 to the coordinates of the integration points of the used finite elements, see Section 4.4.4, can be denoted more simple with x and x'. With large values for L_{corr}, the correlation between distant points increases while it decreases for smaller values. The limit cases are given with $L_{corr} \to 0$ corresponding to the purely stochastic distribution and $L_{corr} \to \infty$ corresponding to the deterministic case. With the autocorrelation coefficients according to Eq. (4.44) and the application of Eq. (4.43), the autocovariance can be determined as

$$\sigma_{YY'}(x,x') = D(Y)D(Y')\exp\left(-\left(\frac{|x - x'|}{L_{corr}}\right)^2\right) \tag{4.45}$$

considering the one-dimensionality of the model. The values obtained from Eq. (4.45) can be assembled in an autocovariance matrix $\mathbf{C}_{auto}$, which has a size of $N_{var} \times N_{var}$. Obviously, the main diagonal of $\mathbf{C}_{auto}$ is allocated with $D(Y)D(Y') = D^2(Y)$, because the underlying distribution function of the field is assumed to be independent of the location, while all other values range between zero and $D^2(Y)$, which makes $\mathbf{C}_{auto}$ symmetric, bounded and positive-definite.

There exist a number of approaches for the approximation of random fields as e. g. the Karhunen-Loève representation, the spectral representation or the sampling representation, see e. g. [Spanos & Zeldin 1998] and [Grigoriu 2006]. In the following, the Karhunen-Loève expansion is applied to characterise the random fields, see [Spanos & Zeldin 1998], [Grigoriu 2006] and [Vořechovský 2008]. The Karhunen-Loève expansion incorporates the solution of the Fredholm integral of the second kind[2]

$$\int_\Omega \sigma_{YY'}(\mathbf{x},\mathbf{x}')\boldsymbol{\psi}^i(\mathbf{x}')\mathrm{d}\Omega_{dim} = \lambda^i\boldsymbol{\psi}^i(\mathbf{x}), \tag{4.46}$$

which defines an eigenvalue problem, where $\boldsymbol{\psi}^i(\mathbf{x})$ are eigenfunctions and λ^i are eigenvalues. The autocovariance function $\sigma_{YY'}(\mathbf{x},\mathbf{x}')$ is also referred to as kernel in this context. In the one-dimensional case, the integration over the domain Ω_{dim} reduces to the integration over the coordinate x. The integral term in Eq. (4.46) can be represented approximately by means of a finite summation, see e. g. [Sudret & Der Kiureghian 2000]. The supporting points for the summation can be chosen according to the integrations points of the bar elements in the model. After such a discretisation, the autocovariance function $\sigma_{YY'}(\mathbf{x},\mathbf{x}')$ can be

[2] A Fredholm integral is characterised by constant integration limits. In an integral equation of the "second kind" the searched function, in this case $\boldsymbol{\psi}$, appears within the integral but also outside. (In an integral of the "first kind", it would only appear within the integral, see also [Bronstein et al. 2008].)

represented by the autocovariance matrix $\mathbf{C}_{auto}$ introduced associated with Eq. (4.45). The eigenfunctions $\boldsymbol{\psi}^i(\mathbf{x})$ can now be interpreted as eigenvectors and determined as well as the eigenvalues λ^i by means of the solution of the standard eigenvalue problem

$$\mathbf{C}_{auto}\boldsymbol{\psi}^i = \lambda^i\boldsymbol{\psi}^i. \tag{4.47}$$

There exist two classes of solution methods for eigenvalue problems, the transformation methods and the iteration methods, where the *Jacobi Transformation* and the *Von Mises Power Iteration* are examples, see e. g. [Press et al. 2007] and [Bronstein et al. 2008]. In practice, the eigenvalue decomposition of large matrices is complicated and incorporates elaborate numerical methods, see e. g. [Press et al. 2007] for an overview. Hence, a subroutine of the linear algebra package LAPACK, see [Anderson et al. 1999], is used for the solution. Eq. (4.47) yields mutually orthogonal (or in other words independent) eigenvectors $\boldsymbol{\psi}^i$, see e. g. [Bronstein et al. 2008].

Based on the eigenvalue decomposition, the expansion of $H(\mathbf{x},\theta)$ can be formulated corresponding to Eq. (4.41) as

$$H(\mathbf{x},\theta) = \sum_{i=1}^{N_{var}} \sqrt{\lambda^i}\xi^i(\theta)\boldsymbol{\psi}^i(\mathbf{x}) \tag{4.48}$$

where $\xi^i(\theta)$ are uncorrelated, standard Gaussian random coefficients. An advantageous property of the Karhunen-Loève expansion is that the only accumulation value of the eigenvalues is zero, see e. g. [Sudret & Der Kiureghian 2000]. Thus, to achieve a given accuracy of the field approximation the descending ordered series of eigenvalues (and respective eigenvectors) can be truncated after the N_{red}-th term, which gives the Karhunen-Loève approximated field

$$\hat{H}(\mathbf{x},\theta) = \sum_{i=1}^{N_{red}} \sqrt{\lambda^i}\xi^i(\theta)\boldsymbol{\psi}^i(\mathbf{x}). \tag{4.49}$$

A possible measure of accuracy is given by [Vořechovský 2008] with

$$c_{N_{red}} = \frac{\sum_{i=1}^{N_{red}} \lambda^i}{\sum_{i=1}^{N_{var}} \lambda^i}. \tag{4.50}$$

Qualitatively, the number N_{red} of random variables necessary to describe the random field to a given accuracy is in inverse proportion to the correlation length L_{corr}. This means that $N_{red} \to N_{var}$ if $L_{corr} \to 0$, and $N_{red} \to 1$ if $L_{corr} \to \infty$.

In Fig. 4.10, visualisations of the eigenfunctions and eigenvalues of a one-dimensional random field ($dim = 1$) of a length L for cases with a short ($L_{corr} = 0.1L$) and a long ($L_{corr} = L$) correlation length L_{corr} are shown. The random field based on the standard Gaussian distribution is discretised with 25 supporting points. It can be seen that for the short L_{corr} considerably more eigenvalues λ^i have values significantly larger than zero, which coincides with the previous discussion of the eigenvalue truncation. Regarding the eigenfunctions $\boldsymbol{\psi}^i$ of the short L_{corr} as shown in Fig. 4.10(a), it is observable that the eigenfunctions with an uneven index have always a symmetric shape related to the spatial centre of the random field (horizontal axis corresponding to discretisation point 13) while the eigenfunctions $\boldsymbol{\psi}^i$ with

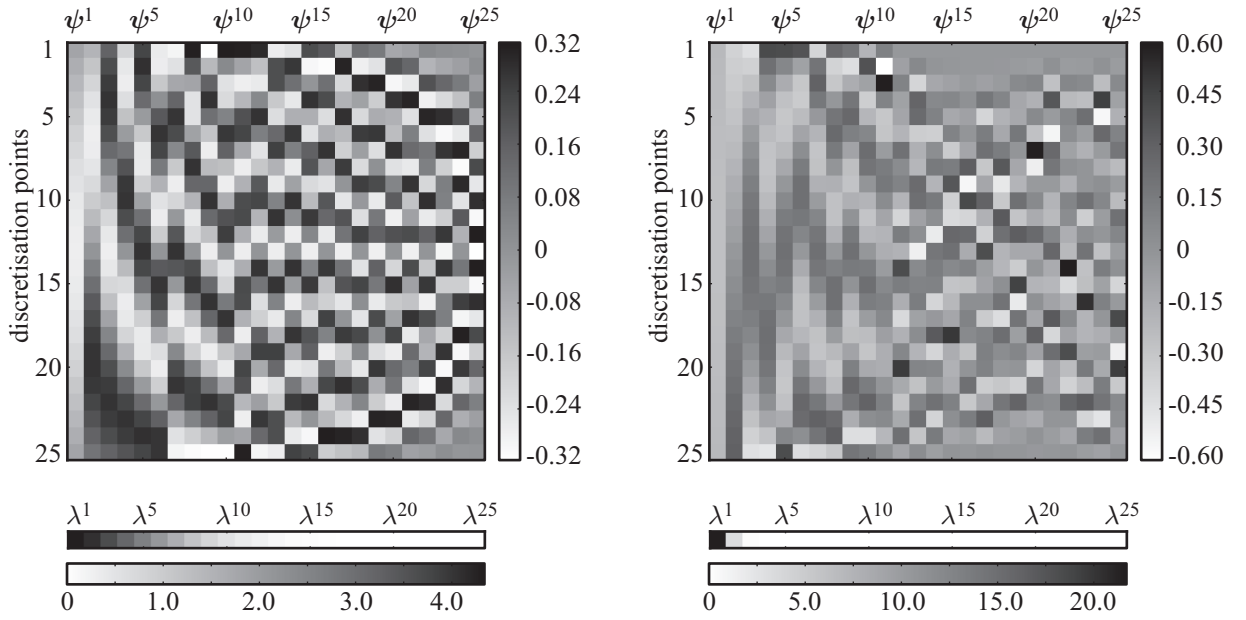

(a) Short correlation length

(b) Long correlation length

Figure 4.10.: Visualisation of the eigenvectors $\boldsymbol{\psi}^i$ and eigenvalues λ^i for a short and a long correlation length

an even index are always antisymmetrically shaped. With the long L_{corr}, this characteristic exists only for the $\boldsymbol{\psi}^i$'s with low indices, see Fig. 4.10(b). For larger indices ($i > 10$), no regular structure is observable. The reason is that the numerical procedure for the decomposition of $\mathbf{C}_{auto}$ given with Eq. (4.47) runs into large round-off errors due to a limited floating-point precision. However, this is not critical because also the corresponding eigenvalues are almost zero and the impact on the sum given in Eq. (4.48) is negligible. As a consequence, often the series of eigenvalues is truncated, as mentioned previously, leading to Eq. (4.49).

The random field representation given with Eq. (4.48) can only be applied in the case of Gaussian random variables. In this case, the values $\xi^i(\theta)$ are independent Gaussian variables, while they are dependent for non-Gaussian variables, see [Grigoriu 1998], where the joint distribution is difficult to obtain. When modelling material properties, it is, however, often not reasonable to assume Gaussian distributions. For instance Young's modulus and tensile strength are always positive-valued, which can not be guaranteed with a Gaussian distribution. In [Grigoriu 1998], it is additionally pointed out that the dependence between the eigenvalues has to be preserved, because otherwise the decomposition loses the original (non-Gaussian) distribution characteristic and becomes Gaussian for an indefinitely increased number of eigenvectors.

The common way to solve this problem is to translate the original non-Gaussian random field into a Gaussian random field by means of a so-called Nataf transformation, see for instance [Grigoriu 1998], [Liu & Der Kiureghian 1986] and [Lebrun & Dutfoy 2009]. Therefor, the coefficients $\rho_{YY',NG}$ of the autocovariance matrix $\mathbf{C}_{auto}$ corresponding to Eq. (4.44), which are now defined in a non-Gaussian domain, have to be transformed to coefficients $\rho_{YY',G}$ in the Gaussian domain via

$$\rho_{YY',NG} = \int_{-\infty}^{\infty}\int_{-\infty}^{\infty}\left(\frac{F^{-1}(\Phi(y)) - E(Y)}{D(Y)}\right)\left(\frac{F^{-1}(\Phi(y')) - E(Y')}{D(Y')}\right)\cdot \phi_2(y, y', \rho_{YY',G})\mathrm{d}y\mathrm{d}y'. \tag{4.51}$$

In this equation, $E(.)$ and $D(.)$ are the expected values and the standard deviations of the non-Gaussian variables according to Eqs. (4.37) and (4.39), respectively. $E(.)$ and $D(.)$ are identical for Y and Y' in this case because the underlying distribution function is assumed spatially constant for the material property described by the random field. Furthermore, $F^{-1}(.)$ and $\Phi(.)$ are the PPF of the non-Gaussian variable, according to Eq. (4.32), and the CDF of the standard Gaussian distribution, according to Eq. (4.34), respectively. The PDF of the bivariate standard Gaussian distribution is defined as

$$\phi_2(y, y', \rho_{YY',G}) = \frac{1}{2\pi\sqrt{1-\rho_{YY',G}^2}}\exp\left(-\frac{y^2 - 2\rho_{YY',G}\, yy' + y'^2}{2(1-\rho_{YY',G}^2)}\right). \tag{4.52}$$

The solution of Eq. (4.51) for $\rho_{YY',G}$ might be difficult for several reasons. Firstly, a direct inversion of this implicit formulation is only possible in a few special cases, see [Liu & Der Kiureghian 1986] and [Vio et al. 2001] for examples. Thus, a numerical solution, which is quite expensive, because of the solution of the double integral, is necessary in most cases. Furthermore, Eq. (4.51) has to be solved more than once to achieve iteratively the value $\rho_{YY',G}$ corresponding to the given $\rho_{YY',NG}$.

Depending on the type of the non-Gaussian distribution, $\rho_{YY',NG}$ can take values in the interval $\rho_{YY',NG} \in [\rho^*_{YY',G}, 1]$ with $-1 \leq \rho^*_{YY',G} \leq 0$, see [Vio et al. 2001]. The case $\rho^*_{YY',G} = -1$ can only be obtained in case of symmetric distribution functions. For asymmetric distribution functions, the Nataf transformation is only possible for values $\rho_{YY',NG}$ between $\rho^*_{YY',G}$ and 1 depending on the properties of the distribution function. Furthermore, the Nataf transformation has the following properties, see [Liu & Der Kiureghian 1986]:

- $\rho_{YY',NG}$ is a strictly increasing function of $\rho_{YY',G}$
- $\rho_{YY',NG}(\rho_{YY',G} = 0) = 0$
- $|\rho_{YY',NG}| \leq |\rho_{YY',G}|$.

Since with the autocorrelation structure given by Eq. (4.44) the interval of $\rho_{YY',NG}$ is $\rho_{YY',NG} \in [0, 1]$, the Nataf transformation can be performed over the entire range of autocorrelation coefficients. In practice, for the transformation of the autocovariance matrix $\mathbf{C}_{auto}$, Eq. (4.51) is evaluated for a set of supporting points ρ_G, which are used to fit the parameters of a suitable approximation function, e. g. a polynomial.

$\mathbf{C}_{auto}$ transformed into Gaussian domain can now be decomposed according to Eq. (4.47) and the truncation of the eigenvalues can be performed. Afterwards, the random vector according to the number of random variables can be sampled and the random field can be expanded with Eq. (4.48) or (4.49). Since the expansion is now in the Gaussian domain, it has to be transformed back in the (original) non-Gaussian domain with

$$\widetilde{H}(\mathbf{x}, \theta) = F^{-1}[\Phi(H(\mathbf{x}, \theta))], \tag{4.53}$$

which is called translation process in [Grigoriu 1998]. With the standard Gaussian CDF $\Phi(H(\mathbf{x},\theta))$ according to Eq. (4.34), the probability of the realisation $H(\mathbf{x},\theta)$ in the Gaussian domain is determined, which is then translated with the non-Gaussian PPF $F^{-1}(.)$ according to Eq. (4.32) to the realisation of $\widetilde{H}(\mathbf{x},\theta)$ into the non-Gaussian domain.

For the mechanical model and its numerical implementation, $\mathbf{C}_{auto}$ is established with the coordinates of the integration points of the finite elements under consideration, e. g. the concrete bar element chain, and a distribution function for the considered material property. Based on $\mathbf{C}_{auto}$, a realisation of the the random field describing the spatial fluctuation of the material property is carried out as described in this section and the point values of the realisation are assigned to the integration points of the finite elements.

4.3.2.3. Formulation and simulation of cross-correlated non-Gaussian random fields

It can be assumed that the spatial variability of different material properties might correlate depending on the underlying physical process. The most basic approach is the assumption that a constant correlation factor exists between two material properties, see e. g. [Vořechovský 2008]. Following this approach, a square, symmetric, positive definite cross-correlation matrix $\mathbf{C}_{cross}$ of order N_f, which is the number of fields corresponding to the number of modelled material properties, can be established. This matrix has elements $C_{cross}^{mn} \in (-1;1)$ with $m,n \in (0;N_f)$, which determine the correlations between each two material parameters. Obviously the main diagonal, i. e. C_{cross}^{mn} for $m=n$, has only entries equal to 1 since these are correlations of a single field with itself.

Similar to the autocovariance matrix $\mathbf{C}_{auto}$, the cross-correlation matrix $\mathbf{C}_{cross}$ has to be transformed to the Gaussian domain if the distribution functions of the random fields are non-Gaussian. The Nataf transformation given in Eq. (4.51) is applied again for this purpose. In general, the values of $E(Y)$, $E(Y')$ and $D(Y)$, $D(Y')$, respectively, are different and also the quantile functions $F^{-1}(.)$ are not the same anymore. For the calculation of the values $\rho_{YY',G}$, an immediate iterative solution for each $\rho_{YY',G}$ is more efficient compared to establishing an approximation function as for the coefficients of $\mathbf{C}_{auto}$. The reason is that for every combination of the N_f random fields, $\rho_{YY',G}$ needs to be determined only once.

The matrix $\mathbf{C}_{cross}$, in the Gaussian domain, can then be decomposed similar to Eq. (4.47) into eigenvalues λ_{cross}^{i} and normalised eigenvectors $\boldsymbol{\psi}_{cross}^{i}$. It is also possible to take advantage of an eigenvalue truncation corresponding to the strategy related to Eq. (4.49). However, since N_f is usually small, the achievable reduction is often negligible.

In order to transfer the cross-correlation structure to the single fields of the material properties, a so-called block cross-correlation matrix $\mathbf{D}_{cross}$

$$\mathbf{D}_{cross} = \begin{bmatrix} \mathbf{I} & C_{cross}^{1,2}\mathbf{I} & \dots & C_{cross}^{1,N_f-1}\mathbf{I} & C_{cross}^{1,N_f}\mathbf{I} \\ & \mathbf{I} & \dots & C_{cross}^{2,N_f-1}\mathbf{I} & C_{cross}^{2,N_f}\mathbf{I} \\ & & \ddots & \vdots & \vdots \\ & \text{sym.} & & \mathbf{I} & C_{cross}^{N_f-1,N_f}\mathbf{I} \\ & & & & \mathbf{I} \end{bmatrix}, \tag{4.54}$$

which is a quadratic matrix of order $N_f \cdot N_{var}$, is established. The $C^{m,n}$ values are the elements of the cross-correlation matrix $\mathbf{C}_{cross}$ and $\mathbf{I}$ are identity matrices of order N_{var}. The matrix $\mathbf{D}_{cross}$ has only non-zero elements on the main diagonal and on the sub-diagonals of the $(N_{var} \times N_{var})$ partial blocks, which makes it suitable for sparse storage. According to [VOŘECHOVSKÝ 2008], the eigenvalue decomposition of $\mathbf{D}_{cross}$ is given as N_{var}-multiples of $\mathbf{C}_{cross}$. The matrix of the eigenvectors $\boldsymbol{\Psi}_D$ of $\mathbf{D}_{cross}$ is given with

$$\boldsymbol{\Psi}_D = \begin{bmatrix} \boldsymbol{\psi}^{1,1}_{cross}\mathbf{I} & \boldsymbol{\psi}^{1,2}_{cross}\mathbf{I} & \dots & \boldsymbol{\psi}^{1,N_f}_{cross}\mathbf{I} \\ \boldsymbol{\psi}^{2,1}_{cross}\mathbf{I} & \boldsymbol{\psi}^{2,2}_{cross}\mathbf{I} & \dots & \boldsymbol{\psi}^{2,N_f}_{cross}\mathbf{I} \\ \vdots & \vdots & \ddots & \vdots \\ \boldsymbol{\psi}^{N_f,1}_{cross}\mathbf{I} & \boldsymbol{\psi}^{N_f,2}_{cross}\mathbf{I} & \dots & \boldsymbol{\psi}^{N_f,N_f}_{cross}\mathbf{I} \end{bmatrix}. \tag{4.55}$$

The eigenvalues can be assembled in a diagonal matrix:

$$\boldsymbol{\Lambda}_D = \begin{bmatrix} \lambda^1_{cross}\mathbf{I} & 0 & \dots & 0 \\ 0 & \lambda^2_{cross}\mathbf{I} & \dots & 0 \\ \vdots & \vdots & \ddots & \vdots \\ 0 & 0 & \dots & \lambda^{N_f}_{cross}\mathbf{I} \end{bmatrix}. \tag{4.56}$$

The eigenvalue decomposition of the block cross correlation matrix $\mathbf{D}_{cross}$ is used to calculate a cross-correlated random vector $\boldsymbol{\chi}_D$:

$$\boldsymbol{\chi}_D = \boldsymbol{\Psi}_D \sqrt{\boldsymbol{\Lambda}_D}\boldsymbol{\xi} \tag{4.57}$$

where $\boldsymbol{\xi}$ is a vector of order $N_f \cdot N_{var}$ of Gaussian distributed independent random variables. The cross-correlated random vector $\boldsymbol{\chi}_D$ can then be split into subvectors $\boldsymbol{\chi}^j_D$ of order N_{var} where $j = 1, 2, ..., N_f$.

Since the auto-correlation matrix $\mathbf{C}_{auto}$ is identical for all N_f fields, the realisations of each random field $\hat{H}^j(\mathbf{x}, \theta)$ corresponding to a certain material property can be calculated using Eq. (4.48) or (4.49) with the eigenvectors $\boldsymbol{\psi}^i$, the eigenvalues λ^i of the (Nataf-corrected) auto-correlation matrix $\mathbf{C}_{auto}$ as well as the respective cross-correlated random subvector $\boldsymbol{\chi}^j_D$. Finally, the realisations of the random fields have to be transformed back into the (original) non-Gaussian domain via Eq. (4.53) leading to values $\widetilde{H}^j(\mathbf{x}, \theta)$.

The stochastically modelled material properties replace the deterministic values in the constitutive laws as given in Section 4.2. Therefore, for every finite element, as introduced in Section 4.4.4, having this property, a separate material definition has to be made as already described at the end of Section 4.3.2.2. This increases the demand of computer memory. Furthermore, a certain number of simulations with different realisations of the stochastic parameters has to be carried out to achieve results at a certain significance level. This increases computational costs considerably and necessitates efficient models for analysing. A last point worth to mention is that by means of stochastic variations of the Young's modulus also heterogeneity is introduced in otherwise homogeneous models. For the Finite Element Method, it is a convenient way to introduce heterogeneity without the need of building complex element meshes adapted to the material structure, e. g. caused by grains and hardened cement paste in the case of concrete.

4.4. Numerical model based on the Finite Element Method

In the previous sections, the geometrical properties of the model and the deterministic as well as the stochastic formulation of the material behaviour were described. However, the solution method was hitherto not specified. At the beginning of this chapter, it was evaluated that a numerical model based on the Finite Element Method (FEM) would be advantageous because of its generality. Hence, in the following the basics of the FEM will be described briefly incorporating also solution methods for the governing equations and the formulation of the used element types.

4.4.1. Basics of the Finite Element Method

There are various starting points and strategies to derive the equations governing the FEM. In the present work, a path is followed, which is called in [Zienkiewicz & Taylor 2000a] the "medium of particular physical applications". In the context of this work, it is naturally related to solid mechanics. This approach is also known as displacement formulation and the most frequently used one. The interested reader might also consult other popular standard works as e. g. [Bathe 1996] or [Wriggers 2001]. The concept of the FEM is to subdivide a body into a limited (or finite) number of sub-volumes, so-called elements, with a limited number of nodes on their boundaries (and for some element types also within the element), see Fig. 4.11. For every point p with coordinates $\mathbf{x}$ in the body, the displacement state $\mathbf{u}_p$ can be determined by the nodal displacements $\mathbf{u}_n$ and so-called shape functions $\mathbf{N}$ by means of

$$\mathbf{u}_p = \mathbf{N}\mathbf{u}_n. \tag{4.58}$$

The vector $\mathbf{u}_n$ contains the displacements $\mathbf{u}_{n,i}$, also referred to as degrees of freedom, of all nodes i and the matrix $\mathbf{N}$ the shape functions of all elements $\mathbf{N}_e$. It is also possible to introduce other quantities in the vectors $\mathbf{u}_n$ and $\mathbf{u}_p$ as e. g. rotations. However, the current derivations are limited to displacements. If the considered point p is within an element then $\mathbf{N}_{e,p} = \mathbf{N}_e$ otherwise $\mathbf{N}_{e,p} = 0$. Clearly, the shape functions have to be chosen such that they yield the nodal displacement if the coordinates of the considered node are used. In Section 4.4.4.1, typical shape functions of an one-dimensional bar element can be found as an example.

Having the displacement state of an element one can proceed with the strain state, which can be described with a relation

$$\boldsymbol{\varepsilon} = \mathbf{S}\mathbf{u}_p \tag{4.59}$$

where $\mathbf{S}$ is a suitable operator for linear kinematics. Inserting Eq. (4.58) into Eq. (4.59) leads to

$$\boldsymbol{\varepsilon} = \mathbf{S}\mathbf{N}\mathbf{u}_n = \mathbf{B}\mathbf{u}_n. \tag{4.60}$$

It turns out that the appropriate operations for $\mathbf{S}$ to obtain $\mathbf{B}$ from $\mathbf{N}$ are the directional derivatives, which yields

$$\mathbf{B} = \frac{\partial \mathbf{N}}{\partial \mathbf{x}}. \tag{4.61}$$

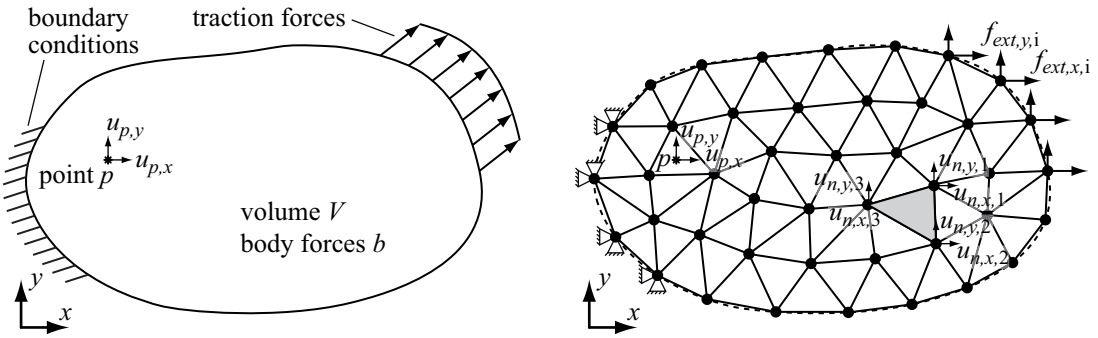

(a) Arbitrary body

(b) Discretisation with triangular finite elements

Figure 4.11.: Transfer of the continuous properties of an arbitrary body to a discretised representation for the FEM

By means of a so-called constitutive relation, the material properties are considered. It couples the strains $\boldsymbol{\varepsilon}$ with the stresses $\boldsymbol{\sigma}$ via

$$\boldsymbol{\sigma} = \mathbf{D}\left(\boldsymbol{\varepsilon} - \boldsymbol{\varepsilon}_0\right) + \boldsymbol{\sigma}_0. \tag{4.62}$$

$\mathbf{D}$ is the so-called elasticity matrix, which contains material properties, e. g. the Young's modulus. Furthermore, Eq. (4.62) contains initial strains $\boldsymbol{\varepsilon}_0$, which might result, e. g., from temperature changes or concrete shrinkage, and initial residual stresses $\boldsymbol{\sigma}_0$. Although initial strains and initial residual stresses are not used in the following, Eq. (4.62) shows how these values can be introduced in the model if required.

Loading on the body can be introduced by means of concentrated nodal forces $\mathbf{f}_{ext}$ and distributed body forces $\mathbf{b}$ on the elements, which might result, e. g., from gravity. To obtain a relation between the externally applied loads and the internal reactions, external and the internal works are evaluated. As the work is given as force multiplied by displacement, it turns out to be advantageous to introduce a virtual displacement $\delta\mathbf{u}_n$ at the nodes. With Eqs. (4.58) and (4.60) this leads to

$$\delta\mathbf{u_p} = \mathbf{N}\delta\mathbf{u}_n \tag{4.63}$$

and

$$\delta\boldsymbol{\varepsilon} = \mathbf{B}\delta\mathbf{u}_n. \tag{4.64}$$

Thus, the external virtual work δW_{ext} done by the external nodal forces $\mathbf{f}_{ext}$ can be calculated as

$$\delta W_{ext} = \delta\mathbf{u}_n^T\mathbf{f}_{ext}. \tag{4.65}$$

In a similar manner also the internal virtual work δW_{int}, which characterises the resistance of a body to a deformation, per volume V can be determined

$$\frac{\mathrm{d}\delta W_{int}}{\mathrm{d}V} = \delta\boldsymbol{\varepsilon}^T\boldsymbol{\sigma} - \delta\mathbf{u}_p^T\mathbf{b} = \delta\mathbf{u}_n^T\left(\mathbf{B}^T\boldsymbol{\sigma} - \mathbf{N}^T\mathbf{b}\right), \tag{4.66}$$

which leads after an integration over V to

$$\delta W_{int} = \int_V \delta \mathbf{u}_n^T \left(\mathbf{B}^T \boldsymbol{\sigma} - \mathbf{N}^T \mathbf{b} \right) \mathrm{d}V. \tag{4.67}$$

As the external virtual work is equal to the internal virtual work, it can be stated

$$\delta \mathbf{u}_n^T \mathbf{f}_{ext} = \delta \mathbf{u}_n^T \left(\int_V \mathbf{B}^T \boldsymbol{\sigma} \mathrm{d}V - \int_V \mathbf{N}^T \mathbf{b} \mathrm{d}V \right) \tag{4.68}$$

and further

$$\mathbf{f}_{ext} = \int_V \mathbf{B}^T \boldsymbol{\sigma} \mathrm{d}V - \int_V \mathbf{N}^T \mathbf{b} \mathrm{d}V. \tag{4.69}$$

Inserting the constitutive relation given by Eq. (4.62) yields

$$\mathbf{f}_{ext} = \int_V \mathbf{B}^T \mathbf{D} \mathbf{B} \mathbf{u}_n \mathrm{d}V - \int_V \mathbf{N}^T \mathbf{b} \mathrm{d}V - \int_V \mathbf{B}^T \mathbf{D} \boldsymbol{\varepsilon}_0 \mathrm{d}V + \int_V \mathbf{B}^T \boldsymbol{\sigma}_0 \mathrm{d}V. \tag{4.70}$$

This formulation is also known as "weak form" of equilibrium as the equality between external and internal forces has to be fulfilled only in an averaged sense over all points of the body but not at every point. The latter is the case in the so-called "strong form". It can be also seen that only nodal displacements $\mathbf{u}_n$ remain in Eq. (4.70) while the displacement state $\mathbf{u}_p$ of an arbitrary point is not determined explicitly. Thus for reasons of simplicity, index n for the nodal displacements is dropped and $\mathbf{u}_n$ is simply referred to as $\mathbf{u}$. If body forces and initial stresses and strains are not existent, Eq. (4.70) can be further simplified to the popular notation

$$\mathbf{f}_{ext} = \mathbf{K}\mathbf{u} \text{ with } \mathbf{K} = \int_V \mathbf{B}^T \mathbf{D} \mathbf{B} \mathrm{d}V \tag{4.71}$$

including the system stiffness matrix $\mathbf{K}$. This approach applies for both one element and a system of several elements. The system stiffness matrix $\mathbf{K}$ is usually constructed in a so-called assembly process. Therefor, the nodal displacements or degrees of freedom u_n of each node of the system, see Fig. 4.11, are numbered consecutively. In the assembly process, the square matrix $\mathbf{K}$, which has a size corresponding to the number of degrees of freedom, is filled at respective positions with entries of the element stiffness matrices of the particular elements. The element stiffness matrices of the applied elements are given in Section 4.4.4. In Section 4.4.5, properties of the assembled system stiffness matrix are presented.

It has to be noted that in general different coordinate systems are defined for the elements and the global structure. This is advantageous concerning the implementation in computer programmes as doing so, every element can be treated equally in its local coordinate system. Only before and after performing the operations on the element, a transformation to the global coordinate system has to be done. However, an essentially one-dimensional model is used as previously mentioned where the directions of the local (element) coordinate system coincides with the directions of the global (structural) coordinate system. Thus, no further attention is paid on this issue.

4.4.2. Application of boundary conditions and loading

Hitherto, no boundary conditions were defined, which gives rise to rigid body motions and a singular stiffness matrix. Boundary conditions are always introduced by prescribed nodal displacements, often equal to zero. There exist different concepts to introduce boundary conditions, e. g., the penalty method, a method manipulating the stiffness matrix and the method of Lagrangian multipliers. In the penalty method, the constraint is enforced by applying penalty factors, which are substantially larger than the largest values in the stiffness matrix. The application scheme is as follows: for a prescribed displacement $\hat{u}_i$, the penalty factor ϕ_p is added to the respective entry of the main diagonal in the stiffness matrix and multiplied with the value of the prescribed displacement to the external force vector, which yields

$$\begin{matrix} & \mathbf{K} & \\ \end{matrix} \begin{matrix} \mathbf{u} \\ \end{matrix} \begin{matrix} \mathbf{f}_{ext} \\ \end{matrix}$$
$$\begin{bmatrix} \ddots & \vdots & \ddots \\ \cdots & K_{ii} + \phi_p & \cdots \\ \ddots & \vdots & \ddots \end{bmatrix} \begin{bmatrix} \vdots \\ u_i \\ \vdots \end{bmatrix} = \begin{bmatrix} \vdots \\ f_{ext,i} + \phi_p \hat{u}_i \\ \vdots \end{bmatrix} . \tag{4.72}$$

As ϕ_p dominates the i-th equation, u_i is enforced to obtain a value of approximately $\hat{u}_i$. Obviously, the difference between u_i and $\hat{u}_i$, also called constraint violation, becomes smaller the larger ϕ_p is. However, the value of ϕ_p is limited by the floating point precision of the computer and increasing round-off errors with increasing ϕ_p. To balance both errors a so-called square root rule

$$\phi_p = 10^k \sqrt{10^p}. \tag{4.73}$$

for the estimation of the penalty factor ϕ_p is proposed in [Felippa 2004] where also the issue of competing constraint violation and round-off error is discussed in more detail. In Eq. (4.73), k is the order of magnitude (10^k) of the largest entry in the stiffness matrix and p is the number of digits of the floating point precision. Thus, an inherent drawback of the penalty method is its inexactness. However, an advantageous property of the penalty method is that size and allocation of the stiffness matrix remain unchanged despite the constraints. Furthermore, it is easy to implement in FEM codes.

A second method to introduce constraints, which is described e. g. in [Ottosen & Ristinmaa 2005] and shown schematically in Fig. 4.12, is to separate prescribed displacements $\mathbf{u}_c$ from unconstrained displacements $\mathbf{u}_u$ and to reorder, at least virtually, Eq. (4.71):

$$\begin{bmatrix} \mathbf{K}_{uu} & \mathbf{K}_{uc} \\ \mathbf{K}_{cu} & \mathbf{K}_{cc} \end{bmatrix} \begin{bmatrix} \mathbf{u}_u \\ \mathbf{u}_c \end{bmatrix} = \begin{bmatrix} \mathbf{f}_{ext,u} \\ \mathbf{f}_{ext,c} \end{bmatrix} . \tag{4.74}$$

The known quantities are the entries of $\mathbf{K}$, the prescribed displacements $\mathbf{u}_c$ and the external forces $\mathbf{f}_{ext,u}$ corresponding to the unconstrained displacements $\mathbf{u}_u$. The sub-vector $\mathbf{f}_{ext,c}$ contains the reaction forces corresponding to the prescribed displacements $\mathbf{u}_c$. Evaluating the first line in Eq. (4.74) yields

$$\mathbf{K}_{uu}\mathbf{u}_u + \mathbf{K}_{uc}\mathbf{u}_c = \mathbf{f}_{ext,u} \tag{4.75}$$

where $\mathbf{u}_u$ are the only unknowns. Thus, for $\mathbf{u}_u$ only

$$\mathbf{K}_{uu}\mathbf{u}_u = \mathbf{f}_{ext,u} - \mathbf{K}_{uc}\mathbf{u}_c \tag{4.76}$$

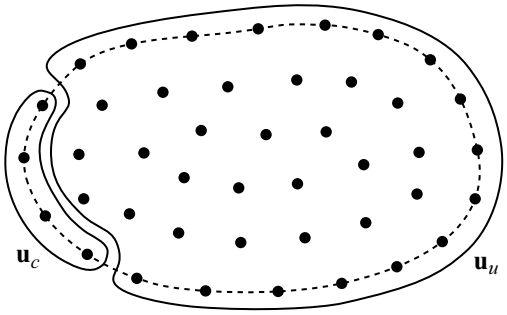

Figure 4.12.: Partitioning of nodes with and without prescribed boundary conditions according to Fig. 4.11(b); corresponding to [Ottosen & Ristinmaa 2005]

needs to be solved while the second line of Eq. (4.74) needs be evaluated only explicitly if the reaction forces $\mathbf{f}_{ext,c}$ are of interest. In order to remain the original structure of the stiffness matrix and the standard solution procedure for Eq. (4.71), one can manipulate $\mathbf{K}$ and $\mathbf{f}$ such that for the solution for $\mathbf{u}$ the entire system has to be solved. Therefor, Eq. (4.74) has to be reformulated as

$$\begin{bmatrix} \mathbf{K}_{uu} & \mathbf{0} \\ \mathbf{0} & \mathbf{I} \end{bmatrix} \begin{bmatrix} \mathbf{u}_u \\ \mathbf{u}_c \end{bmatrix} = \begin{bmatrix} \mathbf{f}_{ext,u} - \mathbf{K}_{uc}\hat{\mathbf{u}}_c \\ \hat{\mathbf{u}}_c \end{bmatrix}. \tag{4.77}$$

where $\mathbf{0}$ and $\mathbf{I}$ are zero and identity matrices, respectively. Furthermore, $\hat{\mathbf{u}}_c$ are the prescribed displacements. It can be seen that it is also not necessary to separate constrained and unconstrained displacements. It is only necessary to allocate the zeros and ones appropriately in the rows and columns of the prescribed displacements as well as to store the non-zero values of the sub-matrix $\mathbf{K}_{uc}$ for the modification of the force vector. The reaction forces can be determined in a subsequent calculation by means of evaluating the second line in Eq. (4.74):

$$\mathbf{K}_{cu}\mathbf{u}_u + \mathbf{K}_{cc}\mathbf{u}_c = \mathbf{f}_{ext,c}. \tag{4.78}$$

Advantages of this method are that the structure of the stiffness matrix remains unchanged and the solution is exact apart from numerical errors.

As a last approach to introduce constraints, the method of *Lagrangian multipliers* shall be briefly described following the physical interpretation in [Felippa 2004]. In this approach, so-called constraint forces λ_c are introduced, which are simultaneously the reaction forces and are called Lagrangian multipliers. For a prescribed displacement $\hat{u}_i$ this yields

$$\begin{bmatrix} \ddots & \vdots & \ddots \\ \cdots & K_{ii} & \cdots \\ \ddots & \vdots & \ddots \end{bmatrix}_{\mathbf{K}} \begin{bmatrix} \vdots \\ \hat{u}_i \\ \vdots \end{bmatrix}_{\mathbf{u}} = \begin{bmatrix} \vdots \\ f_{ext,i} - \lambda_{c,i} \\ \vdots \end{bmatrix}_{\mathbf{f}_{ext}}. \tag{4.79}$$

As $\lambda_{c,i}$ is unknown, it is advantageous to transfer it to the left hand side:

$$\begin{bmatrix} \ddots & \vdots & \ddots & 0 \\ \cdots & K_{ii} & \cdots & 1 \\ \ddots & \vdots & \ddots & 0 \\ 0 & 1 & 0 & 0 \end{bmatrix}_{\mathbf{K}} \begin{bmatrix} \vdots \\ u_i \\ \vdots \\ \lambda_{c,i} \end{bmatrix}_{\mathbf{u}} = \begin{bmatrix} \vdots \\ f_{ext,i} \\ \vdots \\ \hat{u}_i \end{bmatrix}_{\mathbf{f}_{ext}}. \tag{4.80}$$

Evaluating the last line of Eq. (4.80), directly leads to $u_i = \hat{u}_i$. More constraints can be introduced accordingly increasing the order of the stiffness matrix by one for each constraint. The great advantages of this method are that the constraints are exactly fulfilled and also complex constraints as for instance dependent displacements can be introduced. However, the method also has decisive drawbacks. For instance, the stiffness matrix has to be expanded because of the unknown additional Lagrangian multipliers. Furthermore, positive-definiteness of the stiffness matrix is lost, which leaves some linear equation solving methods (e. g. Cholesky decomposition) inapplicable. A more detailed comparison of different methods for constraint application is given, e. g., in [Felippa 2004].

Obviously, the described approaches are also used to apply displacement-controlled loading to the models. In case of force-controlled loading, the respective forces have to be applied directly to the vector of external forces $\mathbf{f}_{ext}$. It is clear that these forces can only take effect if applied to unconstrained nodes.

4.4.3. Solution methods for non-linear FEM equations

With the introduction of boundary conditions and loading, the solution of the system of algebraic equations provided by Eq. (4.71) can be treated. Since $\mathbf{D}$ provided in the constitutive law, Eq. (4.62), and correspondingly also the stiffness matrix $\mathbf{K}$ are in general time and load dependent, the relation between the displacements $\mathbf{u}$ and the external forces $\mathbf{f}_{ext}$ is in general non-linear. This complicates the solution process and the solution of Eq. (4.71) considerably.

4.4.3.1. Solution of linear algebraic equations

In the linear case, Eq. (4.71) constitutes a system of linear algebraic equations where a range of standard solution methods exist, see e. g. [Gill et al. 1991] and [Press et al. 2007]. At least formally, it can be solved directly for $\mathbf{u}$ inverting the stiffness matrix, which leads to

$$\mathbf{u} = \mathbf{K}^{-1}\mathbf{f}_{ext}. \tag{4.81}$$

As long as sufficient boundary conditions are applied to suppress rigid body motions, $\mathbf{K}$ is non-singular (or regular) and, it can be shown, see e. g. [Bronstein et al. 2008], that it always has an inverse $\mathbf{K}^{-1}$. However, the procedure of inverting $\mathbf{K}$ is for large systems numerically costly and inefficient regarding the solution of Eq. (4.71), see e. g. [Gill et al. 1991] and [Press et al. 2007]. Thus, more efficient methods are usually applied. In case that Eq. (4.71) has to be solved only once, *Gaussian elimination* can be efficiently applied, see e. g. [Gill et al. 1991] and [Press et al. 2007]. If $\mathbf{K}$ remains constant for more than one solution, solution procedures based on a decomposition (or factorisation) of $\mathbf{K}$, which incorporates *Gaussian elimination*, are more efficient. One approach to decompose $\mathbf{K}$ of order $n \times n$ is the so-called *LU decomposition* with a lower triangular matrix $\mathbf{L}$, which has only non-zero entries on the main diagonal and below, and an upper triangular matrix $\mathbf{U}$, which has only non-zero entries on the main diagonal and above:

$$\underset{\mathbf{L}}{\begin{bmatrix} L_{11} & 0 & \vdots & 0 \\ L_{21} & L_{22} & \vdots & 0 \\ \dots & \dots & \ddots & \vdots \\ L_{n1} & L_{n2} & \dots & L_{nn} \end{bmatrix}} \underset{\mathbf{U}}{\begin{bmatrix} U_{11} & U_{12} & \vdots & U_{1n} \\ 0 & U_{22} & \vdots & U_{2n} \\ \dots & \dots & \ddots & \vdots \\ 0 & 0 & \dots & U_{nn} \end{bmatrix}} = \underset{\mathbf{K}}{\begin{bmatrix} K_{11} & K_{12} & \vdots & K_{1n} \\ K_{21} & K_{22} & \vdots & K_{2n} \\ \dots & \dots & \ddots & \vdots \\ K_{n1} & K_{n2} & \dots & K_{nn} \end{bmatrix}} . \tag{4.82}$$

As only the elements of **K** are known and the main diagonals of both **L** and **U** have non-zero entries, more unknowns than equations exist. Thus, the values of one of the main diagonal can be chosen arbitrarily. Usually, unit main diagonals, which means all entries equal to one on the main diagonal, of either **L** or **U** are chosen. While a unit main diagonal in **L** is used in so-called *Doolittle's factorisation*, it is applied to **U** in *Crout's factorisation*. Expanding Eq. (4.82) from top left to bottom right leads to equations for the successive determination of the coefficients of **L** and **U**. It appears that every equation has only the coefficient under consideration as unknown while all other coefficients can be determined before.

The method in the presented form fails if **K** has zero entries or entries close to zero in case of numerical calculations on the main diagonal because of division by zero errors. In this case, so-called partial pivoting can be applied, which is performed by means of interchange of rows or columns of **K** such that the main diagonal entry is non-zero. Therefor, a so-called permutation matrix **P** can be built efficiently from a unit matrix by interchanging the ones corresponding to the pivoting, see e. g. [Gill et al. 1991] and [Press et al. 2007] for details. However, zero entries on the main diagonal occur with regard to FEM stiffness matrices in the linear elastic case only if *Lagrangian multipliers* are applied to **K**. Otherwise, the main diagonal has only non-zero entries and entries equal to one at positions where boundary conditions are applied, compare Section 4.4.2.

Having established the factorisation, $\mathbf{K} = \mathbf{LU}$ can be substituted into Eq. (4.71) yielding

$$\mathbf{LUu} = \mathbf{L}(\mathbf{Uu}) = \mathbf{f}_{ext} \text{ with } \mathbf{Uu} = \mathbf{h}. \tag{4.83}$$

This can be solved in two steps for **u** where the first step is the solution of $\mathbf{Lh} = \mathbf{f}_{ext}$ for **h** and the second step is determining **u** by means of $\mathbf{Uu} = \mathbf{h}$. For the first step, a so-called forward elimination is carried out. Again, in every equation the only unknown is the entry of **h** under consideration while the other entries are determined previously. The procedure is slightly different for the second step because the solution has to be started with the last equation, which is the reason why the procedure is also called backsubstitution. It shall be recalled that $\mathbf{f}_{ext}$ includes according to Section 4.4.2 both prescribed forces and displacements. Thus, this procedure is applicable for both force-controlled and displacement-controlled loading. In the developed finite element code, an implementation of the "SuperLU" algorithm by [Demmel et al. 1999] is applied conveniently, which is developed for high performance on sequential computer architectures and takes advantage of sparse matrix allocations as described in Section 4.4.5.

In case that **K** is symmetric and positive-definite, the *Cholesky decomposition*

$$\mathbf{LL}^T = \mathbf{K} \tag{4.84}$$

can be applied where **L** is again the lower triangular matrix. If Eq. (4.84) is expanded similar to Eq. (4.82), it can be seen that the equations for determining the coefficients of

L on the main diagonal include square roots of the main diagonal coefficients of **K**. These are only guaranteed to be larger than zero in case of a positive-definite **K**, see e. g. [Gill et al. 1991]. As pointed out in Section 4.4.2, this is not the case if *Lagrangian multipliers* are applied. Furthermore, also in non-linear models, which account for concrete cracking, **K** might lose positive-definiteness. This is always the case when limit points, for instance global force maxima in the force-displacement response of structures, are exceeded as it is pointed out in [Crisfield 1997]. In this case, the displacement increments increase while the force increments decrease, which cannot be represented with a positive-definite **K**. Thus, although *Cholesky decomposition* is very efficient, it might not be applicable without modifications to models for concrete and is not further treated.

The described solution methods were all so-called *direct solvers*. If **K** is very large, it is often more efficient to solve Eq. (4.71) by means of so-called *iterative solvers*, see e. g. [Press et al. 2007]. However, this is a topic on its own and not further treated in this work. Moreover, in the simulations described in Chapter 5 immediate necessity to use *iterative solvers* was not experienced.

4.4.3.2. Solution of non-linear algebraic equations

Contrary to the linear case, the loading cannot be applied entirely at once in the non-linear case if the material response depends on the loading history. Furthermore, it is often necessary to determine the detailed displacement response of the structure over the entire loading range. Thus, loading has to be subdivided in a sequence of sufficiently small load steps, so-called increments. How small the increments need to be chosen, depends on the problem, which has to be solved, and on the stability of the numerical solution procedure. In the standard references about non-linear FEM, as for instance [Bathe 1996], [Crisfield 1997] and [Zienkiewicz & Taylor 2000b], standard methods for the solution of non-linear equilibrium equations are well documented. A well-arranged summary of these methods is also given in [Ottosen & Ristinmaa 2005].

The strategy of most iterative solution methods is to determine the displacements in such a way that the applied external forces $\mathbf{f}_{ext}$ equilibrate the internal forces $\mathbf{f}_{int}$. Therefor, the non-linear equilibrium equation is

$$\mathbf{r} = \mathbf{f}_{ext} - \mathbf{f}_{int} = \mathbf{0}. \tag{4.85}$$

The internal forces $\mathbf{f}_{int}$ were already used in Eq. (4.67) to determine the internal work. They are defined as

$$\mathbf{f}_{int} = \int_V \mathbf{B}^T \boldsymbol{\sigma} \mathrm{d}V \tag{4.86}$$

if body forces do not appear or remain unconsidered. The external forces $\mathbf{f}_{ext}$ are given according to Eq. (4.70) or Eq. (4.71), respectively, if only traction forces are considered. The vector $\mathbf{r}$ is called the residual vector and represents the remaining gap between $\mathbf{f}_{ext}$ and $\mathbf{f}_{int}$. Thus, if $\mathbf{r} \neq \mathbf{0}$, out-of-balance forces exist and the found solution for $\mathbf{u}$ does not correspond to equilibrium. In the computations, $\mathbf{r} = \mathbf{0}$ will almost never be achieved (except for linear calculations) because of the limited floating-point number accuracy in typically

used computer architectures. Thus, the aim is to achieve $\mathbf{r}(\mathbf{u}) \approx \mathbf{0}$, which can be checked with a convergence criterion, e. g.

$$\| \mathbf{r}(\mathbf{u}) \| < tol \tag{4.87}$$

where the Euclidean norm of $\mathbf{r}$ shall be smaller than the scalar-valued tolerance tol. This criterion is only one of a broad range of proposed criteria, see e. g. [Bathe 1996], [Crisfield 1997] and [Ottosen & Ristinmaa 2005].

As the next step, it is interesting how to achieve this state. Starting at an equilibrium state t where $\mathbf{r}_t = \mathbf{0}$, or $\mathbf{r}_t$ is at least sufficiently small, and $\mathbf{u}_t$ as well as $\mathbf{f}_{ext,t}$ are known, the summation of a sufficiently small increment $\Delta\mathbf{f}_{ext,t+1}$ yields

$$\mathbf{f}_{ext,t+1} = \mathbf{f}_{ext,t} + \Delta\mathbf{f}_{ext,t+1} \tag{4.88}$$

where $\mathbf{f}_{ext,t+1}$ are the external forces of the next load step $t+1$. Corresponding to the change in the loading also a change in the displacements exists:

$$\mathbf{u}_{t+1} = \mathbf{u}_t + \Delta\mathbf{u}_{t+1} \tag{4.89}$$

where the displacement increment $\Delta\mathbf{u}_{t+1}$ is the quantity searched for. In general, an iteration is necessary to determine $\Delta\mathbf{u}_{t+1}$ sufficiently accurate and to satisfy inequality (4.87). Only if the chosen increments and the non-linearity of the system are sufficiently small, inequality (4.87) might be satisfied with the first solution of Eq. (4.71). This corresponds to the so-called *Euler forward scheme* or purely incremental scheme where it is known that the approximated solution increasingly drifts off from the true solution, see e. g. [Ottosen & Ristinmaa 2005] for details.

To perform the iterations, it is advantageous to revert to linear solution schemes as described in Section 4.4.3.1 because they can be efficiently performed. Therefor, a series of iterations of the form

$$\mathbf{K}^i d\mathbf{u}_{t+1}^{i+1} = \mathbf{r}_{t+1}^i \tag{4.90}$$

have to be carried out where the displacement increments $d\mathbf{u}_{t+1}^i$ (note the difference between the incremental d and the differential d) are used to improve the internal forces $\mathbf{f}_{int}$ to equilibrate the external forces $\mathbf{f}_{ext}$. $\mathbf{K}^i$ is the iteration matrix where some properties are specified at the end of this section. As the determination of $\mathbf{K}^i$ is performed differently in various solution methods, this topic is treated subsequently in the respective sections. The subscript i refers to the iteration number. Obviously, if $\mathbf{r}_{t+1}^i \to \mathbf{0}$ also $d\mathbf{u}_{t+1}^i \to \mathbf{0}$. The total displacement increment $\Delta\mathbf{u}_{t+1}^i$ of the load step in Eq. (4.90) can be determined by means of

$$\Delta\mathbf{u}_{t+1}^i = \sum_{k=1}^{i} d\mathbf{u}_{t+1}^k. \tag{4.91}$$

Correspondingly, also the total displacements $\mathbf{u}_{t+1}^i$ up to iteration step i can be determined as

$$\mathbf{u}_{t+1}^i = \mathbf{u}_t + \Delta\mathbf{u}_{t+1}^i. \tag{4.92}$$

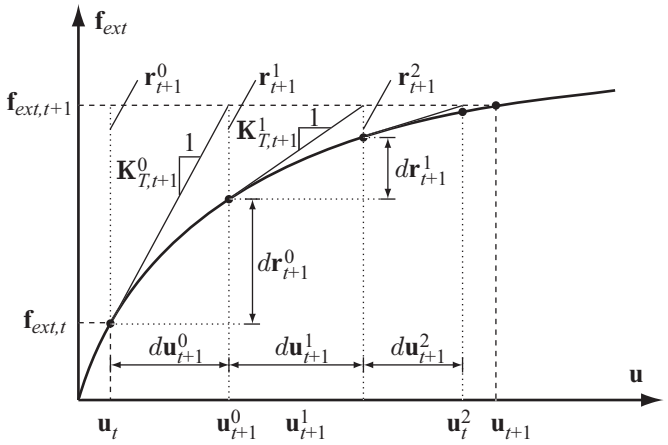

Figure 4.13.: Newton-Raphson scheme for a system with one degree of freedom

where $\mathbf{u}_t$ are the (accepted) displacements at the end of the previous load step. The displacements $\mathbf{u}^i_{t+1}$ are used in every iteration step to determine the strain state $\boldsymbol{\varepsilon}^i_{t+1}$ with Eq. (4.60), which is in turn used to determine the stress state $\boldsymbol{\sigma}^i_{t+1}$ with Eq. (4.62). A source of non-linearity is included in Eq. (4.62) with $\mathbf{D}$, which is often a function of the deformation or strain state and referred to as physical or material non-linearity. Other non-linearities, which are not covered within this work, may arise from geometric properties of the system, as e. g. from large deformations, and are called geometric non-linearities. With $\boldsymbol{\sigma}^i_{t+1}$, Eq. (4.86) is used to determine the internal forces $\mathbf{f}^i_{int,t+1}$. This is a common approach for *incremental-iterative procedures*, which yields in general accurate solutions for $\mathbf{u}_{t+1}$. It is not necessary, in general, to change $\mathbf{K}$ simultaneously to changes in the constitutive relations given with Eq. (4.62) as the determination of $\mathbf{K}$ in Eq. (4.71) might indicate. The reason is that errors in the iterative displacement increment will lead to respective errors in $\mathbf{f}_{int}$. In the next iteration step, this will be corrected, at least theoretically, due to the subtraction of $\mathbf{f}_{int}$ from $\mathbf{f}_{ext}$, which is fixed. This is also the reason why during the incremental-iterative solution procedure $\mathbf{K}$ is often referred to as *algorithmic stiffness*. Nevertheless, it can be advantageous for convergence to update also $\mathbf{K}$ simultaneously to $\mathbf{D}$. Such an approach is given in the subsequent section.

4.4.3.3. Newton-Raphson method

A popular method for the solution of non-linear equations arising in the FEM is the so-called Newton-Raphson method, which is also often called shortly Newton's method. Since this method was derived simultaneously by Newton and Raphson as [Bićanić & Johnson 1979] point out the former name is more appropriate. The basic idea of the Newton-Raphson method is to approximate the residual $\mathbf{r}$ about $\mathbf{u}$ by means of a Taylor expansion ignoring higher order terms with

$$\mathbf{r}(\mathbf{u}^{i+1}_{t+1}) \approx \mathbf{r}(\mathbf{u}^i_{t+1}) + \left(\frac{\partial \mathbf{r}}{\partial \mathbf{u}}\right)^i_{t+1} d\mathbf{u}^i_{t+1}. \tag{4.93}$$

Corresponding to Eq. (4.85), the objective of the iteration is to obtain $\mathbf{r}(\mathbf{u}_{t+1}^{i+1}) = \mathbf{0}$, which yields

$$\mathbf{0} = \mathbf{r}(\mathbf{u}_{t+1}^{i}) + \left(\frac{\partial \mathbf{r}}{\partial \mathbf{u}}\right)_{t+1}^{i} d\mathbf{u}_{t+1}^{i}. \tag{4.94}$$

Analysing $\partial\mathbf{r}/\partial\mathbf{u}$ where $\partial\mathbf{r} = \partial\mathbf{f}_{ext} - \partial\mathbf{f}_{int}$, it can be identified that $\mathbf{f}_{ext}$ is constant while $\mathbf{f}_{int}$ is variable. Applying the sum rule to $\partial\mathbf{r}/\partial\mathbf{u}$, it is obvious that only the internal forces yield non-zero portions. Thus, it can be stated using Eq. (4.86) that

$$\frac{\partial \mathbf{r}}{\partial \mathbf{u}} = -\int_V \mathbf{B}^T \frac{\mathrm{d}\boldsymbol{\sigma}}{\mathrm{d}\mathbf{u}} \mathrm{d}V. \tag{4.95}$$

With the constitutive relation provided with Eq. (4.62) and with Eq. (4.60) $\mathrm{d}\boldsymbol{\sigma}$ can be expressed as

$$\mathrm{d}\boldsymbol{\sigma} = \mathbf{D}_T \mathrm{d}\boldsymbol{\varepsilon} = \mathbf{D}_T \mathbf{B} \mathrm{d}\mathbf{u}, \text{ which yields } \frac{\mathrm{d}\boldsymbol{\sigma}}{\mathrm{d}\mathbf{u}} = \mathbf{D}_T \mathbf{B}. \tag{4.96}$$

$\mathbf{D}_T$ is the tangential value of the slope of the constitutive relation. With substitution of Eq. (4.96) into Eq. (4.95), the tangent stiffness matrix can established as

$$\frac{\partial \mathbf{r}}{\partial \mathbf{u}} = -\int_V \mathbf{B}^T \mathbf{D}_T \mathbf{B} \mathrm{d}V = -\mathbf{K}_T, \tag{4.97}$$

compare Eq. (4.71). Eq. (4.94) can now be rewritten to be applicable in the standard scheme for the solution of linear algebraic equations given in Section 4.4.3.1:

$$\mathbf{K}_{T,t+1}^{i} d\mathbf{u}_{t+1}^{i} = \mathbf{r}_{t+1}^{i}. \tag{4.98}$$

Due to the permanent adaptation of the stiffness matrix the Newton-Raphson iteration scheme has theoretically a superior convergence rate, which is quadratic. This is illustrated in Fig. 4.13 for a system with one degree of freedom. On the other hand, it can be identified that the stiffness matrix has to be established in every iteration step in the Newton-Raphson scheme. As it was already pointed out in Section 4.4.3.1 this is numerically very costly if direct solvers are used because the stiffness matrix has to be assembled in every iteration and a solution has to be performed. The advantage of a *LU decomposition* cannot be exploited as always only one solution can be made with one established decomposition. Further problems may arise with the iteration scheme in the vicinity of limit points where the gradient is zero and the stiffness matrix tends to become singular. See also e. g. [Ottosen & Ristinmaa 2005] for a more detailed treatment of the Newton-Raphson method and its properties.

4.4.3.4. Modified Newton method

A main drawback of the Newton-Raphson method is the necessity for assembling and factorising the stiffness matrix in every iteration step. As it was mentioned in Section 4.4.3.2, it is, however, not mandatory to use the tangent stiffness matrix to achieve accurate results. This is exploited in the so-called modified Newton schemes. The incremental-iterative procedure is identical with the Newton-Raphson method except for the update of $\mathbf{K}$, which is only

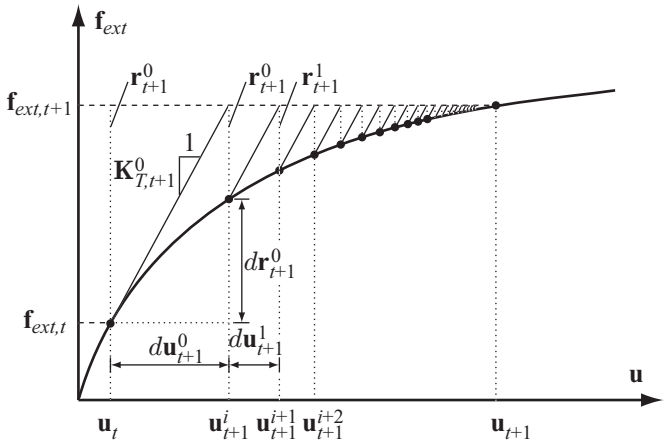

Figure 4.14.: Modified Newton scheme for a system with one degree of freedom

established at the beginning of the iteration and remains unchanged through the iteration. This corresponds to

$$\mathbf{K}^0_{T,t} d\mathbf{u}^i_t = \mathbf{r}^i_{t+1} \tag{4.99}$$

where $\mathbf{K}^0_{T,t}$ is the stiffness matrix before the first iteration step or at the end of the previous iteration. In Fig. 4.14, a visualisation of this approach for a system with one degree of freedom is shown. There exist numerous other approaches for the frequency and "moment", e. g. iteration step, of stiffness matrix updates, see e. g. [Zienkiewicz & Taylor 2000b]. One variation worth to mention is the so-called initial stiffness method where the stiffness matrix is established only once at the very beginning and kept constant during the entire incremental loading. It is obvious that omitting stiffness matrix updates decreases numerical costs considerably because the matrix decomposition has to be performed once at the beginning and subsequently only forward elimination and backward substitution is necessary for the solution of the linear algebraic equations as described in Section 4.4.3.1. However, the numerical efficiency is bought with slower (linear) convergence (if convergence is achieved at all), compare Figs. 4.13 and 4.14. It might be interesting to decide a priori, which algorithm outperforms the other. Therefor, the *No free lunch theorems for optimisation* by [Wolpert & Macready 1997] can be applied as the minimisation of the residual $\mathbf{r}$ can be seen as an optimisation. According to the *No free lunch theorems* one cannot decide, which optimisation algorithm outperforms another one without having further information about the problem behaviour. Thus, it has to be weighed up (based on information of the problem behaviour) or tested, which approach is more efficient at the end. It is conceivable that the modified Newton algorithm is more efficient if the change of the gradient of the system response is small while the (full) Newton-Raphson algorithm outperforms in case of a large change of the gradient because of its second order convergence rate.

4.4.3.5. Quasi-Newton methods

The previous sections showed that at least two methods are at hand to solve non-linear algebraic equations. While in the Newton-Raphson method fast convergence is achieved but the numerical effort in every iteration step is high, the situation is reversed in modified Newton

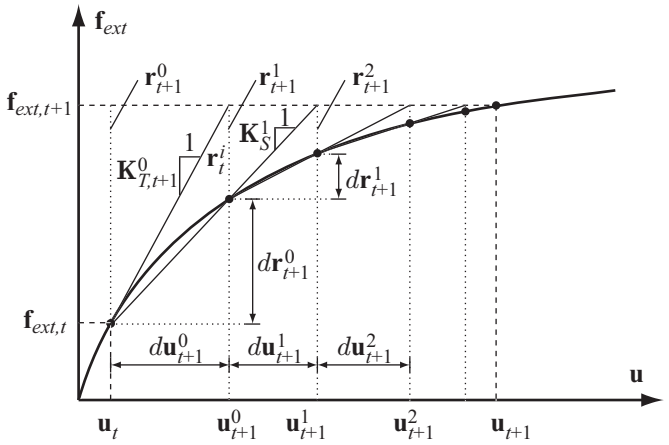

Figure 4.15.: Quasi-Newton scheme for a system with one degree of freedom

methods. It would be desirable to have a method at hand, which combines the advantages of both methods, namely fast convergence and low numerical effort. A class of methods, which have these properties, are the so-called *Quasi-Newton methods* also referred to as *Secant methods*, see e. g. [Bathe 1996], [Zienkiewicz & Taylor 2000b] and [Ottosen & Ristinmaa 2005]. However, it should have become clear from the short discussion of the implications of the *No free lunch theorems* in the previous section that it is impossible to outperform the Newton-Raphson type algorithms in every situation. It is rather a compromise. In quasi-Newton methods, secants instead of tangents are used for $\mathbf{K}$. Therefor, the so-called secant or quasi-Newton relation between two known states $i-1$ and i is established

$$\mathbf{K}^i_S d\mathbf{u}^i = d\mathbf{r}^i \text{ with } d\mathbf{u}^i = \mathbf{u}^i - \mathbf{u}^{i-1} \text{ and } d\mathbf{r}^i = \mathbf{r}^i - \mathbf{r}^{i-1}. \tag{4.100}$$

For a system with one degree of freedom, the determination of the algorithmic stiffness matrix $\mathbf{K}^i_S$ is trivial, see Fig. 4.15, which is not the case with more degrees of freedom as e. g. [Zienkiewicz & Taylor 2000b] point out. Various forms of $\mathbf{K}^i_S$ can satisfy Eq. (4.100) and consequently different methods exist, which lead also to different properties of $\mathbf{K}^i_S$. An approach, which is especially suitable for the application to FEM problems is given with the so-called *BFGS approach*. It is named after Broyden, Fletcher, Goldfarb and Shanno and was proposed for the solution of non-linear FEM equations by [Matthies & Strang 1979].

An advantageous property of this approach is that it preserves symmetry and positive-definiteness of the $\mathbf{K}_S$ (if $\mathbf{K}_S$ has these properties initially). As pointed out in Section 4.4.3.1, positive-definiteness is lost when limit points are exceeded. In [Matthies & Strang 1979], two versions of the BFGS approach are presented. For the first formulation, the iteration matrix has to be positive-definite while it has to be not for the second formulation. Hence, the second formulation is briefly summarised in the following. It is obvious that at least one iteration step is needed before the *BFGS approach* can be performed as otherwise only one supporting point (the initial values) is available while two are needed to establish the secant relation according to Eq. (4.100). The subscript t referring to the incremental load step is dropped in the following for abbreviation as only the update of the iteration matrix (or its inverse) and determination of iterative displacement changes $d\mathbf{u}$ within one load increment are presented. These $d\mathbf{u}$'s can then be used directly in the general incremental-iterative solution scheme given in Section 4.4.3.2.

Having at least these two supporting points and an initial estimation $\mathbf{K}_S^0$ of the algorithmic stiffness, which can be simply the initial tangential stiffness matrix $\mathbf{K}_T^0$ as in the case of the *Newton-Raphson method*, an approximation of the secant stiffness for the next iteration step i of the form

$$(\mathbf{K}_S^i)^{-1} = \underbrace{\left(\mathbf{I} - \varrho^i d\mathbf{u}^i d\mathbf{r}^{iT}\right)}_{=\mathbf{A}^i} (\mathbf{K}_S^{i-1})^{-1} \underbrace{\left(\mathbf{I} - \varrho^i d\mathbf{r}^i d\mathbf{u}^{iT}\right)}_{=\mathbf{B}^i} + \underbrace{\left(\varrho^i d\mathbf{u}^i d\mathbf{u}^{iT}\right)}_{=\mathbf{C}^i}. \tag{4.101}$$

can be made, see [Matthies & Strang 1979]. The vectors $d\mathbf{u}^i$ and $d\mathbf{r}^i$ were defined in Eq. (4.100) while the scalar ϱ^i is defined as $\varrho^i = 1/(d\mathbf{u}^{iT} d\mathbf{r}^i)$. Furthermore, it can be identified that the *BFGS method* operates at the inverse $\mathbf{K}_S^{-1}$. It is beyond the scope of this work to illustrate the derivation of Eq. (4.101) from the very beginning. The interested reader might consult [Dennis & Moré 1977], [Luenberger 2005] and [Nocedal & Wright 1999] for a more mathematical derivation of the *BFGS method*. It is worth to mention that it is not mandatory to handle with the inverse $\mathbf{K}_S^{-1}$. As [Luenberger 2005] points out, Eq. (4.101) can also be rewritten remaining exactly its structure such that it works directly with $\mathbf{K}_S$. Therefor, only the $d\mathbf{u}$'s and $d\mathbf{r}$'s have to be interchanged, which directly yields the so-called *Davidon-Fletcher-Powell method*. The reason is that $\mathbf{K}_S d\mathbf{u} = d\mathbf{r}$ and $\mathbf{K}_S^{-1} d\mathbf{r} = d\mathbf{u}$ are complementary formulae and any procedure, which is able to update $\mathbf{K}_S$, can also be applied to $\mathbf{K}_S^{-1}$ provided that they are regular. One might wonder why the inverse of the iteration matrix is used although it was mentioned in Section 4.4.3.1 that it is numerically inefficient to establish it. Fortunately, it is not necessary to perform these operations explicitly as it will be shown in the following. Considering Eq. (4.101) with the substituted terms $\mathbf{A}^i$, $\mathbf{B}^i$ and $\mathbf{C}^i$ and starting for example at $i = 3$, a recursion for $\mathbf{K}_S^{i^{-1}}$ yields:

$$\begin{aligned}
\mathbf{K}_S^{(3)^{-1}} &= \mathbf{A}^{(3)} \mathbf{K}_S^{(2)^{-1}} \mathbf{B}^{(3)} + \mathbf{C}^{(3)} \\
&= \mathbf{A}^{(3)} \left[\mathbf{A}^{(2)} \mathbf{K}_S^{(1)^{-1}} \mathbf{B}^{(2)} + \mathbf{C}^{(2)}\right] \mathbf{B}^{(3)} + \mathbf{C}^{(3)} \\
&= \mathbf{A}^{(3)} \left[\mathbf{A}^{(2)} \left[\mathbf{A}^{(1)} \mathbf{K}_S^{(0)^{-1}} \mathbf{B}^{(1)} + \mathbf{C}^{(1)}\right] \mathbf{B}^{(2)} + \mathbf{C}^{(2)}\right] \mathbf{B}^{(3)} + \mathbf{C}^{(3)} \\
&= \mathbf{A}^{(3)} \mathbf{A}^{(2)} \mathbf{A}^{(1)} \mathbf{K}_S^{(0)^{-1}} \mathbf{B}^{(1)} \mathbf{B}^{(2)} \mathbf{B}^{(3)} \\
&\quad + \mathbf{A}^{(3)} \mathbf{A}^{(2)} \mathbf{C}^{(1)} \mathbf{B}^{(2)} \mathbf{B}^{(3)} + \mathbf{A}^{(3)} \mathbf{C}^{(2)} \mathbf{B}^{(3)} + \mathbf{C}^{(3)}.
\end{aligned} \tag{4.102}$$

It is observable that Eq. (4.102) contains after the final recursion step only the inverse $\mathbf{K}_S^{(0)^{-1}}$ of the initial iteration matrix as well as the vectors $d\mathbf{u}^i$ and $d\mathbf{r}^i$, which have to be stored. With a reformulation of Eq. (4.90), it can be solved for $d\mathbf{u}^{(4)}$:

$$\begin{aligned}
d\mathbf{u}^{(4)} &= \mathbf{K}_S^{(3)^{-1}} \mathbf{r}^{(3)} \\
&= \Big[\mathbf{A}^{(3)} \mathbf{A}^{(2)} \mathbf{A}^{(1)} \mathbf{K}_S^{(0)^{-1}} \mathbf{B}^{(1)} \mathbf{B}^{(2)} \mathbf{B}^{(3)} + \mathbf{A}^{(3)} \mathbf{A}^{(2)} \mathbf{C}^{(1)} \mathbf{B}^{(2)} \mathbf{B}^{(3)} \\
&\quad + \mathbf{A}^{(3)} \mathbf{C}^{(2)} \mathbf{B}^{(3)} + \mathbf{C}^{(3)}\Big] \mathbf{r}^{(3)}
\end{aligned} \tag{4.103}$$

Based on the exemplary presentation of the recursion for $d\mathbf{u}^{(i+1)}$, which can be determined with the inverse of the initial algorithmic stiffness $\mathbf{K}_S^{(0)^{-1}}$, a more efficient implementation is presented, in the following. Therefor, two auxiliary sets of vectors $\mathbf{q}$ and $\mathbf{v}$ are introduced.

At first, the term $\mathbf{K}_S^{(0)^{-1}} \mathbf{B}^{(1)} \mathbf{B}^{(2)} \mathbf{B}^{(3)} \mathbf{r}^{(3)}$ is extracted from Eq. (4.103). Using a general recursion notation, a $\mathbf{q}^j$ can be introduced substituting $\mathbf{B}^{j+1} \mathbf{q}^{j+1}$ with $\mathbf{B}^{j+1}$ according to Eq. (4.101). This yields a recursion formula to determine $\mathbf{q}^{(0)}$:

$$\mathbf{q}^j = \mathbf{B}^{j+1}\mathbf{q}^{j+1} = \mathbf{q}^{j+1} - d\mathbf{r}^{j+1}\underbrace{\varrho^{j+1}d\mathbf{u}^{j+1^T}\mathbf{q}^{j+1}}_{=\alpha^j} \text{ with } j = i-1, ..., 0. \tag{4.104}$$

The starting value $\mathbf{q}^i$ is obviously just the residual $\mathbf{r}^i$ after the previous iteration step. Optionally, the last (marked) scalar term α^j in Eq. (4.104) can be computed and stored previously as it is needed later again and a repeated computation can be saved. It can be realised that if $\mathbf{B}^{(1)}\mathbf{B}^{(2)}\mathbf{B}^{(3)}\mathbf{r}^{(3)}$ is substituted by $\mathbf{q}^{(0)}$, a vector $\mathbf{v}^{(0)}$ can be determined by matrix-vector multiplication or as a solution of a linear algebraic equation corresponding to Section 4.4.3.1 by means of

$$\mathbf{v}^{(0)} = \mathbf{K}_S^{(0)}\mathbf{q}^{(0)}. \tag{4.105}$$

Thus, it is not necessary at all to establish the inverse of $\mathbf{K}_S^{(0)}$. To determine $d\mathbf{u}^{i+1}$, a generalisation of Eq. (4.103) regarding the recursion step j is performed:

$$\begin{aligned}\mathbf{v}^j &= \left[\mathbf{A}^j(\mathbf{K}_S^{j-1})^{-1}\mathbf{B}^j + \mathbf{C}^j\right]\mathbf{r}^j = \mathbf{A}^j\mathbf{v}^{j-1} + \mathbf{C}^j\mathbf{r}^j \\ &= \left(\mathbf{I} - \varrho^j d\mathbf{u}^j d\mathbf{r}^{j^T}\right)\mathbf{v}^{j-1} + \varrho^j d\mathbf{u}^j d\mathbf{u}^{j^T}\mathbf{r}^j \\ &= \mathbf{v}^{j-1} + d\mathbf{u}^j\left(\underbrace{\varrho^j d\mathbf{u}^{j^T}\mathbf{r}^j}_{=\alpha^{j-1}} - \underbrace{\varrho^j d\mathbf{r}^{j^T}\mathbf{v}^{j-1}}_{=\beta^j}\right)\end{aligned} \tag{4.106}$$

where $(\mathbf{K}_S^{j-1})^{-1}\mathbf{B}^j\mathbf{r}^j$ can be substituted with $\mathbf{v}^{j-1}$ and $d\mathbf{u}^{j+1}$ is substituted with $\mathbf{v}^j$. It can be identified that the scalar values α^{i-1} were already determined in Eq. (4.104). Moreover, according to [Matthies & Strang 1979] also the scalar value β^j can be computed separately before being inserted into Eq. (4.106). Eq. (4.106) has to be repeated for $j = 1, ..., i$. This yields for $j = i$ the displacement change $\mathbf{v}^i = d\mathbf{u}^{i+1}$, which can be used in the general incremental-iterative solution procedure presented in Section 4.4.3.2 in the same way as e. g. in the Newton-Raphson approach. Briefly summarised, for the iteration procedure in the BFGS approach provided in [Matthies & Strang 1979] only an initial iteration matrix is necessary, which is used once in every iteration step to perform an initial approximation of the displacements applying Eq. (4.105). Before and after, only scalar product computations using the iterative changes in the displacements $d\mathbf{u}^i$ and residuals $d\mathbf{r}^i$ have to be performed applying Eqs. (4.104) and (4.106). Although scalar product computations are computationally cheap, the effort to perform these repeated computations increases with increasing number of iterations. Thus, it is advantageous to establish a new tangential iteration matrix before every new load step t.

4.4.3.6. Line searches

As it was pointed out in Section 4.4.3.2, it is not necessary to use a $\mathbf{K}$ based on the material response to the applied deformation to achieve accurate results in the solution of non-linear algebraic equations. The reason is that the internal forces $\mathbf{f}_{int}$ control the residual. Thus, one could also consider to directly manipulate the displacement change $d\mathbf{u}$, which in turn directly changes the internal forces $\mathbf{f}_{int}$ and corrects a potential error introduced. On the other hand, such a manipulation could provide a computationally cheap improvement of the convergence

to the solution if it is chosen in a proper way. Procedures of such kind are usually referred to as *line searches*.

A common way is to use a scalar factor η^i, also called step-length parameter, and manipulate the displacements as follows

$$\mathbf{u}_{t+1}^{i+1} = \mathbf{u}_{t+1}^{i} + \eta^i d\mathbf{u}_{t+1}^{i} \text{ with } \mathbf{u}_{t+1}^{i} = \mathbf{u}_t + \Delta\mathbf{u}_{t+1}^{i-1} \tag{4.107}$$

according to Eq. (4.92). It can be seen that the length of the so-called search direction $d\mathbf{u}_{t+1}^{i}$ is changed with the factor η^i. Thus, η^i plays the role of a predictor. Moreover, as $d\mathbf{u}_{t+1}^{i}$ is a result of an iteration step with one of the previously described methods, *line searches* can be applied to all incremental-iterative methods corresponding to Section 4.4.3.2. The question is how to determine η^i properly. Therefor, the approach presented in [Crisfield 1982, Crisfield 1997] is followed. According to [Crisfield 1982], the optimum value for η^i yields the condition

$$\kappa = d\mathbf{u}_{t+1}^{i}{}^T \mathbf{r}_{t+1}^{i+1}(\mathbf{u}_{t+1}^{i+1}(\eta^i)) = 0 \tag{4.108}$$

because the residual $\mathbf{r}_{t+1}^{i+1}$ as a function of $\mathbf{u}_{t+1}^{i+1}$, which is itself a function of η^i, is zero in this case if $d\mathbf{u}_{t+1}^{i} \neq \mathbf{0}$. In the case of $\kappa = 0$, $d\mathbf{u}_{t+1}^{i}$ and $\mathbf{r}_{t+1}^{i+1}(\mathbf{u}_{t+1}^{i+1}(\eta^i))$ are orthogonal to each other, which is the reason why Eq. (4.108) is often referred to as orthogonality condition. However, as it is pointed out in [Ottosen & Ristinmaa 2005], it cannot be expected to fulfil this condition based on a scalar value η^i. Instead, it is only attempted to achieve a significant reduction of the residual. Another argument why it is not reasonable to achieve a minimum for κ, is that for every line search sub-iteration the residual has to be determined again. Therefor, the stresses, strains and internal forces have to be determined for every element, which increases numerical costs.

After the first Newton iteration, two supporting points $(\eta^{(0)} = 0, \kappa^{(0)})$ and $(\eta^{(1)} = 1, \kappa^{(1)})$ for the line search can be established. The value $\kappa^{(0)}$ corresponds to the end of the previous (Newton) iteration step and can be determined with

$$\kappa^{(0)} = d\mathbf{u}_{t+1}^{i-1}{}^T \mathbf{r}_{t+1}^{i-1}. \tag{4.109}$$

The value $\kappa^{(1)}$ results from the current (Newton) iteration step without a manipulation of the search direction:

$$\kappa^{(1)} = d\mathbf{u}_{t+1}^{i}{}^T \mathbf{r}_{t+1}^{i}. \tag{4.110}$$

The supporting points can be used to establish a linear function, which has exactly one root. This is also the new step-length parameter $\eta^{(2)}$, see Fig. 4.16 for illustration. If in the sub-iterations always two supporting $(\eta^{(0)}, \kappa^{(0)})$ and $(\eta^{i,l}, \kappa^{i,l})$ are used, where the superscript l refers to the line search sub-iteration, the new step-length parameter $\eta^{i,l+1}$ can be determined as:

$$\eta^{i,l+1} = -\frac{\eta^{i,l}\kappa^{(0)}}{\kappa^{i,l} - \kappa^{(0)}}. \tag{4.111}$$

As it was already mentioned, it is not necessary to find the exact root of the η-κ relation as this will in general also not fulfil the orthogonality condition given with Eq. (4.108). Thus,

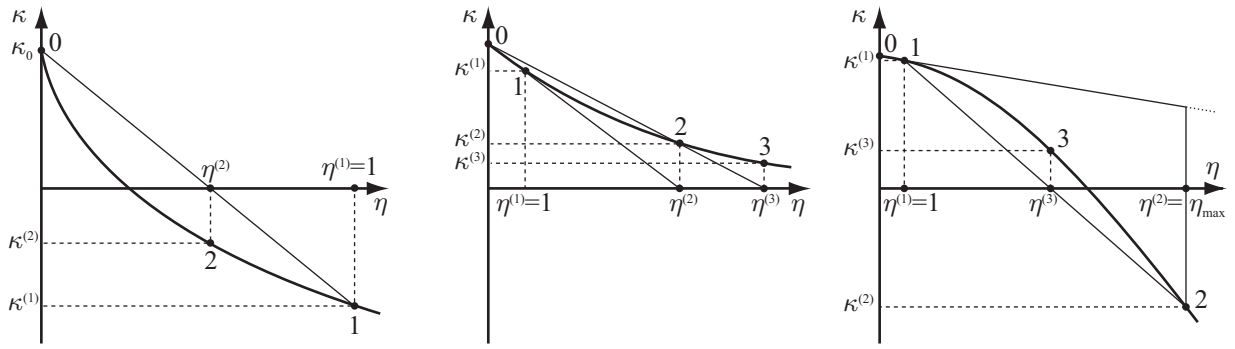

(a) Interpolation (b) Extrapolation (c) Excessive extrapolation

Figure 4.16.: Line search

it is proposed in [Crisfield 1997] that line search sub-iterations are only performed as long as

$$\left| \frac{\kappa^{i,l}}{\kappa^{(0)}} \right| < \beta_{LS} \tag{4.112}$$

is not fulfilled and a maximum number n_{LS} of sub-iterations to be defined is not exceeded. In [Crisfield 1997], values of $\beta_{LS} \approx 0.8$ and $n_{LS} \approx 4$ are recommended. Clearly, the formulation in Eq. (4.111) works stable if the problem is an interpolation, as shown in Fig. 4.16(a), or an extrapolation corresponding to Fig. 4.16(b). However, it happens occasionally that the extrapolation leads to very large values for $\eta^{i,l+1}$, see Fig. 4.16(c). In this case, it is advantageous for stability of the sub-iteration to limit η_{max} where a value of $\eta_{max} \approx 10$ is recommended in [Crisfield 1997]. The convergence of the line search sub-iteration can be improved in this case if it is interpolated between the supporting points $(\eta^{pos}, \kappa^{pos})$ and $(\eta^{neg}, \kappa^{neg})$ with the largest η where κ is positive and the smallest η where κ is negative, respectively. A corresponding example is given in Fig. 4.16(c) where it is interpolated between the supporting point "1" and "2" to determine "3". Therefor, storage of the η and κ values is necessary. The interpolation formula to determine $\eta^{i,l+1}$ is then

$$\eta^{i,l+1} = \eta^{pos} - \kappa^{pos} \frac{\eta^{neg} - \eta^{pos}}{\kappa^{neg} - \kappa^{pos}}. \tag{4.113}$$

Similar to the limitation of the maximum value for extrapolation, it is advantageous to limit also the minimum value of η. Therefor, a value of $\eta_{min} = 0.3$ was chosen. Occasionally, it happens that a negative η is calculated. In this case, line search is aborted and the value $\eta = 1$ is used, which corresponds to original value of the Newton iteration. Due to the "slack" line search accepting $\eta^{i,l}$ if condition (4.112) is fulfilled, often line search sub-iterations are not performed at all because the Newton iteration already provides improvement of the residual in this magnitude. However, especially if concrete cracking is incorporated *line search* often accelerates convergence and is sometimes essential to achieve convergence at all.

Before proceeding to the formulation of the used finite elements in the next section, a final comment concerning the usage of the described incremental-iterative solution procedures shall be given. In numerical tests, which incorporated concrete-reinforcement systems with multiple concrete cracking corresponding to Section 5.3 but were not systematic, the BFGS method combined with line search outperformed at least by experience the Newton-Raphson

and modified Newton methods. The simulations almost always achieved a solution for the entire loading range, which was not always the case with the other methods. Especially the modified Newton method most often failed at the first concrete cracking event. However, it is also worth to mention that for some problems occasionally a large number of iteration steps (>> 100) was necessary to reduce the residual to the prescribed tolerance. As a consequence, the BFGS method in combination with line search is used as solution method for the simulations presented in Chapter 5.

4.4.4. Used element types

4.4.4.1. One-dimensional bar element

Hitherto, the element types used in the model according to Section 4.4.1 and their characteristics were not specified. The first applied element is the one-dimensional bar element with two nodes, which is also the most basic finite element. A nice presentation of the derivation of the element stiffness matrix is given for example in [Felippa 2004]. Besides the one-dimensionality of the element also the model is according to Section 4.4.1 essentially one-dimensional and, thus, only one coordinate per node denoted with x is assumed to have values unequal to zero. In order to establish the element stiffness matrix $\mathbf{K}_{bar}$ corresponding to Eq. (4.71), the displacement shape functions $\mathbf{N}_{bar}$ need to be quantified because the strain-displacement matrix $\mathbf{B}_{bar}$ depends on it according to Eq. (4.60). With the displacement shape functions $\mathbf{N}_{bar}$, the displacements $u_p(x)$ of an arbitrary point at the coordinate x within the element can be calculated from the two nodal displacements $u_{n,1}$ and $u_{n,2}$. These can be also collected according to Eq. (4.58) in a vector $\mathbf{u}_n$:

$$u_p(x) = N_1 u_{n,1} + N_2 u_{n,2} = \begin{bmatrix} N_1 & N_2 \end{bmatrix} \begin{bmatrix} u_{n,1} \\ u_{n,2} \end{bmatrix} = \mathbf{N}_{bar}\mathbf{u}_n. \tag{4.114}$$

The displacement shape functions N_1 and N_2 are linear functions, which can be formulated with the element length L_{el} as

$$N_1 = 1 - \frac{x}{L_{el}} \quad \text{and} \quad N_2 = \frac{x}{L_{el}}. \tag{4.115}$$

This dimensionless representation of the coordinate is also called natural coordinate. In Fig. 4.17, the courses of the displacement shape functions are illustrated. The strain-displacement matrix $\mathbf{B}_{bar}$ is given via an alternative formulation of the strain field $\boldsymbol{\varepsilon}_{bar}$ according to Eq. (4.61) as the derivative of the displacement field $u_p(x)$ with respect to x:

$$\begin{aligned} \boldsymbol{\varepsilon}_{bar} = \frac{\mathrm{d}u_p(x)}{\mathrm{d}x} &= \begin{bmatrix} \frac{\mathrm{d}N_1}{\mathrm{d}x} & \frac{\mathrm{d}N_2}{\mathrm{d}x} \end{bmatrix} \begin{bmatrix} u_{n,1} \\ u_{n,2} \end{bmatrix} = \begin{bmatrix} \frac{-1}{L_{el}} & \frac{1}{L_{el}} \end{bmatrix} \begin{bmatrix} u_{n,1} \\ u_{n,2} \end{bmatrix} \\ &= \mathbf{B}_{bar}\mathbf{u}_n \quad \text{with} \quad \mathbf{B}_{bar} = \frac{1}{L_{el}} \begin{bmatrix} -1 & 1 \end{bmatrix}. \end{aligned} \tag{4.116}$$

Because of the one-dimensionality and the linearity of the displacement shape functions of the element, the strain $\boldsymbol{\varepsilon}_{bar}$ is constant in the element. With Eq. (4.71) the element stiffness matrix $\mathbf{K}_{bar}$ can be determined as

$$\mathbf{K}_{bar} = \int_V \mathbf{B}^T\mathbf{D}\mathbf{B}\mathrm{d}V = EA\mathbf{B}^T\mathbf{B}\int_0^{L_{el}} 1\mathrm{d}x = \frac{EA}{L_{el}} \begin{bmatrix} 1 & -1 \\ -1 & 1 \end{bmatrix} \tag{4.117}$$

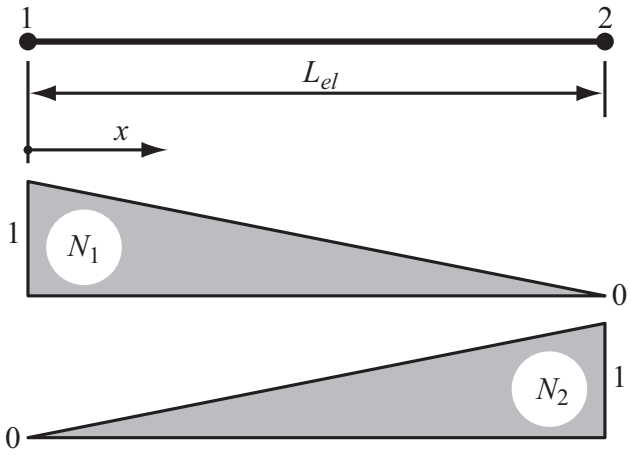

Figure 4.17.: One-dimensional bar element and displacement shape functions

assuming that the elasticity matrix $\mathbf{D}$, which is in the linear elastic case just Young's modulus E, and the cross-sectional area A are constant along x. In the case that the material response is non-linear also E behaves non-linearly. In Section 4.2 evolution laws for E of the used materials in terms of $\mathrm{d}\sigma/\mathrm{d}\varepsilon$ formulations are given, which correspond to tangential values of the stress-strain relation.

4.4.4.2. Bond element

The bond behaviour between the matrix and the reinforcement as well as between parts of the reinforcement is modelled with zero-thickness bond elements with two nodes. Therefor, a simplified implementation of the so-called bond-link element by [Ngo & Scordelis 1967], see Fig. 4.18 (a), is used. This element type was originally derived for plane problems and, thus, has displacement components parallel and perpendicular to the reinforcement direction, while the directions are decoupled. The element has no geometrical dimensions and introduces in principle only additional nodal forces to the model.

Due to the one-dimensionality of the model only the displacement components parallel to the reinforcement directions have to be regarded, which further simplifies the element, see Fig. 4.18 (b). The nodal forces of the element follow from the sum of forces in the equilibrium state

$$\begin{bmatrix} f_1 \\ f_2 \end{bmatrix} = \begin{bmatrix} -1 \\ 1 \end{bmatrix} T, \tag{4.118}$$

see also Fig. 4.19 (b), where T is the bond force, which can be calculated for the present model with

$$T = \tau S. \tag{4.119}$$

In this equation, τ is the bond stress and S is the bond surface area, which can be determined with

$$S = C \cdot L \tag{4.120}$$

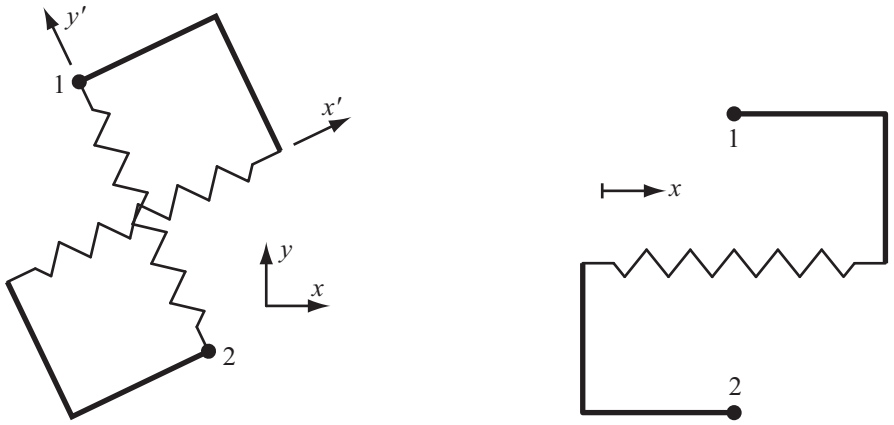

(a) Bond-link element according to [Ngo & Scordelis 1967]

(b) One-dimensional bond-link element

Figure 4.18.: Bond-link elements

where C and L are circumference and length of the bond surface area, e. g. corresponding to the segmentation approach in Section 4.1. In the present model, the bond stress τ is determined by means of bond stress-slip (τ-s) relations corresponding to Section 4.2.3, which contains the bond modulus G, yielding

$$\tau = G \cdot s. \tag{4.121}$$

With Eq. (4.119), the bond force can be formulated as

$$T = G \cdot s \cdot S. \tag{4.122}$$

The slip s, which is the input value for the τ-s relations, is given as the relative displacement of the two nodes of the bond element with

$$s = u_{n,2} - u_{n,1} = \begin{bmatrix} -1 & 1 \end{bmatrix} \begin{bmatrix} u_{n,1} \\ u_{n,2} \end{bmatrix}, \tag{4.123}$$

see Fig. 4.19 (a). With the Eqs. (4.118), (4.119), (4.123) and (4.121), the nodal forces can be described by the nodal displacements with

$$\begin{bmatrix} f_1 \\ f_2 \end{bmatrix} = \begin{bmatrix} -1 \\ 1 \end{bmatrix} \begin{bmatrix} -1 & 1 \end{bmatrix} \begin{bmatrix} u_{n,1} \\ u_{n,2} \end{bmatrix} \frac{\mathrm{d}\tau}{\mathrm{d}s} S = \frac{\mathrm{d}\tau}{\mathrm{d}s} S \begin{bmatrix} 1 & -1 \\ -1 & 1 \end{bmatrix} \begin{bmatrix} u_{n,1} \\ u_{n,2} \end{bmatrix} \quad \text{or}$$

$$\mathbf{f} = \mathbf{K}_{bond} \mathbf{u}_n \quad \text{with} \quad \mathbf{K}_{bond} = GS \begin{bmatrix} 1 & -1 \\ -1 & 1 \end{bmatrix}. \tag{4.124}$$

This corresponds to the notation for the element stiffness matrix of the bar element derived in the previous section, see Eq. (4.117). As the τ-s relation is usually non-linear, the bond modulus G has to be calculated with

$$G = \frac{\mathrm{d}\tau}{\mathrm{d}s}. \tag{4.125}$$

Therefor, the formulation of the bond law given in Section 4.2.3 can be used.

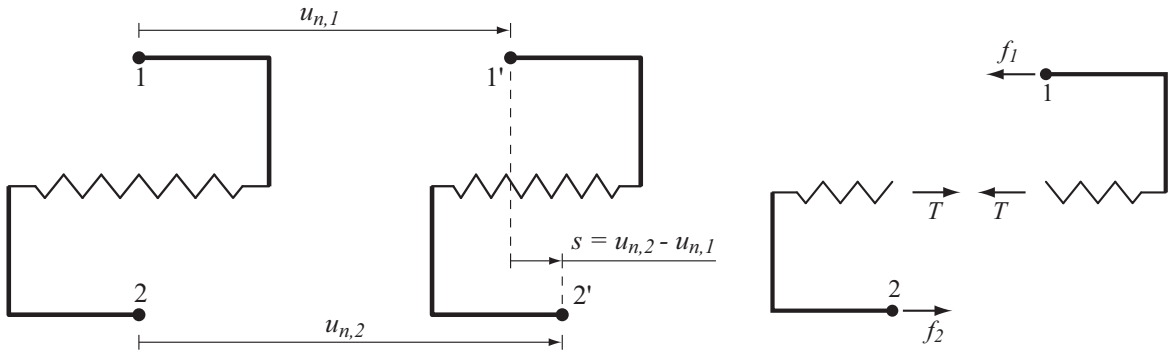

(a) Displacements of the bond-link element

(b) Forces at the bond-link element

Figure 4.19.: Displacements and forces of the one-dimensional bond-link elements

In the derived bond-link element, the bond stress is constant. Thus, a relatively fine discretisation of the bond layer is necessary to approximate the bond stress distribution in longitudinal direction of the model to a certain accuracy using this type of element. A coarser discretisation with less elements would be sufficient for the same accuracy using isoparametric bond elements with linear or higher-order displacement approaches, see [Keuser 1985] for a detailed parametric study. However, within this work the benefit from the possible reduction of the number of elements is not used as already for a proper representation of multiple matrix cracking, which is considered with the bar element chains, a relatively fine discretisation is necessary in the model. The appropriateness of the current approach was verified by [Konrad 2008]. In fact, the current formulation of the bond element is essentially the same as used by [Bruckermann 2007] and [Konrad 2008], compare Section 3.4.3. The only difference is that bond elements are not combined with a bar element as performed in the macro-element used in [Bruckermann 2007] and [Konrad 2008].

4.4.5. Structure and properties of the resulting stiffness matrix

The resulting system stiffness matrix of the model has special properties, which allow the application of efficient numerical methods to solve the systems of equations. As in finite element models usually not all nodes are linked mutually by finite elements, the resulting stiffness matrix is not completely allocated. It is rather the case that the stiffness matrix is filled sparsely, which means that there is a large number of zero entries compared to non-zero entries. As multiplications by zero always result in zero, it is desirable to reduce such operations as much as possible. Moreover, a great amount of computer memory can be saved if zero entries are not stored. It turns out that the system stiffness matrix is symmetric if the element stiffness matrices are symmetric. This is the case in the model under consideration, although it is not mandatory for FEM formulations. For both storage and mathematical operations, it is advantageous if the non-zero entries are concentrated close to the main diagonal, which results in a so-called band matrix. An important property of band matrices is the bandwidth β_t, which can be defined as

$$\beta_t = \beta_u + \beta_l + 1. \tag{4.126}$$

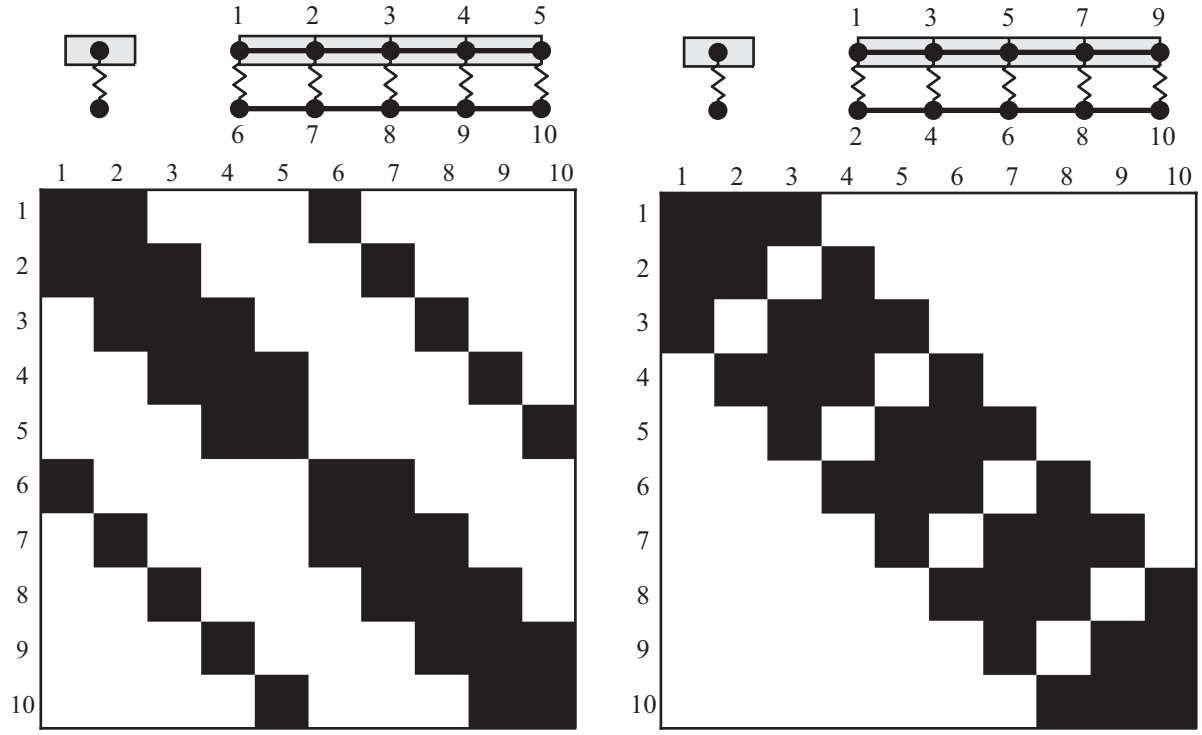

(a) Numbering in longitudinal direction (b) Numbering in transverse direction

Figure 4.20.: Allocation of stiffness matrix due to different numbering schemes (□ = 0, ■ ≠ 0)

The bandwidth consists of the upper bandwidth β_u and a lower band width β_l while the "1" is associated to the main diagonal. As the matrix is assumed symmetric, β_u is equal to β_l and can be determined for a matrix $\mathbf{A}$ of order $n \times n$ with entries a_{ij} as

$$a_{ij} = 0 \quad \text{if} \quad j > i + \beta_u \quad \text{or} \quad i > j + \beta_l, \tag{4.127}$$

see e. g. [Golub & van Loan 1996]. Thus, the upper and lower bandwidth correspond to the respective maximum index of diagonals, which contain non-zero entries. A densely allocated symmetric matrix of order n has a total band width of $\beta_t = 2(n-1)+1$.

For efficient storage and computations of and with the matrix it is advantageous when β_t is minimised. The allocation of the stiffness matrices in the FEM is controlled by the numbering of the degrees of freedom assigned to the nodes. As in the model under consideration every node has only one degree of freedom, which is the longitudinal displacement, the numbering of the nodes can be chosen corresponding to the degrees of freedom. Various numbering schemes might be employed. However, it it is advantageous for an efficient pre- and post-processing to choose a regular scheme as also the model has a regular structure. At least two major schemes exist, which are given with a consecutive numbering in longitudinal or transverse direction. Two respective basic examples corresponding to the segmentation scheme given in Fig. 4.2 are carried out for explanation, see Fig. 4.20. In Fig. 4.20(a), the numbering is performed in longitudinal direction. In contrast, a numbering in transverse direction is performed in the case shown in Fig. 4.20(b). It is observable that the bandwidth of the stiffness matrices differs considerably between the two numbering schemes. While in the longitudinal numbering scheme the bandwidth is $\beta_t = 2 \cdot 5 + 1 = 11$, in the transverse

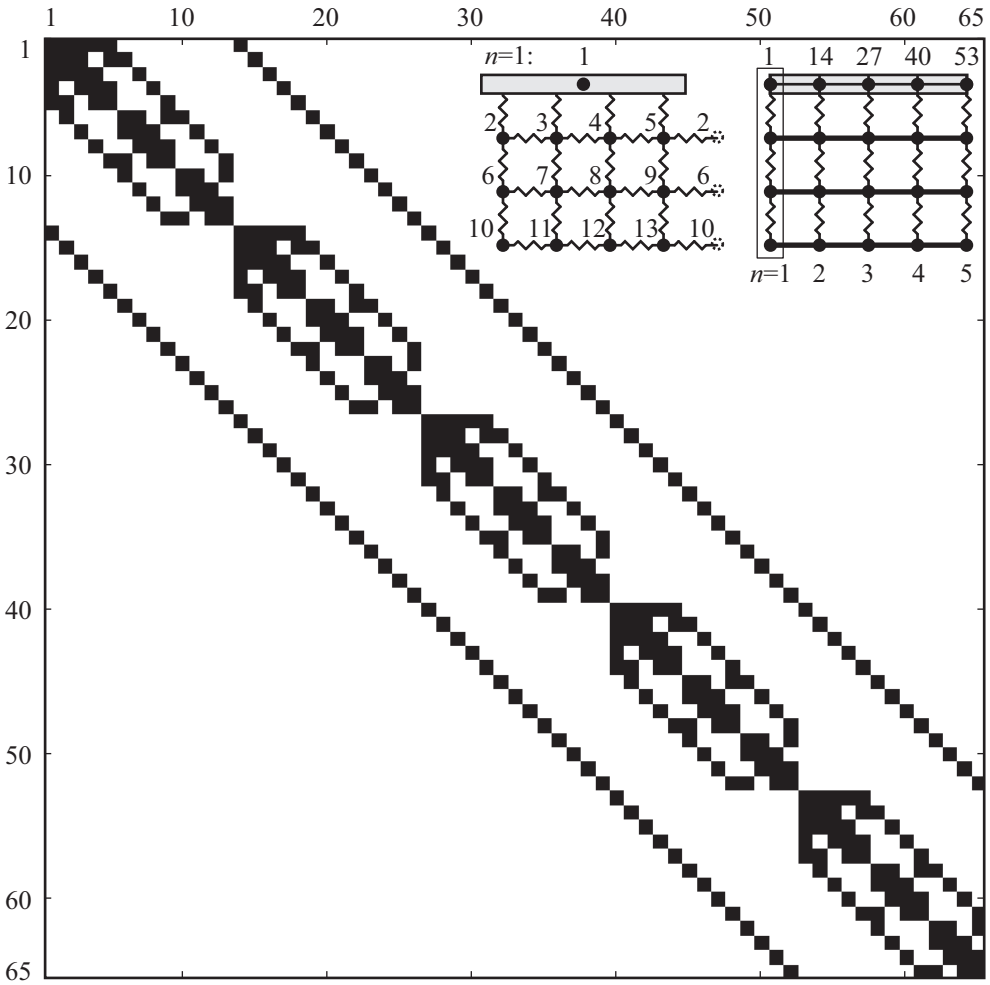

Figure 4.21.: Allocation of stiffness matrix according to the segmentation scheme

numbering scheme the bandwidth is only $\beta_t = 2 \cdot 2 + 1 = 5$. The reason is that the gap between the largest and smallest number of connected nodes is larger for the longitudinal numbering. Moreover, if more elements are arranged in longitudinal direction, the bandwidth increases further in the case of longitudinal numbering as the gap increases. This is not the case with the transverse numbering where the bandwidth remains constant when the number of elements in longitudinal direction is increased. Thus, transverse numbering is used in the following.

If the number of bar element chains is increased also the band width increases. A corresponding example is shown in Fig. 4.21, with a segmentation corresponding to Fig. 4.2. It can be seen that the compactness of the band is lost somewhat compared to Fig. 4.20(b), because in a transverse section less nodes have mutual connections. Interestingly, sparse bands exist between the central band and the outermost bands. It would be desirable to eliminate these sparse bands too. However, this seems impossible, at least with a regular numbering scheme, as the number of nodes in a transverse section is fixed and the minimum gap to the next transverse section, which is the number of bar element chains, is already achieved with the applied numbering scheme. A rearrangement of the node numbers in the cross section would only result in a rearrangement of the entries in the respective block in the stiffness matrix.

There are various storage techniques for sparse matrices. However, as detailed elaborations of this topic exist, e. g. in [Golub & van Loan 1996], [Schendel 1989] and [Silva & Wait 2005], it is not treated further. The same arguments apply also to special algorithms associated with sparse matrix computations. Respective literature is given e. g. with [Golub & van Loan 1996] and [Schendel 1989]. As already mentioned, an implementation of the "SuperLU" package by [Demmel et al. 1999] is used, conveniently.

4.5. Abilities and limitations of the model

In this chapter, a one-dimensional model was developed, which will be used in the subsequent parts of this work to analyse the material behaviour of TRC under predominantly tensile loading. The model consists only of two types of basic finite elements, bar elements and zero-thickness bond elements, which allows for a relatively variable creation of models for different material configurations where continuous reinforcement in the direction of loading is applied. The model is able to cover a broad range of experiments as for instance filament or yarn pull-out tests, but also tensile tests with multiple matrix cracking. However, effects from transverse strains, e. g. due to the Poisson effect or transverse loading, are not covered with the model, which also incorporates effects resulting from transverse reinforcement.

The model gains a lot of complexity from the implemented constitutive relations, which include effects like limited tensile strength of matrix and reinforcement, post-cracking resistance of the matrix, initial waviness of the reinforcement as well as non-linear bond laws. Furthermore, the constitutive relations contain also descriptions for unloading and reloading. This seems to be important for a proper representation of the material behaviour, because unloading and reloading might also occur locally in a monotonic loading regime, e. g. due to local stress redistributions in case of matrix cracking. Regarding the bond laws, it has to be noted that at the cost of a simple determination of geometrical parameters, the bond stress parameters, which have to be applied in the bond laws, will not correspond in general to those in reality. The bond stress values will have to be chosen larger than in reality because the bond surface areas are underestimated due the segmentation approach. An exception is the case of mono-filaments as reinforcement, as e. g. in a filament pull-out test, where a subdivision is unnecessary.

Nevertheless, an important feature of the model is that complex stress and strain distributions in matrix and reinforcement can be analysed, which is possible only with a few other models and can usually not be determined experimentally. Furthermore, material parameters can be varied independently of each other, which is also often not possible in experimental investigations. This allows the determination of the influence of single properties on the material response of the composite. An important feature of the model in its present form, is the ability of a stochastic modelling of the material parameters, which allows a more realistic simulation of the material behaviour. In particular, this enhances the significance of simulated results concerning degradation mechanisms and failure states.

5. Simulations and parametric studies

In this chapter, a number of simulations of different types of tensile tests regarding TRC are carried out applying the model established in the previous chapter. As already mentioned, the entire range of available tests as described in Section 2.3 is covered, i. e. filament and yarn pull-out tests as well as tensile tests with plate specimens and multiple concrete cracking. The main objective of these simulations is to improve the understanding of the load-bearing mechanisms in TRC. In this regard, the investigations were focussed on the tensile tests with multiple matrix cracking, which reflect the essential load-bearing behaviour of TRC as occurring in practical applications. The tensile load-bearing behaviour as observed in yarn pull-out tests depends strongly on the failure behaviour of the multi-filament yarns, which was not investigated in detail within the scope of the present work. Thus, the results of these simulations show yet particular deficiencies, which could be, however, resolved in future investigations. Nevertheless, the main characteristics of the load-bearing behaviour in this type of test can be already reproduced. The results of simulations of filament pull-out tests, which are presented in the next sections, show a good agreement with experimental results. Nevertheless, the relevance of these tests for the comprehension of the load-bearing behaviour of TRC is limited as already pointed out in Section 2.3.2. The results of the investigations concerning the pull-out tests are summarised at the end of the respective main sections. The respective results on tensile tests with multiple concrete cracking are recapitulated in the summary of the work.

5.1. Simulations of filament pull-out tests

As a starting point, the current section is concerned with the most basic material configuration in this context, which is one filament embedded in cementitious matrix corresponding to a filament pull-out test. Further simplifications arise from the constitutive laws. The material behaviour of the matrix and the reinforcement can be assumed linear elastic. Thus, matrix tension softening and reinforcement waviness has not to be considered. Moreover, matrix cracking and filament failure are not expected. Furthermore, the influence of scatter in the material properties is not taken into account. In the following, parametric studies regarding the influence of certain geometrical and material properties on the load-bearing response of the filament-matrix system are carried out.

5.1.1. Reference case

At first, a reference simulation is presented where the computed results coincide well with available experimental results as discussed in Section 2.3.2. The material parameters of the

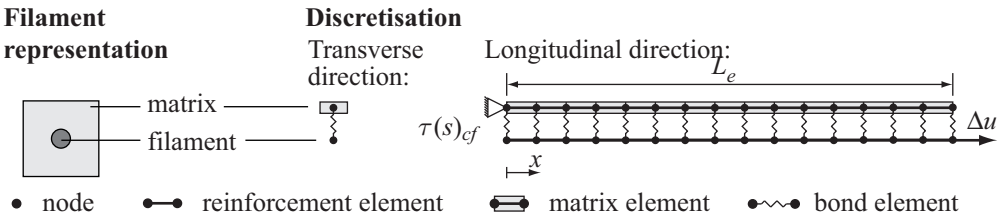

Figure 5.1.: Schematical model for the simulation of a filament pull-out test

matrix and the reinforcement, i. e. Young's moduli and tensile strength, are available from tensile tests. However, the definition of tensile strengths is unnecessary in this case as the occurring stresses are lower in both materials. Also the geometrical configuration is well defined as a mono-filament, which does not require a subdivision corresponding to Section 4.1, is embedded continuously in cementitious matrix. Thus, the only unknowns are the parameters of the bond law $\tau(s)_{cf}$ between the cementitious matrix and the filament, which is also the constitutive relation of the bond elements corresponding to Section 4.4.4.2. The parameters were calibrated such that the simulated force-displacement response showed good correspondence with available experimental results without aiming for a total minimisation of the gap between both. Bond law $\tau(s)_{cf}$ is shown in Fig. 5.3(b) with the supporting points marked with dots. For the simulation, the most basic configuration of the model is used. It consists of two bar element chains, one representing the matrix and the other one to represent the filament. At corresponding nodes both chains are coupled with zero-thickness bond elements. The boundary conditions are given with the fixation of the first node of the concrete chain and prescribed displacements Δu at the last node of the filament chain, see Fig. 5.1. The embedding length L_e of the filament is 1 mm and the cross-sectional areas of the filament and the matrix are $1.9{\cdot}10^{-4}\,\mathrm{mm}^2$ and $1\,\mathrm{mm}^2$, respectively. It is assumed that no free filament length L_f corresponding to Fig. 2.9(a) exists. The Young's modulus of the matrix is assumed with $28\,500\,\mathrm{N/mm}^2$ and of the filament with $79\,950\,\mathrm{N/mm}^2$. For the validation of the model, the simulated results are compared to experimental results of a filament pull-out test, see Fig. 2.10. The experimental results were already discussed in Section 2.3.2.

For the choice of the bar element length L_{el}, a parametric study is carried out. Therefor, the number of bar elements per chain n_{el} and accordingly L_{el} are varied. As bond elements are arranged at corresponding bar element nodes, also the number of bond elements varies corresponding to the number of bar elements. In Fig. 5.2, respective force-displacement relations are shown. The forces F and displacements Δu are recorded from the last node of the reinforcement chain where also the load is applied, compare Fig. 5.1. The best approximation can be expected with the finest discretisation, i. e. with the smallest bar element lengths. This is the case in Fig. 5.2 with $n_{el} = 1000$. It can be seen that for a very low number of elements $n_{el} = 1$ and $n_{el} = 2$, the F-Δu relations show constant parts, which significantly deviates from the course of the finest discretisation. The reason is that deformations and stresses are constant per element and, thus, the entire deformation state and correspondingly also the stress distribution state is only approximated in a very rough manner. The deviations decrease with increasing n_{el} and more importantly converge towards a certain state. For the case of $n_{el} = 500$ the F-Δu relation is virtually identical with those of $n_{el} = 1000$. However, as also computational costs increase with an increasing number of elements and the discretisation with $n_{el} = 100$ shows only marginal deviations to the case of $n_{el} = 1000$, a bar element length of 0.01 mm is chosen. This leads to 100 elements per bar element chain.

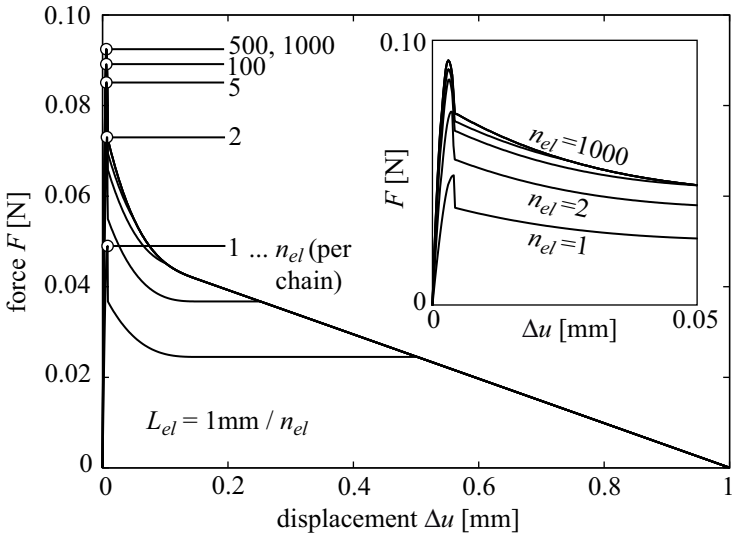

Figure 5.2.: Force-displacement relations for different discretisations

As it can be seen in Fig. 5.3(a), the model can reproduce the experimental force-displacement response although the parameters of the bond law are not tuned perfectly yet. The F-Δu relation initially increases until the maximum bond stress front reaches the end of the model at $x = 0$, see also Fig. 5.3(d). Subsequently, the force drops in Fig. 5.3(a) due to a sudden relaxation of the fibre and decreases further with increasing displacement of the filament. The course of the tail merges from a non-linear decrease to a linear decrease. The non-linear part is finished when the constant bond stress value of $1\,\mathrm{N/mm^2}$, see Fig. 5.3(b), is reached in all bond elements. The linear decrease results solely from the successive reduction of the bond surface area corresponding to algorithm associated with Eq. (4.28) and Fig. 4.8. Corresponding to the model length, the filament is completely pulled out at a displacement of 1 mm associated with a force of 0 N.

In Fig. 5.3(c), the stress distribution in the filament in x-direction with increasing displacement Δu corresponding to Fig. 5.3(a) is shown. As the coordinates of the integration points of the elements in the deformed state $x' = x + u_p$ are used where u_p is the displacement of the integration point, also the displacement state of the filament is observable. In similar fashion, the distribution of the bond forces is shown in Fig. 5.3(d). In Fig. 5.3(c), it can be seen that the stress in the filament at the pulled end is proportional to the applied force. Towards the opposite end of the filament the stress decreases to zero throughout the entire loading regime. Correspondingly, the transferred bond stress decreases from the pulled end to the free end at $x = 0$ before reaching the maximum pull-out force. Afterwards, the peak according to the maximum bond stress corresponding to Fig. 5.3(b) moves towards $x = 0$ while at the pulled end no further forces can be transferred over the interface because the filament is pulled out. The "pull-out front" where the filaments protrudes from the matrix can be also identified in Fig. 5.3(c) as the kinks in the stress profiles at discrete load levels Δu. The pull-out front is always situated at $x'_k \approx 1\,\mathrm{mm}$ as the matrix deformation is negligible and the pulled out length of the filament increases with increasing Δu. Vice versa, the bond length of the filament decreases with increasing Δu up to zero when the filament is completely pulled out, see Fig. 5.3(d).

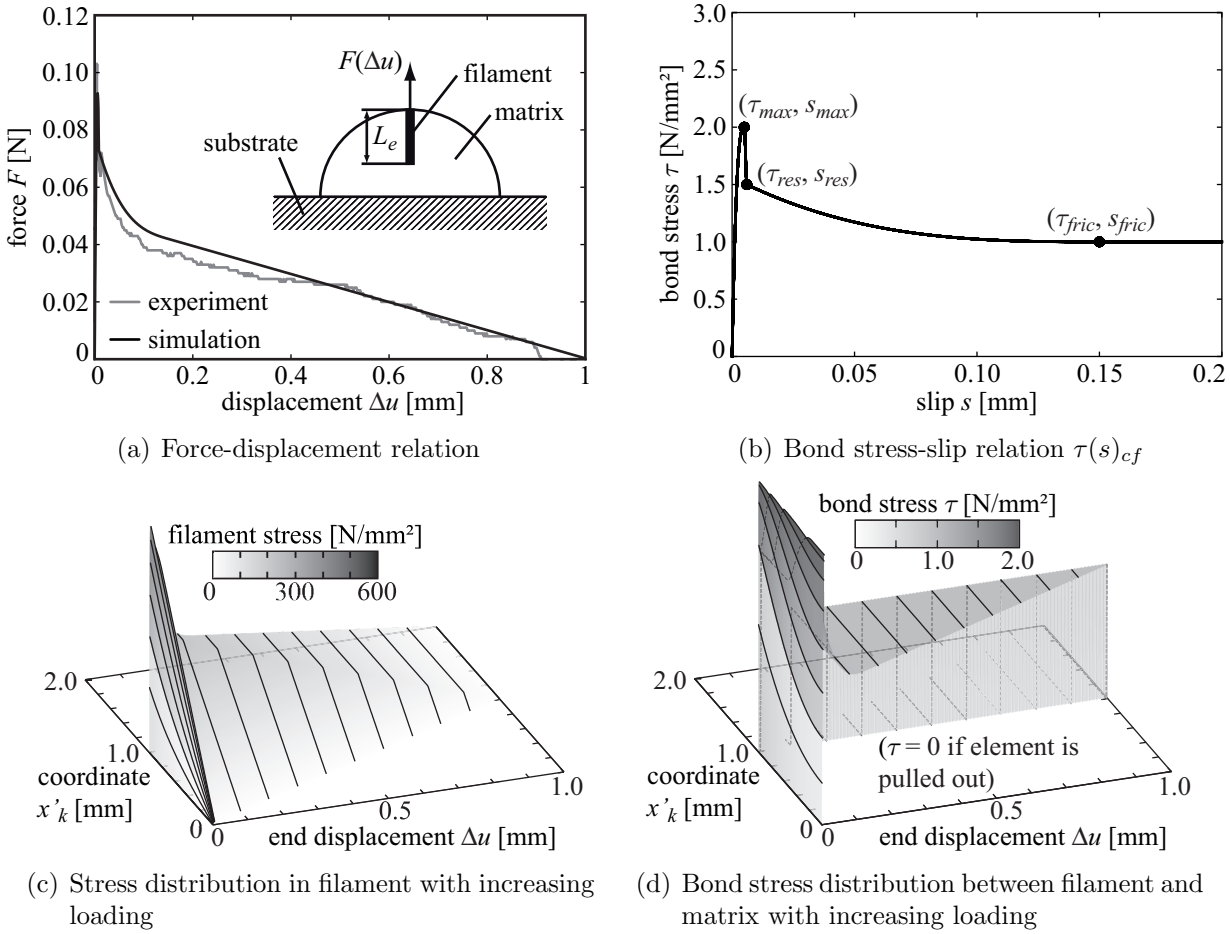

(a) Force-displacement relation

(b) Bond stress-slip relation $\tau(s)_{cf}$

(c) Stress distribution in filament with increasing loading

(d) Bond stress distribution between filament and matrix with increasing loading

Figure 5.3.: Simulated results and applied bond law for filament pull-out test

5.1.2. Influence of free length of not embedded filament parts

As already mentioned in Section 2.3.2, the F-Δu response in filament pull-out tests might be influenced by the position where the load is applied to the non-embedded part of the filament and the displacement is measured. Usually, a certain free length L_f exists between the position where the filament protrudes from the matrix and the position where the load is applied. Thus, besides the deformations of the embedded filament parts a certain linear elastic deformation of the filament along the free length exists, which changes the F-Δu response compared to the reference case in Section 5.1.1.

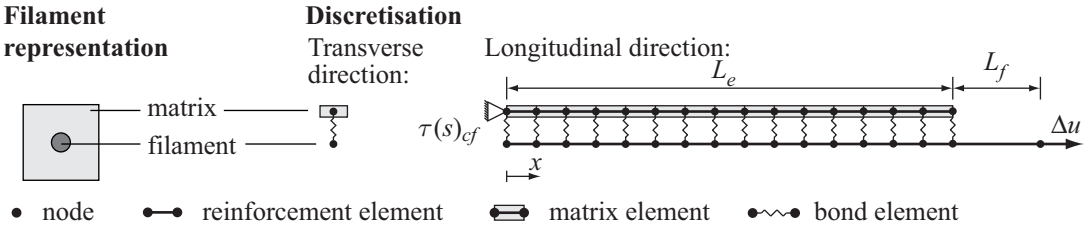

Figure 5.4.: Schematical model for the simulation of a filament pull-out test with a not embedded element

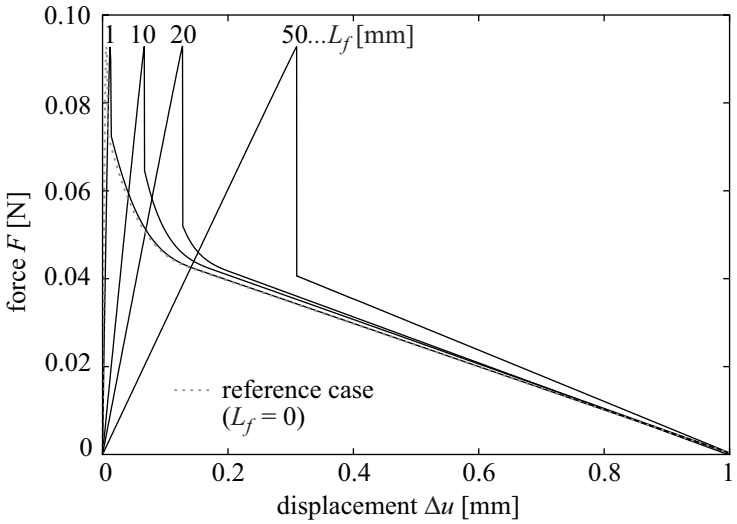

Figure 5.5.: Force-displacement relations for different free lengths L_f

To study this effect, one bar element of length L_f is added to the filament chain at the position where the displacement increments Δu are applied, see Fig. 5.4. All other parameters are chosen as in the reference case in Section 5.1.1. The free length L_f is varied in discrete steps in the range of 0 mm up to 50 mm. The case of L_f=0 mm, where the additional element was omitted, corresponds to the reference case in Section 5.1.1. In Fig. 5.5, the resulting F-Δu relations are shown. It can be seen that with increasing L_f the slope in the initially increasing range decreases because the system response is increasingly dominated by the linear elastic deformation of the free part of the filament. In contrast, the influence of the bond behaviour decreases. Another consequence is that the debonding of the matrix-fibre interface starts at increased filament end displacements Δu with increasing L_f while the maximum force is not influenced.

Furthermore, it can be seen that also the response in the "softening" range, after the maximum force has been reached, changes considerably with increasing L_f. The sudden stress drops become larger with increasing L_f and the smooth transition to the linear decreasing part corresponding to the decreasing part in the bond law in Fig. 5.3(b) shortens. The reason is that the elastic energy stored in the free filament part increases with increasing L_f. When the bond interface cannot resist a further load increase, the bar element (and also the filament) suddenly relaxes until equilibrium between the reduced force in the filament and the residual resistance of the bond interface is achieved. This leads occasionally also to problems in the numerical solution of the non-linear FEM equations and necessitates tuning of the step length parameters and the residual tolerance as described in Section 4.4.3 to find a proper solution. It can be expected that also time-dependent effects appear when the elastic energy is released, which are more pronounced with increasing L_f. However, an analysis of time-dependent effects is beyond the scope of the current investigations and only static analysis is performed. The effect of sudden relaxation is also known as snap-back effect. At least theoretically, F and Δu can be simultaneously reduced and the snap-back path can be traced. Numerically, so-called path-following techniques[1], also referred to as arc-

[1]Essential contributions on this topic were published e. g. by [Riks 1979], [Crisfield 1981] and [Ramm 1981].

length methods, can be applied to trace the snap-back response. However, as no experimental counterpart for comparison exists, respective numerical investigations are of reduced practical importance and, thus, it remains unconsidered. The sudden stress drop in the experimental force-displacement relation, compare the detail in Fig. 2.10(b), indicates that this effect appeared also in the test under consideration, which means that a free filament length did exist.

For the case of L_f=50 mm, F drops directly to the linearly decreasing part, which masks the non-linear part in the bond law entirely. Also for shorter L_f, the non-linear part is truncated considerably. Vice versa, this means that the determination of the bond law parameters will be improper if an existing $L_f > 0$ remains unconsidered. Obviously, this applies also to the bond law used in Section 5.1.1 as certainly a free filament length $L_f > 0$ existed in the respective experiments but was not reported. Unfortunately, it seems as if it is impossible to determine the bond law parameters completely proper (within the limits of a model), also in the case that L_f is known. The reason is that the snap-back response is not traced in the experiments. However, the error can be minimised with very short free lengths L_f.

5.1.3. Influence of the embedding length of the filament

Besides the free length L_f also the embedding length L_e influences the F-Δu response of filament pull-out tests. Therefor, a parametric study with a model corresponding to the reference case as described in Section 5.1.1 is carried out where only L_e is varied. This leads also to a variation of the number of finite elements as the bar element length is kept constant.

In Fig. 5.6, respective F-Δu relations are shown. As it could have been expected the maximum force increases with increasing L_e because also the transferable total force over the interface between matrix and filament increases. If a tensile strength is applied for the filament, the maximum force level is limited. In Fig. 5.6, such a limit is given for an arbitrary filament tensile strength f_{ft} of 1000 N/mm^2. The respective ultimate force can be determined as $F_{ult} = f_{ft} \cdot A_{fil}$. In this case, the filament will fail before being pulled out if the embedding

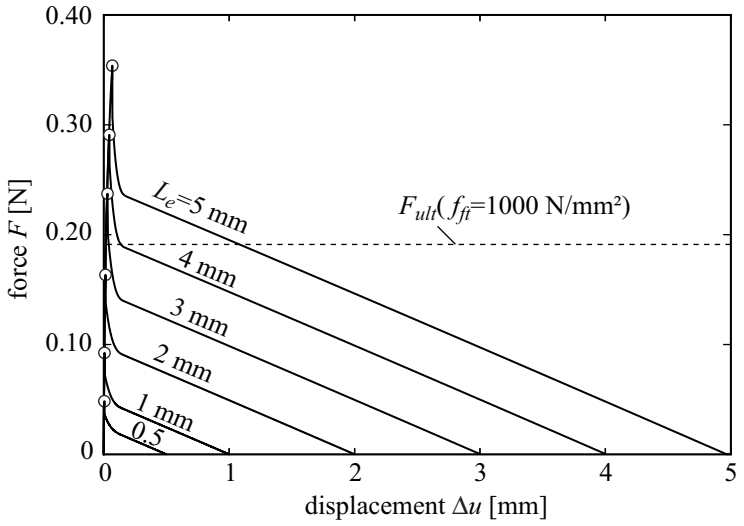

Figure 5.6.: Force-displacement relations for different embedding lengths L_e

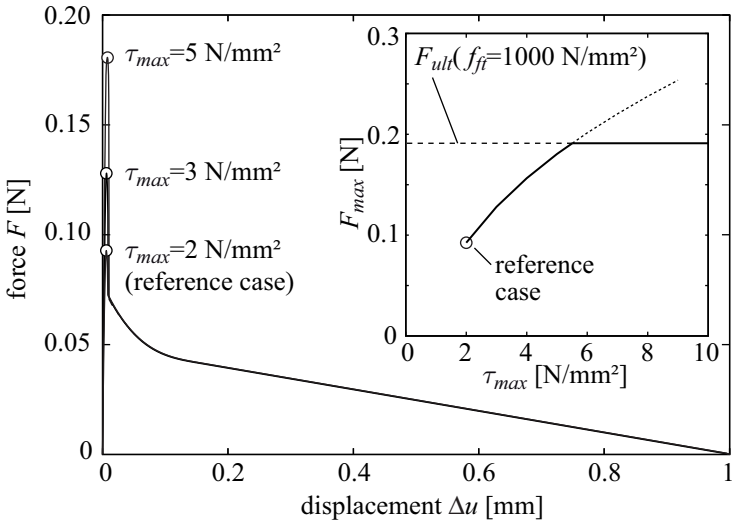

Figure 5.7.: Force-displacement relations for different bond strength values τ_{max}

length is larger than about 2 mm. Similar to the case of increasing L_f in the previous section, the elastic energy stored in the filament increases also with increasing filament length or L_e, respectively. If the bond strength front reaches the embedded end of the filament at $x = 0$, the applied force cannot be resisted any longer and, thus, the force drops after the maximum force is reached. The force drops are larger for long embedding lengths because the released elastic energy is larger compared to short embedding lengths. Thus, the next equilibrium state is reached after a force drop, which increases with increasing L_e. The release of elastic energy gives again also rise to snap-back effects as discussed previously. The pull-out regime is with increasing L_e stronger dominated by reducing frictional load transfer due to a reduction of the bond surface area. This results in linearly decreasing F-Δu relations. Only at the very beginning of the pull-out regime, a non-linear course is observable because of the smooth transition to the constant frictional bond stress in the bond law, see Fig. 5.3(b).

5.1.4. Influence of variation of bond law parameters

Although it was pointed out in Section 5.1.2 that it is not possible to determine the bond laws completely proper, it can be assumed that the effects of the errors in the bond law parameters are rather small compared to the scatter in experimental results. Hence, assuming that the used bond laws reflect the essential characteristics, it might be valuable to know how certain parameters influence the F-Δu response of the filament-matrix system. As there exists a vast number of parameter combinations, only a limited selection based on the bond law shown in Fig. 5.3(b) is considered.

In a first parametric study, the bond strength τ_{max} is varied. All other parameters, are defined as in the reference case. In the F-Δu relations, which are shown in Fig. 5.7, the maximum force F_{max} and the initial stiffness increase with increasing τ_{max}. The relation between F_{max} and τ_{max} is non-linear for this bond law as it can be seen in the inset of Fig. 5.7. Of course, the tensile strength of the filament will be reached at a certain τ_{max} leading to filament failure at a certain ultimate force F_{ult} before pull-out can occur. In the inset of Fig. 5.7, the ultimate force level for an arbitrary filament tensile strength f_{ft} of 1000 N/mm^2 is shown again. Thus,

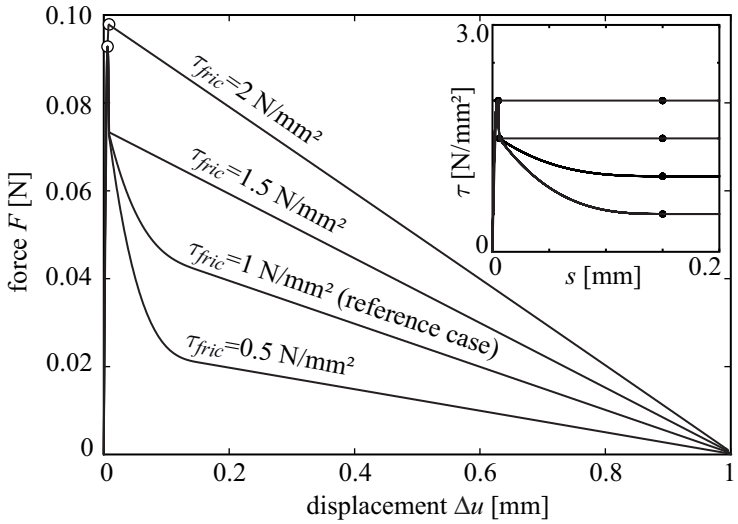

Figure 5.8.: Force-displacement relations for different frictional bond stress values τ_{fric}

the increase of F_{max}, which can be reached with an increase of bond strength, is limited by the tensile strength of the filament. The relation shown in the inset of Fig. 5.7 is specific for the used parameter combination, but can be established also for other combinations, of course. Moreover, the "softening" ranges in the F-Δu relations in Fig. 5.7 are only influenced until the bond stress value τ_{res} at s_{res} is reached, which is characterised by a kink in the F-Δu relation. Thus, a variation of s_{res} will lead to a respective variation of the Δu-value of the kink while a variation of τ_{res} will result in a variation of its F-value.

Finally, a parametric study regarding the influence of the frictional bond stress τ_{fric} is carried out. Again, only τ_{fric} is varied while all other parameters are chosen as in the reference case. The applied bond laws are shown in the inset of Fig. 5.8, which shows also the resulting F-Δu relations. The transferable frictional bond stress influences already the maximum force. The larger τ_{fric} is, the larger is also the maximum force because the interface between matrix and filament is already in the frictional regime at the pulled end while the load is still transferred via adhesion at the embedded end at $x = 0$. However, this effect appears only significantly in the current simulations for the case of τ_{fric}=2 N/mm^2. The decreasing courses in the pull-out regime show qualitative and quantitative differences, which result from the different courses in the bond laws, see the inset in Fig. 5.8. For τ_{fric} values of 0.5 N/mm^2 and 1 N/mm^2, the F-Δu relations decrease initially non-linear according to the bond law characteristics. Afterwards, they merge to a linear course when the constant bond stress range is reached and only the bond surface area reduces. In the bond laws where τ_{fric} are 1.5 N/mm^2 and 2 N/mm^2, the gradual transition between τ_{res} and τ_{fric} is missing. This results in the F-Δu relation for τ_{fric}=1.5 N/mm^2 to an immediate steep decrease after the maximum force state and a subsequently linearly decreasing course. For the case of $\tau_{fric} = \tau_{max}$=2 N/mm^2, the decreasing part of the F-Δu relation has a linear course due to the reducing bond surface area.

Hence, if the bond law is assumed not to change along x, i. e. no local variations e. g. due to material inhomogeneities are considered, the parameters of the bond laws can be readily identified. Shifts of the τ values of the supporting points lead to a shift of the respective F values in the F-Δu relation while shifts of the s values result in shifts of the Δu values.

5.1.5. Remarks on the simulations of the filament pull-out tests

As it was pointed out in the previous sections, the experimental results might be misleading if the test setup is not considered as a whole. Leaving for instance a free filament length unconsidered results in an improper determination of the bond law if the experimental results are used for calibration. Even worse is the case when certain characteristics of the bond law are masked by snap-back effects due to an elastic relaxation of the filament. Thus, it can be recommended to reduce the free filament length in experiments as much as possible. Further influences on the force-displacement response, which were not studied, might also result from slipping of the filaments in the clamps where load is applied and a limited stiffness of the clamps of the testing machine. However, the experimental results are valuable for a quantitative determination of the bond strength and also a qualitative assessment of the debonding behaviour is possible. This is for instance important for an evaluation of the effectiveness of an additional coating for bond improvement, see e. g. [Gao et al. 2004].

As already mentioned, the case of one filament embedded almost perfectly in cement paste reflects the complex situation in a multi-filament yarn only in a very simplified manner. Thus, the presented investigations shall be considered primarily as a proof of applicability of the model to filament pull-out tests. Further investigations on this topic might be, of course, interesting. In this respect, the presented model offers an efficient analysing tool, which can be used, e. g., to study the influence of complex bond characteristics where analytical models usually reach their limits. Moreover, also tests with modified boundary conditions as e. g. the test shown in Fig. 2.9(b) or filament pull-through tests can be studied. However, in the following investigations regarding multi-filament yarns, only limited benefit can be taken from these results.

5.2. Simulations of yarn pull-out tests

In the current section, simulations of yarn pull-out tests corresponding to the experiments by [Butler 2009], see Section 2.3.3, are presented. The complexity of the model increases compared to the simulation of filament pull-out tests because the reinforcement is composed in this case of a large number of filaments. Moreover, the bond laws cannot be assumed constant over the cross section due to the varying penetration of the yarns with matrix or coating. The successive failure of filaments due to the stochastic character of the tensile strength has to be taken into account in the model, as well. As it will be seen in the subsequent sections, a fine subdivision of the reinforcement resulting in a large number of segments is necessary to represent the successive failure behaviour of the reinforcement and the load-bearing response of the specimen appropriately. Thus, long computation times occur. As the simulations of yarn pull-out tests were not the main objective of the work, only a relatively low number of parametric studies were carried out and the presented results serve primarily as a proof of concept.

5.2.1. Estimation of appropriate bar element length and number of reinforcement layers

At first, a parametric study to estimate an appropriate length of the bar elements is carried out. Therefor, a model with geometrical properties according to the specimen in the experiments by [Butler 2009], see Fig. 2.11(b), is used. The waisting of the specimens is reflected in the model by a stepwise variation of the cross-sectional areas of the bar elements of the concrete chain in the respective zones, see Fig. 5.9. Furthermore, a notch is applied in the model at x=0.1 m corresponding to the centre of the specimen by means of a reduction of the cross-sectional area of the respective concrete bar elements to ensure the development of the concrete crack at this position. In the model, it cannot be taken advantage of the symmetric geometry of the specimen because reinforcement failure events occur at both sides distant to the concrete crack at the notch. Thus, the first failure of a reinforcement element, which will occur in general distant to the crack if scattering material properties, e. g. the tensile strength, are considered, destroys the symmetry of the system. The boundary conditions are given with the fixation of the first node of the concrete chain at x=0 and prescribed displacements of Δu=2 mm applied incrementally to the last concrete node at x=L=0.2 m. The support of the specimen by means of glued steel plates is not taken into account in the model because the influence on the load-bearing and failure behaviour, which occurs in sufficient distance to the load application, is insignificant.

The reinforcement, which is given with three yarns each consisting of 800 filaments and having a mean cross-sectional area of 0.11 mm^2, is subdivided arbitrarily, at first, into five layers where each layer is further divided into four segments. The outermost reinforcement layer, referred to as sleeve layer, represents the filaments in the fill-in zone embedded in concrete, which are assumed to share their load uniformly, or in other words globally, while the remaining four layers represent the filaments in the core of the yarn where local load sharing between the filaments is assumed due to the weak frictional stress transfer. It is assumed that 36 % of the cross-sectional area of the yarns, which corresponds to a thickness of the sleeve layer of 20 % of the radius of a yarn corresponding to the segmentation approach in Section 4.1, are situated in the fill-in zone while the remainder represents the core. This ratio is chosen corresponding to results of microscopic investigations of transparent cuts of yarns embedded in fine-grained concrete in [Jesse 2004]. With the assumptions of equal radial thicknesses of the reinforcement layers representing the core and equal segment sizes in a layer, the cross-sectional areas and bond surface areas can be determined according to Section 4.1. As a result of the simulations, force-displacement (F-u) relations can be generated corresponding to the experimental results. Therefor, the force F is determined as reaction force at the concrete node at x=0. The relative displacement u is determined between the two concrete nodes with a distance of 10 mm over the centre of the notch, see Fig. 5.9.

In the reference simulations, the material properties of the concrete and the reinforcement are modelled deterministically. Thus, spatial fluctuations of material properties are not taken into account. Furthermore, the material behaviour of concrete and reinforcement is modelled linear elastic with a limited tensile strength for the concrete. Non-linearities like concrete tension softening and yarn waviness remain unconsidered. The Young's modulus of the concrete is defined corresponding to [Jesse 2004] with 28 500 N/mm^2 and the concrete

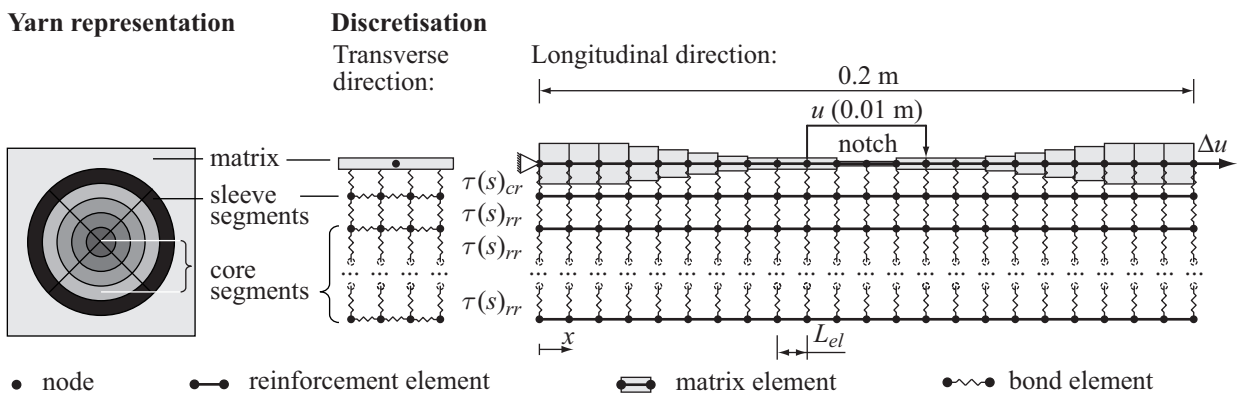

Figure 5.9.: Schematic model for the simulation of a double-sided yarn pull-out test

tensile strength with 5 N/mm^2. The Young's modulus of the reinforcement is defined with 79 950 N/mm^2 according to [Abdkader 2004], compare also Section 2.1.2. In the simulations for the estimation of an appropriate bar element length, it is assumed that the reinforcement does not fail. The bond between the sleeve layer and the concrete as well as between the segments of the sleeve layer is modelled with the bond law $\tau(s)_{cr}$ while the bond between the reinforcement layers and the segments of the core layers is modelled with a bond law $\tau(s)_{rr}$, see the inset of Fig. 5.10. It is assumed for bond law $\tau(s)_{cr}$ that the filaments represented by the sleeve layer have initially adhesive bond to the concrete, which merges after exceeding of a bond strength to friction. The force transfer within the reinforcement is assumed to occur primarily in a frictional manner due to a low number of adhesive cross-linkages failing soon after activation between the filaments leading to the qualitative course of bond law $\tau(s)_{rr}$, see also Section 2.3. The bond law parameters were adopted from simulations of tensile plate specimens with multiple cracking corresponding to Section 5.3 where satisfactory results with these parameter combinations were achieved. Moreover, a successive pull-out of the reinforcement layers at the notch and a pull-in at the ends of the concrete chain modelled according to Section 4.2.3 is taken into account.

In Fig. 5.10, F-u relations as results of simulations with different bar element lengths and correspondingly different numbers of elements are shown. The pre-cracking state is represented in all simulations almost identically. However, significant differences in the F-u relations are observable after the concrete has cracked at the notch. It is again assumed that the best approximation is achieved with the finest discretisation, which corresponds to the case of L_{el}=0.1 mm. In this case, the post-cracking response shows a smoothly increasing F-u relation where the slope successively decreases with increasing u. With larger applied displacements, the reinforcement will be pulled out because of neglecting a tensile strength of the reinforcement. However, corresponding simulations were not performed. For the coarsest discretisation (L_{el}=5 mm), it can be seen that the post-cracking F-u relation shows a number of force drops, which result from the coarse, element-wise constant approximation of the stress field combined with a successive pull-out of the reinforcement strands at the crack. For L_{el}=1 mm, the force drops are significantly reduced but still appearing. For L_{el}=0.5 mm and L_{el}=0.2 mm, the F-u relations are visually identical with the relation for the finest discretisation (L_{el}=0.1 mm). Thus, it is sufficient to use a bar element length of L_{el}=0.5 mm in the following simulations. For the explanation of the experimental F-u response, see Fig. 2.12, it is also interesting that the initial non-linear increase after the concrete has cracked, appears

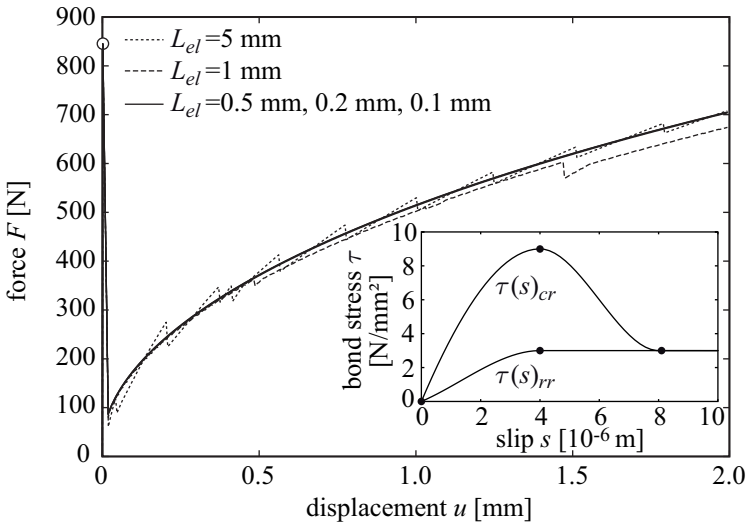

Figure 5.10.: Force-displacement relations of yarn pull-out simulations with different bar element lengths

already without consideration of successive reinforcement failure. This suggests that it is a result of the existing bond characteristics and the successive pull-out of the filaments at the crack. To reproduce the decreasing part of the experimental F-u relation, consideration of filament failure seems to be crucial, especially when the decrease shall start at relatively low displacements. Otherwise, a decrease in the post-cracking range can also be achieved with reinforcement pull-out, which incorporates larger displacements and necessitates high filament tensile strength.

At the beginning of this section, five reinforcement layers with one sleeve layer and four core layers were chosen arbitrarily for the discretisation of the reinforcement. A further parametric study was performed to investigate the influence of the number of layers on the tensile response in the yarn pull-out test. Therefor, a model with a bar element length L_{el}=0.5 mm was used where only the number n_{core} of layers representing the core is varied from 1 to 9. It was still assumed that the core layers have equal layer thickness. The F-u relations show for $n_{core} \geq 2$ virtually no differences compared to the respective F-u relation with L_{el}=0.5 mm and n_{core}=4 shown in Fig. 5.11. However, the stress distributions in concrete and reinforcement are different for each n_{core}, of course. Similar investigations with different n_{core} on tensile specimens with multiple concrete cracking, presented in Section 5.3.1.2, revealed that the changes in the stress distributions due to different n_{core} are small for $n_{core} \geq 4$. Thus, the original choice of one sleeve layer and four core layers is retained for the following investigations.

5.2.2. Influence of reinforcement layer subdivision

In the previous section, reinforcement failure was neglected, although it has obviously a large influence on the F-u relation after the crack in the concrete has occurred. Thus, in this section reinforcement failure due to a limited tensile strength f_{rt} is taken into account while the other model parameters are chosen as defined in the previous section. The assumption of a deterministic f_{rt} uniform for all reinforcement layers will obviously lead to an unstable, brittle

failure of the reinforcement once f_{rt} is reached in one reinforcement segment as the relocation of loading leads to even higher stresses in intact segments. Thus, a stochastic description of f_{rt} is necessary. Although the random field implementation according to Section 4.3.2 is at hand, a "purely" random distribution of the tensile strength in longitudinal direction x is assumed for all segments. The reason for this approach is that a potentially existing correlation length resulting from the atomic structure of the glass has to be assumed of several magnitudes lower compared to the applicable length of a bar element in the model. Thus, also if correlation between neighbouring material points might exist, it would not take effect in the model.

In the model, a two-parametric Weibull distribution, see Appendix A.3, of the filament tensile strength with an expected value of $2200\,\mathrm{N/mm^2}$ and relative standard deviation of about $25\,\%$ is assumed, which corresponds to investigations by [Curbach et al. 2006]. The random modelling of the tensile strength necessitates the performance of a series of computations within a Monte-Carlo type simulation to achieve results of a certain confidence level. However, as it is only intended to show the applicability of the model for the simulation of yarn pull-out tests, only results of exemplary computations are shown. In the simulations, cracking of concrete elements and failure of reinforcement elements are aspired to be restricted to one event per load increment. After the cracking or failure event, the system is recalculated at the same load level with the Young's modulus of the respective element set equal to zero. Due to a large number of reinforcement segments and the load relocation, often several elements fail simultaneously in one load increment. If this is the case, the load is tried to be reduced in an adaptive manner such that the stresses are below the respective strengths in all elements. If a pre-defined lower limit of reduction is reached, simultaneous failure of several reinforcement elements is, however, accepted.

It can be expected that the subdivision of the reinforcement layers influences the simulated failure of the reinforcement. With a low number of segments, which have a relatively large cross-sectional area, a more brittle response might be expected because the elastic energy stored in the respective chain is large and the relocation onto the remaining segments leads to higher loading compared to a large number of segments with low cross-sectional areas. This effect is investigated in a parametric study where the number of segments per reinforcement layer is varied. Four simulations with subdivisions into 4, 10, 20 and 40 segments per layer were carried out. The computation time increases considerably with an increasing number of segments because both the algebraic system of equations of the finite element model and the failure events increase. For the simulations with 5×40 segments, the computation time was about one week, which also illustrates why a Monte-Carlo type simulation can not be conveniently performed with the model in its current form.

In Fig. 5.11, the simulated and a corresponding experimental F-u relation corresponding to [Butler 2009] are shown. At least qualitatively, the main characteristics of the experimental results are reproduced with the model. One of these characteristics is an initially increasing relation until the tensile strength of the concrete is reached at the notch, which is followed by a stress drop. The maximum force is underestimated in the model. The reason is that either the concrete tensile strength or the cross-sectional area of the concrete at the notch, or both, are underestimated compared to the specific experiment. However, also the experimental results show large scatter especially concerning the force where the concrete cracks. Thus, an optimisation of the respective model parameters will not significantly improve the quality

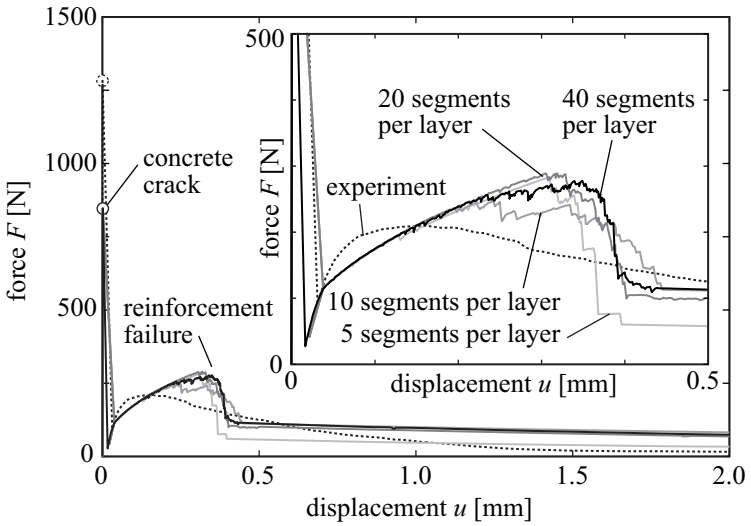

Figure 5.11.: Force-displacement relations of yarn pull-out simulations with different subdivisions of the reinforcement layers

of the simulated results. After the stress has dropped, the F-u relation increases again due to the activation of the reinforcement. The increase is stronger in the experimental results compared to the simulations, which indicates an underestimation of the bond stiffness in the model. As already recognised in the previous section, the non-linear increasing course of the F-u relation is at least partly a result of the non-linear bond stress-slip relations. Nevertheless, also the first reinforcement failure events occur already before the second force maximum is reached, which is described in more detail in the next section. The reinforcement failure starts in the sleeve layer because of the strong bond to the concrete and proceeds to the core of the reinforcement where longer transfer lengths are needed to reach sufficiently high stresses for filament failure because of the weaker bond.

With the applied number of yarns, the maximum force in the post-cracking state is considerably lower compared to the force level where the concrete cracked, which is also the reason why no further concrete cracks occur. In all simulations, the force corresponding to the second maximum is overestimated compared to the experiment. In the simulations, a distribution function for the reinforcement tensile strength corresponding to filament tensile tests, see Section 2.1.2, is used. This indicates for the experiments that the tensile strengths of the filaments embedded in the concrete are reduced compared to filaments before embedded in concrete. This might result from additional flaws introduced to the filaments during the processing, which might be amplified due to chemical reactions in the concrete. Regarding the different simulations no significant differences in the values of the second force maximum are observable. However, only one simulation for each case is presented. It can be supposed that the deviations in the results for different realisations of the scattering reinforcement tensile strength increase with decreasing number of reinforcement segments because the influence of one failing reinforcement segment on the behaviour of the entire reinforcement increases.

After the second maximum in the F-u relation is reached, a relatively steep decrease is observable, see Fig. 5.11. In all simulations, the decrease is much steeper compared to the experiment. The steepest decrease is observable for the coarsest subdivision. However, it has to be taken into that only one simulation for each case is shown. As already supposed, the

reason is that with the failure of one segment a larger amount of cross-sectional area of the entire yarn is lost with a decreasing number of segments. Thus, the remaining intact segments are higher loaded, which leads to earlier failure of the intact segments compared to a fine discretisation. As a consequence, the F-u relations become smoother with increasing number of reinforcement segments. A significant change in the failure behaviour of the reinforcement is, however, not observable. The steep decrease is supposedly a result of the assumed constant bond law $\tau(s)_{rr}$ between the reinforcement layers. A successively decreasing frictional bond stress towards the innermost core layer might delay the failure of the inner segments. This is studied in the next section. Moreover, filament waviness might lead to larger displacements in the softening range and a less brittle failure. However, this will supposedly decrease the initial slope of the F-u relation in the reloading regime after the concrete crack. Furthermore, also bond degradation and tensile strength distribution of the reinforcement influence the behaviour in the post-cracking regime.

Besides these effects also pull-out of the reinforcement leads to a reduction of the force with increasing displacement. If the transferable forces and the transfer length in the yarn cores are too small to reach the tensile strength also pull-out of entire filaments can occur in the experiments. However, this is not the case in the present simulation as in every reinforcement chain corresponding to the segments at least one element fails. In the simulations, failure of reinforcement elements is finished at a deformation $u < 0.5\,\text{mm}$. The positions of the failed bar elements are usually in some distance to the concrete crack as tensile strength minima are usually not situated at the position of the cracked concrete element. This topic is covered more detailed in the next section. Thus, the almost linearly decreasing course for $u > 0.5\,\text{mm}$ results from successive pull-out of remaining intact reinforcement pieces bridging the crack. The slower decrease in the simulation compared to the experiment might result from an overestimation of the frictional bond stress and failure positions in a too large distance to the concrete crack. Due to a number of simultaneous effects, it is difficult to determine the influence of these effects solely from the F-u relation.

5.2.3. Influence of varying bond between the reinforcement layers

In the previous section, it was argued that a main source of the relatively brittle failure of the reinforcement in the simulation is the assumption of a constant bond law $\tau(s)_{rr}$ between all reinforcement segments. Therefor, another simulation is performed with a successively decreasing bond quality towards the centre of the reinforcement yarns. In contrast to the previous parametric studies, the bond laws are applied with successively decreasing bond stress values towards the innermost core layer as shown in Fig. 5.12(a). For the simulation, each reinforcement layer is subdivided into 40 segments where neighbouring segments are connected by bond elements with respective bond laws corresponding to Fig. 5.12(a). All other parameters correspond to the reference case as defined in Section 5.2.1.

Fig. 5.12(b) shows the F-u relation as a result of the simulation. Until reaching the second force maximum in the F-u relation no significant differences are observable compared to the respective results with constant bond laws between the reinforcement layers. Nevertheless, the reduction of the bond quality leads to a slower decrease of the force with increasing deformation in the softening range, compare Figs. 5.12(b) and 5.11. This can be explained

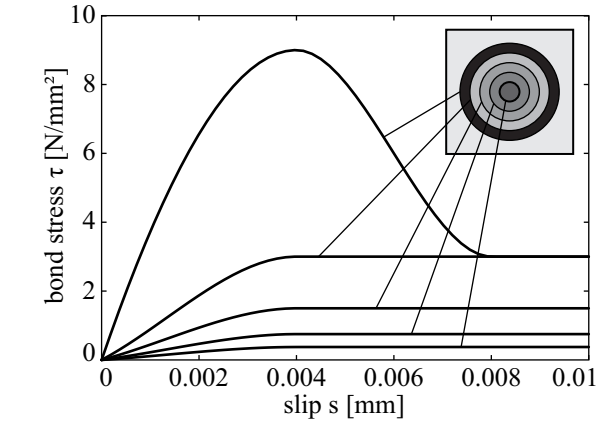

(a) Bond stress-slip relations

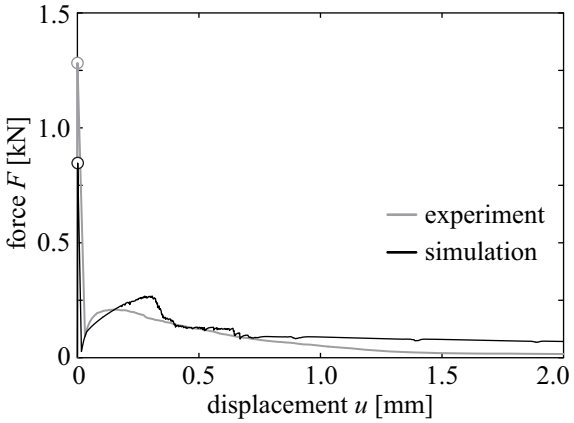

(b) Force-displacement relation

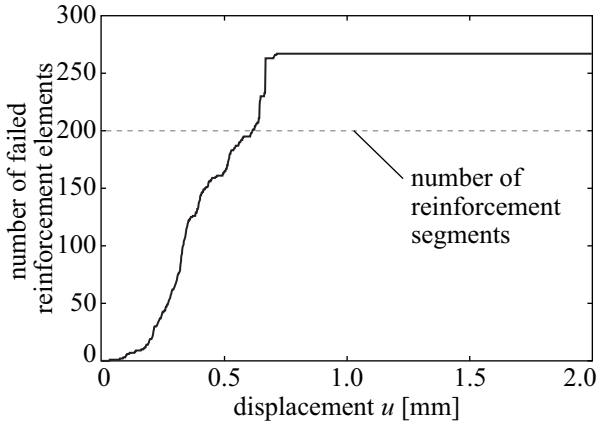

(c) Number of reinforcement failure events with increasing loading

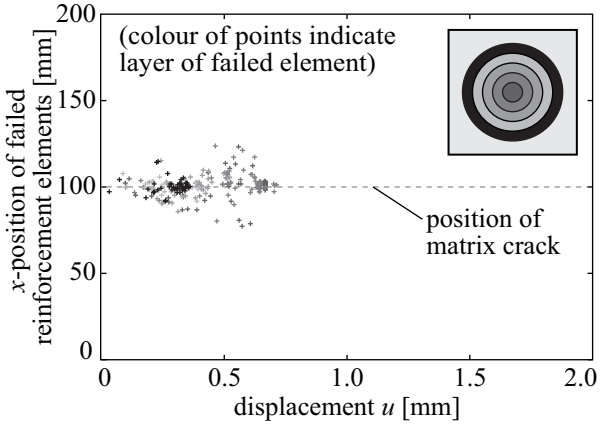

(d) Positions of reinforcement failure with increasing loading

Figure 5.12.: Simulated results and applied bond laws for yarn pull-out test

with larger stress transfer lengths in the core, which have to be activated to reach the tensile strength in the core layers due to the weaker bond.

Besides the simulation of the F-u relation, the model is also able to provide further information concerning the failure behaviour of the reinforcement. In Fig. 5.12(c), the number of failed reinforcement bar elements is shown with increasing deformation u corresponding to the F-u relation in Fig. 5.12(b). Such relations can also serve as an input for models on higher modelling scales where the successive reinforcement failure is not taken into account in a detailed manner, e. g. in the Strand Pull-Out Model by [Banholzer 2004] or the modelling framework by [Lepenies 2007]. In Fig. 5.12(c), it is observable that more failure events occur than the model has reinforcement segments. This means that in some of the reinforcement bar element chains more than one element fail. Therefor, sufficiently high forces have to be retransferred to the respective reinforcement chain via bond to reach a tensile strength minimum again. However, this is only possible if the failing elements are not positioned in the cross section of the concrete crack.

This is the case in the simulation as it can be seen in Fig. 5.12(d), which shows the positions of the concrete crack and the failed reinforcement elements depending on the displacements u. Failed reinforcement elements are situated up to 25 mm distant to the crack. The dis-

tribution of the failure positions result from the stochastic modelling of the reinforcement strength. This leads to the effect that local stress concentrations in the reinforcement as at the concrete crack do not necessarily determine the failure position of a segment but are only preferential positions while failure can also occur at positions with lower stress and strength. In Fig. 5.12(d), it can be also seen that failure events occur at first in the sleeve layer and propagate towards the core. At the end of failure development, the failing reinforcement elements are situated in the inner core segments. This telescopic failure behaviour coincides with experimental observations in FILT tests by [Banholzer 2004], see Section 2.3.3. Interestingly, reinforcement elements fail at both sides of the concrete crack, which corresponds to experimental observations by [Butler 2009] where filaments usually protrude at both concrete crack faces. In Fig. 5.12(c,d), it can be also seen that the failure of reinforcement elements has finished after a deformation u of about 0.7 mm. As already expected in the previous section, the subsequent force reduction in the F-u relation results from pull-out effects similar to the simulations of filament pull-out tests, see Section 5.1.

5.2.4. Remarks on the simulations of yarn pull-out tests

In the previous sections, simulations of yarn pull-out tests were presented. At least qualitatively, the model can reproduce the typical tensile behaviour in the double-sided yarn pull-out tests by [Butler 2009]. Nevertheless, the extent of the presented simulations is far from being exhaustive. The main reason for this limitation is the huge computation time for each simulation if an appropriate subdivision of reinforcement is applied. Moreover, the investigations in this work are primarily focussed on the load-bearing behaviour of TRC and less on the failure behaviour of the reinforcement, which does not judge to invest more effort on this topic within this work. Thus, the presented results can be only regarded as a proof of concept for the considered approach.

For further investigations with this model, computation time has to be considerably reduced. Therefor, some parallelisation algorithms within the FEM formulation might be applied. Alternatively, the number of elements might be reduced, which can be achieved with a simple increase of the element size in parts of the model where no filament failure events occur. More difficult is the application of different subdivisions of the reinforcement in longitudinal direction. In parts distant to the notch where no failure events are expected the reinforcement might be modelled with a layer approach without a subdivision of the layers. In the vicinity of the notch, the layer might be further subdivided into segments to represent the failure and subsequent pull-out behaviour of the reinforcement appropriately.

Besides a larger number of parametric studies, e. g. on the influence of reinforcement waviness, also a much larger number of simulations per parameter combination has to be carried out because of the applied scatter in the reinforcement tensile strength. Nevertheless, the presented results demonstrate interesting abilities of the model as e. g. the determination of the distribution of failure positions of the filaments, which might be directly compared to experimental results based on acoustic emission analysis as e. g. determined in [Kang et al. 2009]. Moreover, the failure development in the reinforcement with increasing loading can be determined, which might be useful as an input for models on higher modelling scales, e. g. the macroscopic scale.

5.3. Simulations of tensile plate specimen tests

In the following, simulations on tensile specimens with multiple concrete cracking corresponding to experimental investigations by [Jesse 2004], see also Section 2.3.4, are carried out. Contrary to the filament and yarn pull-out tests treated before, these experiments reflect the essential material response of the composite to uniaxial tensile loading as occurring in practice because similar reinforcement ratios are applied. As already pointed out in Section 2.3.4, the governing mechanisms that lead to the macroscopically observable behaviour of the composite are not entirely understood. In this context, the presented model can support this understanding by means of parametric studies where particular material parameters are varied while others are kept constant. Such an approach is often not possible in experimental investigations. Moreover, the model provides additional information about load-bearing mechanisms, which remain usually inaccessible in experimental investigations as e. g. stress distributions between concrete and reinforcement. However, the multitude of parameters in the model prevents an exhaustive consideration of all possible parameter combinations. Thus, only a selection of parameter combinations, which promise explanations for certain characteristics of the load-bearing response of TRC, is treated in the following. Furthermore, the influence of the transverse yarns of the textiles perpendicular to loading direction remains unconsidered, although at least the cross-sectional area of the bar elements representing the concrete could be reduced in the model at the respective positions. However, this is not done and only unidirectional reinforcement is assumed in the following. Results of respective experimental investigations are available in [Jesse 2004] and are used also for verification of the simulated results.

5.3.1. Reference simulations

5.3.1.1. Estimation of appropriate bar element length

At first, a parametric study is carried out to estimate an appropriate length of the bar elements and correspondingly the number of bond elements to approximate the detailed stress profiles in the composite accurately. Furthermore, a sufficiently large number of elements is important for a proper representation of multiple concrete cracking.

In the respective simulations, the material properties of the concrete and the reinforcement are modelled deterministically. Furthermore, the material behaviour of concrete and reinforcement is modelled linear elastic with brittle failure if the tensile strength is reached, see Fig 5.13. Thus, non-linearities like concrete tension softening and yarn waviness remain unconsidered, at first. The material properties of the reinforcement correspond to AR-glass yarns of a fineness of 310 tex produced by "Nippon Electric Glass", which possess a cross-sectional area of A_{yarn}=0.11 mm^2. According to [Abdkader 2004], the mean value of the Young's modulus of these yarns is E_r=79 950 N/mm^2. Failure of the reinforcement is of subordinate importance in the first instance and, thus, the tensile strength is defined somewhat arbitrarily with f_{rt}=1000 N/mm^2. The mean values of the Young's modulus and the tensile strength of the concrete are chosen corresponding to [Jesse 2004] with E_c=28 500 N/mm^2 and f_{ct}=5 N/mm^2. The cross-sectional area of the concrete is given cor-

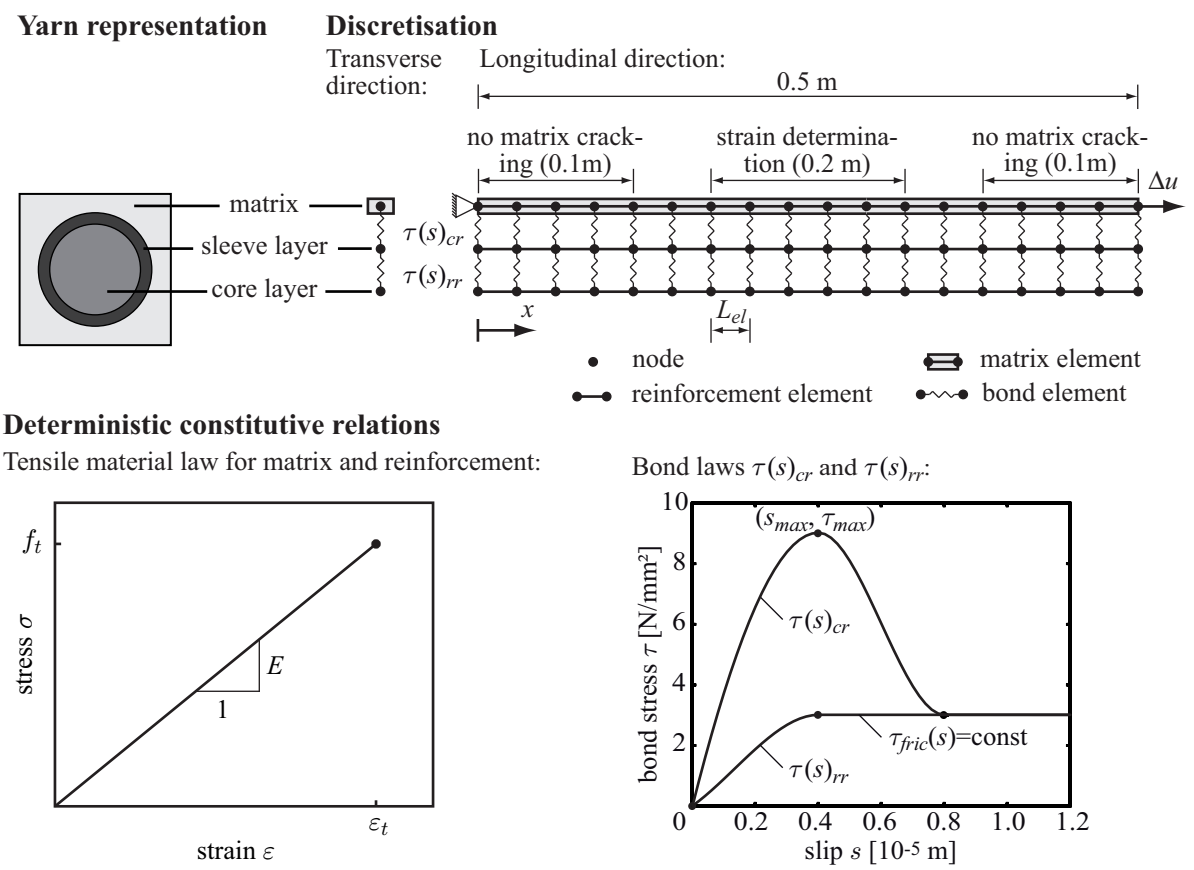

Figure 5.13.: Schematic model with a subdivision of the yarn into two layers for the simulation of tensile plate specimens and assumed constitutive relations

responding to Fig. 2.13(b) with 8 mm·100 mm=800 mm^2 neglecting the reduction due to embedded reinforcement. The total cross-sectional area of the reinforcement can be calculated from the reinforcement ratio V_f, which is chosen with 2 %, according to Eq. (2.3). This corresponds to 146 yarns and a cross-sectional area of 16.1 mm^2. In the simulations for the estimation of an appropriate bar element length, the reinforcement is subdivided into two layers where one layer represents the filaments in the fill-in zone, which is also referred to as sleeve layer, and the other layer corresponds to the filaments in the core zone, see Fig 5.13. A subdivision of the layers into segments is not performed.

The cross-sectional area of the reinforcement A_r, which is determined by the cross-sectional area A_{yarn} and the number n_{yarn} of the yarns, can be subdivided into two parts A_{sleeve} and A_{core} representing the filaments in the sleeve and the core zone. This yields:

$$A_r = A_{sleeve} + A_{core} = n_{yarn} \cdot A_{yarn} = n_{yarn} \cdot \pi \cdot r_{yarn}^2. \tag{5.1}$$

where r_{yarn} is the radius of the yarn assuming a perfectly circular shape. Correspondingly, the total cross-sectional area of the core A_{core} can be determined as

$$\begin{aligned} A_{core} &= n_{yarn} \cdot \pi \cdot r_{core}^2 = n_{yarn} \cdot \pi \cdot (\alpha \cdot r_{yarn})^2 = n_{yarn} \cdot \pi \cdot \alpha^2 \cdot r_{yarn}^2 \\ &= n_{yarn} \cdot \alpha^2 \cdot A_{yarn} = \alpha^2 \cdot A_r \text{ with } 0 \leq \alpha \leq 1 \end{aligned} \tag{5.2}$$

where α is the percentage of the radius of the reinforcement core on the total radius of a circular shaped yarn. With Eq. (5.1), the cross-sectional area of the sleeve layer can be

determined as

$$A_{sleeve} = n_{yarn} \cdot (1 - \alpha^2) \cdot A_{yarn} = (1 - \alpha^2) \cdot A_r. \tag{5.3}$$

The bond surface areas of the bond elements can be determined according to Eq. (4.6) with n=1.

It is assumed that 20 % of r_{yarn} represent the filaments in the fill-in zone while 80 % of r_{yarn} represent the core. This ratio corresponds to a circular cross section of a yarn with a subdivision into an inner circle, which possesses 64 % of the total cross-sectional area of the reinforcement, while the remaining 36 % of the total cross-sectional area are situated in the outer layer. This ratio is chosen corresponding to values by [Jesse 2004] based on microscopic investigations of transparent cuts of yarns embedded in fine-grained concrete. Between the concrete chain and the reinforcement chain representing the fill-in zone, the bond law $\tau(s)_{cr}$ corresponding to the assumption of initially adhesive load transfer merging to friction after exceeding the bond strength τ_{max} is used. Between the reinforcement chains, the bond law $\tau(s)_{rr}$ corresponding to the assumption of a low number of adhesive cross-linkages between the filaments failing soon after activation and resulting in an essentially frictional load transfer is applied, see Fig. 5.13. The values of the supporting points of both bond laws were obtained from a calibration process, which led to a satisfactory correspondence between experimental and numerical results. The influence of changes in the bond law parameters is presented in Section 5.3.2.

In longitudinal direction, the specimens under consideration have a length of 0.5 m, see Fig. 2.13(b). In the experiments, the specimens are fixed in the testing machine by means of clamps on lengths of 0.1 m at both ends of the specimens. The influence of the load application on the experimental and numerical results is studied in Section 5.3.5.3. In the following simulations, the load is applied with displacement control at the last node of the concrete chain at x=0.5 m while the first concrete node at x=0 is fixed, see Fig 5.13. Therefor, the concrete elements corresponding to the clamping zones are assumed not to crack to facilitate an undisturbed load transfer from the concrete to the reinforcement. This leads at higher load levels to stresses in the concrete elements corresponding to the clamping zones, which are higher than the nominal concrete tensile strength, see Fig. 5.17(c). This is only a minor drawback in the model as also in the experiments concrete cracking is significantly reduced in the load application range due to the support of steel plates.

The experimental results are given as mean stress-mean strain ($\overline{\sigma}$-$\overline{\varepsilon}$) relations. Corresponding to the experiments, see Section 2.3.4, $\overline{\sigma}$ is determined in the simulations as reaction force divided by the cross-sectional area of the concrete. $\overline{\varepsilon}$ is determined as mean strain of the concrete elements (cracked and intact) on a length of 0.2 m in the centre of the model, see Fig. 5.13. This corresponds to the determination of the mean strain in the experiments based on the relative displacement of two positions at the specimen in a distance of 0.2 m in the centre of the specimen related to this distance. It provides also a proper representation of $\overline{\varepsilon}$ in the results of the simulations as disturbances due to boundary effects at the transition to the zones in the model where concrete cracking is not allowed are not taken into account, compare also Fig. 5.17(c) and Section 5.3.5.3. Cracking of concrete is allowed only in one element per load step. In this case, the system is recalculated on the same load level with a correspondingly adapted stiffness matrix. If in the recalculated step (without load elevation) in another element the tensile strength is exceeded, the load is reduced in an adaptive

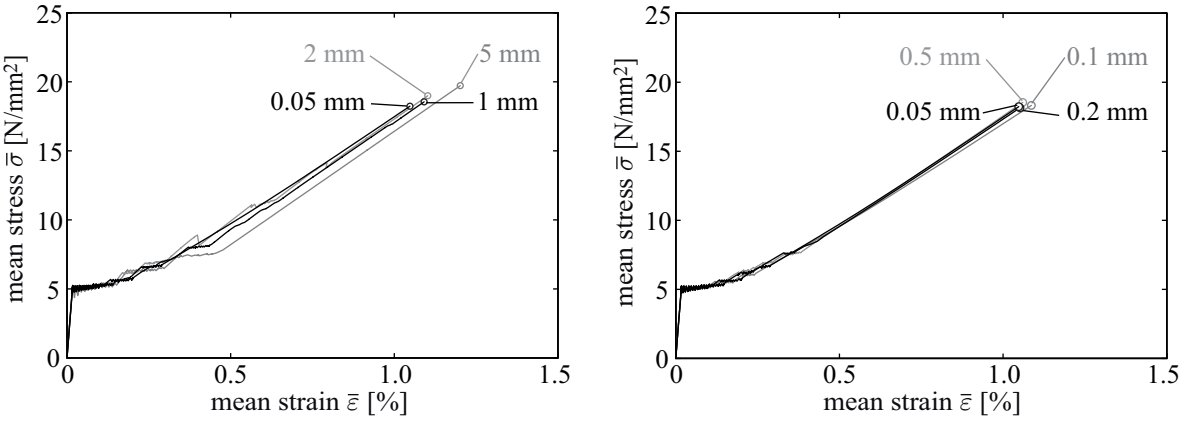

(a) Coarse discretisations of L_{el}=5 mm, 2 mm, 1 mm and as a reference L_{el}=0.05 mm

(b) Fine discretisations of L_{el}=0.5 mm, 0.2 mm, 0.1 mm and as a reference L_{el}=0.05 mm

Figure 5.14.: $\overline{\sigma}$-$\overline{\varepsilon}$ relations for different bar element lengths L_{el}

manner until the stresses are in all bar elements below the respective tensile strength. This occurs, however, only occasionally, e. g. if a large number of concrete cracks develop considering concrete tension softening. Furthermore, it is assumed that the reinforcement fails when one reinforcement element fails reaching f_{rt}. In this case, the calculation is stopped. The subsequent successive failure of the reinforcement is not studied. This approach is also justified by investigations in [Curbach et al. 2006] based on enhanced fibre bundle models by [Daniels 1945] where it was shown that usually the failure of about 10% up to 20% of the filaments of a yarn is sufficient for the failure of the entire yarn.

In the parametric study, the bar element length L_{el} is varied in a range of 5 mm down to 0.05 mm, which leads with the length of the simulated specimens of 0.5 m to 100 up to 10 000 elements per bar element chain. In Fig. 5.14, the simulated $\overline{\sigma}$-$\overline{\varepsilon}$ relations are shown. At least qualitatively, the tripartite course of the experimental results with uncracked state, state of multiple cracking and post-cracking state as shown, e. g., in Figs. 2.14-2.17 is reproduced by the model. A more detailed analysis of the deficiencies existing in the simulated results compared to experimental results is given in Section 5.3.1.3. A perfect agreement between the different discretisations cannot be expected because the stress-strain response is significantly influenced by concrete cracking where the crack patterns are in general different for all discretisations. This is especially observable in Fig. 5.14(a) where the results of the coarser discretisations are shown. Especially the results of the simulations with L_{el} of 2 mm and 5 mm show significant deviations from the course of the smallest L_{el} equal to 0.05 mm, which is assumed to provide the most accurate results. In the $\overline{\sigma}$-$\overline{\varepsilon}$ relations of the finer discretisations, see Fig. 5.14(b), the differences between the different L_{el} decrease significantly although especially in the state of concrete cracking deviations exist.

Based on these global results, a bar element length of 0.5 mm seems to be sufficient. However, in [Jesse 2004] crack spacing of often less than 5 mm is reported. With L_{el}=0.5 mm, the stress profile between two cracks in concrete, reinforcement and bond layers would be represented by less than 10 elements, which appears to be relatively coarse. Thus, instead a bar element length of 0.2 mm is used in most of the subsequent simulations, which allows for a representation of the stress profile between two cracks with about 25 elements. Thus, a typical bar element chain consists of 2500 elements. However, with some parameter com-

binations used in the following parametric studies, crack spacing less than 5 mm occurs. In these cases, a bar element length of 0.1 mm is used.

5.3.1.2. Influence of the reinforcement discretisation

For the estimation of an appropriate bar element length in the previous section, the reinforcement was subdivided into two layers - one representing the filaments in the fill-in zone and one for the filaments in the core zone. For the fill-in zone, the assumption of global load sharing between the filaments, which means a uniform load distribution to all filaments, seems to be valid. This justifies the representation of the filaments in the fill-in zone as a single sleeve layer. For the reinforcement core, local load sharing has to be assumed, which means load distribution depending on the position of the filament in the yarn core. This calls for a finer subdivision. Therefor, a parametric study with different numbers of core layers is carried out to investigate the influence of the reinforcement discretisation in transverse direction. Between the core layers, the bond law $\tau(s)_{rr}$ as shown in Fig. 5.13 is applied. All other parameters are chosen as defined in Section 5.3.1.1.

It is assumed that for the core layers the condition

$$r_i - r_{i+1} = \frac{r_{core}}{n_{core}} = \frac{\alpha r_{yarn}}{n_{core}} = \frac{\alpha\sqrt{\frac{A_{yarn}}{\pi}}}{n_{core}} = const \tag{5.4}$$

holds where r_{core} is the radius of the entire core corresponding to Eq. (4.3) and n_{core} is the number of core layers. This condition is chosen because it seems to represent the telescopic behaviour of the yarns more realistic as for example a subdivision with equal cross-sectional areas where the impact of the inner core layers might be overweighted. In the following numerical studies, only a subdivision of the reinforcement in radial direction is performed. While this is appropriate for a deterministic approach, stochastic variations of the filament strength would require an additional segmentation in tangential direction as it was performed in Section 5.2 in the simulation of yarn pull-out tests. This remains unconsidered here. Thus, for a core layer i, the cross-sectional area is given according to Eq. (4.4) with $n = 1$. Furthermore, the respective bond areas S_i are given according to Eq. (4.6).

In Fig. 5.15, the $\overline{\sigma}$-$\overline{\varepsilon}$ relations for different numbers of core layers are shown. Except for the case of n_{core}=1, the $\overline{\sigma}$-$\overline{\varepsilon}$ relations are very similar. In the simulation with n_{core}=1, the mean crack spacing s_{cr} is considerably smaller compared to the other cases, see Figs. 5.16 and 5.18(c). This leads to a lower participation of the concrete on the load-bearing between cracks because less forces can be transferred from the reinforcement to the concrete over the shorter stress transfer length. Thus, tension stiffening, compare Section 2.3.4, is reduced for n_{core}=1 compared to the other cases and the $\overline{\sigma}$-$\overline{\varepsilon}$ relation in the post-cracking state is shifted towards larger strains. Also for the cases with larger n_{core}, the $\overline{\sigma}$-$\overline{\varepsilon}$ relations show different courses in the cracking state resulting from different crack plateau positions. These crack plateaus can be explained with the deterministic modelling of f_{ct}, which leads in the $\overline{\sigma}$-$\overline{\varepsilon}$ relation to stepwise increasing cracking stresses. This results from concrete cracking between already existing cracks, which requires some load increase to active a longer stress transfer length between concrete and reinforcement to reach f_{ct} in the concrete again. As the normal stress distributions in the concrete and the reinforcement layers in longitudinal direction x, which

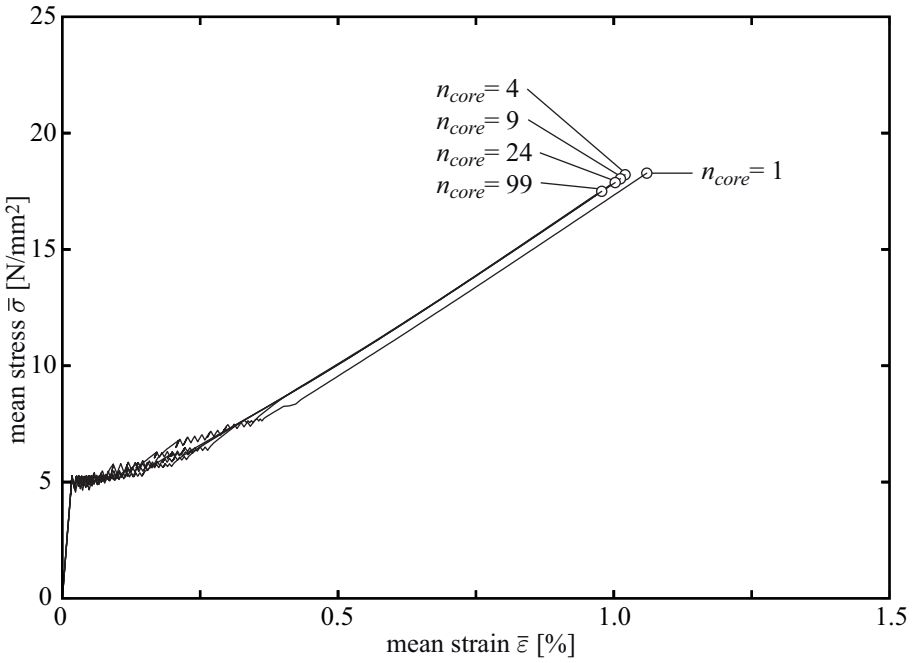

Figure 5.15.: $\overline{\sigma}$-$\overline{\varepsilon}$ relations for different numbers of core layers

are shown for the cases of one, four and nine core layers in Fig. 5.16, vary with n_{core}, also the crack patterns and crack plateau positions are different. Two crack development states are distinguished in Fig. 5.16, which are a single crack and the post-cracking state right before ultimate failure reaching the tensile strength of the reinforcement f_{rt}=1000 N/mm^2 in the sleeve layer. Respective bond stress distributions are shown for the case of n_{core}=4 in Fig. 5.27 (a,b). The maxima in the reinforcement stresses correspond to stresses in the concrete equal to zero indicating concrete cracks. As it can be seen in the Figs. 5.16 (a,c,e), the load transfer length of the reinforcement layers increases towards the innermost layer. This effect is amplified with an increasing number of layers and is associated with different stress distributions.

In Fig. 5.18(a), the distribution of the normal stresses σ_r in the sleeve layer, the innermost and the outermost core layers of the reinforcement right after the first concrete crack occurred is shown for the cracked cross section for different numbers of core layers. It is observable that the normal stresses in the sleeve layer increase slightly with increasing n_{core}. The increasing effect is especially pronounced for low values of n_{core}. Simultaneously, the normal stresses in the outermost core layer increase while the normal stresses in the innermost core layer decrease with increasing numbers of core layers. These changes are larger compared to the sleeve layer but correspondingly stabilise for larger values of n_{core}. These effects result from the load distribution between sleeve layer and core layers, which depends on their stiffness. The stiffness of the sleeve layer remains constant in the parametric study while the stiffness of the core decreases with increasing n_{core} due to imperfect bond. As a consequence, the sleeve layer has to bear larger loads with increasing n_{core} compared to the core. A similar effect occurs for the outermost core layer on which the highest stresses of all core layers are transferred via bond. The transferred loads decrease towards the innermost core layers and, thus, also the stress in the innermost core layer decreases with increasing n_{core}. This leads also to a different development of cracks in the concrete and to different final crack patterns,

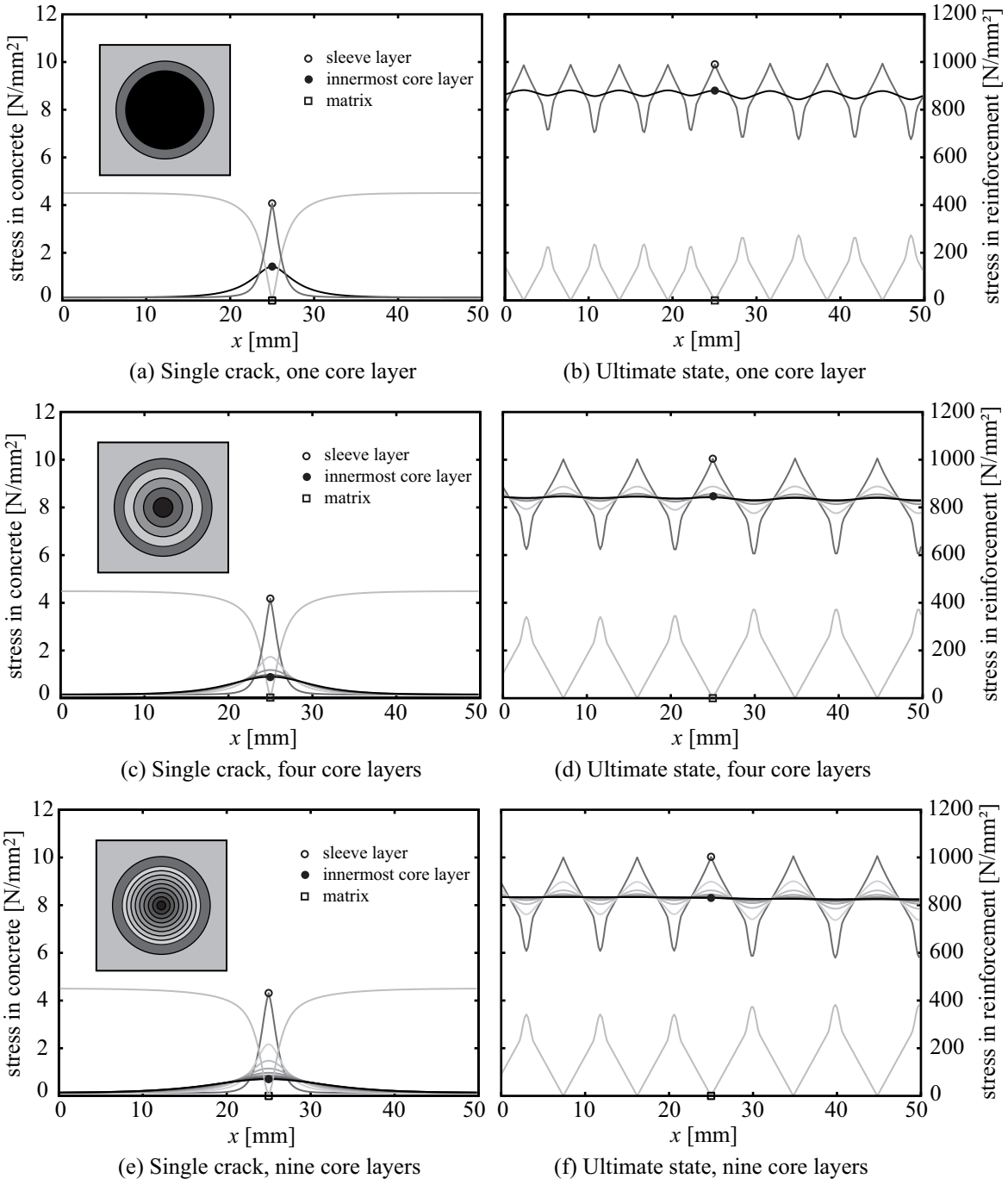

Figure 5.16.: Normal stresses in longitudinal direction in the centre part of the model at a single crack and in the ultimate state for various subdivisions of the reinforcement core

see Figs. 5.16 (b,d,f). Regarding the normal stress distribution in longitudinal direction, it can be observed in Figs. 5.16 (b,d,f) that the highest reinforcement stress occurs in the sleeve layer at a concrete crack. Vice versa, the core layers have higher normal stresses in the uncracked concrete parts compared to the sleeve layer, which is stronger supported by the concrete. Moreover, the stress amplitudes become smaller from the sleeve layer towards the innermost core layer indicating that only low forces are transferred to the inner core layers

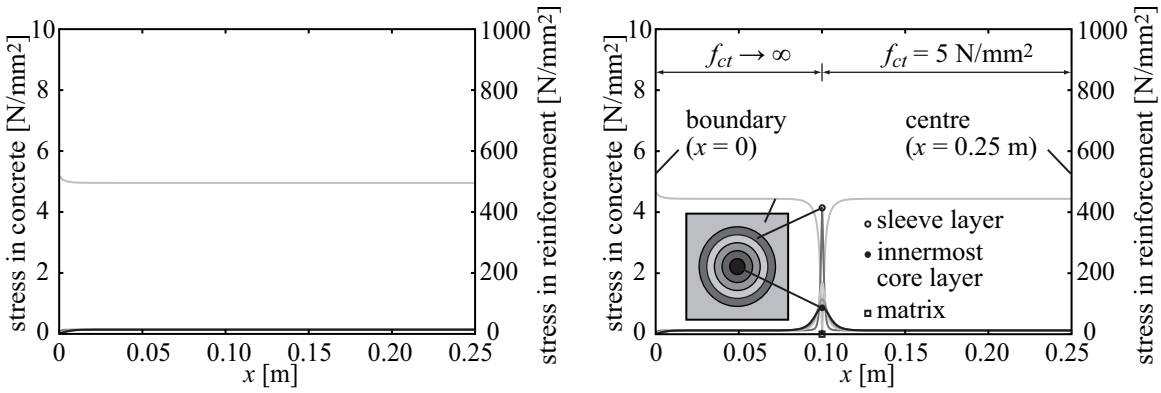

(a) Before first concrete crack

(b) After first concrete crack

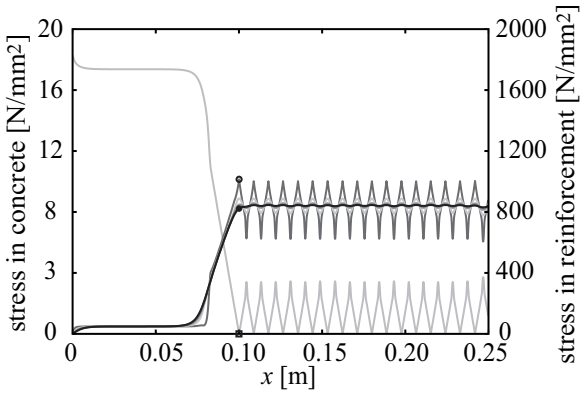

(c) Right before ultimate failure

Figure 5.17.: Normal stress distribution in longitudinal direction in the range of $0 \leq x \leq 0.25\,\mathrm{m}$ at different load levels for the reference model

between concrete cracks. The stress is transferred to the core layers primarily in the load application range on both ends of the model, see Fig. 5.17. The stress distributions of the cases with more than one core layer show correspondingly almost constant stresses in the innermost core layers, which is not the case with only one core layer.

The courses of the $\overline{\sigma}$-$\overline{\varepsilon}$ relations in Fig. 5.15 virtually coincide except for the case of n_{core}=1 as already mentioned. However, it can be also seen that the ultimate stress $\overline{\sigma}_{ult}$ decreases with increasing n_{core}. This is also shown in Fig. 5.18(b) associated with the development of the respective ultimate strains $\overline{\varepsilon}_{ult}$. It is observable that the ultimate stresses and strains slightly decrease with increasing n_{core}. This is caused by the earlier failure of the sleeve layer as the tensile stresses in the sleeve layer increase with increasing numbers of core layers as mentioned previously.

For the design of structural elements also crack widths w are of interest. In Fig. 5.18(c), the mean crack width at $\overline{\varepsilon}$=1 % and the mean crack spacing s_{cr} in the ultimate state are shown. The crack width is determined from a cracked concrete element corresponding to Eq. (4.14) as

$$w = \begin{cases} 0 & \text{for} \quad \varepsilon_{tot} \leq \frac{f_{ct}}{E_{c,0}} \\ (\varepsilon_{tot} - \varepsilon_{elast})\, L_{el} = \left(\varepsilon_{tot} - \frac{f_{ct}}{E_{c,0}}\right) L_{el} & \text{for} \quad \varepsilon_{tot} > \frac{f_{ct}}{E_{c,0}} \end{cases} \tag{5.5}$$

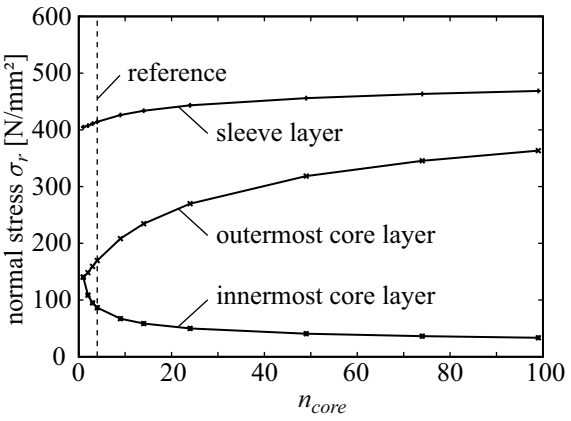

(a) Normal stresses in selected reinforcement layers in the cracked cross section right after the first concrete crack

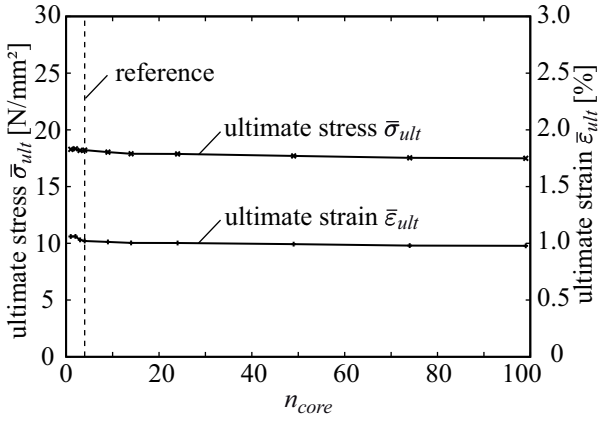

(b) Ultimate mean stresses $\bar{\sigma}_{ult}$ and strains $\bar{\varepsilon}_{ult}$

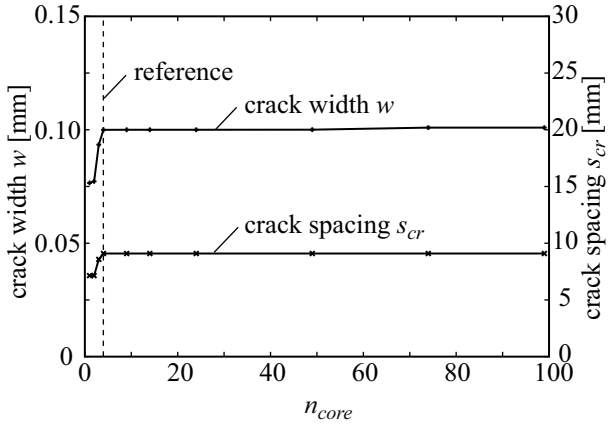

(c) Mean crack width at $\bar{\varepsilon}$=1 % and mean crack spacing in the ultimate state

Figure 5.18.: Various simulation results for different numbers of core layers n_{core}

where ε_{tot} is the strain of the cracked concrete element in the simulation. The mean crack width is determined as the sum of the crack widths within the measurement length of 0.2 m in the centre of the model divided by the respective number of cracks. The results in Fig. 5.18(c) show that for low numbers of n_{core} smaller mean crack widths and mean crack spacing occur. This can be explained with a larger stress transfer to the reinforcement as the entire core is stiffer for a small n_{core} than for large n_{core}. However, this effect influences crack widths and crack spacing in the current simulations only up to a value of $n_{core} = 4$. With larger values this effect seems to be negligible as crack widths and crack spacing are almost constant.

For the following parametric studies, a number of core layers has to be chosen. Because of the strongly increasing computation time with increasing numbers of elements, n_{core} has to be limited. Therefor, a model with one sleeve layer and four core layers is chosen for the following parametric studies. However, it should be noted that the given results are based on a special parameter combination. Previous investigations published in [Hartig et al. 2008] showed, e. g., that for a smaller proportion of the cross-sectional area of the sleeve layer, the softening effects have a stronger influence on the results with increasing n_{core}. This would perhaps require a larger number of core layers to achieve a better representation of the occurring

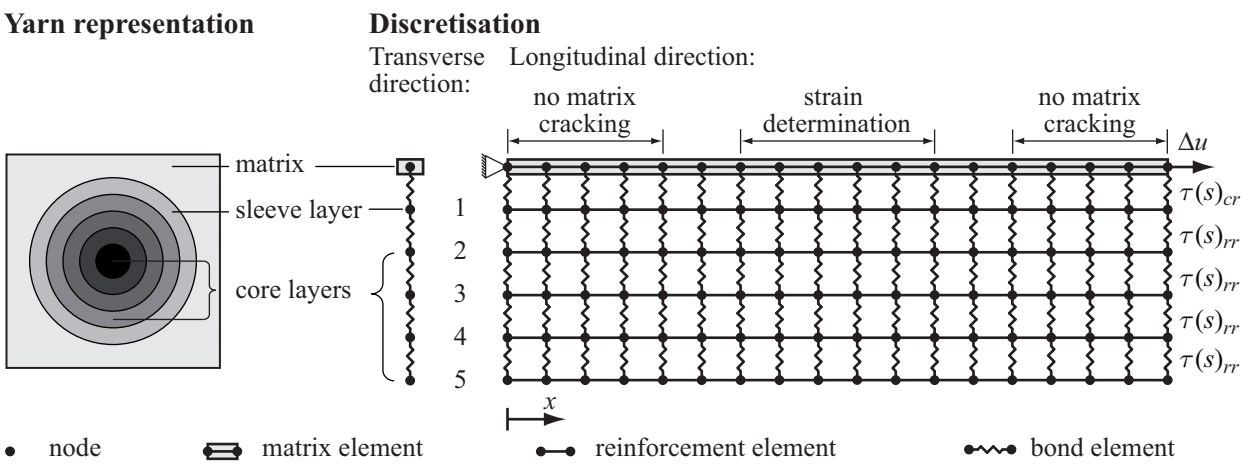

Figure 5.19.: Reference model (schematic) with a subdivision of the yarn into one sleeve layer and four core layers for the simulation of tensile plate specimens

mechanisms. On the other hand, a too large number of core layers might be also inappropriate as the number of filaments in a yarn is limited and the physical meaning of a discrete layer might be lost. In [Konrad & Chudoba 2009], where TRC with epoxy-impregnated yarns is analysed, the thickness of the reinforcement layers, which is associated with their number, is identified as a material length scale inherent to the type of yarn. In the current work, primarily qualitative effects shall be identified, where n_{core}=4 seems to be sufficient. In the following visualisations of the computational results, the chosen configuration is marked as the reference case with a dashed line. This should facilitate the comparison between the results of the parametric studies. In summary, the most important parameters of the model in the reference case, which is also schematically visualised in Fig. 5.19, are as follows:

- six bar element chains (one for the concrete, one for the sleeve layer and four for the core layers) of each 2500 elements (L_{el}=0.2 mm)
- linear elastic behaviour for concrete and reinforcement with E_c=28500 N/mm^2, E_r=79950 N/mm^2, f_{ct}=5 N/mm^2 and f_{rt}=1000 N/mm^2
- geometrical properties of concrete according to Fig. 2.13(b) and reinforcement ratio of 2 % with 36 % of the cross-sectional area in the sleeve layer and 64 % in the core layers (cross-sectional areas of core layers according to assumption of uniform layer thickness)
- bond elements with bond law $\tau(s)_{cr}$ between concrete and sleeve chain and bond elements with bond law $\tau(s)_{rr}$ between the reinforcement chains (bond laws $\tau(s)_{cr}$ and $\tau(s)_{rr}$ according to Fig. 5.13)
- boundary conditions according to Fig. 5.19.

5.3.1.3. Influence of different reinforcement ratios

To analyse the quality of the results of the model, simulations with different reinforcement ratios V_f corresponding to Eq. (2.3) in a range of 0.75 % up to 5 % are carried out. At the same time, also the influence of different V_f on the load-bearing behaviour is studied.

Significantly lower values of V_f than 0.75 % lead to reinforcement failure simultaneously with the first concrete crack or before multiple concrete cracking has finished while V_f larger than 5 % is ususally not applied in practice because of production issues. In Fig. 5.20, a selection of the simulated $\overline{\sigma}$-$\overline{\varepsilon}$ relations is shown as well as corresponding experimental stress-strain relations. For V_f significantly larger than 3 %, experimental data is not available for the used parameter combination.

In the uncracked state, no significant differences are observable between the $\overline{\sigma}$-$\overline{\varepsilon}$ relations of the different V_f. Differences start to appear when the concrete begins to crack. The respective mean stress value σ_{cr1} where the first concrete crack occurs increases with increasing V_f. This effect is also known as suppression of cracks, compare Section 2.3.4. In Fig. 5.21(c), σ_{cr1} related to the assumed concrete tensile strength f_{ct} is shown for the different V_f. It shall be noted that σ_{cr1} is not determined exactly in the simulations but depends somewhat on the applied load step size as concrete cracking is detected when the stress in a concrete bar element exceeds the concrete tensile strength. In case of concrete cracking the FE system is recalculated with the Young's modulus of the respective bar element set equal to zero. Only the results before f_{ct} was exceeded and the recalculated results are stored. Thus, suppression of cracks is always underestimated in the stored results of the simulations. It would be possible to perform an iteration to determine the cracking stress of the composite exactly. However, the respective effort seems not to justify the gain of information. The model predicts a linear increasing relation between suppression of cracks and V_f with elevations of σ_{cr1} compared to f_{ct} of about 1 % for V_f=0.75 % and about 13 % for V_f=5 %. At least the increasing function, coincides with the experimental results by [Jesse 2004]. However, it cannot be assessed based on the available experimental results if the relation is also linear in the experiments because both the determination of the concrete tensile strength and the value corresponding to σ_{cr1} in the experimental results is associated with large uncertainties.

In Fig. 5.21(a), the normal stresses σ_r in the sleeve layer as well as in the outermost and innermost core layers in the cracked cross section are shown for the first concrete crack right after its development. As already shown in Fig. 5.16, the sleeve layer has the highest stresses while they decrease towards the innermost core layer. With increasing V_f, the stresses in the reinforcement decrease, because more reinforcement is available to bear the forces released at a concrete crack. For the core layers, the reduction decreases for higher values of V_f. This trend is less pronounced in the sleeve layer. The reason for this difference is that the slip between the layers decreases because of the stiffer reinforcement and, thus, the core layers become less activated via the weak frictional bond law. Moreover, the activation of the sleeve layer is almost reversed proportional to V_f due to the strong adhesive bond. The absolute stresses in the sleeve layer decrease from about 500 N/mm^2 for a V_f=0.75 % to about 200 N/mm^2 for a V_f=5.0 %. This is well below the assumed tensile strength of the reinforcement of f_{rt}=1000 N/mm^2, which is however only a rough estimation. Nevertheless, this contradicts at least for higher values of V_f with the assumption of a simultaneous failure of the filaments in the fill-in zone with concrete cracking by [Jesse 2004].

After the first concrete crack, a state of multiple cracking follows, which is associated with a stiffness reduction in the $\overline{\sigma}$-$\overline{\varepsilon}$ relations, see Fig. 5.20. It is observable that the strain range, where concrete cracks occur, decreases with increasing V_f. However, the differences are small between V_f larger than 2 %. In some configurations, the strain range for cracking increases also again for higher values of V_f. For instance, in the case of V_f=3 % some cracks occur when

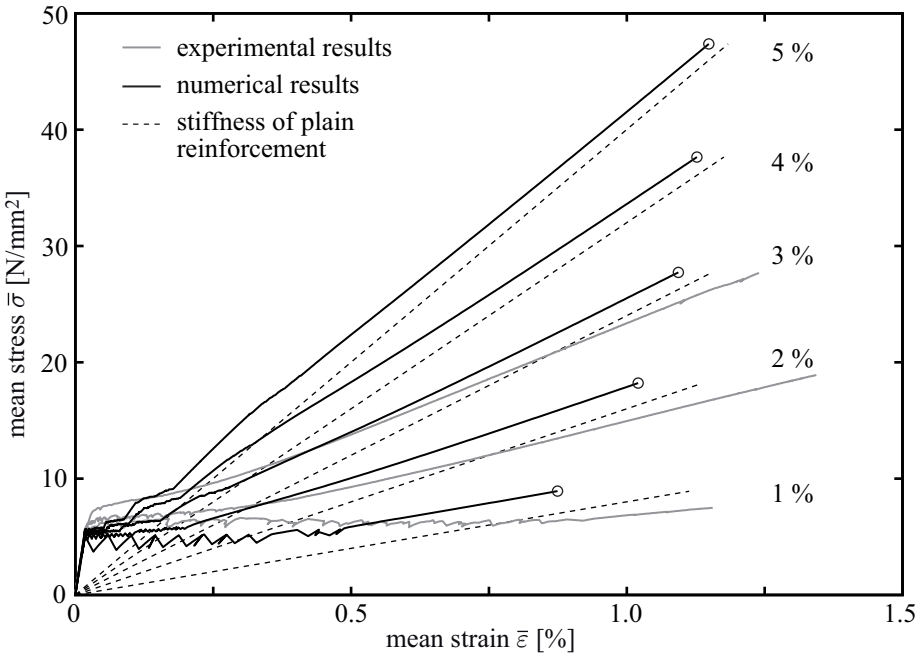

Figure 5.20.: $\overline{\sigma}$-$\overline{\varepsilon}$ relations for different reinforcement ratios and respective experimental data (provided by subproject B1 of SFB 528)

cracking in the case of V_f=2 % is already finished. The reason for this effect is additional cracking between existing cracks at higher load levels, which does not occur in this particular case for V_f=2 %. This is also influenced by the deterministic modeling of the concrete tensile strength, which leads to discrete cracking plateaus. Obviously, this is a deficiency of the model, which can be counteracted with a stochastic modelling of the concrete tensile strength. This is performed in Section 5.3.4.2.

Right after concrete cracking is finished, a non-linear transition of the $\overline{\sigma}$-$\overline{\varepsilon}$ relation towards an almost linear course occurs in all cases. The slope of the $\overline{\sigma}$-$\overline{\varepsilon}$ relation at the end of the post-cracking state corresponds almost to the stiffness of the reinforcement. A significant reduction as reported from experiments in [Jesse 2004] and also observable in experimental results in Fig. 5.20 does not appear in the computational results. The slope of the $\overline{\sigma}$-$\overline{\varepsilon}$ relation in the post-cracking state m_{pc} corresponding to the stiffness of the plain reinforcement is given according to Eq. (2.6). In Fig. 5.20, the linear functions corresponding to m_{pc} are given with dashed lines. To quantify the difference between the slope expected from simple mechanical considerations and the simulated slope in the post-cracking state, the ratio m_{sim}/m_{pc} is established. The simulated slope m_{sim} is determined from the stress and strain values of the last two load steps corresponding to Fig. 5.20. In Fig. 5.21(c), the ratio m_{sim}/m_{pc} is shown for different V_f. Especially for the higher values of V_f virtually no deviation of m_{sim} from m_{pc} is observable. For the lower values of V_f, deviations of $\pm$5 % occur, which result primarily from an unfinished transition from the cracking state to the post-cracking state where the bond laws influence the course of the $\overline{\sigma}$-$\overline{\varepsilon}$ relations considerably and from different crack widths within the measurement range. The influence of the measurement range on the apparent stiffness in the post-cracking state is discussed more detailed in Section 5.3.5.3. Thus, also for lower values of V_f virtually no deficit of stiffness appears. The missing deficit of stiffness as occurring in the experimental results is also a deficiency of the reference model.

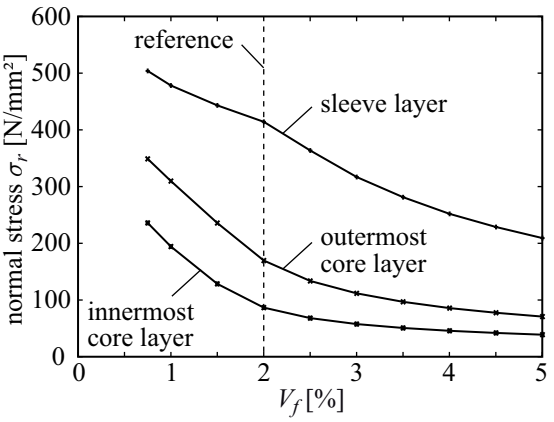

(a) Normal stresses in selected reinforcement layers in the cracked cross section right after the first concrete crack

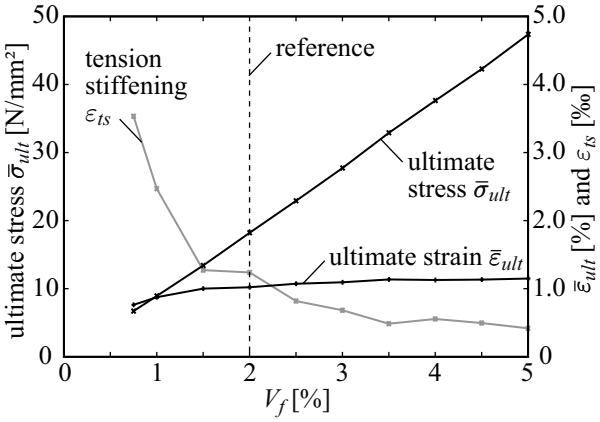

(b) Ultimate mean stresses $\overline{\sigma}_{ult}$ and strains $\overline{\varepsilon}_{ult}$ as well as tension stiffening ε_{ts}

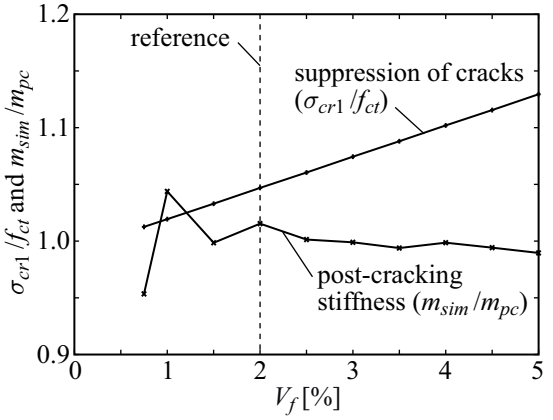

(c) Suppression of cracks and post-cracking stiffness before ultimate failure

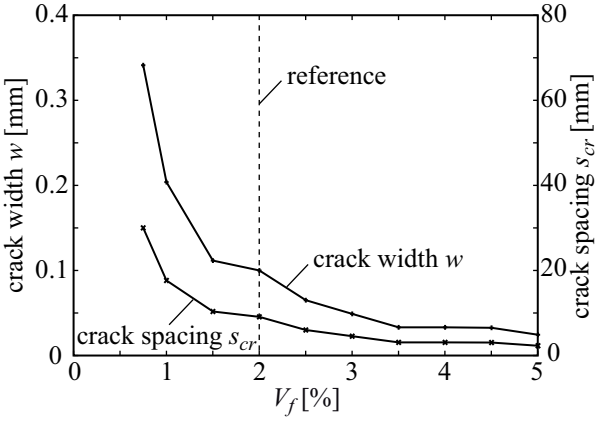

(d) Mean crack width at $\overline{\varepsilon}$=1 % and mean crack spacing in the ultimate state

Figure 5.21.: Various simulation results for different reinforcement ratios

At the end of the post-cracking state ultimate failure occurs in a brittle manner as successive reinforcement failure is not taken into account in the underlying model. As it can be seen in Fig. 5.21(b), the ultimate stresses $\overline{\sigma}_{ult}$ increase with increasing V_f. The deterministic model predicts an almost linear dependency between the ultimate stress and V_f. The ultimate strains $\overline{\varepsilon}_{ult}$ also increase with increasing V_f. However, with large values of V_f, the increase reduces because the stress concentrations in the sleeve layer reduce as Fig. 5.21(a) shows and the ultimate strain $\overline{\varepsilon}_{ult}$ approaches the failure strain of the plain reinforcement $\varepsilon(f_{rt}) \approx 1.25\,\%$. This is an upper limit for the case neglecting waviness of the reinforcement. Increasing ultimate stresses and less increasing ultimate strains with increasing V_f coincide also with experimental results. Furthermore, tension stiffening due to participation of the concrete on load-bearing between concrete cracks occurs with all values of V_f. Tension stiffening ε_{ts} is determined from the computational results as strain shift

$$\varepsilon_{ts} = \frac{\overline{\sigma}_{ult}}{m_{pc}} - \overline{\varepsilon}_{ult}. \tag{5.6}$$

It can be seen in Fig. 5.21(b) that tension stiffening decreases with increasing V_f. The reason is that also the crack spacing decreases with increasing V_f as it is observable in Fig. 5.21(d)

and, thus, less forces can be transferred to the concrete, which in turn participates less in load-bearing between the cracks. Compared to the experimental results by [Jesse 2004], the mean crack spacing seems to be somewhat overestimated. The trend that the decrease of crack spacing is lower with large values of V_f compared to low values of V_f coincides with most of the experimental observations, which show, however, relatively large variations for different yarn types, see [Jesse 2004]. Corresponding to the crack spacing also the crack widths decrease as it is also shown in Fig. 5.21(d).

In summary, it can be assessed that already with the quite basic model a relatively good agreement with the experimental results is obtained. However, also deficiencies exist. In the following, results of further parametric studies are presented to investigate the sources of the differences and to show further effects associated with varied material parameters.

5.3.2. Influence of bond properties

The subsequent numerical studies deal with the influence of parameters of the bond law on the load-bearing behaviour of the composite. Except for the varied parameters of the bond law, the parameters of the reference model, see Fig. 5.19, are applied as summarised at the end of Section 5.3.1.2. It should be pointed out again that the absolute bond stress values cannot be directly compared to experimental values because the values in the model have to be overestimated due to the underestimation of the bond surface area in the segmentation approach, see Section 4.1. However, for the qualitative evaluation of the influence of the bond properties on the load-bearing response of the composite this approach seems to be appropriate also because significant experimental values of bond stress and slip values for local bond laws as used in the model are still missing.

5.3.2.1. Influence of the frictional load transfer in the reinforcement core

In this section, the influence of the bond stress τ_{fric} characteristic of the frictional bond law $\tau(s)_{rr}$ according to Fig. 5.13 between the reinforcement layers on the tensile behaviour of TRC is studied. Therefor, τ_{fric} is varied uniformly in all interfaces possessing bond law $\tau(s)_{rr}$ in a range of $0.01\,\mathrm{N/mm^2}$ up to $50\,\mathrm{N/mm^2}$. While the lower values correspond to a very weak frictional inner bond, the larger values correspond to a strong inner bond, e. g. due to an impregnation of the yarns. However, it is questionable whether in the case of an impregnated yarn the assumption of friction is valid or essentially elastic, adhesive bond has to be assumed. Such a bond law is applied in another parametric study in Section 5.3.5.3. Moreover, also the parameters of bond law $\tau(s)_{cr}$ might change in this case.

A stepwise reduction of the bond stress similar to the simulations of yarn pull-out tests, see Fig. 5.12(a), leads at least in the medium range of τ_{fric} values to virtually no changes in the simulated results. The reason is that as long as sufficient stresses can be transferred to the core layers in the load transfer range at both ends of the bar element chains, and no pull-out mechanisms occur, the stress variations in the core layers are relatively small between the cracks, see also Fig. 5.16 (c,d). Furthermore, the influence of the core layers on the load-bearing behaviour of the composite decreases towards the innermost core layer.

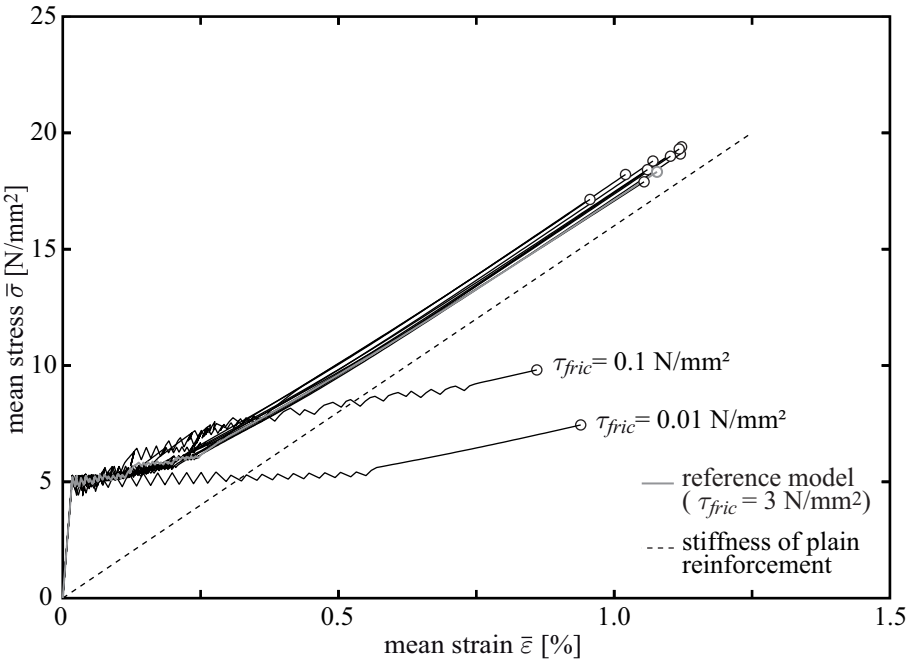

Figure 5.22.: $\overline{\sigma}$-$\overline{\varepsilon}$ relations for different values of τ_{fric} in bond law $\tau(s)_{rr}$ in the reinforcement core

Thus, the bond law $\tau(s)_{rr}$ with constant values of τ_{fric} is applied between all reinforcement layers in the following.

Except for very low values of τ_{fric}, the $\overline{\sigma}$-$\overline{\varepsilon}$ relations are similar to the reference case, see Fig. 5.22. However, particular characteristics of the load-bearing behaviour show differences for varied values of τ_{fric}. In Fig. 5.23(a), the normal stresses σ_r in the sleeve layer as well as the innermost and outermost core layers right after the first concrete crack occurred are shown. It is observable that with increasing values of τ_{fric} in the reinforcement core, the normal stress in the sleeve layer decreases while the normal stresses in the core layers increase. For large values of τ_{fric}, the stresses converge to a certain value. For considerably larger values of τ_{fric} than applied in this parametric study, it can be assumed that the values of the normal stresses adjust to homogeneity, because the load transfer changes from a local to a global load sharing.

Regarding the ultimate mean stresses and mean strains, it can be concluded that values of τ_{fric} larger than 2-3 N/mm^2 do not improve the structural performance significantly. In Fig. 5.23(b), it can be seen that up to this threshold the ultimate mean stresses and mean strains strongly increase with increasing τ_{fric}. With larger values of τ_{fric}, these values only increase slightly. This can be explained with the successive stress transfer from the outer reinforcement layers to the inner layers, compare Figs. 5.16(c,d), where the absolute transferable bond stress is limited by the bond law $\tau(s)_{cr}$ between concrete and sleeve layer. An upper limit for the ultimate stress is given with the case of a mono-filament where only shear deformations but no slip between the layers occur. In this case, the stress transferable to the reinforcement is still limited by the bond law $\tau(s)_{cr}$ of the concrete-reinforcement interface. However, for low values of τ_{fric}, the ultimate stresses and strains are considerably reduced. A lower limit is given with the case of $\tau_{fric} \to 0$ where only the sleeve layer participates in crack

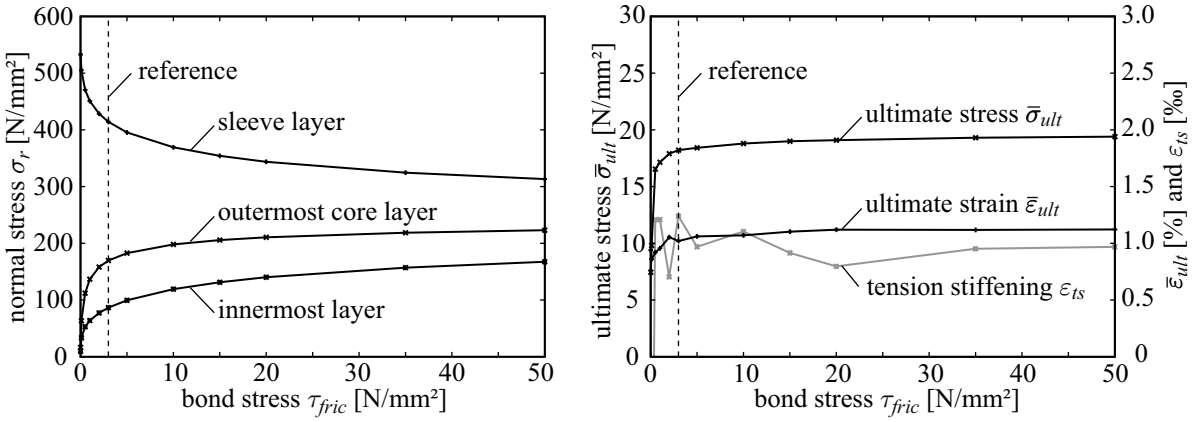

(a) Normal stresses in selected reinforcement layers in the cracked cross section right after the first concrete crack

(b) Ultimate mean stresses $\bar{\sigma}_{ult}$ and strains $\bar{\varepsilon}_{ult}$ as well as tension stiffening ε_{ts}

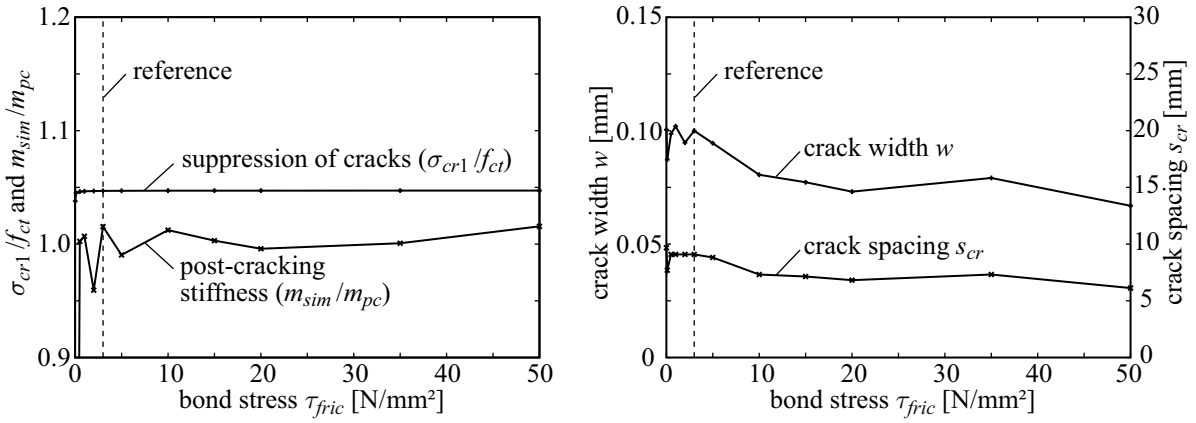

(c) Suppression of cracks and post-cracking stiffness before ultimate failure

(d) Mean crack width at $\bar{\varepsilon}$=1 % and mean crack spacing in the ultimate state

Figure 5.23.: Various simulation results for different values of the frictional bond stress in the bond law $\tau(s)_{rr}$ in the reinforcement core

bridging. This leads to significantly increased normal stresses in the sleeve layer at the crack and correspondingly reduced ultimate stresses and strains. This case is also very similar to a reduced reinforcement ratio, compare Section 5.3.1.3. In Fig. 5.23(b), it is also observable that the course of the ultimate strains is not as smooth as that of the ultimate stresses. This can be explained by different concrete crack distributions in each simulation leading to different participation of the concrete on load-bearing between cracks, which results in different tension stiffening.

Crack spacing and correspondingly also crack widths, which are are shown in Fig. 5.23(d), decrease only little with increasing τ_{fric}, especially for low values of τ_{fric} as occurring in unimpregnated yarns. As already pointed out, the crack patterns differ for different τ_{fric}, which leads to non-smooth relations in Fig. 5.23(d). Furthermore, it can be seen in Figs. 5.23(c) that suppression of cracks is virtually not influenced by τ_{fric}. This applies also for tension stiffening, see Fig. 5.23(b), and the slope in the post-cracking state, see Fig. 5.23(c), for τ_{fric} values larger than approximately 0.5 N/mm². For lower values of τ_{fric}, the core layers participate virtually not in crack bridging as already pointed out. Thus, only the stiffness of

the sleeve layer is available in the post-cracking state, which leads to an apparently deficit of stiffness in the post-cracking state, see Fig. 5.23(c), and even negative tension stiffening, see Fig. 5.23(b). This can be also seen well in the $\overline{\sigma}$-$\overline{\varepsilon}$ relations in Fig. 5.22. However, it is questionable if such low bond stresses occur in practice. Furthermore, a deficit of stiffness also appears with coated yarns where definitely larger bond stresses occur in the core of the yarns. Moreover, the simulations show that the core layers are more than 1 mm pulled into the concrete at the ends of the concrete bar element chain, which should be observable in reality but is not reported from the experiments. Thus, low available bond stresses in the yarn core are supposedly not responsible for the deficit of stiffness in the post-cracking state and negative tension stiffening occasionally appearing. In the current parametric study, the reinforcement ratio of 2 % was fixed. However, it can be supposed that for other reinforcement ratios similar results are obtained.

5.3.2.2. Influence of the adhesive bond strength

In this section, the influence of the bond strength τ_{max} in the bond law $\tau(s)_{cr}$ between the concrete and the sleeve layer, see Fig. 5.13, is studied to show the effect of a bond improvement in the fill-in zone on the load-bearing characteristics of the composite. The respective $\overline{\sigma}$-$\overline{\varepsilon}$ relations are shown in Fig. 5.24.

In Fig. 5.25(a), the normal stresses σ_r in the sleeve layer as well as the outermost and innermost core layers right after occurrence of the first concrete crack are shown for values of τ_{max} in a range of 3 up to 50 N/mm^2. The normal stresses in the sleeve layer increase with increasing values τ_{max} and converge towards a certain value. The reason is that besides τ_{max} also the initial bond modulus increases because the slip s_{max} corresponding to τ_{max} is kept constant. Thus, the sleeve layer is increasingly stiffer bonded to the concrete, which increases also the loading of the sleeve layer in case of concrete cracking. An upper limit is given with a direct connection of the sleeve layer to the concrete. Neglecting participation of the core layers on crack bridging, the maximum stress in the sleeve fibres σ_{sleeve} can be estimated by a simple balance of forces between the concrete and the sleeve layer:

$$f_{ct}A_c = \sigma_{sleeve}A_{sleeve} \;\Rightarrow\; \sigma_{sleeve} = \frac{f_{ct}A_c}{A_{sleeve}} = \frac{f_{ct}}{V_{f,sleeve}} = \frac{5\,\mathrm{N/mm^2}}{0.36 \cdot 0.02} = 694\,\mathrm{N/mm^2}. \quad (5.7)$$

The value $V_{f,sleeve}$ is the fibre volume content of the sleeve fibres, which is 36 % of the total reinforcement ratio of 2 %. From Eq. (5.7), it can be also concluded that with the assumed size of the sleeve layer of 36 % and the assumed reinforcement tensile strength f_{rt}=1000 N/mm^2 simultaneous failure of the sleeve layer with concrete cracking will not occur. However, if $V_{f,sleeve}$ or f_{rt} are reduced sufficiently such a simultaneous failure can occur with relatively large bond strength values. This also reduces the ultimate stresses and strains as it was already shown in previous investigations, see [Hartig et al. 2008]. A lower limit is given with a pull-out of the reinforcement if the bond stresses in $\tau(s)_{cr}$ are too small to resist the forces released in the case of concrete cracking. This case is not included in the results presented in Fig. 5.25.

Corresponding to the increasing stresses in the sleeve layer, the stresses in the core layers decrease, in general. However, the normal stresses in the outermost core layer right after

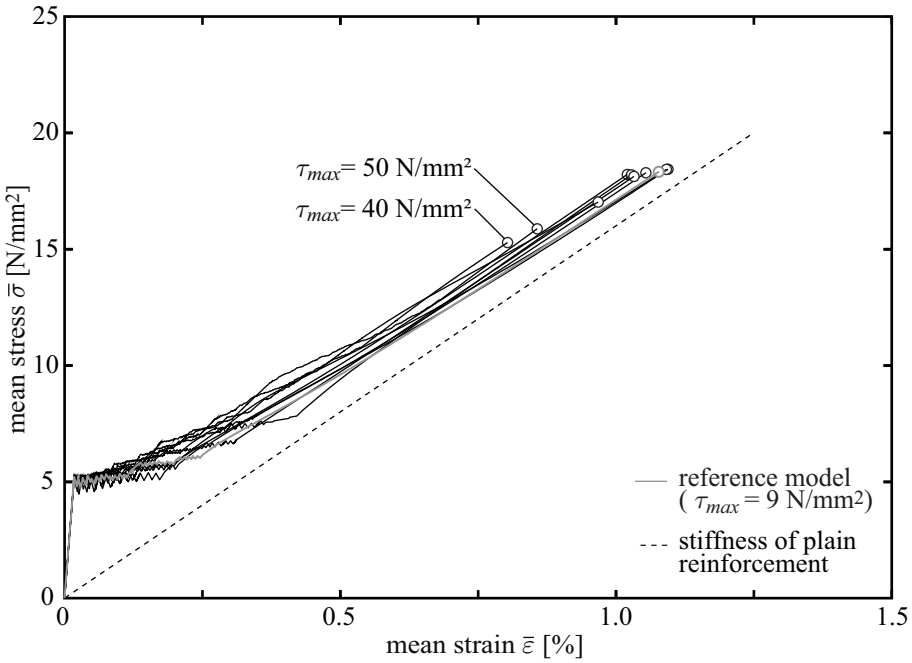

Figure 5.24.: $\overline{\sigma}$-$\overline{\varepsilon}$ relations for different bond strength values τ_{max} between concrete and sleeve layer

the development of the first concrete crack increase in the cracked cross section slightly for increasing bond stresses $\tau_{max} < 6\,\mathrm{N/mm^2}$, see Fig. 5.25(a). This can be explained as follows. In case of $\tau_{max} < 6\,\mathrm{N/mm^2}$, the slip between the concrete and the sleeve layer is relatively large, which leads to a large activated stress transfer length. This results also in larger stress transfer lengths to and between the cores layers, which increase in general towards the innermost core layer. Thus, the core layers are relatively strong activated. In case of $\tau_{max} > 6\,\mathrm{N/mm^2}$, the stress transfer length between concrete and sleeve layer becomes smaller because of an increasing bond stiffness. Thus, there is also a smaller stress transfer length between the sleeve layer and the outermost core layer, which leads to lower bond stresses transmitted to the core and to smaller normal stresses in the core layers. The innermost core layer is less affected by the change of the maximum bond stress τ_{max} between the concrete and the sleeve layer because the influence of the concrete cracks and the respective stress transfer length between the reinforcement layers decrease towards the innermost core layer. This leads to continuously decreasing normal stresses in the innermost core layer with increasing values of τ_{max}.

The ultimate stresses and strains increase slightly up to $\tau_{max} \approx 20\,\mathrm{N/mm^2}$, see Fig. 5.25(b). This is quite unexpected as the stress differences between the sleeve layer and core layers at the cracks should increase with increasing τ_{max}, which, in turn, should reduce the ultimate stress. However, these large stress concentrations are only present right after concrete cracking. With increasing loading, the differences in the normal stresses at the cracks between the sleeve layer and the core layers decrease. To visualise the stress development, the stresses in the reinforcement layers in the cross section where the reinforcement fails are plotted in Fig. 5.26 versus $\overline{\varepsilon}$ corresponding to Fig. 5.24. It can be seen that the core participates stronger in crack bridging with increased loading, which leads to a reduction of the stress differences between the reinforcement layers and to not decreasing ultimate stresses. In fact,

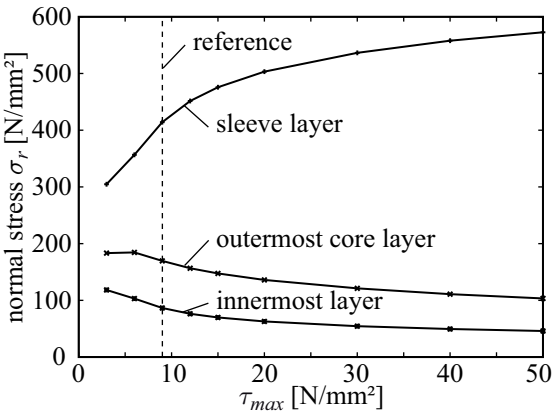

(a) Normal stresses in selected reinforcement layers in the cracked cross section right after the first concrete crack

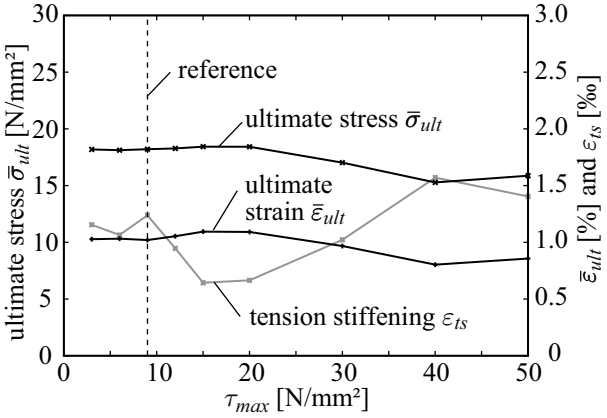

(b) Ultimate mean stresses $\overline{\sigma}_{ult}$ and strains $\overline{\varepsilon}_{ult}$ as well as tension stiffening ε_{ts}

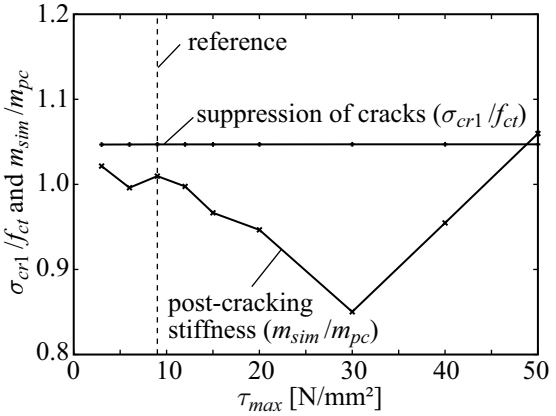

(c) Suppression of cracks and post-cracking stiffness before ultimate failure

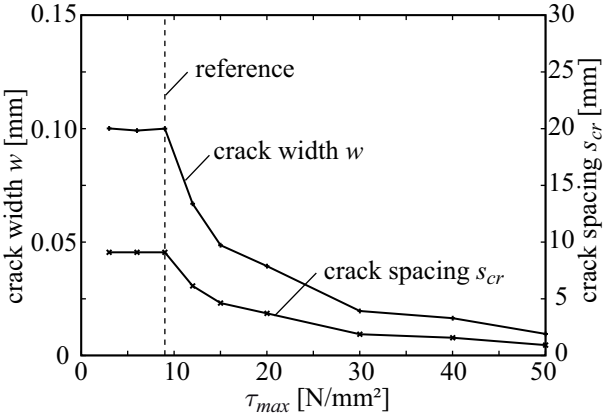

(d) Mean crack width at $\overline{\varepsilon}$=1 % and mean crack spacing in the ultimate state

Figure 5.25.: Various simulation results for different maximum bond stress values τ_{max} between concrete and sleeve layer

rather a decreasing participation of the sleeve layer occurs, which results from the successive delamination of the concrete-sleeve layer interface. This can be seen in Fig. 5.27, which shows the bond stresses in the interfaces between the different bar element chains in case of a single crack and right before ultimate failure on a length of 20 mm in the centre part of the model for τ_{max} values of 9 N/mm² and 40 N/mm². The corresponding normal stress distributions are similar to the Figs. 5.16 (c,d). In the case of a single crack, the bond stress distributions are qualitatively similar for both bond strength values, see Figs. 5.27 (a,c). It can be seen that the bond stresses transferred in the interface between concrete and sleeve layer according to bond law $\tau(s)_{cr}$ are considerably larger than in the interfaces between the reinforcement layers according to bond law $\tau(s)_{rr}$. With increasing deformations, the peaks equal to τ_{max} move towards the centres between the cracks. Correspondingly, the frictional tail of bond law $\tau(s)_{cr}$ is reached at the crack faces. This results also in larger stress transfer lengths, which reduce stress concentrations in the reinforcement layers in the cracked cross sections. In the case of τ_{max}=9 N/mm², large parts of the concrete-sleeve layer interface are already in the frictional tail of bond law $\tau(s)_{cr}$ in the ultimate state, see Fig. 5.27 (b). This reduces the stress concentrations at the cracks and leads to relatively large ultimate stresses.

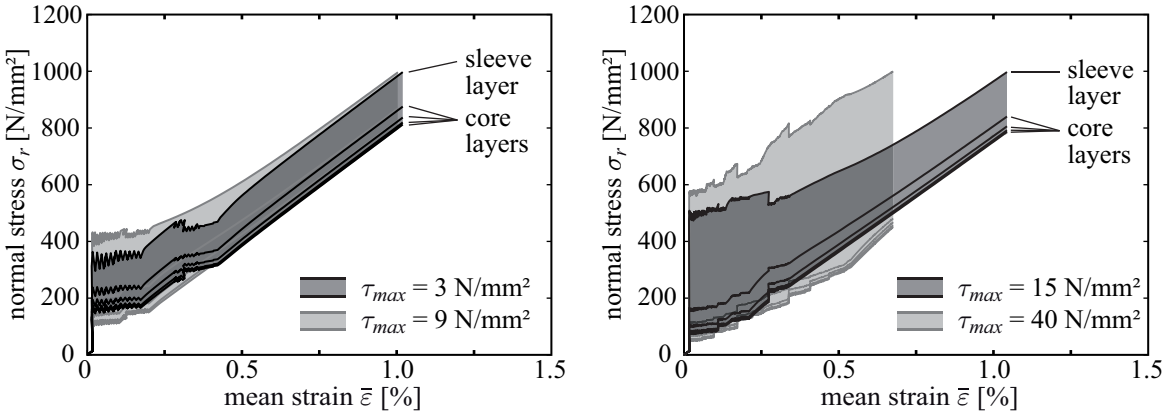

(a) Low values of τ_{max}

(b) High values of τ_{max}

Figure 5.26.: Reinforcement stress distributions at a crack with increasing $\bar{\varepsilon}$ for various τ_{max}

In contrast, Fig. 5.27 (d) shows that in the case of τ_{max}=40 N/mm^2 the transition to the frictional tail has only started in the ultimate state. Thus, relatively large stress concentrations exist on an already high normal stress level in the sleeve layer, which results in earlier failure and low ultimate stresses and strains. This example is typical for values of τ_{max} larger than 20 N/mm^2. In Fig. 5.26(b), it can be seen that during the state of multiple cracking large differences between the stresses in the sleeve layer and the core layers exist. After concrete cracking has finished, the stress differences decrease similar to the case of low τ_{max}. However, the tensile strength is reached in the sleeve layer before the convergence of the stresses in the reinforcement layers is finished. Thus, for large values of τ_{max} the improved bond leads to a reduction of load-bearing capacity of the composite. This was already shown in [Hartig et al. 2008] and also in [Konrad & Chudoba 2009] corresponding results are presented. As a result, it is often not advantageous in practice to achieve very stiff bond with high bond strength, because this can result in reduced strength of the composite. Nevertheless, the bond must be sufficient to prevent pull-out of the reinforcement at the available load transfer length, which is 0.1 m at both ends in the model. Alternatively, the available stress transfer or anchorage lengths have to be increased.

Crack widths and crack spacing do virtually not change up to a value $\tau_{max} \approx 9$ N/mm^2, see Fig. 5.25(d). Subsequently, a strong decrease is observable with increasing τ_{max}. For large values of τ_{max}, crack width and crack spacing converge asymptotically to zero. For the medium range of τ_{max}, the increasing bond strength results in larger stresses transferred to the concrete between cracks. This leads to additional cracking and reduced crack spacing and crack widths. Supposedly, the additional forces transferred to the concrete are not sufficient to reduce crack spacing for increasing low values of $\tau_{max} < 9$ N/mm^2. For large values, crack spacing is already small and, thus, the bond stresses transferred to the concrete have to increase excessively to compensate the decreasing transfer length, which limits the minimum crack spacing. Because of the small crack spacing, the bar element length in the simulations with τ_{max} equal to 20 N/mm^2 and 30 N/mm^2 was reduced to 0.1 mm and for τ_{max} equal to 40 N/mm^2 and 50 N/mm^2 to 0.05 mm to achieve more accurate results.

Moreover, the results of the simulations show that suppression of cracks is not influenced by the bond strength τ_{max}, see Fig. 5.25(c). The stiffness in the ultimate state as shown in

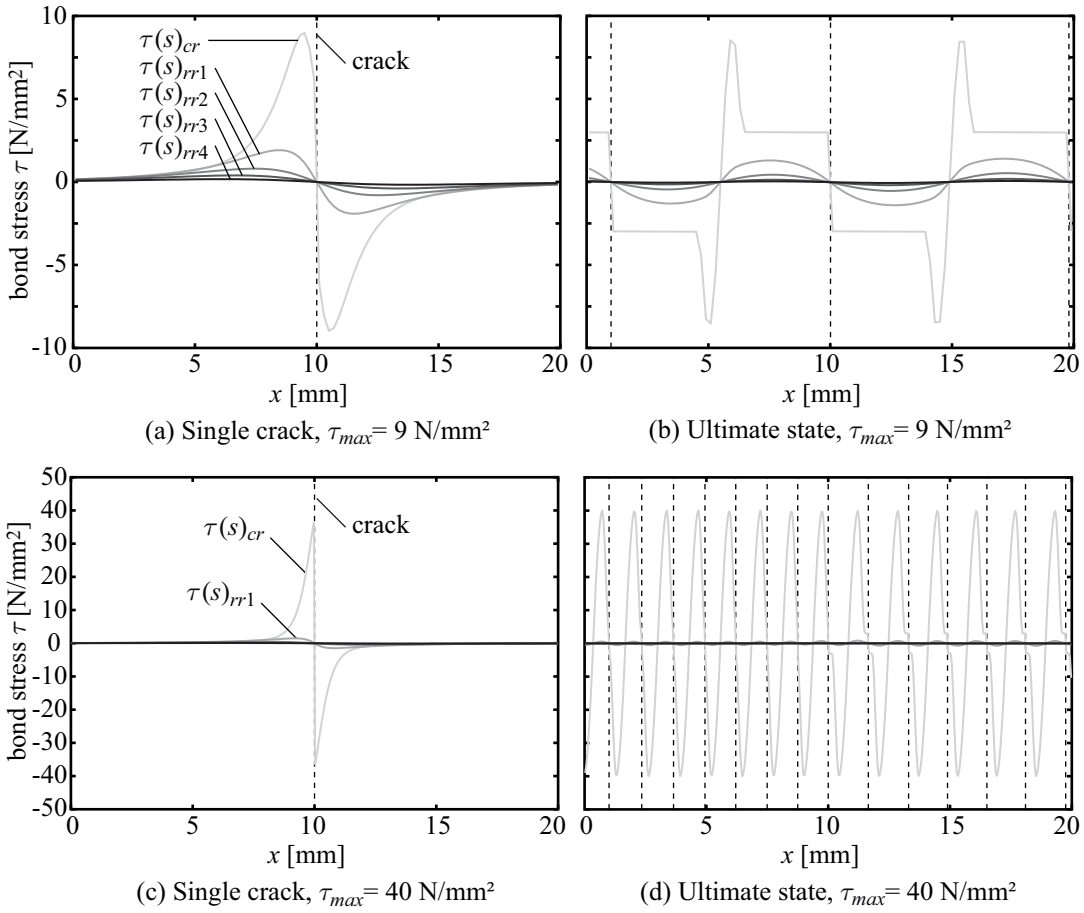

Figure 5.27.: Bond stresses in longitudinal direction in the centre part of the model at a single crack and in the ultimate state for different τ_{max} in bond law $\tau(s)_{cr}$

Fig. 5.25(c) is also virtually not influenced for $\tau_{max} < 9\,\mathrm{N/mm^2}$. For $\tau_{max} > 9\,\mathrm{N/mm^2}$, the stiffness decreases up to $\tau_{max} > 30\,\mathrm{N/mm^2}$ and increases again for further increased τ_{max} up to $50\,\mathrm{N/mm^2}$. This is caused by the initially "wavy" course of the $\overline{\sigma}$-$\overline{\varepsilon}$ relations in the post-cracking state, which shows at the very beginning an increase of the slope, which subsequently decreases and finally increases again. This is caused by the initially increasing activation of bond in bond law $\tau(s)_{cr}$ combined with subsequently successive degradation. For the values of τ_{max} equal to $40\,\mathrm{N/mm^2}$ and $50\,\mathrm{N/mm^2}$, the $\overline{\sigma}$-$\overline{\varepsilon}$ relations are in the ultimate state still in the initially increasing part of the post-cracking state. For τ_{max}=$30\,\mathrm{N/mm^2}$, the $\overline{\sigma}$-$\overline{\varepsilon}$ relation is in the ultimate state in the decreasing "intermediate" post-cracking state, which leads to the minimum value of post-cracking stiffness. Thus, it is more a pseudo-effect resulting from reinforcement failure before reaching the final slope of the $\overline{\sigma}$-$\overline{\varepsilon}$ relation in the post-cracking state. Similar arguments apply also for tension stiffening, see Fig. 5.25(b), which shows a quite irregular evolution for increasing τ_{max}.

5.3.2.3. Influence of scatter in bond strength

Hitherto, the model was purely deterministic, i. e. scatter in geometrical and material properties was not taken into account. In the following simulations, the spatial distribution of the

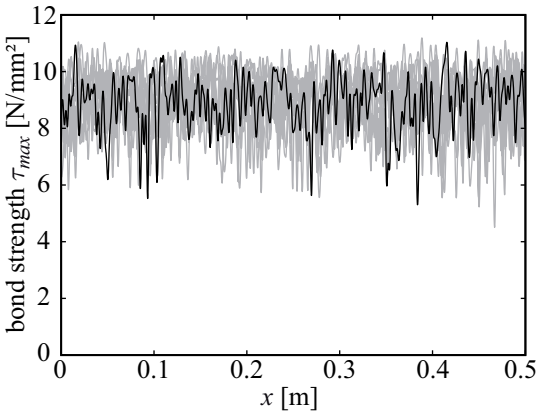

Figure 5.28.: Realisations of random fields for τ_{max} in bond law $\tau(s)_{cr}$

bond strength τ_{max} of bond law $\tau(s)_{cr}$ is modelled stochastically. Therefor, the random field approach as presented in Section 4.3.2.2 is applied. Apart from that, the model corresponds to the reference model as specified at the end of Section 5.3.1.2. For the simulation of the random fields, a correlation length L_{corr}=2 mm is assumed, which corresponds to twice the maximum aggregate size of the concrete. This has to be seen as a first approach as corresponding experimental observations are missing. The parametrisation of the bond laws is chosen corresponding to Fig. 5.13. For the bond strength τ_{max} of the bond law $\tau(s)_{cr}$, which has an expected value of 9 N/mm^2 corresponding to the reference model, a relative standard deviation of 10 % is assumed. Respective experimental data is also missing. Furthermore, τ_{max} is modelled with a two-parametric Weibull distribution, see Appendix A.3. This type of distribution function is chosen because a strong correlation of τ_{max} with the tensile strength of the concrete f_{ct} is assumed where a Weibull distribution is applied. The case of scattering f_{ct} is studied in Section 5.3.4.2.

The realisations of the random fields are computed at the positions of the integration points of the bar elements, which is advantageous for simulations of cross-correlated random fields. As the integration point positions of the bond elements and the respective bar elements do not coincide, an interpolation of the τ_{max} values is necessary. This is performed with the calculation of the mean value of τ_{max} at the positions of the integration points of the two neighbouring bar elements of the bond element under consideration. In order to reduce disturbances of the random fields at the boundaries, the discretisation range is artificially extended for 0.02 m at both ends of the model. Ten realisations of the random field, which are used in respective simulations, are shown in Fig. 5.28. One realisation corresponding to the black $\overline{\sigma}$-$\overline{\varepsilon}$ relation shown subsequently in Fig. 5.29 is emphasised in black.

For the statistical evaluation of the simulated results, a sufficiently large number of samples and corresponding simulations is necessary to achieve results on a certain confidence level. This is beyond the scope of this work where only the influence of certain effects and mechanisms on the load-bearing behaviour of TRC is investigated. Thus, the results of the simulations are primarily evaluated qualitative, in the following. In Fig. 5.29, the $\overline{\sigma}$-$\overline{\varepsilon}$ relation as results of the simulations with different realisations of scattering τ_{max} are shown. At least in the used parameter combination, the stochastic modelling of τ_{max} has only minor influence on the $\overline{\sigma}$-$\overline{\varepsilon}$ relations. As the bond laws influence the load transfer length between concrete and reinforcement, only the crack plateaus of the concrete cracks, which develop

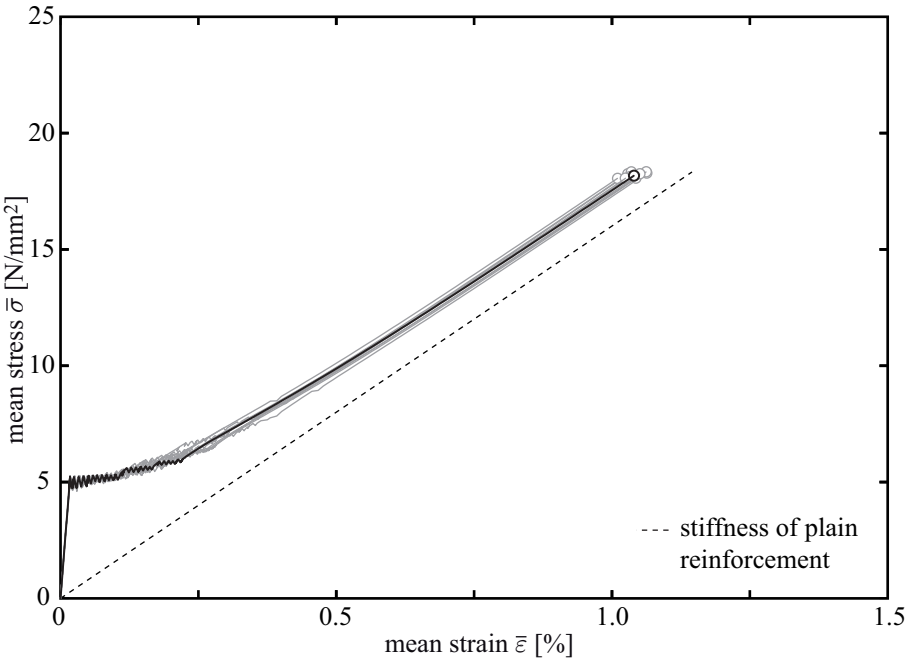

Figure 5.29.: $\overline{\sigma}$-$\overline{\varepsilon}$ relations for different realisations of scattering values of τ_{max} in bond law $\tau(s)_{cr}$

between existing cracks, show scatter in the $\overline{\sigma}$-$\overline{\varepsilon}$ relations. The cracking stresses in the $\overline{\sigma}$-$\overline{\varepsilon}$ relations do not significantly vary as in the cases of stochastically modelled f_{ct} and E_c, see Sections 5.3.4.2 and 5.3.4.4, but several crack plateaus with almost constant stresses develop. This can be explained with the constant value of f_{ct}, which does not allow for such stress variations. The stiffness in the post-cracking state shows also virtually no variations between different simulations, see Fig. 5.29. However, tension stiffening varies, which is essentially a result of different crack spacing due to different numbers of cracks. Considering also results of simulations with a similar model but increased deterministic f_{ct} published in [Hartig & Häussler-Combe 2010], it can be concluded that the variations in tension stiffening increase with increasing f_{ct}. The reason is that variations in crack spacing increase with increasing f_{ct} because less cracks can develop and the positions of the first cracks control the positions of subsequent cracks. As a result, it can be concluded that the scatter in τ_{max} of the concrete-sleeve layer interface influences the load-bearing response of the composite but it is of minor importance.

5.3.2.4. Influence of variation of slip s_{max} corresponding to τ_{max} in bond law $\tau(s)_{cr}$

In the previous sections, the influences of variations in bond stress parameters of the bond laws $\tau(s)_{cr}$ and $\tau(s)_{rr}$ on the load-bearing response of TRC were studied. However, each bond stress parameter has a corresponding slip value, which was kept constant. In this section, variations of the slip s_{max} corresponding to the bond strength τ_{max} in bond law $\tau(s)_{cr}$ are analysed. Therefor, s_{max} is varied over several orders of magnitude in a range of $1 \cdot 10^{-3}$ m down to $1 \cdot 10^{-7}$ m. Larger values seem to be unrealistic, while lower values lead to severe problems in the numerical solution during the simulations because of large gradient changes in the bond law in the vicinity of s_{max}, which prevents an investigation.

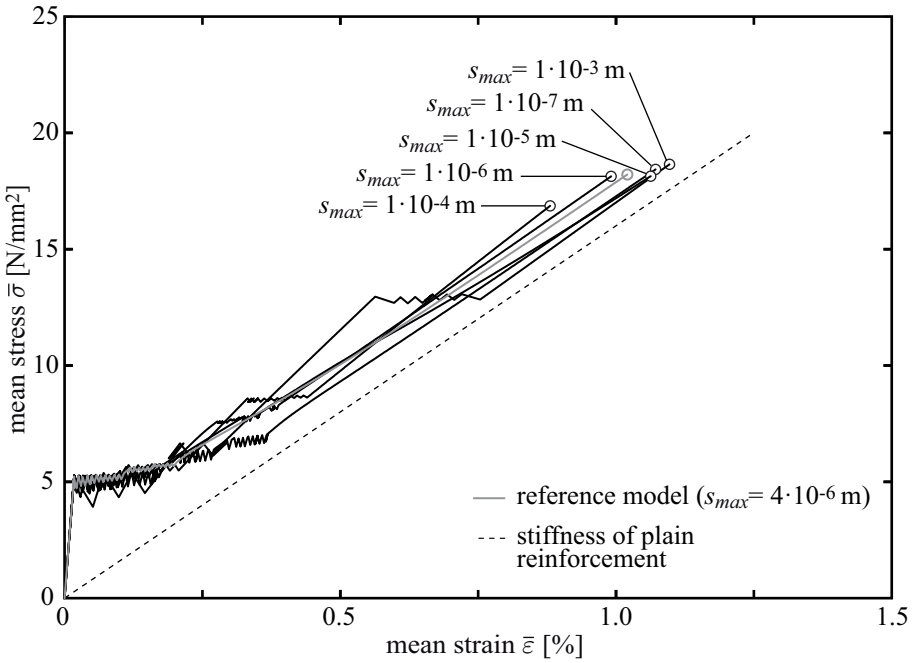

Figure 5.30.: $\overline{\sigma}$-$\overline{\varepsilon}$ relations for different s_{max} corresponding to τ_{max} in bond law $\tau(s)_{cr}$

In Fig. 5.30, the $\overline{\sigma}$-$\overline{\varepsilon}$ relations for the different values of s_{max} are shown. It can be seen that especially for large values of s_{max}, e. g. s_{max}=1 mm, the $\overline{\sigma}$-$\overline{\varepsilon}$ relations show relatively large deviations compared to the reference case, especially concerning the cracking behaviour. In Fig. 5.31, additional results of the simulations are shown where for the abscissae a logarithmic scale is used. Fig. 5.31(a) shows the stresses σ_r in the reinforcement after the first concrete crack in the cracked cross section. It can be seen that for a value of s_{max}=1 mm, which is the largest value under consideration, the stresses are almost equal in all layers. The reason is that due to the low bond stiffness only low bond stresses, which are considerably lower than τ_{max}, are transferred in the concrete-sleeve layer interface. With increasing bond stiffness corresponding to decreasing s_{max}, the differences in the stresses between the reinforcement layers increase because higher bond stresses are transferred between the concrete and sleeve layer. As a result, the stress in the outermost core layer increases only moderately while the innermost core layer is virtually not influenced. Thus, the increasing stress differences originate primarily from increasing stresses in the sleeve layer. Furthermore, it can be seen in Fig. 5.31(a) that the stress increase in the sleeve layer proceeds only up to a value between 10^{-5} m and 10^{-6} m. With lower values of s_{max}, the stress in the sleeve layer decreases again, which can be explained with the exceeding of the bond strength τ_{max} on an increasing stress transfer length due to an increasing bond stiffness but constant bond strength. This means that right after concrete cracking, a bond stress distribution similar to Fig. 5.27 (b) with frictional load transfer in a part of the concrete-sleeve layer interface is present while for larger values of s_{max} the interface is still in the adhesive state similar to Fig. 5.27 (a).

The ultimate stresses and strains are only influenced insignificantly by varied s_{max}, as it can be seen in Fig. 5.31(b). The variations of the ultimate strains can be also assessed by the course of tension stiffening, which behaves reversed proportional to the ultimate strains, see Fig. 5.31(b). Also suppression of cracks is virtually not influenced by increasing bond stiffness or decreasing s_{max}, respectively, see Fig. 5.31(c). The stiffness at the end of the post-

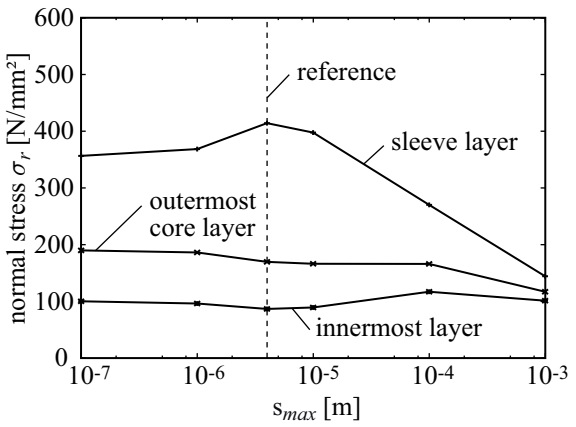

(a) Normal stresses in selected reinforcement layers in the cracked cross section right after the first concrete crack

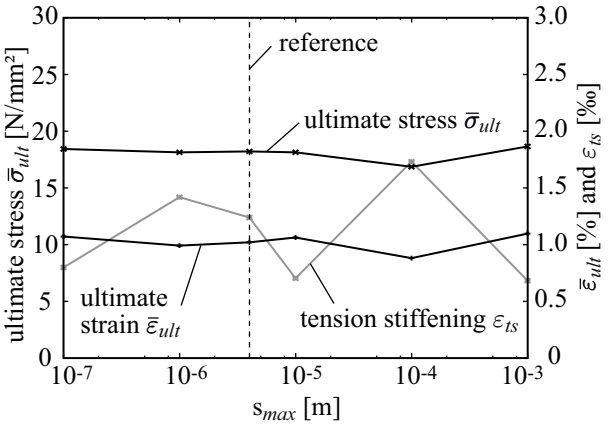

(b) Ultimate mean stresses $\bar{\sigma}_{ult}$ and strains $\bar{\varepsilon}_{ult}$ as well as tension stiffening ε_{ts}

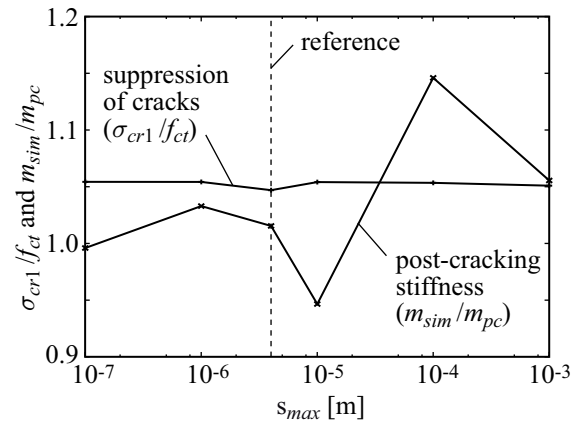

(c) Suppression of cracks and post-cracking stiffness before ultimate failure

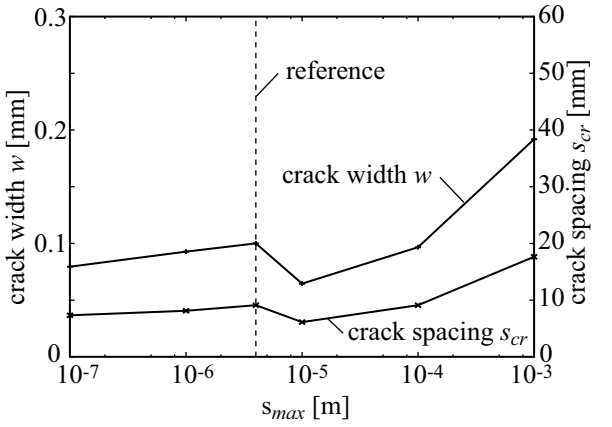

(d) Mean crack width at $\bar{\varepsilon}$=1 ‰ and mean crack spacing in the ultimate state

Figure 5.31.: Various simulation results for different s_{max} corresponding to τ_{max} in bond law $\tau(s)_{cr}$

cracking state shows no clear trend for varied s_{max}, see Fig. 5.31(c). The variations result from different cracking plateaus at different $\overline{\sigma}$ levels and a different transition to the linear course in the post-cracking state after finished concrete cracking, respectively. Crack width and crack spacing decrease with decreasing s_{max}, see Fig. 5.31(d). Therefor, similar explanations as for the stress distribution in the reinforcement layers in Fig. 5.31(a) concerning the stress transfer length are valid. It can be also seen that a local increase of crack width and crack spacing occurs for values of s_{max} where the reinforcement stress in the sleeve layer has its maximum. Finally, it can be concluded that the load-bearing response of the composite is relatively insensitive to variations of s_{max} if it is chosen in a reasonable range.

5.3.3. Influence of material properties of the reinforcement

In the subsequent sections, the influence of the material properties of the reinforcement on the load-bearing response of the composite is studied. However, the investigations are lim-

ited to the properties related to the stiffness of the reinforcement. The analysis of the failure behaviour of the reinforcement is not a part of the current studies. The stiffness of the reinforcement is proportional to the reinforcement ratio, which was studied in Section 5.3.1.3, and the Young's modulus. However, the reinforcement ratio also influences the bond surface area, which will lead to different load-bearing characteristics of the composite compared to Section 5.3.1.3. Moreover, the parametric studies are limited again to one special reinforcement ratio, which is V_f=2 % corresponding to the reference model defined at the end of Section 5.3.1.2. For predictions of the load-bearing response with different reinforcement ratios, the results in Section 5.3.1.3 have to be taken into account, too.

5.3.3.1. Influence of Young's modulus of reinforcement

The Young's modulus E_r is different for most reinforcement materials, e. g., glass, carbon or steel. In the following, a parametric study is carried out to show the influence of E_r, which is varied in a range of 10 000 N/mm^2, e. g. typical for polymeric fibres, up to 300 000 N/mm^2, e. g. typical for carbon fibres, on the load-bearing properties of the composite. Thus, cases with E_r lower and larger than the applied Young's modulus of concrete E_c= 28 500 N/mm^2 are considered. It is assumed that geometrical and bond properties of the different reinforcement materials are identical, which is not necessarily the case in reality. The $\overline{\sigma}$-$\overline{\varepsilon}$ relations of the simulations are presented in Fig. 5.32.

In Fig. 5.33(a), the distributions of stresses σ_r in the reinforcement right after the first concrete crack occurred are shown for various E_r. It can be seen that in the case of low E_r the differences in the reinforcement stresses between the layers are small. This can be explained with relatively large deformations of the reinforcement in case of concrete cracking, which leads to a large activated stress transfer length of the reinforcement and a reduction of stress concentrations in the reinforcement layers at the concrete crack. With increasing E_r, the stress differences between the sleeve and the core layers increase. It is observable that this primarily results from the increasing stresses in the sleeve layer while the stresses in the reinforcement core change less. This can be explained with the stronger interface between concrete and sleeve layer, which results in combination with increasing E_r to increasing stress concentrations in the sleeve layer at the cracks.

Concerning the ultimate stresses, the stress concentrations in the sleeve layer after concrete cracking have only minor influence, see Fig. 5.33(b). This can be explained as already pointed out in Section 5.3.2.2 with a successive delamination of the concrete-sleeve layer interface, which results in a reduction of the differences in the stresses between the reinforcement layers. Nevertheless, ultimate stresses decrease slightly with increasing E_r. The effect is much stronger for the ultimate strains, which decrease considerably with increasing E_r. This results primarily from the increased reinforcement stiffness, which decreases the failure strain $\varepsilon(f_{rt})$ of the reinforcement as the reinforcement tensile strength f_{rt} is kept constant. It was already pointed out in Section 5.3.1.3 that $\varepsilon(f_{rt})$ is the upper limit for $\overline{\varepsilon}_{ult}$ if yarn waviness is not taken into account.

Crack spacing decreases with increasing E_r, see Fig. 5.33(d). However, although E_r increases for more than one order of magnitude, crack spacing only reduces by half. This can be explained with limited bond stresses, which can be transferred over the concrete-reinforcement

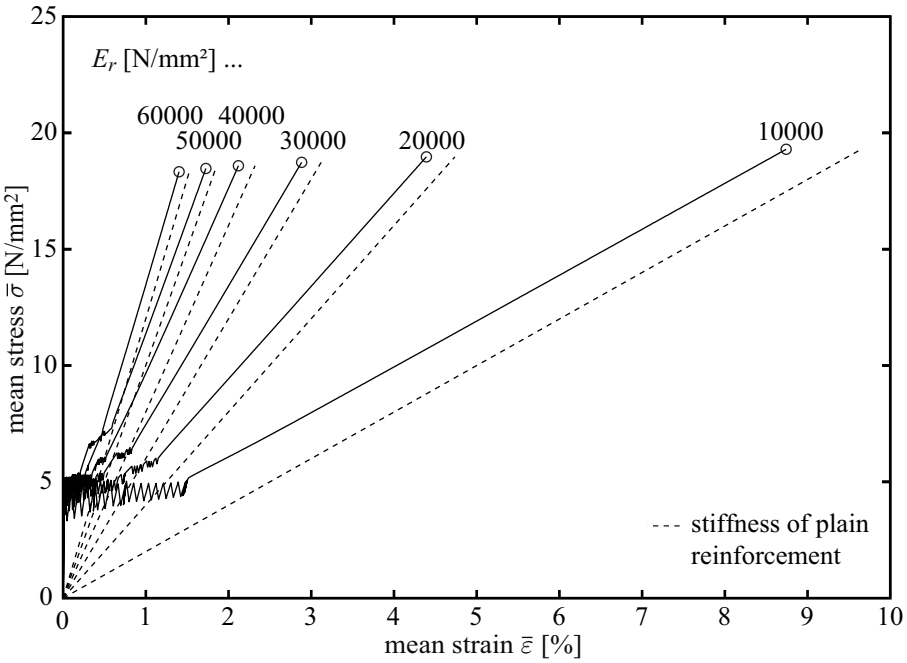

(a) Low values of E_r

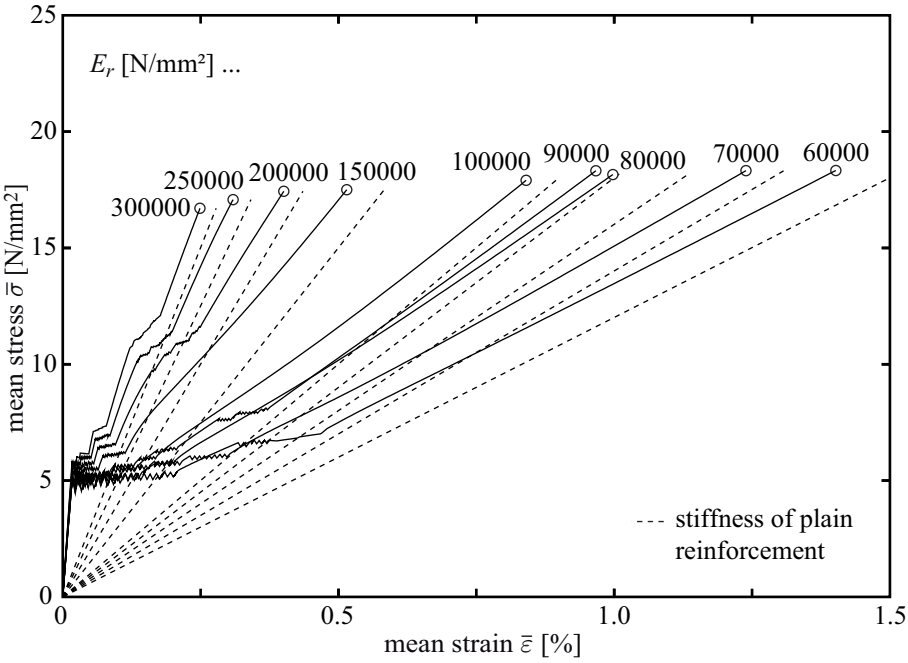

(b) High values of E_r

Figure 5.32.: $\overline{\sigma}$-$\overline{\varepsilon}$ relations for different E_r

interface. Nevertheless, the deformations of the reinforcement increase with decreasing E_r, which results in strongly increasing crack widths with decreasing E_r as already pointed out, see Fig. 5.33(d). Moreover, tension stiffening increases with decreasing E_r, which is a consequence of the increasing crack spacing and allows for a stronger participation of the concrete on load-bearing between cracks. Additionally, the Young's modulus of the concrete is larger compared to the reinforcement for very low E_r, which consequently increases the stiffening effect compared to the plain reinforcement stiffness. Suppression of cracks as shown

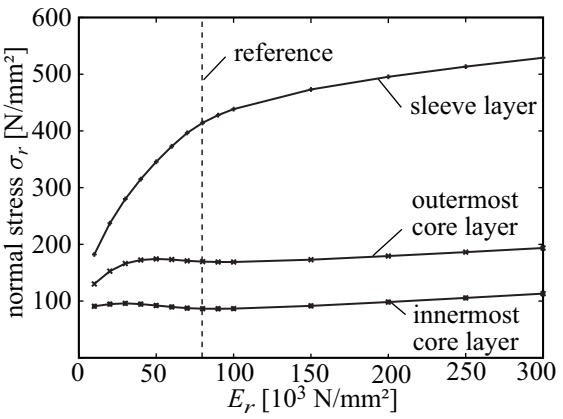

(a) Normal stresses in selected reinforcement layers in the cracked cross section right after the first concrete crack

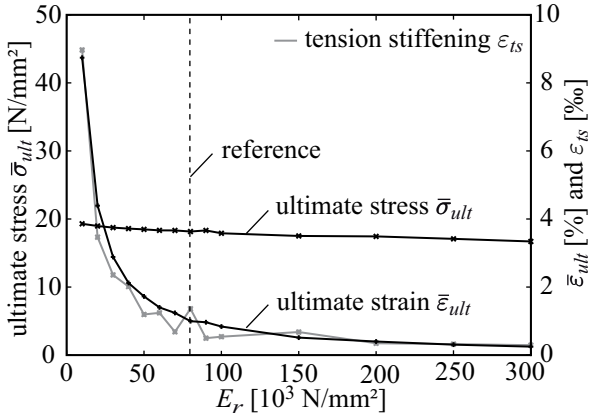

(b) Ultimate mean stresses $\overline{\sigma}_{ult}$ and strains $\overline{\varepsilon}_{ult}$ as well as tension stiffening ε_{ts}

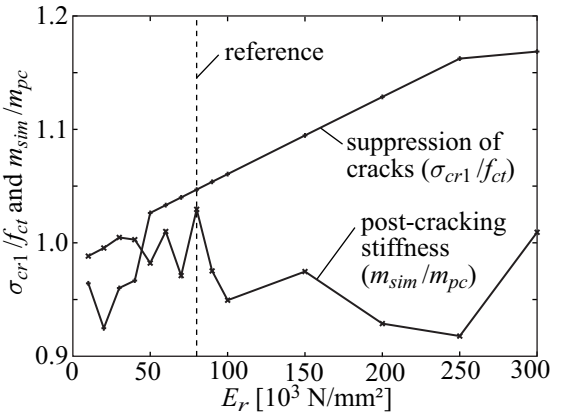

(c) Suppression of cracks and post-cracking stiffness

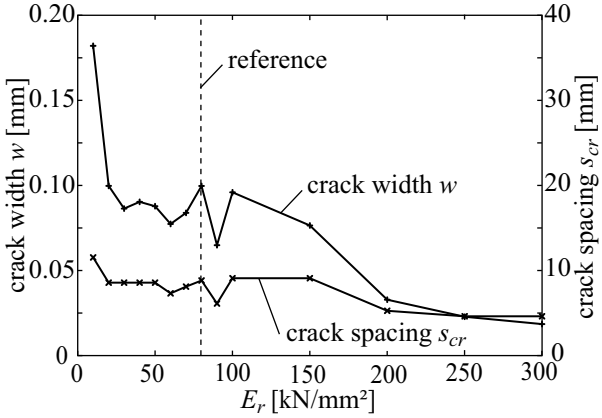

(d) Mean crack width at $\overline{\varepsilon}$=1 % and mean crack spacing in the ultimate state

Figure 5.33.: Various simulation results for different reinforcement Young's moduli E_r

in Fig. 5.33(c) increases with increasing E_r. For values of E_r smaller than 50 000 N/mm², Fig. 5.33(c) indicates "negative" suppression of cracks. However, this is only an artificial effect, which results from the data storage in the simulations where only the results of the step before the concrete crack occurred and of the recalculated system after concrete cracking are stored as mentioned in Section 5.3.1.3. The course of the post-cracking stiffness in the ultimate state, which is also observable in Fig. 5.33(c), shows no clear trend. For low values of E_r, the simulated stiffness m_{sim} coincides essentially with the theoretical value m_{pc} apart from normal variations resulting, e. g., from the determination of $\overline{\varepsilon}$ on a limited measurement range, which leads to an influence of $\overline{\varepsilon}$ by the positions of concrete cracks especially with a low number of cracks. For large values of E_r, an influence of the variations of the stiffness in the post-cracking state appears, which results from bond activation and degradation as already described in Section 5.3.2.2, leading to stronger variations of the post-cracking stiffness in the ultimate state.

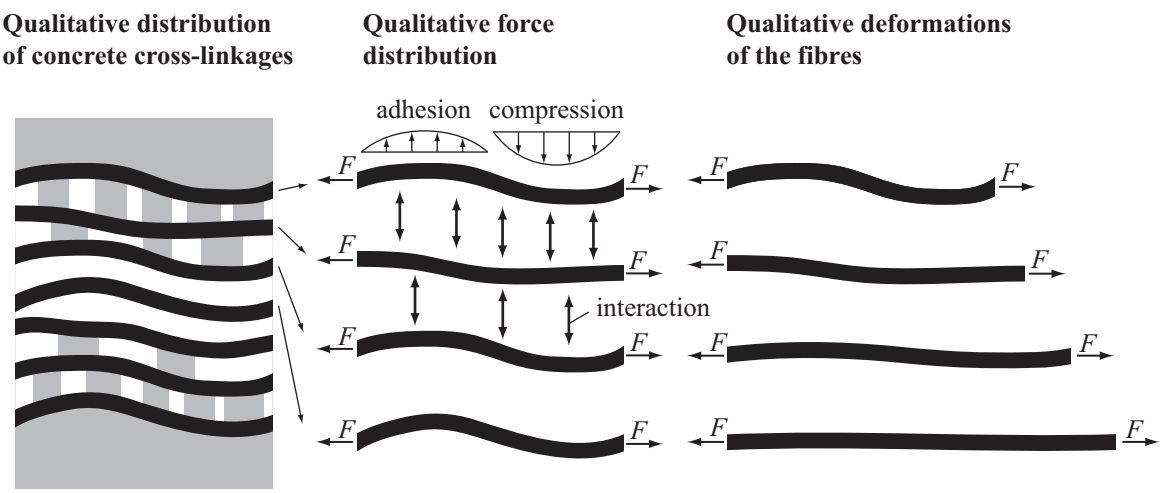

Figure 5.34.: Qualitative differences in deformation resistance of reinforcement fibres due to reducing concrete penetration towards the yarn core

5.3.3.2. Influence of waviness of reinforcement yarns

As already pointed out in Section 2.1.2, the multi-filament yarns usually exhibit a certain waviness. This results in an apparently reduced initial Young's modulus, which merges successively to the Young's modulus of single filaments. Sources of the waviness are an imperfect parallel alignment of the filaments in the yarn production process and often more importantly in the textile processing. With Eq. (4.19), a constitutive law for the reinforcement was established, which takes initial waviness into account by means of an exponential function merging to the linear course corresponding to the stretched state. For the definition of the parameters of the exponential function some considerations are made in the following.

When the yarns are embedded in concrete, only the filaments in the fill-in zone are continuously in contact with the concrete. Consequently, these filaments in the fill-in zone are restrained from an initial free deformation, which results in local transverse stresses and an earlier activation of these filaments. These transverse stresses can be tensile stresses due to adhesion or compressive stresses due to contact pressure. It can be assumed that larger stresses can be transferred due to contact pressure than due to adhesion. Towards the core of the yarn, the number of concrete cross-linkages reduces, which leads to a lower constraint of transverse deformations. For the innermost filaments, it is conceivable that on a certain length quasi no constraint of transverse deformations occurs, which results in an instantaneous stretching of the filaments. As a consequence, the initial stiffness is apparently higher for the filaments in the fill-in zone, but the stretched state is reached at a higher stress level compared to the filaments in the core of the yarn. These effects are shown qualitatively in Fig. 5.34 for transverse bond stresses only. The axial portions of the bond stresses are incorporated in the bond laws and are not shown in Fig. 5.34.

For the filaments in the core of the yarns this would mean that they deform initially without possessing significant stresses. It can be assumed that waviness is different in the filaments of a yarn because otherwise the initial stress-strain relation of plain multi-filament yarns would show some inelastic strains without a significant stress increase. However, this is not the case in Fig. 2.3(b). It is rather observable that also the stress increases significantly

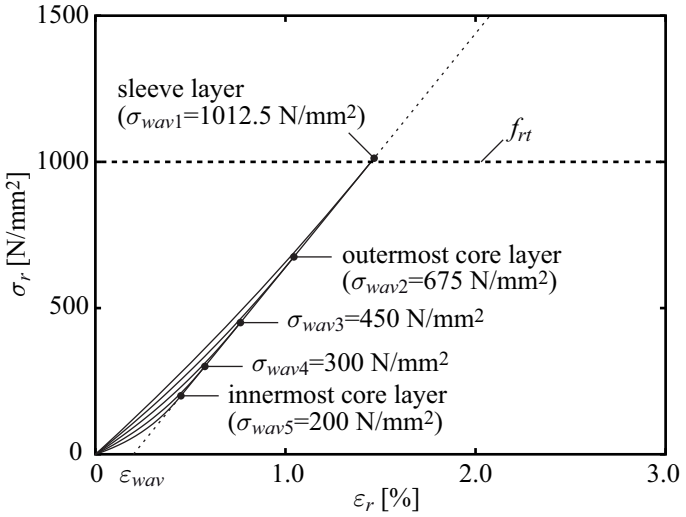

Figure 5.35.: Assumed constitutive relations with waviness of the reinforcement layers for a waviness ε_{wav}=2 ‰

before reaching the slope corresponding to the Young's modulus of a single filament, which indicates that the load is applied successively to an increasing number of filaments. Moreover, it can be assumed that a macroscopic waviness is stretched out in the experiments of plain yarns before data is recorded, which complicates the estimation of the extent of yarn waviness in the composite. Concerning the constitutive relation given with Eq. (4.19), the previous argumentation results in different parameter values of the exponential part for the different reinforcement layers. This situation is not entirely satisfactory as influences from the boundary conditions, given in this case by the surrounding concrete, are introduced in the constitutive relation. However, this approach is followed as it is a convenient way to consider this effect with regard to the used essentially one-dimensional model. Moreover, already the application of the initial exponential function introduces some kind of influence of boundary condition in terms of the imperfect alignment of the filaments.

In Fig. 5.35, the assumed constitutive relations corresponding to Eq. (4.19) for the different reinforcement layers are shown for a mean waviness ε_{wav}=2 ‰. The stresses σ_{wav} where the filaments are assumed to be completely stretched decrease non-linearly from the sleeve layer to the innermost core layer. The stress values are kept constant in the subsequent parametric study while ε_{wav} is varied in a range of 0 ‰ up to 5 ‰. The stress-strain relation of the sleeve layer shows a non-linear course up to a stress of 1012.5 N/mm^2, which is slightly larger than the assumed tensile strength of $f_{rt} = 1000\,\mathrm{N/mm^2}$ in the reference model. All other parameters are chosen as in the reference case. It shall be noted that a too low initial slope in the constitutive relation leads to problems in the incremental-iterative solution procedure in the simulations as the initial stiffness of the reinforcement elements approaches zero.

The simulated $\overline{\sigma}$-$\overline{\varepsilon}$ relations for different values of ε_{wav} are shown in Fig. 5.36, while Fig. 5.37 shows further evaluations of the simulated results. In Fig. 5.36, it can be seen that suppression of cracks (not further evaluated) is not significantly influenced by reinforcement waviness for the investigated values of ε_{wav}. The reinforcement stresses σ_r in the sleeve layer in the cracked cross section right after the first concrete crack occurred decrease with increasing ε_{wav}, see Fig. 5.37(a), which can be explained with an increasing activated stress transfer length in

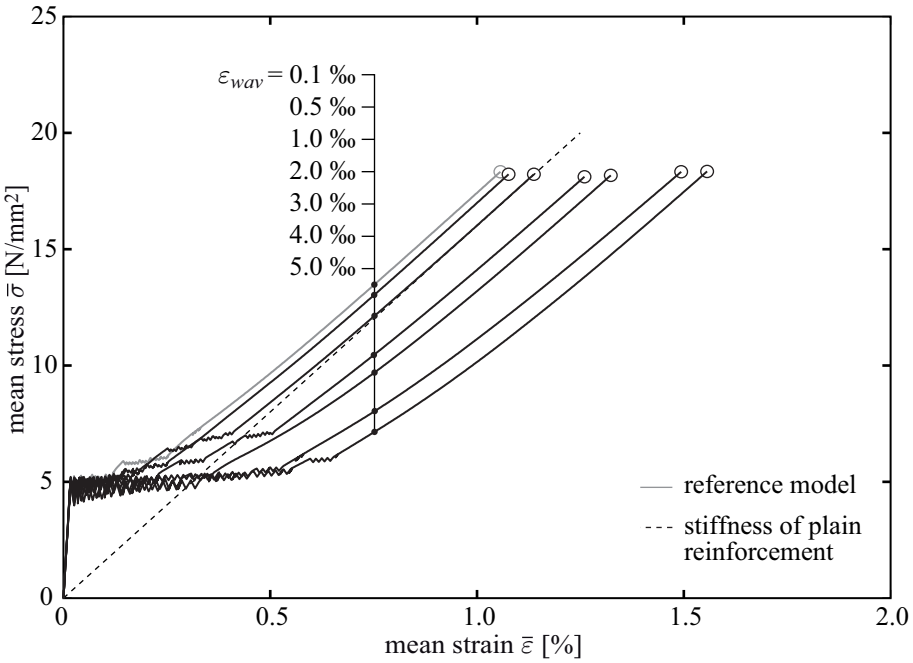

Figure 5.36.: $\overline{\sigma}$-$\overline{\varepsilon}$ relations for different values of ε_{wav}

the interface to the concrete due to the decreasing initial stiffness of the reinforcement. The respective stresses in the core layers decrease also with increasing ε_{wav}, see Fig. 5.37(a). However, the reduction is more pronounced in the inner core layers than the outer core layers. The reason is that similar to the sleeve layer, the stress elevation is distributed along a larger stress transfer length with increasing ε_{wav}. Correspondingly, also the stress drops in the $\overline{\sigma}$-$\overline{\varepsilon}$ relations, see Fig. 5.36, increase with increasing ε_{wav}. The final crack spacing is, apart from normal variations due to different initial crack patterns, virtually not influenced by increasing ε_{wav}, which is also valid for the crack widths for $\overline{\varepsilon}$=1 ‰, see Fig. 5.37(d). However, if the crack widths would be compared at an equal $\overline{\sigma}$ level or right after a concrete crack occurred, increasing crack widths with increasing waviness ε_{wav} could be observed. In Fig. 5.36, it can be also seen that the strain range where concrete cracking occurs increases with increasing ε_{wav}.

The ultimate stresses of the composite, which are shown in Fig. 5.37(b), are not significantly influenced by different ε_{wav}. The ultimate strains, which are also shown in Fig. 5.37(b), increase corresponding to ε_{wav}. Tension stiffening is shown in Fig. 5.37(e) for three maximum reinforcement stress levels $\sigma_{r,max}$. It can be seen that tension stiffening decreases with increasing ε_{wav}. With $\varepsilon_{wav} > 1$ ‰, $\overline{\varepsilon}$ is increased in the post-cracking state such that the $\overline{\sigma}$-$\overline{\varepsilon}$ relation is shifted beyond the stress-strain relation corresponding to the stiffness of the plain reinforcement without waviness, see also Fig. 5.36. This is referred to as "negative" tension stiffening. It is also observable that for $\varepsilon_{wav} > 1$ ‰, the absolute values of "negative" tension stiffening increases with increasing $\overline{\sigma}$ levels. This can be explained with a non-linear development of the post-cracking stiffness, which is shown again for the three $\sigma_{r,max}$ levels in Fig. 5.37(c). It can be seen that for the lowest stress level, the post-cracking stiffness is significantly below the stiffness of the plain reinforcement. While the stiffness is for values of $\varepsilon_{wav} < 1$ ‰ about 90 % of those of the plain reinforcement, it decreases with increasing values of $\varepsilon_{wav} > 1$ ‰ down to about 80 %. However, with increasing stress levels also the

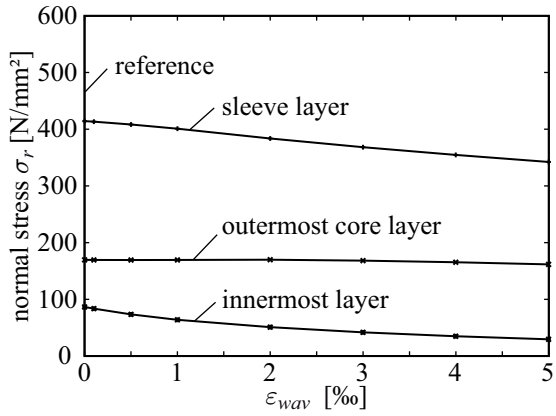

(a) Normal stresses in selected reinforcement layers in the cracked cross section right after the first concrete crack

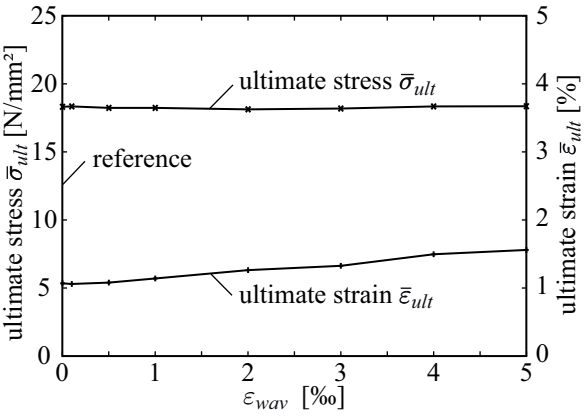

(b) Ultimate mean stresses $\overline{\sigma}_{ult}$ and strains $\overline{\varepsilon}_{ult}$

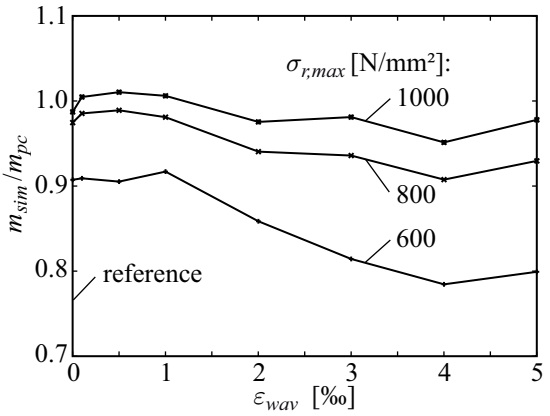

(c) Post-cracking stiffness at different stress levels

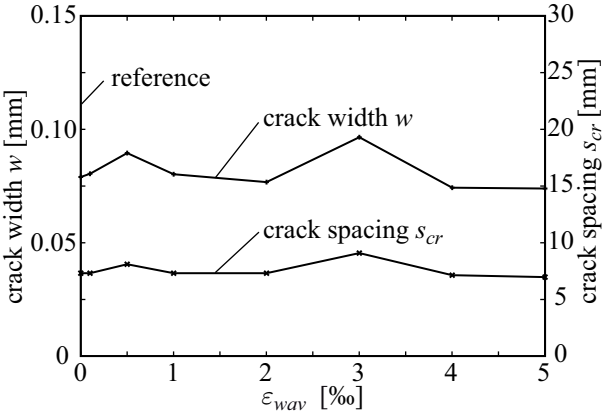

(d) Mean crack width at $\overline{\varepsilon}$=1 % and mean crack spacing in the ultimate state

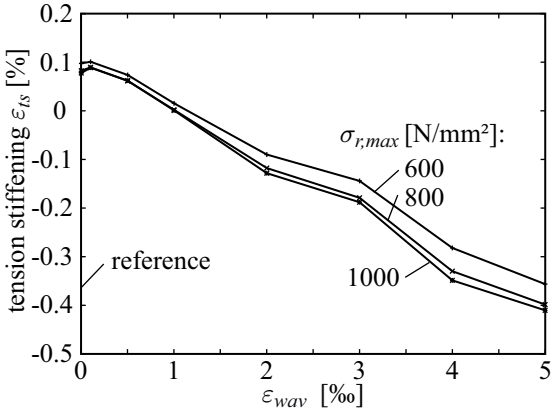

(e) Tension stiffening at different stress levels

Figure 5.37.: Various simulation results for different values of ε_{wav}

stiffness increases because the reinforcement stiffens successively until it is stretched and the effect diminishes. Taking into account that single filaments fail at lower load levels than the ultimate load, which is not considered in these simulations, leads to a "softening" at higher $\overline{\sigma}$ levels in the composite. This might compensate the successive stiffening.

Thus, waviness of the reinforcement might be one of the main reasons for the reduced stiffness in the post-cracking state as observable in the experiments.[2] This explanation corresponds to a reduced value of E_r, which was used e. g. in the model by [Bruckermann 2007] to represent the post-cracking stiffness of TRC appropriately. The significant difference between both approaches is that incorporating waviness a physical explanation can be given for the reduced stiffness without the questionable posit of a reduced value of E_r, which has no experimental evidence.

5.3.4. Influence of material properties of concrete

In the subsequent sections, results of parametric studies concerning selected material properties of the concrete are presented. The considered material properties are Young's modulus and tensile strength where also the influence of spatial fluctuations is taken into account. Furthermore, concrete shows post-cracking resistance also referred to as tension softening, as pointed out in Section 2.2.2, which is also considered. Besides the varied parameters all other parameters are applied again as in the reference model summarised at the end of Section 5.3.1.2.

5.3.4.1. Influence of concrete tensile strength

The tensile strength of concrete f_{ct} is one of the main parameters, which controls concrete cracking in the composite. Some of the consequences of a deterministic variation of f_{ct} can be forecast without performing any simulation. It is, e. g., obvious that the stress level in the $\overline{\sigma}$-$\overline{\varepsilon}$ relation and crack widths as well as the crack spacing will increase with increasing f_{ct}. However, some effects might be not that obvious. Thus, a parametric study is performed to investigate the influence of a deterministic variation of f_{ct} on the load-bearing behaviour of the composite in the reference case. Therefor, f_{ct} is varied in a range of $1\,\mathrm{N/mm^2}$ up to $20\,\mathrm{N/mm^2}$. The upper value corresponds approximately to the ultimate stress of the composite. In the reference model, a value of f_{ct}=$5\,\mathrm{N/mm^2}$ is used. Except for values of f_{ct} in the range of $1\,\mathrm{N/mm^2}$ up to $3\,\mathrm{N/mm^2}$, where a bar element length of 0.1 mm is used because of small expected crack spacing, all other model parameters correspond to the reference model as defined at the end of Section 5.3.1.2.

The $\overline{\sigma}$-$\overline{\varepsilon}$ relations of the respective simulations are shown in Fig. 5.38. As already expected, the $\overline{\sigma}$ levels of concrete cracking increase with increasing f_{ct}. Furthermore, also the stress drops after cracking events increase with increasing f_{ct}. In Fig. 5.39(a), it can be seen that the stresses σ_r right after concrete cracking in the cracked cross section increase in all reinforcement layers with increasing f_{ct}. The reason is that the reinforcement is stronger activated due to larger forces released by the concrete. In Fig. 5.39(a), a kink at a value of f_{ct} between $4\,\mathrm{N/mm^2}$ and $5\,\mathrm{N/mm^2}$ is observable in the stresses of the sleeve layer. For values $f_{ct} < 5\,\mathrm{N/mm^2}$, the stresses in the sleeve layer increase stronger than for larger values. However, for the stress in the innermost core layer the situation is reversed and the stresses in the

[2] It is worth to note that the idea that reinforcement waviness delays achieving the plain reinforcement stiffness in the post-cracking state of TRC was developed during a discussion with my colleague Dipl.-Ing. Dirk Jesse before the simulations were performed.

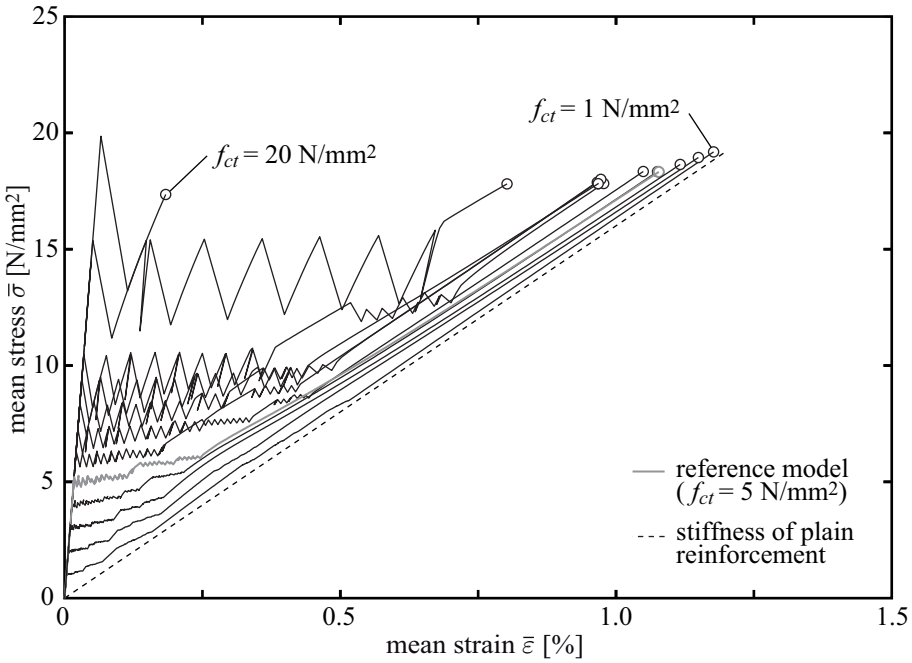

Figure 5.38.: $\overline{\sigma}$-$\overline{\varepsilon}$ relations for different values of f_{ct}

outermost core layer have an intermediate behaviour. This can be explained as follows: with the low values of f_{ct}, primarily the adhesive bond stresses associated with a large bond stiffness are activated in the sleeve layer due to low relative displacements in the concrete-sleeve layer interface. If the relative deformations are sufficiently large to reach the frictional part of the bond law right after concrete cracking, the absolute increase of the transferred bond stress is only the increase of the constant frictional bond stress. This results in a smaller increase of the stress in the sleeve layer with increasing f_{ct} compared to the strong increase due to large bond stiffness in the adhesive part of bond law $\tau(s)_{cr}$. As a consequence, the differences in the transferred bond stresses between the sleeve layer and the core layers are relatively large for $f_{ct} < 5\,\mathrm{N/mm^2}$ but decrease for $f_{ct} > 5\,\mathrm{N/mm^2}$ due to bond degradation between the sleeve layer and the concrete. In the reference case, significant bond degradation does not occur until the post-cracking state is reached as it can be seen e. g. in Fig. 5.26. This behaviour depends of course on the assumed bond laws and can only be assessed qualitatively in this regard. Nevertheless, it is conceivable that such a behaviour also occurs in reality when the interface between concrete and filaments is destroyed simultaneously with concrete cracking and primarily frictional stress transfer occurs in the interface. An experimental verification will be, however, difficult as the concrete tensile strength cannot be manipulated arbitrarily without also changing other concrete properties like post-cracking behaviour, Young's modulus and bond behaviour with the reinforcement.

The number of cracks, which develop in the state of multiple cracking decrease with increasing f_{ct}. Correspondingly, crack spacing increases as well as the cracks widths as already expected, see Fig. 5.39(c). For f_{ct}=20 N/mm², the reinforcement fails after the first matrix crack. However, the failure does not occur simultaneously with the concrete crack but in the state of increasing $\overline{\sigma}$ before the next matrix crack can develop. Nevertheless, simultaneous failure of the reinforcement associated with the first concrete crack will occur if f_{ct} is further increased. In the post-cracking state, the stiffness is virtually not influenced by the variation

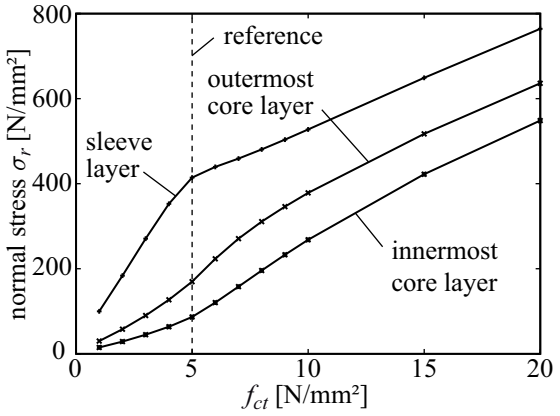

(a) Normal stresses in selected reinforcement layers in the cracked cross section right after the first concrete crack

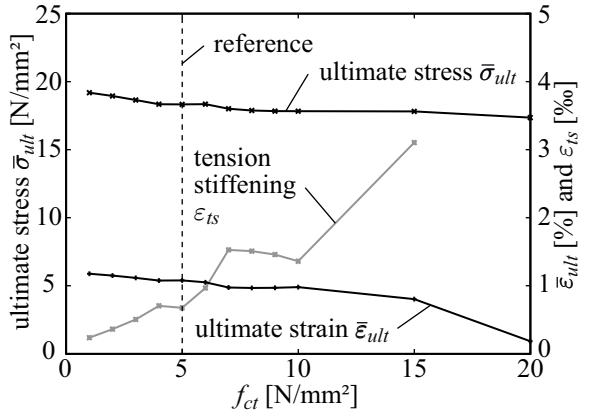

(b) Ultimate mean stresses $\bar{\sigma}_{ult}$ and strains $\bar{\varepsilon}_{ult}$ as well as tension stiffening ε_{ts}

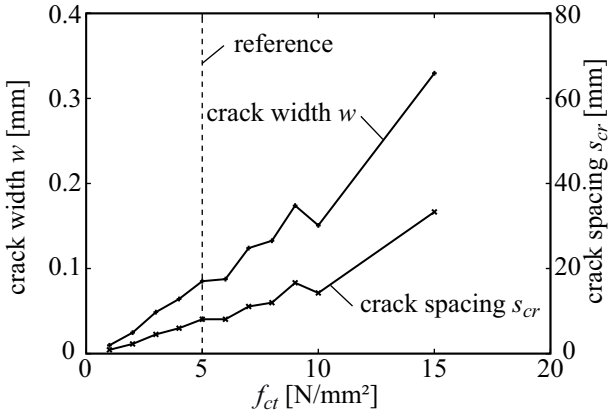

(c) Mean crack width at $\bar{\varepsilon}$=1 % and mean crack spacing in the ultimate state for f_{rt}=1000 N/mm²

Figure 5.39.: Various simulation results for different values of f_{ct}

of f_{ct}. Tension stiffening increases corresponding to increasing crack spacing, see Fig. 5.39(b). However, due to variations in crack spacing, which does not increase continuously with increasing f_{ct}, also tension stiffening shows some reduction in the medium range of applied f_{ct}.

Regarding the ultimate state, it can be seen that the ultimate strains decrease with increasing f_{ct} corresponding to increasing tension stiffening, see Fig. 5.39(b). The ultimate stresses decrease also with increasing values of f_{ct}, see Fig. 5.39(b). However, the decrease is almost linear and not as strong as the increase of the stress in the sleeve layer right after concrete cracking. The reason is that up to ultimate failure the stress concentrations in the sleeve layer decrease as it was already shown in Fig. 5.26. Nevertheless, for values $f_{ct} \geq 15\,\mathrm{N/mm^2}$ both ultimate stresses and strains decrease significantly as no distinctive post-cracking state can develop or the composite already fails during the cracking state as it is the case for f_{ct}=20 N/mm², see Fig. 5.38. Thus, it can be seen that if the concrete tensile strength increases, the ultimate stress of the composite will decrease. In reality this effect might be attenuated by concrete tension stiffening. However, this requires that tension softening also increases with increasing f_{ct}. Experimental investigations, e. g. by [Remmel 1994], indicate

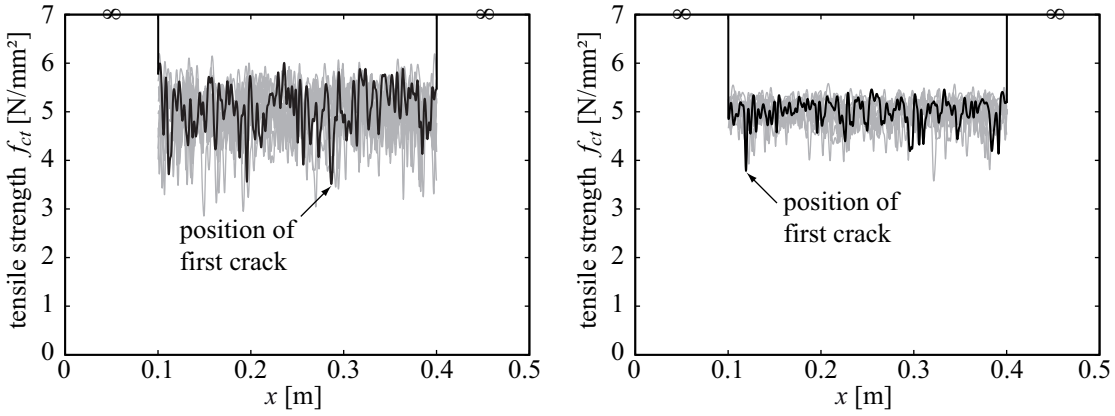

(a) Relative standard deviation of 10 % (b) Relative standard deviation of 5 %

Figure 5.40.: Realisations of the concrete tensile strength f_{ct} distribution along x with different relative standard deviations

that plain concrete has an upper limit of fracture energy if a certain tensile strength is exceeded. The effect of a decreasing composite strength with increasing f_{ct} is also similar to the energetic size effect, compare [Bažant 2002]. However, the elastic energy stored in the concrete is increased in this case not by the geometrical size but by elevated tensile strength. This results in an increased loading of the reinforcement when the stored elastic energy is released and to a potentially earlier failure.

5.3.4.2. Influence of scatter in concrete tensile strength

In the previous section, results of a parametric study with a deterministic variation of the concrete tensile strength f_{ct} were presented. However, the material properties of the concrete are usually subjected to scatter. Especially, spatial variations of f_{ct} seem to influence the response of the composite material TRC to tensile loading significantly. To investigate these effects, simulations with fluctuating f_{ct} modelled by means of random fields as described in Section 4.3.2.2 are carried out. It is assumed that f_{ct} follows a two-parametric Weibull distribution, see Appendix A.3, with a mean value of 5.0 N/mm². For the relative standard deviation two values are tested: 5 % and 10 %. Furthermore, a correlation length of 2 mm, which is twice the maximum aggregate size, is assumed in a first approach. As already pointed out in Section 5.3.2.3, the results are only evaluated in a qualitative manner. However, ten simulations were carried out for each of the two standard deviations where the realisations of the random field for f_{ct} are shown in Fig. 5.40. One realisation is plotted in black for each case to facilitate visibility. Except for the modelling of f_{ct}, the other parameters coincide with the reference model as summarised at the end of Section 5.3.1.2.

In Fig. 5.41, the simulated $\overline{\sigma}$-$\overline{\varepsilon}$ relations for both relative standard deviations of f_{ct} are shown. The $\overline{\sigma}$-$\overline{\varepsilon}$ relations plotted in black correspond to the distributions of f_{ct} plotted in black in Fig. 5.40. Due to the variations in f_{ct} with a minimum value lower than the mean value of 5.0 N/mm², the first concrete cracks occur at a lower stress level compared to the reference case. The positions of the first cracks are determined by the lowest f_{ct} in the realisation of the random field as the stress is almost constant in the centre part of the model before

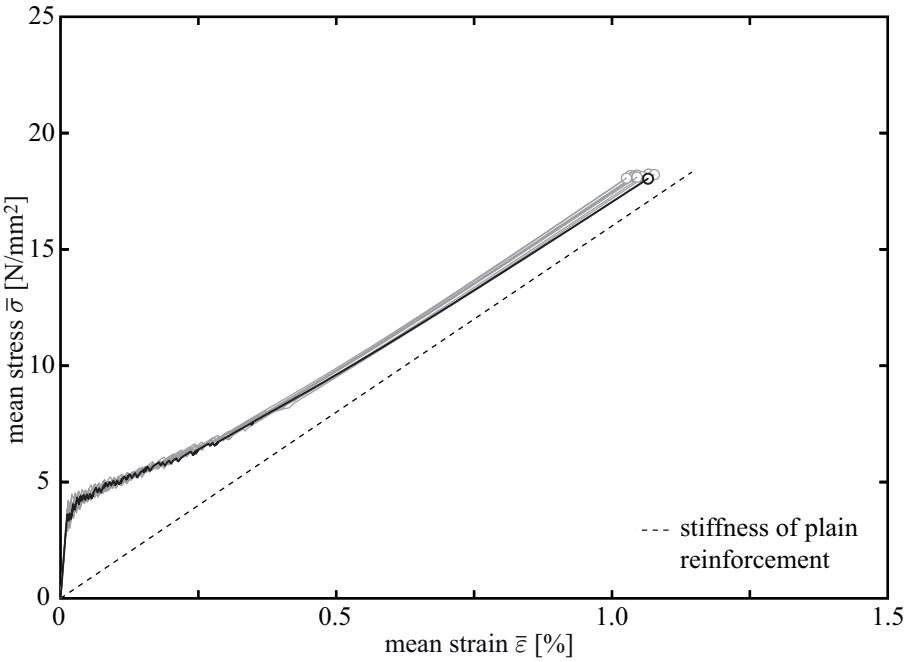

(a) Relative standard deviation of f_{ct} of 10 %

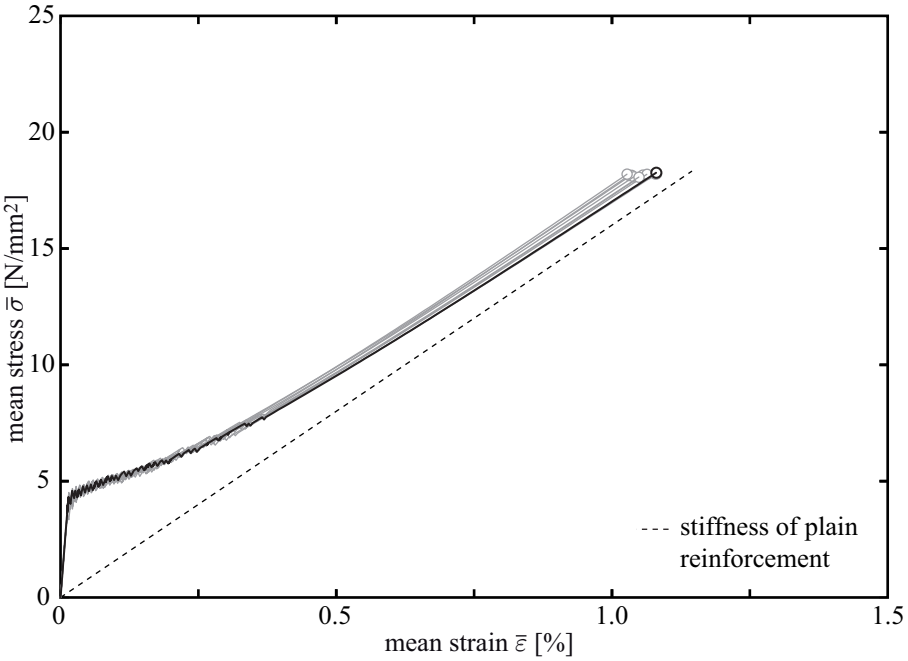

(b) Relative standard deviation of f_{ct} of 5 %

Figure 5.41.: $\overline{\sigma}$-$\overline{\varepsilon}$ relations for different realisations of scattering f_{ct}

cracking. In Fig. 5.40, the respective position is marked. The subsequent crack positions cannot be predicted that simple as they depend on both the stress transfer lengths between the concrete and the reinforcement and the next local minimum of f_{ct}. Thus, the strength minima do not necessarily determine the crack locations but are preferential positions. In the $\overline{\sigma}$-$\overline{\varepsilon}$ relations, a smoothing in the cracking state can be observed compared to the results of the deterministic reference model. Crack plateaus as still present in the case considering scattering bond strength in Section 5.3.2.3 are missing. However, some kind of clustering

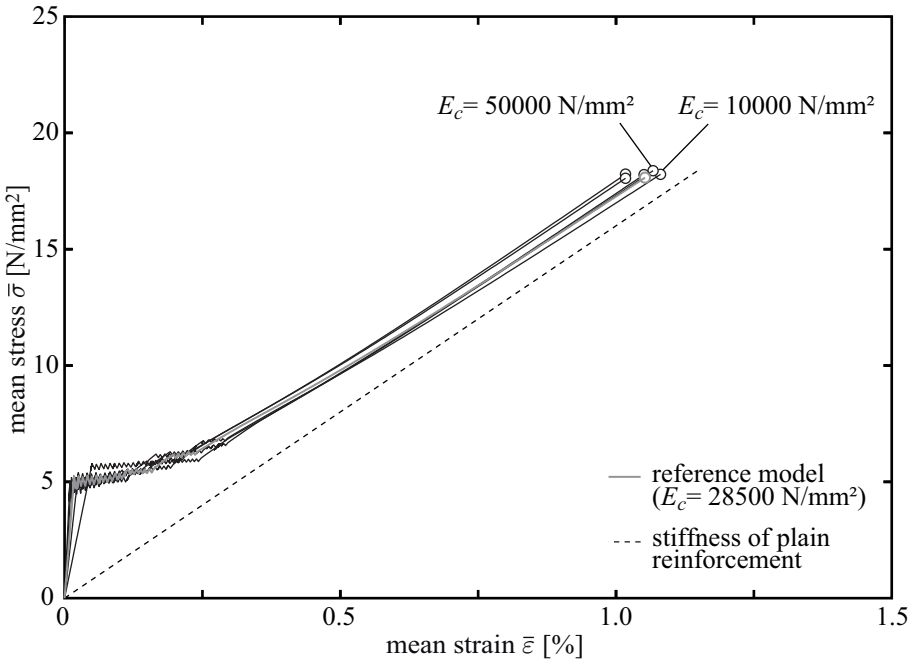

Figure 5.42.: $\overline{\sigma}$-$\overline{\varepsilon}$ relations for different values of E_c

of cracks at increasing strain levels occurs occasionally. This can be explained with crack development between existing cracks, which might require some deformation increment to activate a longer stress transfer length between concrete and reinforcement to reach f_{ct} again. Furthermore, it is observable that the mean slope of the cracking state is somewhat steeper for the relative standard deviation of 10 % compared to 5 %. Thus, it can be expected that while the expected value of f_{ct} controls the $\overline{\sigma}$ level of the cracking state, the standard deviation controls the mean slope.

In the post-cracking state, the courses of the $\overline{\sigma}$-$\overline{\varepsilon}$ relations differ for the different realisations of the random field of f_{ct}, see Fig. 5.41. It can be seen that the differences between the realisations of both applied relative standard deviations are insignificant as far as it can be evaluated based on the small sample size. The main reason for the variations of the course of the $\overline{\sigma}$-$\overline{\varepsilon}$ relations in the post-cracking state is different crack spacing, which leads to different tension stiffening as already pointed out in previous sections. However, also the slopes vary slightly. This might be explained with variations in the crack widths of the different cracks. For the lower slopes, more cracks with larger crack widths are supposed to be situated within measurement range of $\overline{\varepsilon}$ leading to an apparently reduced stiffness. In the ultimate state, the ultimate strains vary corresponding to the variations in tension stiffening. The ultimate stresses show, however, only insignificant variations and correspond to the reference case.

5.3.4.3. Influence of Young's modulus of concrete

In this section, the influence of the Young's modulus E_c of the concrete is investigated. Therefor, E_c is varied in a range of 10 000 N/mm^2 up to 50 000 N/mm^2. The respective $\overline{\sigma}$-$\overline{\varepsilon}$ relations are shown in Fig. 5.42 where it can be seen that E_c primarily influences the pre-cracking state. The cracking state and the post-cracking state are less influenced by E_c.

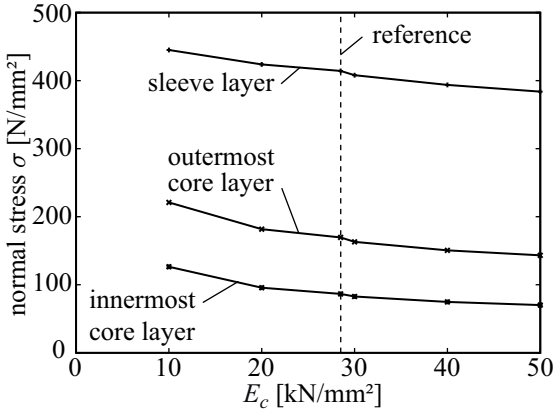

(a) Normal stresses in selected reinforcement layers in the cracked cross section right after the first concrete crack

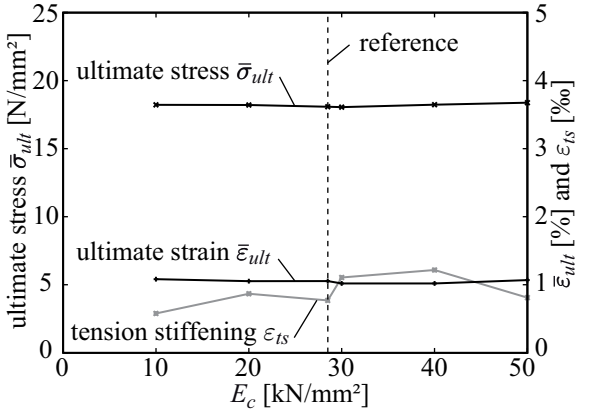

(b) Ultimate mean stresses $\overline{\sigma}_{ult}$ and strains $\overline{\varepsilon}_{ult}$ as well as tension stiffening ε_{ts}

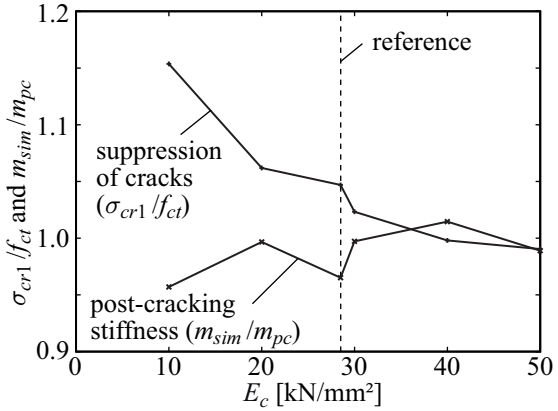

(c) Suppression of cracks and post-cracking stiffness before ultimate failure

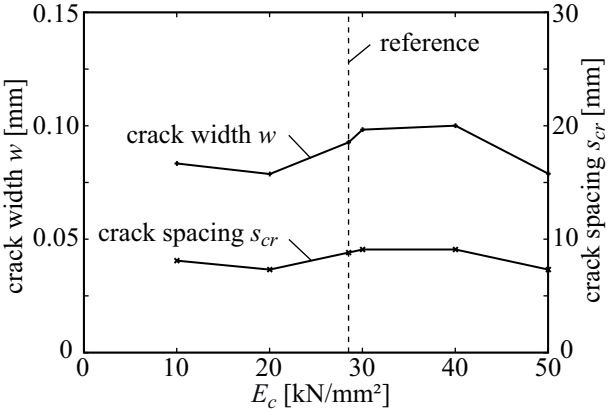

(d) Mean crack width at $\overline{\varepsilon}$=1 % and mean crack spacing in the ultimate state

Figure 5.43.: Various simulation results for different concrete Young's moduli E_c

In the pre-cracking state, the stiffness of the composite increases obviously with increasing E_c. Furthermore, it is observable in Figs. 5.42 and 5.43(c) that suppression of cracks decreases with increasing E_c. This can be explained with a larger activation of the reinforcement due to larger deformations of the concrete with low E_c compared to large E_c. This is also the reason why the stresses in the reinforcement σ_r after the first concrete crack occurred are larger for low E_c than for large E_c as it can be seen in Fig. 5.43(a). However, this does virtually not influence the concrete crack development as it is observable in Fig. 5.43(d), which shows crack spacing in the ultimate state and crack width at $\overline{\varepsilon}$=1 %. Except for common variations due to different crack patterns because of different bond stress distributions, no significant differences are observable. Also regarding the post-cracking state where tension stiffening and post-cracking stiffness as shown in Figs. 5.43(b) and 5.43(c), respectively, are evaluated as characteristic properties, only negligible impact by E_c is observable. Tension stiffening increases slightly when crack widths increase due to a larger participation of the concrete on load-bearing between the concrete cracks. The ultimate stresses and strains are also virtually not influenced by E_c as it can be seen in Fig. 5.43(b). Thus, the Young's modulus of the concrete has in the investigated parameter combination only a minor influence on the global

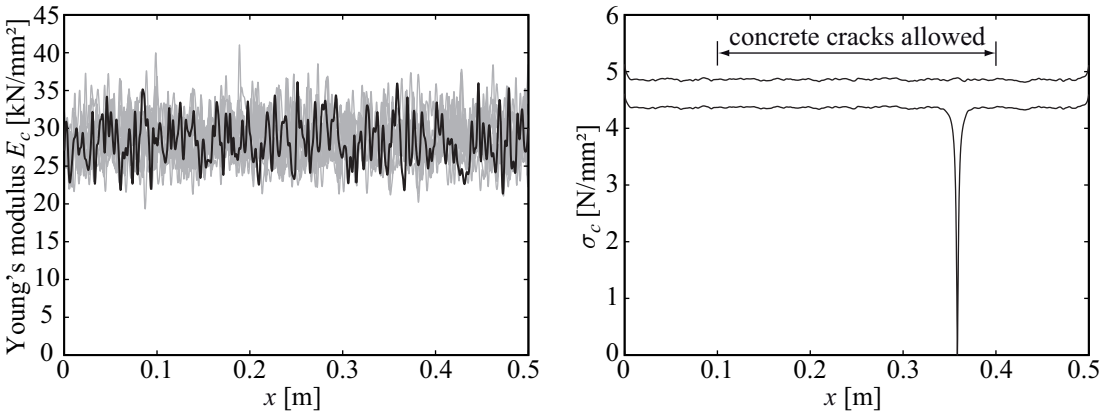

(a) Realisations of random fields for E_c

(b) Stress in concrete σ_c along x right before and after first crack

Figure 5.44.: Realisations of random fields for E_c and concrete stress distributions

load-bearing behaviour of TRC. Only in the pre-cracking state, which represents a fraction of the entire $\overline{\sigma}$-$\overline{\varepsilon}$ relation of the composite, a significant impact is observed.

5.3.4.4. Influence of scatter in Young's modulus of concrete

In the previous section, it was concluded that a deterministic variation of the Young's modulus E_c of the concrete only influences the pre-cracking state significantly. However, spatial variations of E_c in longitudinal direction x will influence the stress distribution between concrete and reinforcement as well as concrete cracking, respectively. Thus, further simulations are carried out to investigate the influence of variations of E_c along x. It is assumed the E_c follows a log-normal distribution, which corresponds to the recommendation in [PMC 2001]. The most important properties of the log-normal distribution are summarised in Appendix A.2. The expected value of E_c is chosen with $28\,500\,\mathrm{N/mm^2}$ corresponding to the deterministic simulations. The relative standard deviation is assumed with 10 %. Furthermore, a correlation length of 2 mm corresponding to the simulations in the Sections 5.3.2.3 and 5.3.4.2 is applied again. The application of spatial fluctuations in E_c introduces also heterogeneity in the previously homogeneous modelled concrete, which is an important feature of the stochastic modelling. All other parameters are chosen as in the reference model defined in Section 5.3.2.2. Ten simulations with different realisations of the random field for E_c, which are shown in Fig. 5.44(a), were carried out. The respective results are analysed again only in a qualitative manner.

The simulated $\overline{\sigma}$-$\overline{\varepsilon}$ relations are shown in Fig. 5.45. The $\overline{\sigma}$-$\overline{\varepsilon}$ relation plotted in black corresponds to the realisation of E_c, which is plotted also in black in Fig. 5.44(a). In principle, similar effects as for fluctuating f_{ct} are observable as the concrete stress σ_c is coupled to E_c via Eq. (4.9). As the concrete is also connected to the reinforcement, the impact on the $\overline{\sigma}$-$\overline{\varepsilon}$ relations are, however, smaller as local concrete stress concentrations are balanced by the activation of the reinforcement by means of bond mechanisms. In Fig. 5.44(b), the distributions of the concrete stresses σ_c before and after the first concrete crack are shown. The course of σ_c before the crack is smoother compared to E_c as the stiffness differences are balanced by the activation of the reinforcement by means of bond as already mentioned. Furthermore,

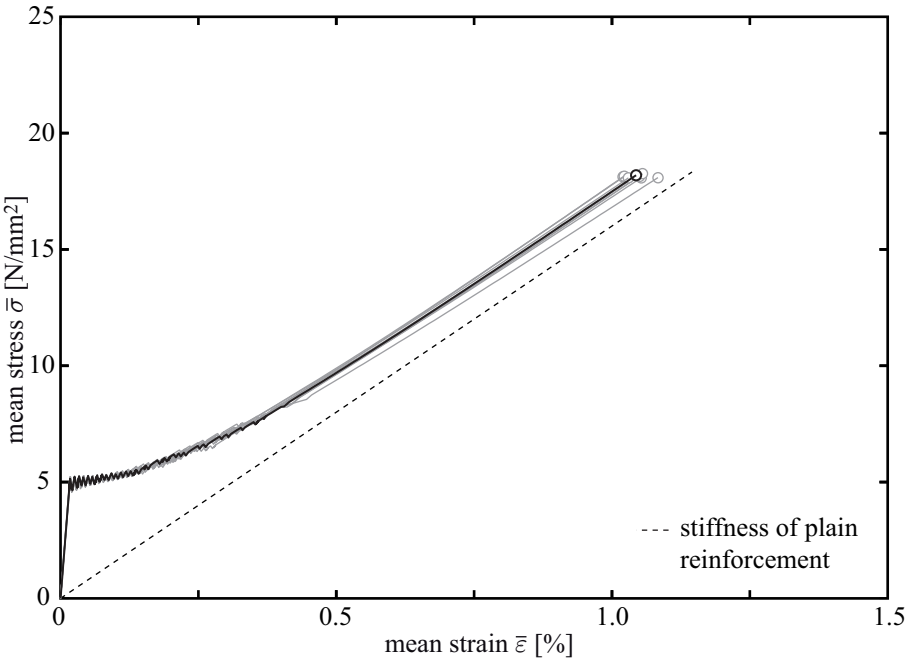

Figure 5.45.: $\overline{\sigma}$-$\overline{\varepsilon}$ relations for different realisations of scattering E_c

it is observable that the first concrete crack occurs in the stiffest element corresponding to the highest value E_c. The $\overline{\sigma}$ of the first crack is always smaller in the $\overline{\sigma}$-$\overline{\varepsilon}$ relations compared to the deterministic simulation although the effect is of subordinated importance in this parameter combination. The same applies for the subsequent concrete cracking where at the beginning only small differences between the different simulations with fluctuating E_c exist, see Fig. 5.45. Scatter in the $\overline{\sigma}$-$\overline{\varepsilon}$ relations starts to appear only at the crack development between existing concrete cracks. Furthermore, the stresses where concrete cracks occur increase successively, see Fig. 5.45, in contrast to the deterministic simulation where discrete crack plateaus with constant cracking stresses develop. As in the case of fluctuating f_{ct}, variations of the $\overline{\sigma}$-$\overline{\varepsilon}$ courses between the simulations appear in the post-cracking state, which can be explained similar to the case of varying f_{ct}, see Section 5.3.4.2. Also the explanations for the variations of the ultimate stresses and strains in the different simulations given in Section 5.3.4.2 are valid for scatter in E_c.

5.3.4.5. Influence of concrete tension softening

As pointed out in Section 2.2.2, cementitious matrices show usually post-cracking resistance. For the used fine-grained concrete, realistic values of the fracture energy as a measure for tension softening and for the maximum crack widths where the concrete stress σ_c becomes zero in the cracked cross section are G_f=40 N/m and w_2=0.2 mm, respectively. These values correspond to investigations by [Brockmann 2005] on a cementitious matrix similar to the used fine-grained concrete, see also Section 2.2.2. In the model, an implementation of Eqs. (4.15) and (4.16) is used to represent concrete tension softening. With G_f and w_2 as well as the assumptions that c=1, f_{ct1}=4.9 N/mm² and f_{ct2}=0.1 N/mm², the crack width w_1 is determined with $6.12{\cdot}10^{-3}$ mm.

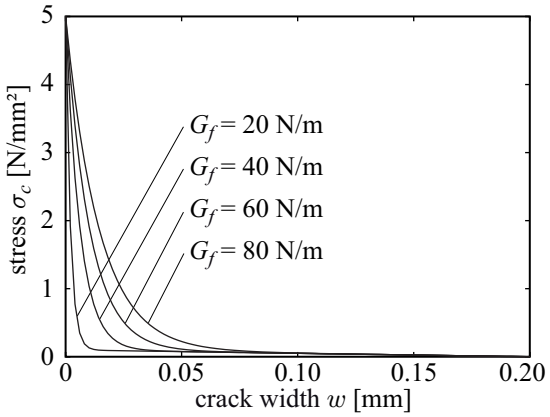

Figure 5.46.: Concrete tension softening relations for different values of G_f

In the subsequent parametric study, G_f is varied in a range of 20 N/m up to 80 N/m to investigate the influence of varied post-cracking resistance of the concrete on the tensile behaviour of the composite. While G_f is varied, the other properties are kept constant except for w_1, which has to be determined for each G_f. The different concrete tension softening relations are shown in Fig. 5.46. As pointed out in Section 4.2.1, the crack width w is related to the bar element length, which yields a stress-strain relation and leads to mesh-objective results. The other parameters of the model used in the current parametric study correspond to the reference case defined at the end of Section 5.3.1.2, except for the bar element length in the case of G_f=80 N/m, which is chosen with 0.1 mm because of small expected crack spacing.

The simulated $\overline{\sigma}$-$\overline{\varepsilon}$ relations are shown in Fig. 5.47. The uncracked state is not influenced by tension softening because it obviously only appears after a concrete crack has developed. The same applies also for suppression of cracks, see Fig. 5.48(c). The state of cracking is characterised by lower stress drops after concrete cracking events compared to the reference simulation, where concrete tension softening is neglected, because the concrete still transfers stresses over the crack and consequently the cracks open less. Moreover, the stress drops decrease with increasing G_f. However, the occurrence of significant changes in the $\overline{\sigma}$-$\overline{\varepsilon}$ response of the composite requires a sufficient reinforcement ratio such that the stress in the concrete element where f_{ct} is exceeded does not drop close to zero due to a large crack width. For the applied cases of 2 % reinforcement ratio, considerable stress σ_c remains in the concrete for the realistic value of G_f=40 N/m and higher values, see Fig. 5.48(a). Furthermore, it is observable that the remaining σ_c increases with increasing G_f while for low G_f, e. g. 20 N/m, the stress transfer in the concrete is almost negligible. For low and large values of G_f, the increase of σ_c is small while in the intermediate range a strong increase with increasing G_f occurs. The reason for the small increase in the case of low G_f is that after the crack development a sudden large crack opening occurs where instantaneously the flat tail of the stress-crack width relation is reached. For large values of G_f, the dropped σ_c is already close to f_{ct}, which is the upper limit for σ_c. This results from an insignificant crack opening. It shall be also mentioned that with increasing G_f also increasing problems to find solutions in the incremental-iterative solution procedure emerge. The reason is that the stress drops in the cracked concrete elements reduce with increasing G_f and the number of cracks increases. As a result the stiffness differences between cracked and uncracked elements become insignif-

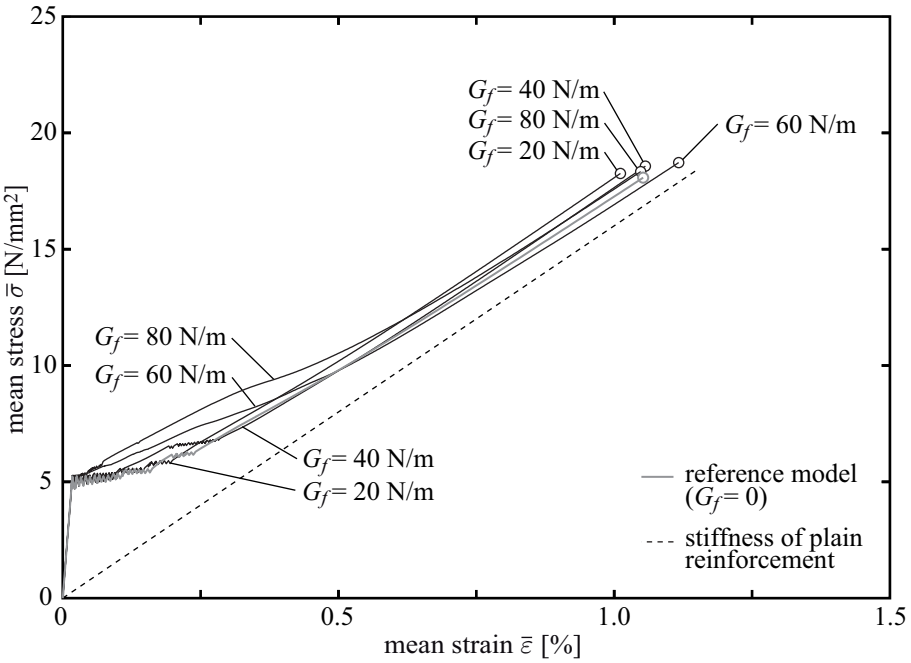

Figure 5.47.: $\overline{\sigma}$-$\overline{\varepsilon}$ relations for different values of G_f

icant. Furthermore, also the tensile strength is reached faster in intact concrete elements, which prevents considerable stress reductions in the cracked elements due to increasing crack widths. As a consequence, the dilemma emerges that an enlargement of the load increments, which would lead to a stronger reduction of the stress in the cracked concrete elements right after crack development can not be applied because this results technically in simultaneous failure of several concrete elements, which is not allowed in the solution procedure. Thus, the applicable amount of tension softening has an upper limit in the current implementation depending on the applied model parameters, as e. g. reinforcement ratio or bond laws. If this upper limit is exceeded other modelling approaches have to be applied.

Corresponding to the increasing stress in the cracked concrete elements right after the cracking events, the stresses in the reinforcement σ_r decrease with increasing G_f, see Fig. 5.48(a). Thus, the absolute value of the gradient of the reduction is also the largest in the medium range of applied G_f. It is further observable that the largest decrease occurs in the sleeve layer while the stresses are less influenced towards the innermost core layer. However, the ultimate stresses are virtually not influenced by the initial differences in the reinforcement stress distributions, see Fig. 5.48(b). The reason is that especially for the case of low G_f where large stress concentrations occur in the sleeve layer right after concrete cracking, the stress differences reduce with increasing loading as it was already shown in previous parametric studies, see e. g. Fig. 5.26(a). For high values of G_f, the stress concentrations are already small in the sleeve layer right after concrete cracking. Also the ultimate strains show only small differences associated with different G_f. The ultimate strain depends on tension stiffening, see Fig. 5.48(b), which does not show a clear trend. The reason might be that at least two opposite effects occur associated with concrete cracking. With increasing G_f, the number of cracks increases and crack width as well as crack spacing decrease, see Fig. 5.48(d). This is also another consequence of the increasing stress transfer in the concrete over the cracks with increasing G_f. Thus, assuming that no stress is transferred in the concrete over

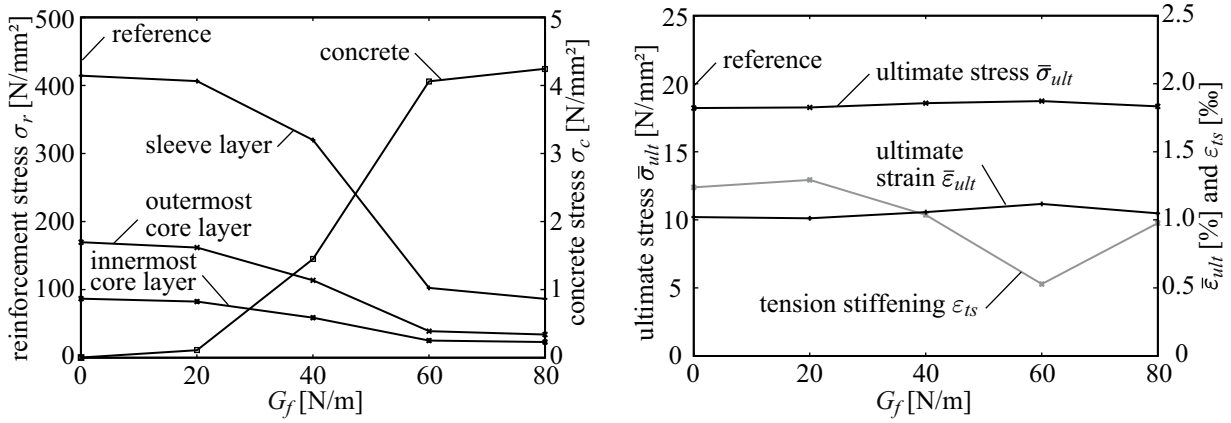

(a) Normal stresses in the concrete and selected reinforcement layers right after first exceeding of f_{ct} in the cross section of this concrete element

(b) Ultimate mean stresses $\overline{\sigma}_{ult}$ and strains $\overline{\varepsilon}_{ult}$ as well as tension stiffening ε_{ts}

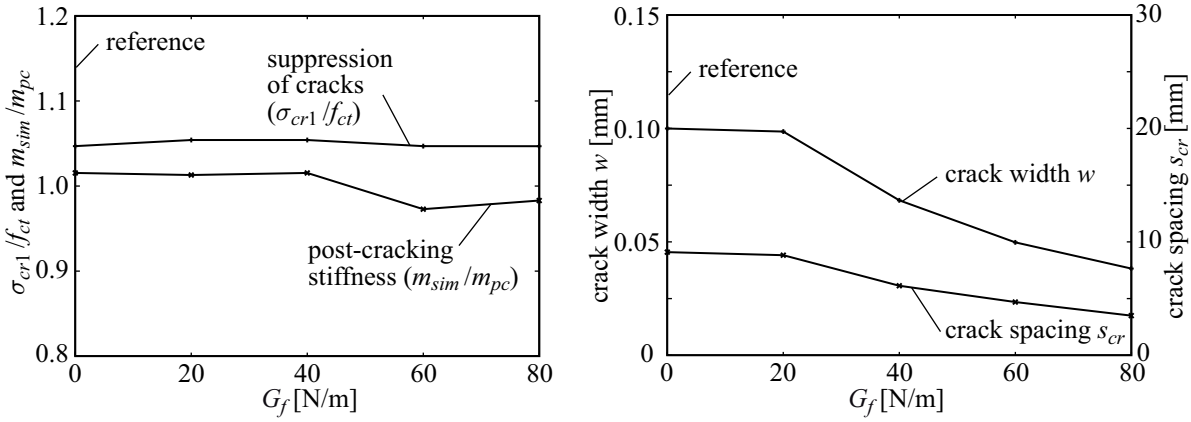

(c) Suppression of cracks and post-cracking stiffness before ultimate failure

(d) Mean crack width at $\overline{\varepsilon}$=1 % and mean crack spacing in the ultimate state

Figure 5.48.: Various simulation results for different values of G_f

the crack, tension stiffening should reduce because of less participation of the concrete in load-bearing between the cracks. This effect is counteracted by the increasing participation of the concrete on the crack bridging, which increases tension stiffening. The dominating effect depends on the parameter combination.

Also the development of the stiffness in the post-cracking state depends on tension softening as it is a non-linear function. Nevertheless, a clear identification of the influence of tension softening is difficult because it interacts with the bond properties. This might be also the reason why the $\overline{\sigma}$-$\overline{\varepsilon}$ relations show "softening" in the intermediate range of the post-cracking state and subsequent "re-hardening" for the large values of G_f, see Fig. 5.47. However, the influence of tension softening is almost diminished in the ultimate state although the mean crack widths are smaller in all cases than the maximum crack width w_2=0.2 mm in the softening law, see Fig. 5.48(d) where the mean crack width at $\overline{\varepsilon}$=1 % is shown. For $w > 0.05$ mm, the transferred stress in the concrete over the cracks is almost zero for all values of G_f, see Fig. 5.46. In summary, tension softening influences in the investigated parameter combinations primarily the crack development and the $\overline{\sigma}$-$\overline{\varepsilon}$ relation at the beginning of the post-cracking state.

5.3.5. Further investigations

The following sections are devoted to more practical topics concerning the tensile behaviour of TRC. In the first of these sections, the material non-linearities due to reinforcement waviness and concrete tension softening are considered simultaneously with scatter in tensile strength and Young's modulus of the concrete as well as the bond strength in the bond law between the concrete and the filaments in the fill-in zone. In the subsequent section, the representation of the tensile behaviour of TRC exposed to cyclic loading by the model is presented. In the last of these sections, the influence of the load application construction in different experimental test setups on the ultimate loads is investigated. Moreover, also the influence of different ways of the determination of $\overline{\varepsilon}$ on the $\overline{\sigma}$-$\overline{\varepsilon}$ relation of the composite is shown in the last section.

5.3.5.1. Combination of all effects

In the current section, non-linearities in the material behaviour and spatial stochastic variations of material properties, which were studied mutually independent in the previous sections, are combined. Besides the non-linear bond laws, non-linearities resulting from reinforcement waviness and concrete tension softening are taken into account. Moreover, scatter in concrete tensile strength f_{ct}, concrete Young's modulus E_c and bond strength τ_{max} in bond law $\tau(s)_{cr}$ are considered. For particular properties the values are changed compared to the corresponding parametric studies carried out previously to achieve a better adaptation of the simulated results to the experimental results. For the simultaneous scatter of the concrete material parameters and the bond parameter, the cross-correlated random field approach according to Section 4.3.2.3 is used. The cross-correlations between f_{ct}, E_c and τ_{max} are assumed as follows

$$\mathbf{C}_{cross} = \begin{bmatrix} {}^{(f_{ct})}1.0 & 0.8 & 0.9 \\ 0.8 & {}^{(E_c)}1.0 & 0.8 \\ 0.9 & 0.8 & {}^{(\tau_{max})}1.0 \end{bmatrix}. \tag{5.8}$$

Between these material properties a relatively strong correlation is assumed while the correlation between f_{ct} and τ_{max} is expected to be slightly higher than with E_c. This has to be accepted as an assumption as significant experimental data is missing. For f_{ct} and τ_{max}, Weibull distributions according to Appendix A.3 with expected values of $E(f_{ct})$=7 N/mm^2 and $E(\tau_{max})$=9 N/mm^2 are applied. The expected value of f_{ct} is increased compared to Section 5.3.4.2 as the experimental results show higher stress levels in the state of multiple cracking compared to the simulations in Section 5.3.4.2. For E_c, a log-normal distribution corresponding to Appendix A.2 with an expected value of $E(E_c)$=28 500 N/mm^2 is applied. For all three parameters, relative standard deviations of 5 % are assumed. Furthermore, a correlation length of 2 mm is applied again. As f_{ct} is not constant in the bar elements representing the concrete also the parametrisation of the tension softening law has to be adjusted to the respective tensile strength. Therefor, only f_{ct} is varied for the determination of the parameters of the softening law while G_f=40 N/m and w_2=0.2 mm as well as the ratiof_{ct1}/f_{ct2}=4.9/0.1 are applied corresponding to Section 5.3.4.5. Furthermore, reinforcement waviness is considered with ε_{wav}=1 ‰. The stress levels where the reinforcement layers are assumed to be completely stretched, see Fig. 5.49(a), are increased compared to

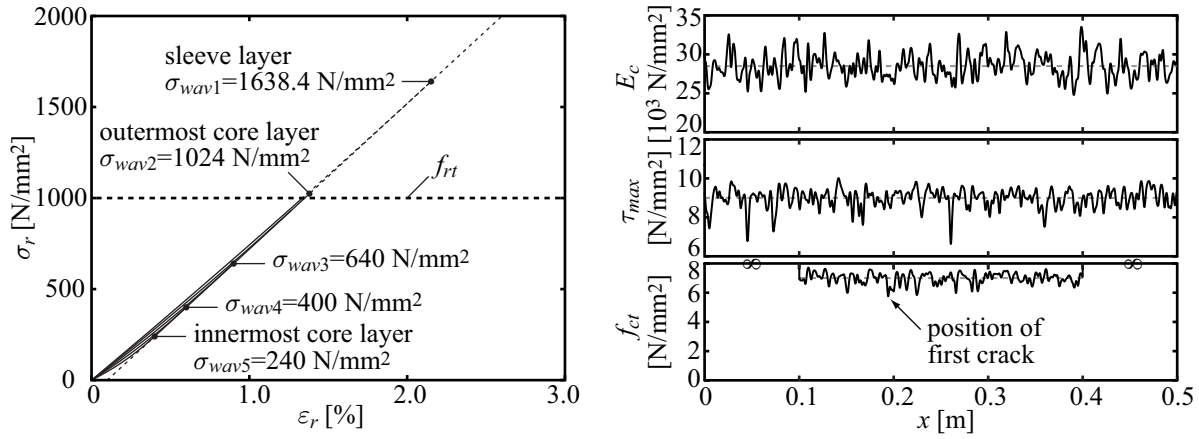

(a) Assumed constitutive relations of the reinforcement layers

(b) Distributions of E_c, τ_{max} and f_{ct} along x

Figure 5.49.: Constitutive relations of reinforcement layers and distributions of concrete material properties

Section 5.3.3.2 to achieve a larger reduction of the stiffness at the end of the post-cracking state in the $\overline{\sigma}$-$\overline{\varepsilon}$ relation corresponding to the experimental results. The other model parameters are chosen corresponding to the reference case defined at the end of Section 5.3.1.2. In the following, results of simulations with different reinforcement ratios V_f in the range of 0.75 % up to 5 % are presented. For each reinforcement ratio, one exemplary simulation was carried out to show the qualitative differences of the $\overline{\sigma}$-$\overline{\varepsilon}$ response of the composite. In all simulations, identical distributions of E_c, τ_{max} and f_{ct} along x according to Fig. 5.49(b) are applied, which facilitates a better comparison of the results between different V_f.

In Fig. 5.50, selected $\overline{\sigma}$-$\overline{\varepsilon}$ relations as results of the simulations are shown as well as experimental results for V_f of 1 %, 2 % and 3 % as already shown in Fig. 5.20. The representation of the tensile behaviour of the composite as observable in the experiments is considerably improved compared to the simulated results neglecting reinforcement waviness, matrix tension softening and stochastic variations as presented in Section 5.3.1.3, which are referred to as reference simulations in the following. Due to the consideration of scatter in the concrete material properties and the bond law $\tau(s)_{cr}$, the smooth course of the cracking state as occurring in the experiments can be appropriatly reproduced with the model. However, it can be also recognised that the stress levels of the cracking state increase with increasing V_f stronger in the experiments than in the simulations. This might be a result of an underestimation of suppression of cracks, which is shown depending on V_f in Fig. 5.51(c). Compared to the reference simulations no qualtitative changes in suppression of cracks, which increases almost linearly with increasing V_f, occurs, although the absolute values differ due to different concrete tensile strength and artifical effects resulting from the determination of suppression of cracks in the simulations as pointed out in Section 5.3.1.3. The scatter in E_c and τ_{max} as well reinforcement waviness seem to have negligible influence on suppression of cracks in the simulations.

The consideration of concrete tension softening leads compared to the reference simulations to a reduction of the stresses σ_r in the reinforcement layers right after concrete cracks occurred, see Fig. 5.51(a). Nevertheless, increased reinforcement deformations due to waviness

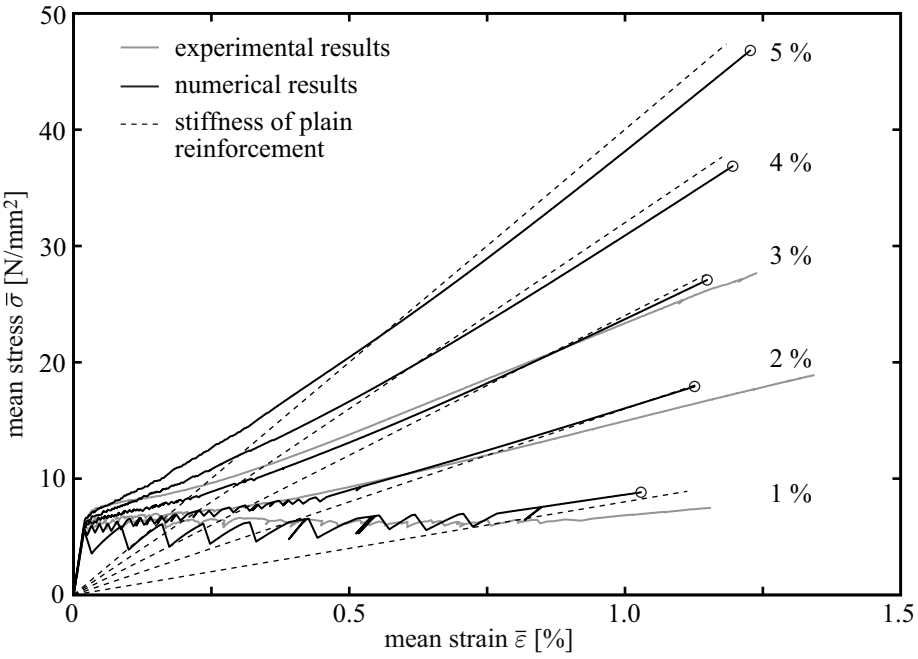

Figure 5.50.: $\overline{\sigma}$-$\overline{\varepsilon}$ relations for different reinforcement ratios considering reinforcement waviness, concrete tensile strength and scatter in concrete material properties

attenuate the effects of tension softening. The influence of concrete tension softening increases with increasing V_f as the concrete stresses σ_c show in Fig. 5.51(a). The reason is that the crack widths decrease with increasing V_f resulting in higher concrete stresses according to the tension softening law, see Fig. 5.46. This is also the reason for the additionally decreasing stresses in the reinforcement compared to the reference simulations where the reinforcement stresses already decreased due to increasing V_f, compare Figs. 5.21(a) and 5.51(a). The concrete stress σ_c has an upper limit of approximately 5.75 N/mm^2 corresponding to the tensile strength where the first concrete crack occurred. The position of the first concrete crack is also shown in Fig. 5.49(b). The positions of the subsequent cracks depend on several properties and mechanisms. It might be for instance interesting to point out again as already indicated in Section 5.3.4.4 that a proportional variation of E_c and f_{ct} leads to opposing effects concerning cracking. While the reduction of f_{ct} leads to an elevation of failure probability, a decrease of E_c decreases failure probability due to a reduction of the concrete stress.

As already mentioned, the smooth course of the $\overline{\sigma}$-$\overline{\varepsilon}$ relation in the cracking state as also occurring in the experiments is well reproduced in the current simulations. In Fig. 5.50, it can be seen that the stress drops after concrete crack development decrease and diminish with increasing V_f, which corresponds at least qualitatively also to the experimental results. This effect results primarily from the consideration of concrete tension softening. Compared to the reference simulations, the $\overline{\varepsilon}$ range of crack development increases in the current simulations. The main reasons are reinforcement waviness resulting in increased $\overline{\varepsilon}$ and scattering concrete material properties leading to a distribution of concrete cracking events. The mean crack spacing and crack width, which are shown as a function of V_f in Fig. 5.51(d), decrease with increasing V_f. This results primarily from the increased bond surface area between the concrete and the sleeve layer of the reinforcement, which facilitates a larger transfer

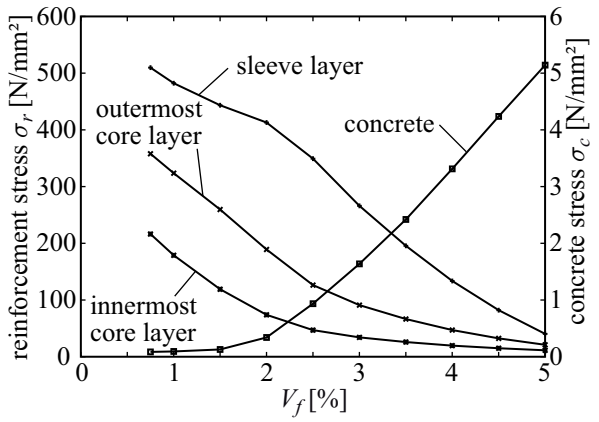

(a) Normal stresses in the concrete and selected reinforcement layers in the cracked cross-section right after the first concrete crack occurred

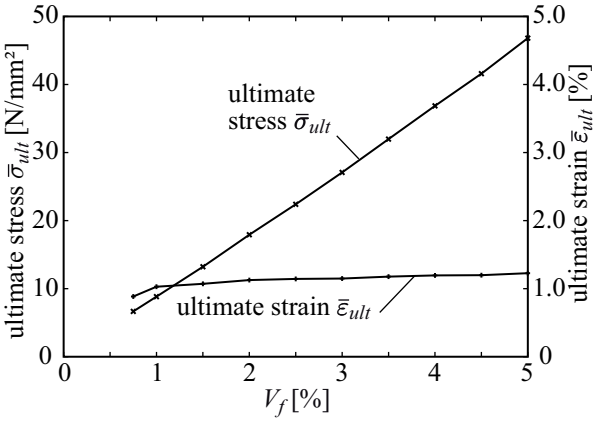

(b) Ultimate mean stresses $\bar{\sigma}_{ult}$ and strains $\bar{\varepsilon}_{ult}$

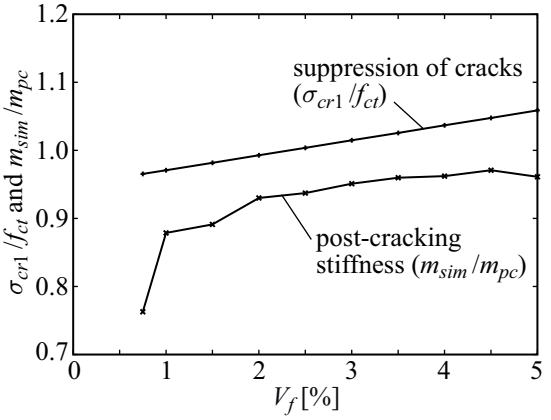

(c) Suppression of cracks and post-cracking stiffness before ultimate failure

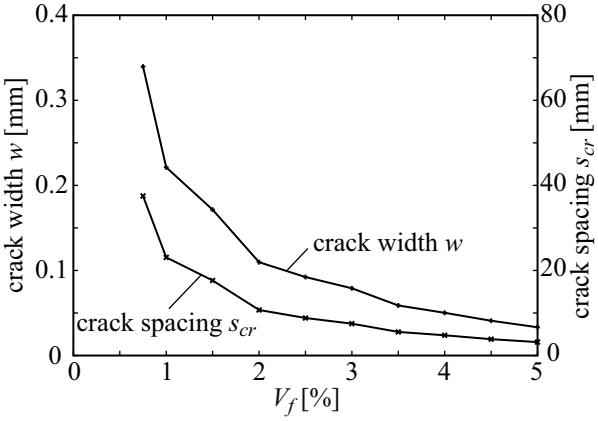

(d) Mean crack width at $\bar{\varepsilon}$=1 % and mean crack spacing in the ultimate state

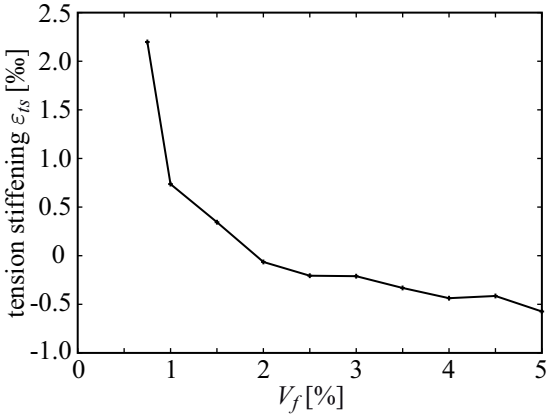

(e) Tension stiffening right before the ultimate state

Figure 5.51.: Various simulation results for different V_f considering reinforcement waviness, concrete tension softening and scatter in material properties

of stresses from the reinforcement to the concrete leading to shorter stress transfer length and more cracks. With increasing V_f, also tension softening has an increasing impact on cracking as stresses can be increasingly transferred over the crack in the concrete. However,

the differences compared to the reference simulations are small because the effect of tension softening is counteracted by reinforcement waviness, see 5.37(d).

In the post-cracking state, a smooth transition of the $\overline{\sigma}$-$\overline{\varepsilon}$ relation to the slope corresponding to the plain reinforcement is observable, see Fig. 5.50. At the beginning of the post-cracking state, the non-linear course of the tension softening relation and the initial non-linear courses of the constitutive laws of the reinforcement layers influence the $\overline{\sigma}$-$\overline{\varepsilon}$ relations. With increased loading, the influence of tension softening diminishes and more slowly also the influence of reinforcement waviness. Thus, the deficiency of the slope in the post-cracking state right before ultimate failure reduces with increasing V_f as it can be seen in Fig. 5.51(c). Although, this is an improvement compared to the reference simulations where virtually no deficit of stiffness in the post-cracking state appeared, see Fig. 5.21(c), the deficit of stiffness is still underestimated compared to the experiments. The main reason might be that successive failure of the reinforcement at higher load levels is not taken into account in the simulations as it was already supposed in Section 5.3.3.2. Moreover, also the stress levels in the constitutive relations, see Fig. 5.49(a), where the filaments are assumed to be completely stretched, which were already increased compared to Section 5.3.3.2, and the waviness stress ε_{wav} might still be underestimated.

Reinforcement waviness influences also tension stiffening. Tension stiffening decreases in the simulations with increasing loading because of increasing activation of yarn waviness, see Fig. 5.50. Furthermore, tension stiffening decreases with increasing V_f due to decreasing crack spacing. This reduces the participation of the concrete on load-bearing between the cracks. The result of these effects is shown for the ultimate state in Fig. 5.51(e). While for low values of V_f tension stiffening is still positive, it decreases to negative values for large V_f. At least qualitatively, this effect is also observable in the experimental results.

The ultimate stresses increase with increasing V_f, see Fig. 5.51(b), which coincides with experimental results. Compared to the reference simulations, virtually no differences are observable, although the initial stress concentrations in the sleeve layer of the reinforcement are lower in the current simulations from which delayed reinforcement failure could be expected. However, the stress reduction in the reinforcement results primarily from concrete tension softening, as already pointed out. With increasing loading, the cracks open and the stresses transferred in the concrete over the crack diminish. Thus, in the ultimate state only insignificant differences in the stress distribution between the reference simulations and the current simulations appear in the ultimate state also because the differences in the mean crack spacing are low. The ultimate strains, which are lower compared to the experiments, increase slightly with increasing V_f, see Fig. 5.51(b). Due to lower tension stiffening, the increase is somewhat larger compared to the reference simulations.

This parametric study showed that considering scatter in the material properties and material non-linearities like concrete tension softening and reinforcement waviness, the $\overline{\sigma}$-$\overline{\varepsilon}$ response of the composite can be simulated quite realistically. Regarding the ultimate state, it might be sufficient to consider only the additional deformations due to reinforcement waviness to gain realistic results for ultimate stresses and strains.

5.3.5.2. Cyclic loading

Hitherto, only monotonic tensile loading was applied. In this section, the prediction of the model regarding cyclic tensile loading is presented. Concerning the behaviour of TRC exposed to cyclic loading much less experimental data exists compared to monotonic loading. This is the reason why only results of one simulation are presented where a reinforcement ratio of V_f=1.9 % was chosen corresponding to available experimental results. In the simulation, four load cycles on different load levels are applied. The load levels where unloading is initiated were chosen corresponding to the experimental $\overline{\sigma}$-$\overline{\varepsilon}$ relation. Reloading was started always when the reaction force at the first concrete node became smaller than zero. The load is applied with displacement control corresponding to all previous simulations. Apart from the reinforcement ratio and the tensile strength of the reinforcement, which is increased to f_{rt}=1200 N/mm^2 to reach the stress level of the last load cycle corresponding to the experiment, all other parameters were applied as defined in Section 5.3.5.1.

In Fig. 5.52, the simulated and the corresponding experimental $\overline{\sigma}$-$\overline{\varepsilon}$ relations are shown. The $\overline{\sigma}$-$\overline{\varepsilon}$ relation for the case of monotonic loading is the envelope for the cyclic $\overline{\sigma}$-$\overline{\varepsilon}$ relation. Thus, the uncracked state, the state of multiple cracking and the post-cracking state are computed with the same quality as described for the case of monotonic loading in the previous section. The first load cycle was executed in the state of multiple cracking. The shape of the $\overline{\sigma}$-$\overline{\varepsilon}$ relation in the computed cycle coincides at least qualitatively with the experimental observations. After a steep decrease the unloading path becomes flatter. However, the unloading path reaches a lower strain level in the simulations compared to the experiment, which means that the macroscopically observable inelastic deformations are underestimated. The reason is most likely the neglect of inelastic deformations regarding concrete crack closure due to the modelling of unloading based on the concept of damage mechanics with an unloading relation back to the origin of the stress-strain relation in Eq. (4.17). Nevertheless, it can be assumed that the cracks in the concrete do not close perfectly, e. g. due to loosened particles and incompatibilities of the closing crack faces, compare Section 2.2.2, which leads to inelastic deformations. This effect remains to be implemented in the model. Another source of possible plastic deformations exists in the unloading path of the bond law described in Section 4.2.3. The slope of this unloading path in the bond law is already chosen based on the concept of plasticity, which is the upper limit of possible inelastic deformations resulting from the bond law. The shape of the reloading path of the experimental $\overline{\sigma}$-$\overline{\varepsilon}$ relation agrees with the assumption of a moderate local compressive stressing of the concrete, because at the beginning of the reloading the $\overline{\sigma}$-$\overline{\varepsilon}$ relation increases according to the Young's modulus of the concrete. This is not observable in the simulated $\overline{\sigma}$-$\overline{\varepsilon}$ relation where the reloading starts with a flatter slope caused by the bond law and the stiffness of the reinforcement. Afterwards, in both the experimental and the simulated $\overline{\sigma}$-$\overline{\varepsilon}$ relations the reloading path merges towards the monotonic $\overline{\sigma}$-$\overline{\varepsilon}$ relation and follows it during further loading.

In the subsequent load cycles, the characteristics described for the first cycle are repeated, in principle, but the differences between simulation and experiment become more pronounced. Especially the local compression of the concrete near the end of the unloading regime is clearly observable in the last cycle of the experimental data. There, as well as in the previous cycles, the unloading path becomes stiffer near the abscissa. As mentioned before, this is not observable in the simulation, because inelastic deformations of the cracked concrete are not implemented in the model. As a consequence, also the reloading paths in the computed $\overline{\sigma}$-$\overline{\varepsilon}$

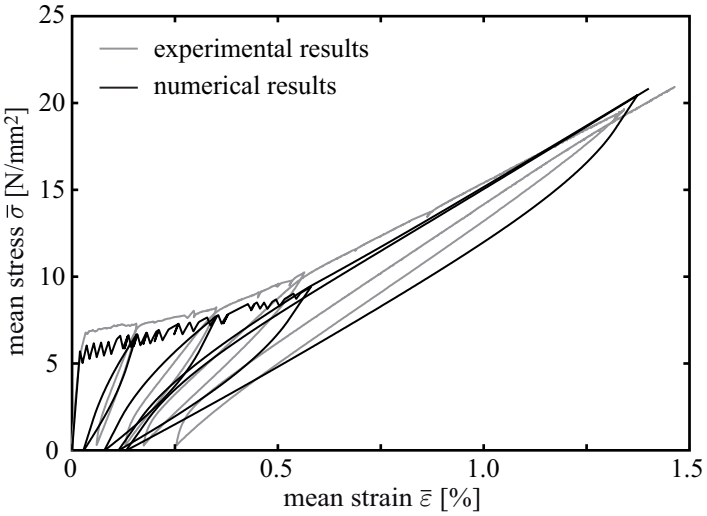

Figure 5.52.: $\overline{\sigma}$-$\overline{\varepsilon}$ relations under cyclic loading for V_f=1.9 %

relation start always flatter than in the experimentally obtained relation. In agreement with the experimental data, the cycles on lower load levels behave stiffer than cycles on higher load levels and the hystereses become larger as well. The area in between a hysteresis is a measure of the dissipated energy. In Fig. 5.52, it can be seen that in the simulation too much energy is dissipated compared to the experiments. Besides the underestimation of the inelastic deformations, another reason is the simulated stiffness in the final cracking state, which is larger than in the experiment. This leads to more pronounced hystereses.

The presented results showed that the typical hysteretic behaviour of TRC exposed to cyclic loading can be reproduced with the model. Nevertheless, inelastic deformations are underestimated, which most likely results from the implementation of the unloading behaviour of cracked concrete elements. Moreover, only one reinforcement ratio was taken into account. For other reinforcement ratios similar results can be expected.

5.3.5.3. Influence of load application construction

As pointed out in Section 2.3.4, the load is applied in the experiments by [Jesse 2004] with clamping constructions where rubber interlayers are placed between the specimen and the steel plates of the clamps to reduce stress concentrations in the specimen. Another strategy is followed for instance by [Molter 2005] with a waisting of the specimen while applying the load by means of steel plates embedded in the specimen. This is similar to a load transfer by means of glued steel plates on the specimen. The way the load is applied to the specimens by the testing machine might influence the observed tensile behaviour and especially the failure behaviour of the composite. To investigate this influence in a parametric study, a model similar to the reference case according to Section 5.3.1.2 is applied.

However, the model is enhanced concerning the representation of the load application to the specimen, which was performed in the reference case simply by a prescription of displacements at the end nodes of the concrete bar element chain. To model the load transfer by means of a stiff attachment due to glued or embedded steel plates corresponding to the test

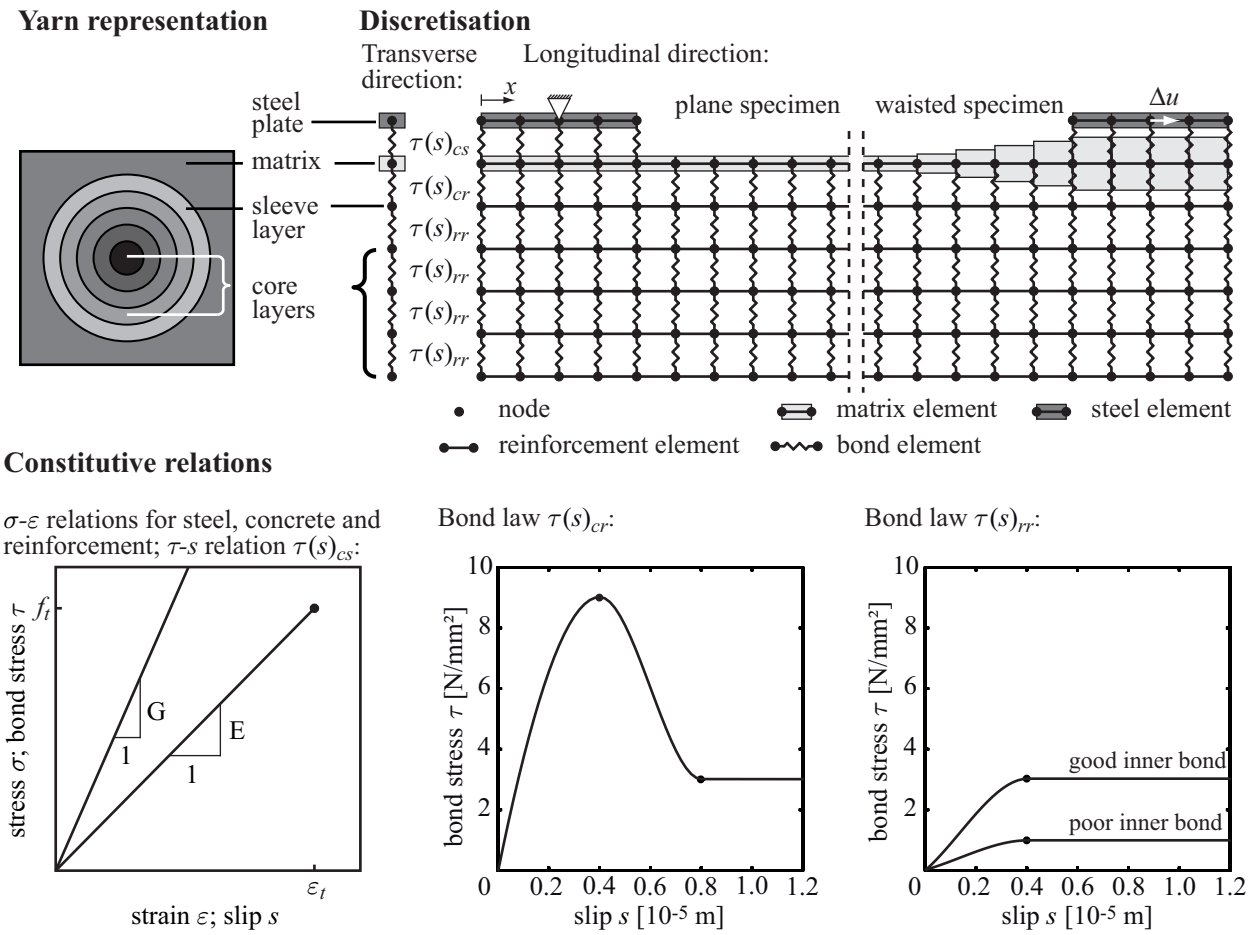

Figure 5.53.: Enhanced model for simulations regarding the load application constructions of different test setups on the tensile strength of the composite and used constitutive relations

setup shown in Fig. 2.13(a) referred to as type A setup in the following or the friction-based clamping in the test setup corresponding to Fig. 2.13(b) (type B) more realistic, additional bar elements are used representing these plates, see Fig. 5.53. At corresponding element nodes, bond elements link these bar elements to the concrete elements. In a first approach, linear elastic bond laws $\tau(s)_{cs}$ with different bond moduli G, corresponding to Eq. (4.121), for the cases of rubber interlayers in the clamping constructions (G=100 MN/m^3) and the glued steel plates (G=1·10^{10} MN/m^3) are applied. The bond surface area S necessary for the determination of the bond force T according to Eq. (4.122) is the width of the specimen equal to 100 mm multiplied by the length of a bar element (L_{el}=0.2 mm). The bar elements representing the steel plates have a cross-sectional area of 1000 mm^2. Moreover, linear elastic behaviour with a Young's modulus of 210 000 N/mm^2 is assumed for the steel. The boundary conditions are applied at the nodes in the centre of the steel bar element chains at x=0.05 m, which is fixed, and at x=0.45 m where displacements are prescribed.

The material parameters are used corresponding to the reference case in Section 5.3.1.2, which means that, except for limited tensile strength, non-linearities in the constitutive behaviour of concrete and reinforcement as well as scatter in the material properties are not considered. While the bond law $\tau(s)_{cr}$ is applied between concrete and the sleeve layer of

the reinforcement, three different bond laws $\tau(s)_{rr}$ are used at the interfaces between the reinforcement layers in separate simulations, see Fig. 5.53. The first variant of bond law $\tau(s)_{rr}$ represents poor inner bond with a low frictional bond stress, which corresponds, e. g., to a case with negligible concrete penetration to core, the second represents good inner bond with a higher frictional bond stress, e. g. for the case of some concrete or coating penetration, and the third represents perfect inner bond assuming perfect adhesion between the filaments with a linear elastic bond law similar to $\tau(s)_{cs}$, e. g. due to perfect impregnation of the yarns with polymeric coating. For the latter case, the bond stiffness was estimated based on investigations on a nano-clay polymeric coating by [Gao et al. 2007], which revealed a Young's modulus of about $6000\,\mathrm{N/mm^2}$. Assuming a Poisson's ratio equal to zero leads to a shear modulus of $3000\,\mathrm{N/mm^2}$. Assuming further an effective distance between the filaments of 10 μm leads in the assumed linear elastic bond stress-slip relation to a slope of $G = 3{\cdot}10^8\,\mathrm{MN/m^3}$. The parameters of the other bond laws were estimated based on the results in Section 5.3.2. To model the waisted parts of the specimens, the cross-sectional areas of the respective concrete elements were varied linearly similar to the simulations of the yarn pull-out tests in Section 5.2. If considered, waisting was applied on lengths of 50 mm before the clampings with element-wise linearly varying element thickness from 8 to 24 mm.

In Fig. 5.54, stress distributions in reinforcement and concrete at the clamping in the post-cracking state right before ultimate failure are shown as results of the simulations. The stresses in the reinforcement have maxima at the concrete cracks where the concrete is free of stress. Over the reinforcement cross section, the stresses decrease at the crack in all cases from the sleeve layer to the core layers while the stress distribution is reversed at the centre between two cracks. The stress differences in the reinforcement over the cross section decrease with improved inner bond and vanish for the case of perfect inner bond.

Fig. 5.54(a) shows stress distributions for the type A clamping with different qualities of bond in the reinforcement core for a plane specimen. In case of poor inner bond, see Fig. 5.54(a,left), the overall maximum value of reinforcement stress develops in the crack at the transition between the supported and the free range at $x = 0.1$ m. Towards the centre of the specimen the local stress maxima of the reinforcement decrease and are almost constant starting from the second crack distant to the clamping zone. In case of good inner bond, see Fig. 5.54(a,centre), this stress increase at the transition to the supported range is considerably reduced and disappears completely for the perfect inner bond case, Fig. 5.54(a,right).

For a type B clamping, see Fig. 5.54(b), it turns out that the stress increase at the clamping is still noticeable but much less distinct. At least for the chosen bond parameters the impact on ultimate load or tensile strength, respectively, is negligible. However, experimental data show that the number of specimens failing close or at the clamping is still significant but seems to have negligible influence on measured strength [Jesse et al. 2009].

The results for waisted specimens with glued steel plates are shown in Fig. 5.54(c). Compared to a pure type A clamping, see Fig. 5.54(a), the stress concentration in the sleeve layer close to the transition to the clamping has a similar extent. However, the position of the respective crack is not situated directly at the transition to the support but in the waisted range in some distance because the concrete tensile strength is not reached in the elements with the largest thickness. There is also a slightly increased maximum stress for the case of good inner bond, which seems to be caused by larger crack spacing. For the case of perfect inner bond, the stress increase in the reinforcement in the waisting zone diminishes.

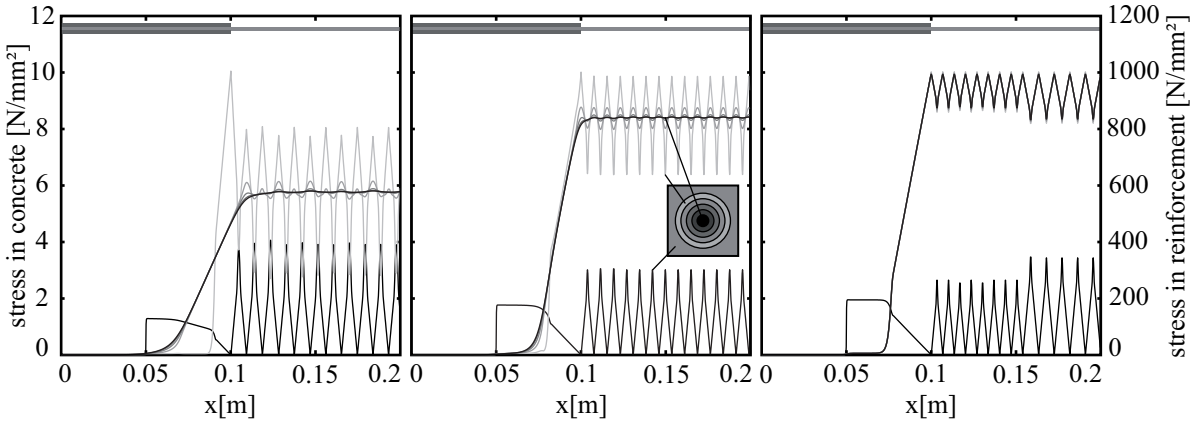

(a) Plane specimens with glued steel plates

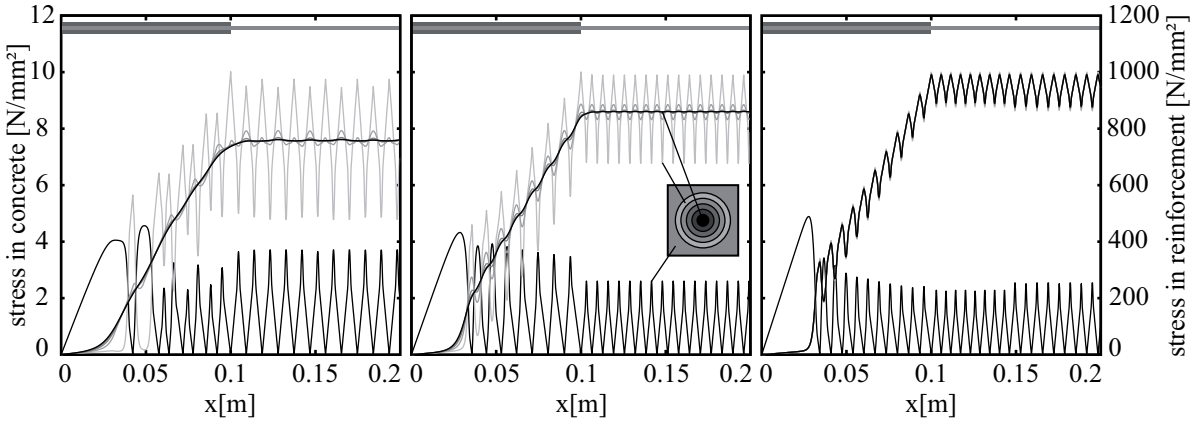

(b) Plane specimens with soft interlayer

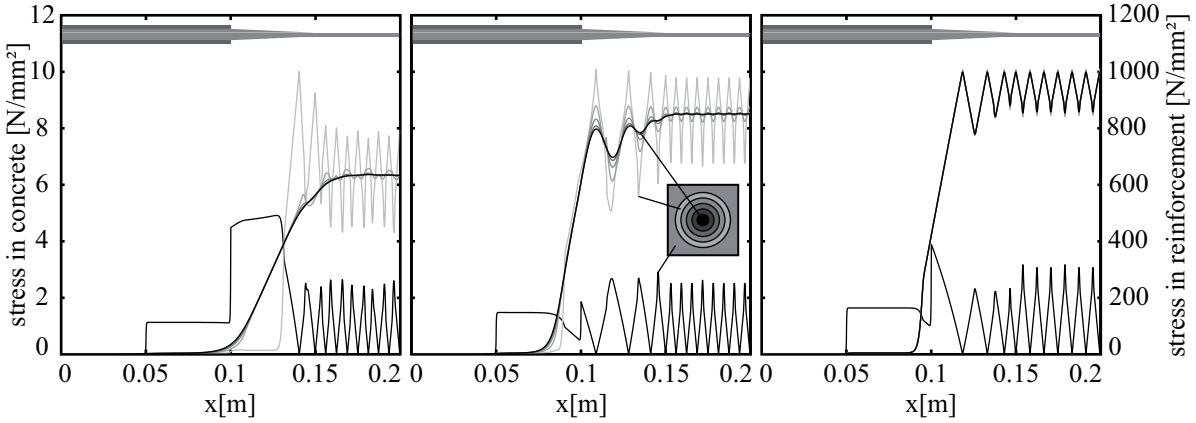

(c) Waisted specimens with glued steel plates

Figure 5.54.: Stress distribution for different types of load application, specimen shape and inner bond laws (left: poor inner bond, centre: good inner bond, right: perfect inner bond)

If the failure mechanism is simplified and it is assumed that failure occurs when the sleeve layer reaches its defined tensile strength, the composite strength can be determined for each case as the integral force over a cross section divided by the cross-sectional area of the concrete. These values are compiled in Table 5.1. As reference values, the ultimate stresses

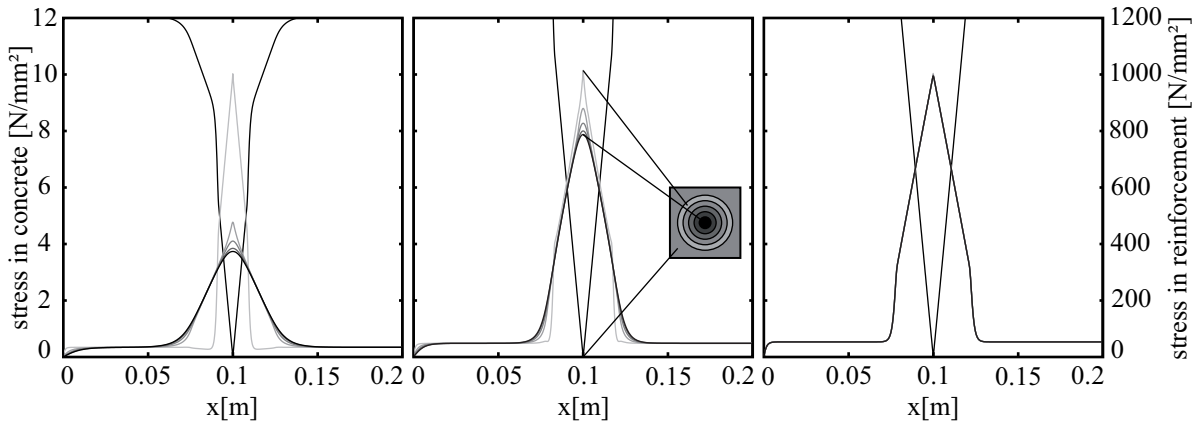

Figure 5.55.: Comparative simulations of single cracks (left: poor inner bond, centre: good inner bond, right: perfect inner bond)

are determined based on exceeding of the tensile strength of the reinforcement elements on a range of 0.2 m in the centre of the model, which corresponds to the determination in the previous parametric studies. Thus, the earlier failure of the reinforcement due to boundary effects is left unconsidered in the reference ultimate stresses.

Table 5.1 reveals that in general the tensile strength of the composite increases with the improvement of inner bond. Summarising, type A clamping leads to a stress increase in the reinforcement at the transition to the clamping, which decreases the ultimate failure load. However, this effect is more pronounced with poor bond quality in the reinforcement core. The case of a single crack (e. g. double-sided yarn pull-out) is probably the lower limit case regarding the influence of stress distribution in the reinforcement on composite strength. Corresponding results of simulations where only one concrete element is allowed to crack are shown in Fig. 5.55. Especially for the case of poor inner bond, a large difference in the reinforcement stresses between the sleeve layer and the core layers is observable, which is similar to the stress distribution of type A clamping, compare Fig. 5.54(a). Due to the earlier failure of the sleeve layer this leads also to an earlier ultimate failure of the composite compared to the case with type B clamping where the stress differences in the reinforcement are lower, compare Fig. 5.54(b). Thus, the case of single cracks probably constitutes the lower limit of composite strength while the reference case of a perfect strain specimen is the upper limit for the composite strength for each conducted bond quality.

The findings based on the simulated results can be summarised as follows: Any influence from specimen geometry and clamping, which leads to changing concrete cracking behaviour, affects the ultimate load-bearing capacity of the composite due to changes in the stress distribution in the reinforcement. Changing the regular multiple cracking of TRC to single cracking as with a type A clamping can reduce the failure load of the composite considerably. If waisted specimens are used to prevent other failure types, this can also cause a significant strength reduction due to changing stress distributions in the reinforcement associated with increased crack spacing. However, most of these effects are especially pronounced with low bond strength in the reinforcement core and become less distinct or negligible with increasing bond quality e.g. due to additional polymeric coatings. The open question is what the material strength related to practical application is. Furthermore, it is interesting how it can be measured in a simple and robust test setup. Test setups of type A, where ultimate

Table 5.1.: Composite strength as measured force related to the cross-sectional area of the concrete [N/mm²]

bond quality	**reference**	**single crack**	**plane/ stiff**	**plane/ soft**	**waisted/ stiff**
poor inner bond	17.3 (100 %)	12.4 (71.7 %)	13.1 (75.7 %)	16.7 (96.5 %)	13.6 (78.6 %)
good inner bond	18.3 (100 %)	17.8 (97.3 %)	17.9 (97.8 %)	18.3 (100 %)	18.0 (98.4 %)
perfect inner bond	20.0 (100 %)	19.7 (98.5 %)	19.8 (99.0 %)	19.9 (99.5 %)	20.0 (100 %)

failure is dominated by single cracking corresponding to double sided pull-out tests seem to give a lower limit for composite strength. Test setups of type B, where in the specimens a regular multiple crack pattern can develop, seem to give an upper limit for the tensile strength. In practice both cases might be the dimensioning criterion. Following this argumentation, a conservative approach possibly should then use type A clamping. However, the statistical size effect appearing with brittle fibres under tensile loading has to be considered. According to Weibull theory, see [Weibull 1939], the probability of failure increases with increasing fibre length because also the number of the flaws increases and glass fibre strength depends almost entirely on surface flaws. Therefor, the size of the stressed surface is of importance to characterise the strength. In type B specimens, a large number of cracks with a relatively uniform stress distribution exists, which corresponds to a large fibre length and increases the probability of failure. In contrast, in type A specimens a few cracks with elevated reinforcement stresses exist at the clamping where ultimate failure occurs. This corresponds to a short "effective" fibre length and nominally increased strength. However, type A specimens will mask the statistical size effect as long as it is smaller than the impact from strength reducing stress concentrations at the clamping. As type B clamping takes also the statistical size effect in the measured strength into account, it can be assessed as the conservative approach. The results of the present numerical study and experimental results presented in [Jesse et al. 2009] show that the impact from clamping is less pronounced the better the inner bond is. Since the application of textile reinforcement without secondary coating for controlling and improving inner bond, structural stability and handling on site is not recommended for practical applications, the problems that arise with poor inner bond and type A clamping should not be overrated.

As a last investigation, the influence of the measurement length and its position at the specimen on the appearing stiffness in the post-cracking state in the $\overline{\sigma}$-$\overline{\varepsilon}$ relation of the composite is studied. The change of regular multiple cracking in the undisturbed centre of the specimen to single cracking at the transition to supported specimen parts leads to differences in the crack widths of the respective cracks. The cracks at the transition from the free to the supported parts of the specimens have larger crack widths than in the free parts where boundary effects diminish. From different crack widths also differences in the mean deformations apart from the basic differences between intact and cracked concrete parts follow, which might influence the strains in the global $\overline{\sigma}$-$\overline{\varepsilon}$ response. To investigate this effect, different measurement lengths and positions for the determination of $\overline{\varepsilon}$ were

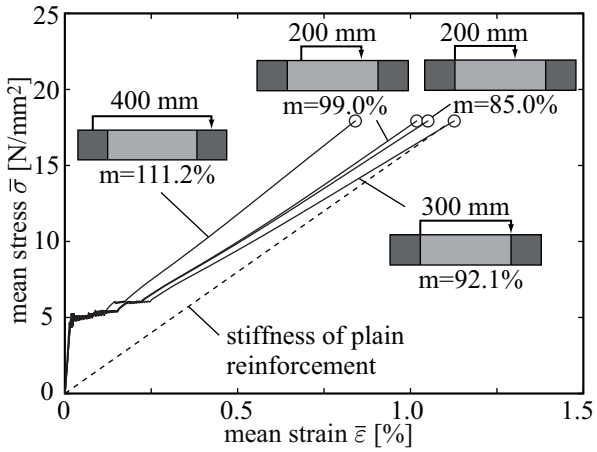

(a) Plane specimens with glued steel plates

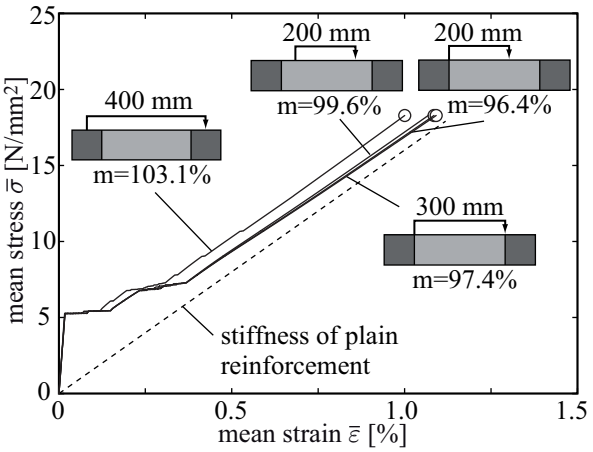

(b) Plane specimens with soft interlayer

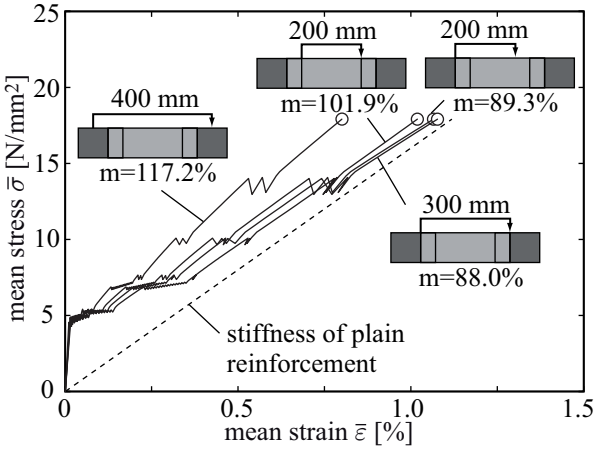

(c) Waisted specimens with glued steel plates

Figure 5.56.: Stress-strain relations for different deformation measurement lengths and types of load application for the case of good inner bond ($m = m_{sim}/m_{pc}$)

considered. Based on $\overline{\varepsilon}$ and $\overline{\sigma}$, where the determined values do not change between the different $\overline{\sigma}$-$\overline{\varepsilon}$ relations of one simulation, the ratio ($m = m_{sim}/m_{pc}$) between the simulated slope m_{sim} and the theoretical slope m_{pc} of the $\overline{\sigma}$-$\overline{\varepsilon}$ relation in the post-cracking state is established corresponding to Section 5.3.1.3.

For the three investigated combinations of specimen shape and clamping construction, the cases with good inner bond corresponding to the stress distributions in the centre of Fig. 5.54 are used in the following for description. The cases of poor and perfect inner bond provide similar results, although the stress concentrations in the reinforcement at the transition to the supported parts of the specimen reduce with improved bond. The reason is that the cracking characteristics of single and multiple cracking do not significantly change due to a change of the inner bond quality. For the measurement length, four cases are investigated, which are:

- a measurement length of 200 mm in the centre of the specimen corresponding to the reference case
- a measurement length of 200 mm shifted to the margin of the free length of the specimen

- a measurement length of 300 mm between both margins of the free length of the specimen
- a measurement length of 400 mm between the positions of load application.

In Fig. 5.56, which shows the respective $\overline{\sigma}$-$\overline{\varepsilon}$ relations, similar effects but different extents can be seen for all cases of specimen shape and clamping type. The measurement length of 200 mm in the centre of the specimen corresponding to the reference case, provides in all cases approximately the expected value of the stiffness in the post-cracking state m_{pc}. The lowest value of m_{sim} results if the measurement length of 200 mm is shifted to the margin of the free length of the specimen, which results from the incorporation of large crack widths at the margin of the free length due to single cracking mechanisms. A similar m_{sim} follows from the measurement length of 300 mm between both margins of the free length of the specimen. The reduction is, however, smaller because the undisturbed parts of the free length have a larger influence compared to the previous case. If $\overline{\varepsilon}$ is determined based on a measurement length of 400 mm between the positions of load application, m_{sim} has the highest values, which are larger than m_{pc} because the supported parts of the concrete with very low deformations compared to the free parts are incorporated. For a type A clamping, this corresponds to a $\overline{\varepsilon}$ determination based on displacements of the load application construction.

For the cases of a plane and a waisted specimen with stiff type A clamping as shown in Figs. 5.56(a), relatively large deviations of m_{sim} compared to m_{pc} of approximately $\pm 15\,\%$ are observable. As already mentioned, this results from large crack widths at the margins of the free specimen parts due to single crack mechanisms. For the case of the waisted specimen, these theoretical findings are also supported by experimental investigations by [Hegger et al. 2006a, Bruckermann 2007] based on the experimental setup by [Molter 2005] where the crack width distribution was determined by means of photogrammetric methods. These experimental results show increased crack width in the waisted parts of the respective specimen. Moreover, $\overline{\varepsilon}$ was determined in these experiments similar to the case of the measurement length of 300 mm in Fig. 5.56(c) incorporating the waisted parts of the specimen. Thus, in the results of these experimental investigations, $\overline{\varepsilon}$ is artificially underestimated. In contrast, the plane specimen with soft type B clamping, shows only deviations of m_{sim} compared to m_{pc} of approximately $\pm 5\,\%$. The reason is that with the soft clamping not single cracks develop at the transition from the free to the supported part but cracking proceeds with succesively reducing crack widths in the supported parts of the specimen, compare Fig. 5.54(b).

These theoretical investigations showed that the $\overline{\sigma}$-$\overline{\varepsilon}$ relations resulting from experimental measurement can be significantly influenced by the way $\overline{\varepsilon}$ is determined. Especially if both, single and multiple cracking mechanisms, occur within the measurement range associated with significant differences in the crack widths, the stiffness of the composite in the post-cracking state might be apparently reduced. With this regard, the strain measurement in the experimental setup by [Molter 2005] has to be assessed as inappropriate for the determination of the $\overline{\sigma}$-$\overline{\varepsilon}$ relation because besides the incorporation of single large crack widths also varying cross-sectional areas of the concrete are taken into account within the measurement length. In contrast, $\overline{\varepsilon}$ can be determined in the test setup by [Jesse 2004] in a robust manner as no thickness variations of the specimen exist and also single cracking mechanisms are considerably reduced. In all considered test setups, a determination of $\overline{\varepsilon}$ based on deformations

of the testing machine similar to the presented case of the measurement length of 400 mm between the positions of load application in the model is inappropriate as it represents a mixture of deformations of supported and free parts of the specimens. This leads in general to an underestimation of the deformations of the composite in the post-cracking state and to an overestimation of the respective stiffness.

In the previous parametric studies, presented in the Sections 5.3.1.1-5.3.5.2, the load application constructions were not explicitly modelled. Instead the first node of the concrete bar element chain was fixed while displacements were applied at the last concrete node. The results in the current section revealed that this approach is appropriate as long as only the undisturbed parts in the centre of the model are considered for the determination of the tensile behaviour of the composite. The correspondence of the simulated results between the realistic modelling of the load application according to the test setup by [Jesse 2004] and the simplified boundary conditions in the centre part of the model where boundary effects diminished can be also seen when the stress distributions in Fig. 5.54 for good inner bond are compared to the stress distribution in the reference case in Fig. 5.17(c). In the previous parametric studies, strains, crack widths and crack spacing were determined in a proper manner on a length of 200 mm in the centre of the model.

6. Summary, conclusions and outlook

6.1. Summary and conclusions

In the present work, the load-bearing behaviour of the composite textile reinforced concrete (TRC) subjected to uniaxial tensile loading was investigated based on numerical simulations. The main objective of the work was the theoretical investigation of effects in the load-bearing behaviour of TRC, which cannot be explained solely by available experimental results. Therefor, a model was developed, which can describe the tensile behaviour of TRC in different experimental test setups with a unified approach.

As a starting point, the main ideas, which led to the development of the composite TRC, were summarised briefly and some examples of application, which are e. g. thin new structures and the strengthening of existing structures, were presented. Furthermore, existing knowledge about the constituents of the composite, which are multi-filament yarns of alkali-resistant glass as reinforcement and a fine-grained concrete matrix, as well as the composite TRC itself was presented. This included descriptions of structural properties of the materials as well as their constitutive behaviour. In this context, also different tensile tests concerning TRC, which are the filament pull-out test, the yarn pull-out test and tensile tests of TRC with a sufficient reinforcement ratio to achieve multiple matrix cracking were described. These tests were also intended to be described with a unified model.

Already existing models for the uniaxial tensile behaviour of TRC were summarised. The description was subdivided into parts concerning the modelling of the constitutive behaviour of concrete and reinforcement as well as their interaction due to bond. A result of this study was that among the existing models for TRC no one enables the description of all aforementioned experiments with a unified approach. Regarding an improved model, it was concluded that a numerical model based on the FEM is advantageous compared to analytical formulations due to its variability. However, a fully three-dimensional model was assessed to be not applicable due to unacceptable computation times. Thus, a reduction of the detailedness was accepted while consideration of essential mechanisms and properties was requested.

Based on these requirements, a one-dimensional model neglecting effects resulting from Poisson's effect was developed, which was implemented in a FEM framework. However, other transverse effects are taken into account by a subdivision of the reinforcement yarns into so-called segments. The model gains most of its complexity from non-linearities arising from the constitutive relations. Such non-linearities are, e. g., limited tensile strength of concrete and reinforcement, tension softening of the concrete, waviness of the reinforcement and non-linear bond laws. Besides a deterministic description of the material behaviour, also a stochastic formulation based on a cross-correlated random field approach was introduced in the model. The model incorporates two types of finite elements, a one-dimensional bar

element and a zero-thickness bond element. Furthermore, some effort was spent to reduce computation time by using efficient incremental-iterative solution methods where the BFGS approach in combination with line search was chosen because of its good performance. The model has a number of advantageous features, which are provided in this combination only in a few other models concerning TRC. It provides stress distributions in the reinforcement and the concrete as well as properties of concrete crack development like crack spacing and crack widths, which are in some of the existing models input parameters and not a result of the simulations. Moreover, the successive failure of the reinforcement can be studied with the model, which was, however, only performed for simulations of yarn pull-out tests. The model was applied to three types of tests, the filament pull-out test, the yarn pull-out test and tensile tests with multiple concrete cracking.

The results of the simulations regarding the filament pull-out tests showed good correspondence with experimental results. Parametric studies were performed to show the influence of free filament length between the position where the filament protrudes from the concrete and the position where the load is applied. It was concluded that the bond law cannot be entirely determined with these tests due to snap-back effects. Moreover, parametric studies with varied values of bond law parameters and embedding lengths were performed. Despite these results, it had to be concluded that the results of the filament pull-out tests have only limited importance for TRC as applied in practice. The reason is that this type of test represents a filament almost perfectly embedded in cementitious matrix, which does not occur as general case in TRC, in practice.

The presented results of simulations of yarn pull-out tests demonstrated the applicability of the model to this type of test. It has been shown that a relatively fine subdivision of the reinforcement is necessary to represent the successive failure of the reinforcement yarns appropriately. Therefor, virtually unacceptable computation times occur with the model in its current implementation. This prevented more detailed investigations concerning yarn pull-out tests within this work. However, the presented results showed that the model is in principle able to provide the distribution of failure positions of the filaments, which might be directly compared to experimental results based on acoustic emission analysis as e. g. presented in [Kang et al. 2009]. Furthermore, the degradation development in the reinforcement with increasing loading can be determined, which might be useful as an input for models, which use a smeared formulation of the reinforcement material behaviour.

One of the main objectives of this work was to investigate effects concerning the tensile material behaviour of TRC, which could not be explained, hitherto, based solely on experimental results. Hence, a large number of simulations was performed concerning tensile tests with multiple concrete cracking, which reflect the tensile behaviour of TRC as occurring in practice. The results of the simulations showed that the model is able to reproduce the typical tripartite mean stress-mean strain response of TRC consisting of the uncracked state, the state of multiple cracking and the post-cracking state as known from experimental investigations. The best agreement between simulated and experimental results was achieved considering scatter in the material properties associated with the concrete as well as concrete tension softening and reinforcement waviness. Also other load-bearing characteristics like crack spacing and tension stiffening were reflected in a satisfactory manner. Moreover, a number of parametric studies was carried out concerning bond, reinforcement and concrete properties to analyse their influence on load-bearing properties of the composite TRC. Such

characteristics are e. g. suppression of cracks, stiffness in the post-cracking state, tension stiffening as well as ultimate stresses and strains.

Suppression of cracks, which is the elevation of the stress level of concrete cracking in the mean stress-mean strain relation of the composite compared to the nominal concrete tensile strength due to a participation of the reinforcement on load-bearing before concrete cracking, is primarily influenced by the reinforcement ratio and the Young's modulus of the reinforcement. With increasing values of both properties, also suppression of cracks increases. Nevertheless, it can be expected that also initial stopping mechanisms of cracks developing transversely to the loading direction occur at the longitudinally aligned reinforcement yarns. This increases suppression of cracks but is not reflected by the essentially one-dimensional model.

For an appropriate representation of the cracking behaviour of the concrete, scattering material properties have to be considered. Especially scattering concrete tensile strength leads to smoothly increasing cracking stresses with increased loading. A similar effect results from scatter in the Young's modulus of the concrete where in contrast to scatter in tensile strength primarily cracking at higher load levels is influenced. Scatter of the bond strength in the interface between concrete and filaments in the fill-in zone has a negligible effect on concrete cracking in particular and the load-bearing response of the composite in general. Crack widths and crack spacing reduce significantly with increasing reinforcement ratio, bond strength between concrete and filaments in the fill-in zone, Young's modulus of the reinforcement and concrete fracture energy.

In the post-cracking state, experiments reveal a reduced stiffness of the composite compared to the corresponding stiffness of the plain reinforcement. The reasons for this effect are discussed controversially in the "TRC community". The parametric studies indicate that the deficit of post-cracking stiffness has several sources. A main source is the waviness of the reinforcement yarns, which leads to a delayed activation of the filaments. The effect of waviness diminishes at higher load levels where the increasing stiffness might be compensated by failing filaments, which reduces the stiffness of the composite already before ultimate failure. At the very beginning of the post-cracking state also the bond characteristics influence the stiffness. Another effect results from the way the mean strain in the experiments is determined, especially if large variations in the crack widths occur within the measurement range. Moreover, it was shown that a simultaneous failure of the filaments in the fill-in zone with concrete cracking as supposed in [Jesse 2004] is most likely not responsible for the deficit of post-cracking stiffness if a sufficient reinforcement ratio is applied. In this case, the normal stresses in the reinforcement are considerably lower than the characteristic reinforcement tensile strength. Only for very low reinforcement ratios such a simultaneous failure might occur. Nevertheless, it is conceivable that a small fraction of filaments already fails during production and processing resulting in an apparently smaller available reinforcement ratio. Furthermore, it was shown that the assumption of very low bond stress in the core of the yarns is most likely not the reason for a reduced stiffness in the post-cracking state because in this case the core filaments would be considerably pulled into the concrete at the specimen ends. This is not observed in experiments.

With the model also the effect of tension stiffening in the post-cracking state was studied, which results from the participation of the concrete on load-bearing between the cracks

and leads to a reduction of the strains compared to the stress-strain relation corresponding to the plain reinforcement. Tension stiffening is strongly influenced by crack spacing. The larger crack spacing is, the larger is in general also tension stiffening. Thus, the statements concerning the most influencing parameters of crack spacing apply also for tension stiffening. However, in the experiments often "negative" tension stiffening is observed. Simulations showed that the primary reason for this effect is waviness of the reinforcement. This leads to additional deformations of the reinforcement and larger mean strains in the composite.

For dimensioning of structural elements, it is important to know the ultimate stresses and strains. In context of this work, only qualitative statements are possible as only an arbitrary value for the reinforcement tensile strength was used. The detailed failure behaviour of the reinforcement concerning TRC was not part of the investigations. However, the parametric studies showed that the ultimate stresses and strains of the composite increase with increasing reinforcement ratio, which is known from the experiments. Vice versa, very large bond strength values in the interface between the concrete and the filaments in the fill-in zone can reduce ultimate stresses and strains because of stress concentrations in these filaments leading to earlier failure. Increasing Young's modulus of the reinforcement leads to strongly decreasing ultimate strains while the ultimate stresses decrease only insignificantly. The ultimate strain of the composite increases with increasing reinforcement waviness, which does not influence the respective ultimate stresses, because only additional deformations of the reinforcement are introduced.

Additionally, a simulation with cyclic loading was carried out to show the applicability of the model to more complicated loading conditions. The simulation showed that the typical hysteretic behaviour of the load cycles can be reproduced with the model. However, the remaining inelastic strains after unloading are underestimated by the model. This results primarily from the neglect of inelastic deformation in the closing regime of cracks, e. g., due to incompatibilities in the crack faces.

Finally, a study concerning the influence of the load application in experimental test setups was performed, which is of importance concerning the determination of the tensile strength of the composite and associated for the dimensioning of structural elements of TRC. The results of the simulations showed that for an accurate experimental determination of the tensile strength of the composite a distinctive multiple cracking state needs to be achieved because effects resulting from single crack mechanisms reduce the ultimate stress in the composite due to large stress concentrations in the reinforcement at these cracks. With this regard, plane specimens with a load application by means of soft clamping were assessed to perform well while test setups where the load is applied with stiff, glued steel plates revealed deficiencies. Similar arguments apply also for the determination of the mean strains in these test setups.

In summary, the investigations revealed that essential aspects of the complex load-bearing behaviour of TRC exposed to uniaxial tensile loading can be reproduced with the presented one-dimensional model. Moreover, predictions of the load-bearing behaviour with hitherto not experimentally tested combinations of material properties were given in the parametric studies, which have to be checked for their validity in future experiments.

6.2. Outlook

The investigations presented in this work based on the one-dimensional model are only a selection of possible investigations. Concerning filament pull-out tests, the model can be applied to estimate differences in the bond properties due to varying parameter combinations. The investigations regarding the yarn pull-out tests where limited to a proof of concept. For a more extensive analysis of these tests, some effort has to be spent to considerably reduce computation time. Therefor, it is conceivable to apply some parallelisation algorithms to the FEM formulation. Furthermore, the number of elements in parts of the model where no filament failure events occur might be reduced, which can be achieved with a simple increase of the element size. More difficult but also conceivable is the modelling of the reinforcement with a layer approach in parts distant to the concrete crack where no failure events are expected and a subdivision into segments in the vicinity of the concrete crack.

Besides further parametric studies with varied parameter combinations, the model can be also extended. The model offers great variability in the formulation and extension as the FEM is used. Such extensions can be for instance the incorporation of imposed loading, e. g. due to thermal loading or concrete shrinkage. Corresponding investigations with a model very similar to the model in this work were already published in [Häussler-Combe & Hartig 2009] for conventional steel-reinforced concrete. This also allows for investigations of special characteristics of TRC with reinforcement of carbon fibres, which have in contrast to the concrete a negative thermal expansion coefficient. Moreover, also inelastic deformations in the closing regime of cracks can be implemented.

Another field of application for the model is the combination of different reinforcement materials. A straightforward application is the combination of existing steel reinforced concrete with existing concrete cracks, which is subsequently strengthened with TRC. Such investigations can support and improve corresponding investigations by [Weiland 2009]. Another field where the model can be applied is the optimisation of composite properties by means of a combination of different reinforcement materials as it was investigated by [Kato 2010].

Due to the available stochastic formulation of the constitutive laws, the model in its present form can be directly embedded into a statistical analysis framework. This facilitates the determination of statistical properties of the load-bearing characteristics of the composite like crack widths, stiffness in the post-cracking state and tensile strength. Furthermore, also investigations concerning size effects are facilitated. Besides the energetic size effect, which results primarily from post-cracking resistance of the concrete, also the statistical size effect, which has its source in the scatter of the tensile strengths of concrete and reinforcement, can be studied with the model.

Bibliography

[Abdkader 2004] Abdkader, A.: *Charakterisierung und Modellierung der Eigenschaften von AR-Glasfilamentgarnen für die Betonbewehrung*. TU Dresden: Dresden, 2004 – Dissertation

[Abrishami & Mitchell 1996] Abrishami, H.H.; Mitchell, D.: Analysis of Bond Stress Distributions in Pullout Specimens. *Journal of Structural Engineering*, 1996, 122(3):255–261

[Al-Masri & Wulfhorst 2001] Al-Masri, A.; Wulfhorst, B.: Mechanische Charakterisierung und Modellierung der Eigenschaften von AR-Glasfilamentgarnen für die Betonbewehrung. In: Hegger, J. (Ed.): *Textilbeton - 1. Fachkolloquium der Sonderforschungsbereiche 528 und 532*. RWTH Aachen: Aachen, 2001, pp. 59–70

[Anderson et al. 1999] Anderson, E.; Bai, Z.; Bischof, C.; Blackford, L.S.; Demmel, J.; Dongarra, J.; Du Croz, J.; Hammarling, S.; Greenbaum, A.; McKenney, A.; Sorensen, D.: *LAPACK Users' guide*. Society for Industrial and Applied Mathematics: Philadelphia, 3rd ed., 1999

[Aveston et al. 1971] Aveston, J.; Cooper, G.A.; Kelly, A.: Single and multiple fracture. In: *The properties of fiber composites*. IPC Science and Technology Press: Guildford, 1971, pp. 15–24

[Aveston & Kelly 1973] Aveston, J.; Kelly, A.: Theory of multiple fracture of fibrous composites. *Journal of Materials Science*, 1973, 8(3):352–362

[Banholzer 2004] Banholzer, B.: *Bond behaviour of a Multi-Filament Yarn embedded in a cementitious Matrix*. RWTH Aachen: Aachen, 2004 – Dissertation

[Banholzer et al. 2005] Banholzer, B.; Brameshuber, W.; Jung, W.: Analytical simulation of pull-out tests - the direct problem. *Cement & Concrete Composites*, 2005, 27(1):93–101

[Barthold et al. 1997] Barthold, F.J.; Gross, D.; Reinhardt, H.W.; Stein, E.: *Der Ingenieurbau: Grundwissen - Werkstoffe, Elastizitätstheorie*. Ernst & Sohn: Berlin, 1997

[Bathe 1996] Bathe, K.J.: *Finite Element Procedures*. Prentice-Hall: Englewood Cliffs, New Jersey, 1996

[Bažant 2002] Bažant, Z.P.: *Scaling of Structural Strength*. Hermes Penton Science: London, 2002

[Bažant & Oh 1983] Bažant, Z.P.; Oh, B.H.: Crack band theory for fracture of concrete. *Materials & Structures*, 1983, 16(3):155–177

[Bažant & Prat 1988] Bažant, Z.P.; Prat, P.C.: Microplane model for brittle-plastic material: I. Theory. *Journal of Engineering Mechanics*, 1988, 114(10):1672–1688

[Beckmann et al. 2010] Beckmann, B.; Hummeltenberg, A.; Weber, T.; Curbach, M.: Concrete under high strain rates: Local material and structure response to impact loading. In: Li, Q.; Hao, H.; Li, Z.X.; Yankelevsky, D. (Eds.): *Proceedings of the First International Conference of Protective Structures (ICPS-2010)*. Manchester (UK), 2010, Book of abstracts & CD of full papers

[Bentur & Mindess 1990] Bentur, A.; Mindess, S.: *Fibre reinforced cementitious composites*. Elsevier: London, 1990

[Bićanić & Johnson 1979] Bićanić, N.; Johnson, K.H.: Who was '-Raphson'? *International Journal for Numerical Methods in Engineering*, 1979, 14(1):148–152

[de Boor 1978] de Boor, C.: *A Practical Guide to Splines*. Springer-Verlag: New York, 1978

[Bournas et al. 2007] Bournas, D.A.; Lontou, P.V.; Papanicolaou, C.G.; Triantafillou, T.C.: Textile Reinforced Mortar versus Fiber-Reinforced Polymer Confinement in Reinforced Concrete Columns. *ACI Structural Journal*, 2007, 104(6):740–748

[Brameshuber 2006] *State-of-the-Art Report of RILEM Technical Committee 201 TRC: Textile Reinforced Concrete (RILEM Report 36)*. RILEM: Bagneux, 2006

[Brockmann 2005] Brockmann, T.: *Mechanical and fracture mechanical properties of fine grained concrete for textile reinforced composites*. RWTH Aachen: Aachen, 2005 – Dissertation

[Bronstein et al. 2008] Bronstein, I.N.; Semendjajew, K.A.; Musiol, G.; Mühlig, H.: *Taschenbuch der Mathematik*. Verlag Harri Deutsch: Frankfurt am Main, 7th ed., 2008

[Bruckermann 2007] Bruckermann, O.: *Zur Modellierung des Zugtragverhaltens von textilbewehrtem Beton*. RWTH Aachen: Aachen, 2007 – Dissertation

[Butler 2009] Butler, M.: *Zur Dauerhaftigkeit von Verbundwerkstoffen aus zementgebundenen Matrices und alkaliresistenten Glasfaser-Multifilamentgarnen*. TU Dresden: Dresden, 2009 – Dissertation

[Butler et al. 2009] Butler, M.; Mechtcherine, V.; Hempel, S.: Experimental investigations on the durability of fibre-matrix interfaces in textile-reinforced concrete. *Cement & Concrete Composites*, 2009, 31(4):221–231

[Chudoba et al. 2006] Chudoba, R.; Vořechovský, M.; Konrad, M.: Stochastic modeling of multi-filament yarns. I. Random properties within the cross-section and size effect. *International Journal of Solids and Structures*, 2006, 43(3-4):413–434

[Cornelissen et al. 1986] Cornelissen, H.A.W.; Hordijk, D.A.; Reinhardt, H.W.: Experimental Determination of Crack Softening Characteristics of Normalweight and Lightweight Concrete. *Heron*, 1986, 31(2):45–56

[Crisfield 1981] Crisfield, M.A.: A fast incremental/iterative solution procedure that handles "snap-through". *Computers & Structures*, 1981, 13(1-3):55–62

[Crisfield 1982] Crisfield, M.A.: Accelerated Solution Techniques and Concrete Cracking. *Computer Methods in Applied Mechanics and Engineering*, 1982, 33:585–607

[Crisfield 1997] Crisfield, M.A.: *Non-linear Finite Element Analysis of Solids and Structures – Vol. 1: Essentials*. John Wiley & Sons: Chichester, 1997

[Curbach 2003] Curbach, M. (Ed.): *Textile Reinforced Structures - Proceedings of the 2nd Colloquium on Textile Reinforced Structures (CTRS2)*. TU Dresden: Dresden, 2003

[Curbach & et al. 1998] Curbach, M.; et al.: *Sachstandbericht zum Einsatz von Textilien im Massivbau (DAfStb Heft 488)*. Beuth: Berlin, 1998

[Curbach et al. 2007] Curbach, M.; Graf, W.; Jesse, D.; Sickert, J.U.; Weiland, S.: Segmentbrücke aus textilbewehrtem Beton: Konstruktion, Fertigung, numerische Berechnung. *Beton- und Stahlbetonbau*, 2007, 102(6):342–352

[Curbach & Jesse 2009] Curbach, M.; Jesse, F. (Eds.): *Textilbeton - Theorie und Praxis: Proceedings of the 4. Kolloquium zu textilbewehrten Tragwerken (CTRS4) und zur 1. Anwendertagung*. TU Dresden: Dresden, 2009

[Curbach et al. 2006] Curbach, M.; Schicktanz, K.; Jesse, F.; Hartig, J.: Stochastische Eigenschaften der Zugfestigkeit freier und zementös eingebetteter Filamentbündel aus AR-Glas. In: Ruge, P.; Graf, W. (Eds.): *10. Dresdner Baustatik-Seminar, Neue Bauweisen - Trends in Statik und Dynamik*. TU Dresden: Dresden, 2006, pp. 91–100

[Cuypers & Wastiels 2006] Cuypers, H.; Wastiels, J.: Stochastic matrix-cracking model for textile reinforced cementitious composites under tensile loading. *Materials & Structures*, 2006, 39(8):777–786

[Daniels 1945] Daniels, H.E.: The statistical theory of the strength of bundles of threads. I. *Proceedings of the Royal Society of London*, 1945, A183:405–435

[Demmel et al. 1999] Demmel, J.W.; Eisenstat, S.C.; Gilbert, J.R.; Li, X.S.; Liu, J.W.H.: A supernodal approach to sparse partial pivoting. *SIAM Journal on Matrix Analysis and Applications*, 1999, 20(3):720–755

[Dennis & Moré 1977] Dennis, J.E.; Moré, J.J.: Quasi-Newton methods, motivation and theory. *SIAM Review*, 1977, 19(1):46–89

[Eligehausen et al. 1983] Eligehausen, R.; Popov, E.P.; Bertero, V.V. (1983). Local bond stress-slip relationships of deformed bars under generalized excitations. Technical Report, University of California, Berkeley

[Fehling et al. 2008] Fehling, E.; Schmidt, M.; Stürwald, S. (Eds.): *Ultra High Performance Concrete (UHPC): Proceedings of the Second International Symposium on Ultra High Performance Concrete Kassel, Germany*. Kassel University Press: Kassel, 2008

[Felippa 2004] Felippa, C.A.: *Introduction to Finite Element Methods*. University of Colorado: Boulder (Colorado), 2004

[Focacci et al. 2000] Focacci, F.; Nanni, A.; Bakis, C.E.: Local Bond-Slip Relationship for FRP Reinforcement in Concrete. *Journal of Composites for Construction*, 2000, 4(1):24–31

[Fritsch & Carlson 1980] Fritsch, F.N.; Carlson, R.E.: Monotone Piecewise Cubic Interpolation. *SIAM Journal on Numerical Analysis*, 1980, 17(2):238–246

[Gao et al. 2004] Gao, S.L.; Mäder, E.; Plonka, R.: Coatings for glass fibers in a cementitious matrix. *Acta Materialia*, 2004, 52(16):4745–4755

[Gao et al. 2007] Gao, S.L.; Mäder, E.; Plonka, R.: Nanostructured coatings of glass fibers: Improvement of alkali resistance and mechanical properties. *Acta Materialia*, 2007, 55(3):1043–1052

[Gill et al. 1991] Gill, P.E.; Murray, W.; Wright, M.H.: *Numerical linear algebra and optimization - Volume 1*. Addison-Wesley Publishing Company: Redwood City (CA), 1991

[Golub & van Loan 1996] Golub, G.H.; van Loan, C.F: *Matrix Computations*. The Johns Hopkins University Press: Baltimore, 3rd ed., 1996

[Gopalaratnam & Shah 1985] Gopalaratnam, V.S.; Shah, S.P: Softening Response of Plain Concrete in Direct Tension. *ACI Journal*, 1985, 28(3):310–323

[Grigoriu 1998] Grigoriu, M.: Simulation of stationary non-Gaussian translation processes. *Journal of Engineering Mechanics*, 1998, 124(2):121–126

[Grigoriu 2006] Grigoriu, M.: Evaluation of Karhunen-Loève, Spectral, and Sampling Representations for Stochastic Processes. *Journal of Engineering Mechanics*, 2006, 132(2):179–189

[Hartig & Häussler-Combe 2010] Hartig, J.; Häussler-Combe, U.: A model for the uniaxial tensile behaviour of Textile Reinforced Concrete with a stochastic description of the concrete material properties. In: Bićanić, N.; de Borst, R.; Mang, H.; Meschke, G. (Eds.): *Computational Modelling of Concrete Structures - Proceedings of the EURO-C 2010*. Taylor & Francis: London, 2010, pp. 153–162

[Hartig et al. 2008] Hartig, J.; Häussler-Combe, U.; Schicktanz, K.: Influence of bond properties on the tensile behaviour of Textile Reinforced Concrete. *Cement & Concrete Composites*, 2008, 30(10):898–906

[Hartig et al. 2009] Hartig, J.; Jesse, F.; Häussler-Combe, U.: Influence of different mechanisms on the constitutive behaviour of textile reinforced concrete. In: Curbach, M.; Jesse, F. (Eds.): *Textilbeton - Theorie und Praxis: Proceedings of the 4. Kolloquium*

zu textilbewehrten Tragwerken (CTRS4) und zur 1. Anwendertagung. TU Dresden: Dresden, 2009, pp. 157–168

[Hegger et al. 2006a] Hegger, J.; Brameshuber, W.; Will, N. (Eds.): *Textile Reinforced Concrete - Proceedings of the 1st International RILEM Symposium (RILEM Proceedings Pro 50)*. RILEM: Bagneux, 2006

[Hegger et al. 2002] Hegger, J.; Littwin, R.; Bruckermann, O.: Simulation of pull-out-tests of multi-filament yarns in a cementitious matrix using the finite-element method. In: Balázs, G.L.; Bartos, P.J.M.; Cairns, J.; Borosnyói, A. (Eds.): *Bond in Concrete - from research to standards*. Budapest University of Technology and Economics: Budapest, 2002, pp. 735–743

[Hegger et al. 2006b] Hegger, J.; Will, N.; Bruckermann, O.; Voss, S.: Load-bearing behaviour and simulation of textile reinforced concrete. *Materials & Structures*, 2006, 39(8):765–776

[Herrmann 1978] Herrmann, L.R.: Finite element analysis of contact problems. *Journal of the Engineering Mechanics Division (ASCE)*, 1978, 104:1043–1059

[Hillerborg et al. 1976] Hillerborg, A.; Modéer, M.; Petersson, P.E.: Analysis of crack formation and crack growth in concrete by means of fracture mechanics and finite elements. *Cement and concrete research*, 1976, 6(6):773–782

[Häussler-Combe & Hartig 2007] Häussler-Combe, U.; Hartig, J.: Bond and failure mechanisms of textile reinforced concrete (TRC) under uniaxial tensile loading. *Cement & Concrete Composites*, 2007, 29(4):279–289

[Häussler-Combe & Hartig 2008] Häussler-Combe, U.; Hartig, J.: Formulation and numerical implementation of a constitutive law for concrete with strain-based damage and plasticity. *International Journal of Non-Linear Mechanics*, 2008, 43(5):399–415

[Häussler-Combe & Hartig 2009] Häussler-Combe, U.; Hartig, J.: Rissbildung von Stahlbeton bei Zwangbeanspruchungen. *Bauingenieur*, 2009, 84(12):546–556

[Häussler-Combe & Jesse 2005] Häussler-Combe, U.; Jesse, F.: Rechnerische Untersuchungen zum einaxialen Tragverhalten von Textilbeton. *Bauingenieur*, 2005, 80:131–141

[Häussler-Combe et al. 2004] Häussler-Combe, U.; Jesse, F.; Curbach, M.: Textile reinforced concrete - overview, experimental and theoretical investigations. In: Li, V.C.; Leung, C.; Willam, K.; Billington, S. (Eds.): *Fracture Mechanics of Concrete Structures. Proceedings of the fifth international Conference on Fracture Mechanics of Concrete and Concrete Structures*. Vail (Colorado), 2004, pp. 749–756

[Jesse 2004] Jesse, F.: *Tragverhalten von Filamentgarnen in zementgebundener Matrix*. TU Dresden: Dresden, 2004 – Dissertation

[Jesse et al. 2009] Jesse, F.; Schicktanz, K.; Curbach, M.: Obtaining Characteristic Material Strength of Textile Reinforced Concrete (TRC) from Laboratory Tests. In: Djausal, A.; Alami, F.; Naaman, A.E. (Eds.): *International Symposium on Ferroce-*

ment and Thin Reinforced Cement Composites (FERRO-9): Green Technology for Housing and Infrastructure Construction. Bali (Indonesia), 2009, pp. 305–318

[Kaliakin & Li 1995] Kaliakin, V.N.; Li, J.: Insight into deficiencies associated with commonly used zero-thickness interface elements. *Computers & Geotechnics*, 1995, 17(2):225–252

[Kang et al. 2009] Kang, B.G.; Hannawald, J.; Brameshuber, W.: Schallemissionsanalyse zur Untersuchung des Schädigungsverhaltens im Auszugversuch eines in Beton eingebetteten Multifilamentgarns. In: Curbach, M.; Jesse, F. (Eds.): *Textilbeton - Theorie und Praxis: Proceedings of the 4. Kolloquium zu textilbewehrten Tragwerken (CTRS4) und zur 1. Anwendertagung*. TU Dresden: Dresden, 2009, pp. 169–184

[Kato 2010] Kato, J.: *Material Optimization for Fiber Reinforced Composites applying a Damage Formulation*. Universität Stuttgart: Stuttgart, 2010 – Dissertation

[Köckritz 2007] Köckritz, U.: *In-Situ Polymerbeschichtung zur Strukturstabilisierung offener nähgewirkter Gelege*. TU Dresden: Dresden, 2007 – Dissertation

[Keuser 1985] Keuser, M.: *Verbundmodelle für nichtlineare Finite-Element-Berechnungen von Stahlbetonkonstruktionen*. (Fortschritt-Berichte VDI Reihe 4 Nr. 71). VDI-Verlag: Düsseldorf, 1985

[Kühne 1984] Kühne, K.: *Werkstoff Glas*. Akademie-Verlag: Berlin, 1984

[Konrad & Chudoba 2009] Konrad, M.; Chudoba, R.: Tensile Behavior of Cementitious Composite Reinforced with Epoxy Impregnated Multifilament Yarns. *International Journal for Multiscale Computational Engineering*, 2009, 7(2):115–133

[Konrad 2008] Konrad, M.O.A.: *Effect of multifilament yarn crack bridging on uniaxial behavior of textile reinforced concrete*. RWTH Aachen: Aachen, 2008 – Dissertation

[Krüger 2004] Krüger, M.: *Vorgespannter textilbewehrter Beton*. Universität Stuttgart: Stuttgart, 2004 – Dissertation

[Le Bourhis 2008] Le Bourhis, E.: *Glass - Mechanics and Technology*. Wiley-VCH: Weinheim, 2008

[Lebrun & Dutfoy 2009] Lebrun, R.; Dutfoy, A.: An innovating analysis of the Nataf transformation from the copula viewpoint. *Probabilistic Engineering Mechanics*, 2009, 24(3):312–320

[Lepenies et al. 2007] Lepenies, I.; Meyer, C.; Schorn, H.; Zastrau, B.: Modeling of Load Transfer Behavior of AR-Glass-Rovings in Textile Reinforced Concrete. In: Aldea, C.M. (Ed.): *ACI Special Publication*, Vol. 244. ACI: Farmington Hills (MI), 2007, pp. 109–124

[Lepenies et al. 2001] Lepenies, I.; Richter, M.; Zastrau, B.: Zur mechanischen Modellierung der Ablöseerscheinungen im Faser-Matrix-Interface von unidirektional bewehrtem Textilbeton im Zugversuch. In: Hegger, J. (Ed.): *Textilbeton - 1. Fachkolloquium der Sonderforschungsbereiche 528 und 532*. RWTH Aachen: Aachen, 2001, pp. 179–192

[Lepenies 2007] Lepenies, I.G.: *Zur hierarchischen und simultanen Multi-Skalen-Analyse von Textilbeton*. TU Dresden: Dresden, 2007 – Dissertation

[Li 2003] Li, V.C.: On Engineered Cementitious Composites (ECC) - A review of the Material and Its Applications. *Journal of Advanced Concrete Technology*, 2003, 1(3):215–230

[Littwin 2001] Littwin, R.: Verifizierung und Optimierung eines Verbundgesetzes. In: Hegger, J. (Ed.): *Textilbeton - 1. Fachkolloquium der Sonderforschungsbereiche 528 und 532*. RWTH Aachen: Aachen, 2001, pp. 137–150

[Liu & Der Kiureghian 1986] Liu, P.L.; Der Kiureghian, A.: Multivariate distribution models with prescribed marginals and covariances. *Probabilistic Engineering Mechanics*, 1986, 1(2):105–112

[Luenberger 2005] Luenberger, D.G.: *Linear and Nonlinear Programming*. Springer: New York, 2nd ed., 2005

[Matheas 2006] Matheas, J.: *Entwicklung von Finiten Schalenelementen zur Berechnung von Verstärkungen aus Textilbeton bei Flächentragwerken*. TU Dresden: Dresden, 2006 – Dissertation

[Matthies & Strang 1979] Matthies, H.; Strang, G.: The solution of non-linear finite element equations. *International Journal for Numerical Methods in Engineering*, 1979, 14(11):1613–1626

[Mäder et al. 2004] Mäder, E.; Plonka, R.; Schiekel, M.; Hempel, R.: Coatings on Alkali-Resistant Glass Fibres for the Improvement of Concrete. *Journal of Industrial Textiles*, 2004, 33(3):191–207

[Mechtcherine & Jun 2007] Mechtcherine, V.; Jun, P.: Stress-strain behaviour of Strain-Hardening Cement-based Composites (SHCC) under repeated tensile loading. In: Carpinteri, A.; Gambarova, P.G.; Ferro, G.; Plizzari, G.A. (Eds.): *Fracture Mechanics of Concrete and Concrete Structures (FraMCoS-6). Vol. 2: Design, Assessment and Retrofitting of RC- Structures*. Taylor & Francis: Catania (Italy), 2007, pp. 1441–1448

[van Mier 1996] van Mier, J.G.M.: *Fracture processes of concrete: assessment of material parameters for fracture models*. CRC Press: Boca Raton, 1996

[van Mier & van Vliet 2002] van Mier, J.G.M.; van Vliet, M.R.A.: Uniaxial tension test for the determination of fracture parameters of concrete: state of the art. *Engineering Fracture Mechanics*, 2002, 69(2):235–247

[ModelCode 1990] *CEB-FIP Model Code 1990*. Comité Euro-International du Béton: Lausanne, 1990

[Moler 2004] Moler, C.B.: *Numerical Computing with MATLAB*. SIAM: Philadelphia, 2004

[Molter 2005] Molter, M.: *Zum Tragverhalten von textilbewehrtem Beton*. RWTH Aachen: Aachen, 2005 – Dissertation

[Naaman 2000] Naaman, A.E.: *Ferrocement & Laminated Cementitious Composites*. Techno Press 3000: Ann Arbor, 2000

[Ngo & Scordelis 1967] Ngo, D.; Scordelis, A.C.: Finite Element Analysis of Reinforced Concrete Beams. *ACI Journal*, 1967, 64:152–163

[Nocedal & Wright 1999] Nocedal, J.; Wright, S.J.: *Numerical Optimization*. Springer-Verlag: New York, 1999

[Ohno & Hannant 1994] Ohno, S.; Hannant, D.J.: Modeling the Stress-Strain Response of Continuous Fiber Reinforced Cement Composites. *ACI Materials Journal*, 1994, 91(3):306–312

[Ottosen & Ristinmaa 2005] Ottosen, N.S.; Ristinmaa, M.: *The Mechanics of Constitutive Modeling*. Elsevier: Amsterdam, 2005

[Ožbolt et al. 2002] Ožbolt, J.; Lettow, S.; Kožar, I.: Discrete Bond Element for 3D Finite Element Analysis of Reinforced Concrete Structures. In: Balázs, G.L.; Bartos, P.J.M.; Cairns, J.; Borosnyói, A. (Eds.): *Bond in Concrete - from research to standards. fib International Symposium*. Budapest University of Technology and Economics: Budapest, 2002, pp. 9–19

[Petersson 1981] Petersson, P.E.: *Crack growth and development of fracture zones in plain concrete and similar materials*. Lund Institute of Technology: Lund (Sweden), 1981

[PMC 2001] *Probabilistic Model Code*. Joint Committee on Structural Safety: Zürich, 2001

[Pröchtel & Häussler-Combe 2008] Pröchtel, P.; Häussler-Combe, U.: On the dissipative zone in anisotropic damage models for concrete. *International Journal of Solids and Structures*, 2008, 45(16):4384–4406

[Press et al. 2007] Press, W.H.; Teukolsky, S.A.; Vetterling, W.T; Flannery, B.P.: *Numerical recipes: the art of scientific computing*. Cambridge University Press: Cambridge, 3rd ed., 2007

[Ramm 1981] Ramm, E.: Strategies for Tracing the Nonlinear Response Near Limit Points. In: Wunderlich, W.; Stein, E.; Bathe, K.-J. (Eds.): *Nonlinear Finite Element Analysis in Structural Mechanics - Proceedings of the Europe-U.S. Workshop Ruhr-Universität Bochum, Germany, July 28-31, 1980*. Springer: Berlin, 1981, pp. 63–89

[Ramm 2007] Ramm, W.: Über die faszinierende Geschichte des Betonbaus vom Beginn bis zur Zeit nach dem 2. Weltkrieg. In: *Gebaute Visionen - 100 Jahre Deutscher Ausschuss für Stahlbeton 1907-2007*. Beuth: Berlin, 2007, pp. 27–130

[Remmel 1994] Remmel, G.: *Zum Zug- und Schubtragverhalten von Bauteilen aus hochfestem Beton (DAfStb Heft 444)*. Beuth: Berlin, 1994

[Richter 2005] Richter, M.: *Entwicklung mechanischer Modelle zur analytischen Beschreibung der Materialeigenschaften von textilbewehrtem Feinbeton*. TU Dresden: Dresden, 2005 – Dissertation

[Riks 1979] Riks, E.: An incremental approach to the solution of snapping and buckling problems. *International Journal of Solids and Structures*, 1979, 15(7):529–551

[Rinne 2003] Rinne, H.: *Taschenbuch der Statistik*. Verlag Harri Deutsch: Frankfurt am Main, 3rd ed., 2003

[Scheffler et al. 2009a] Scheffler, C.; Gao, S.L.; Plonka, R.; Mäder, E.; Hempel, S.; Butler, M.; Mechtcherine, V.: Interphase modification of alkali-resistant glass fibres and carbon fibres for textile reinforced concrete I: Fibre properties and durability. *Composites Science and Technology*, 2009, 69(3-4):531–538

[Scheffler et al. 2009b] Scheffler, C.; Gao, S.L.; Plonka, R.; Mäder, E.; Hempel, S.; Butler, M.; Mechtcherine, V.: Interphase modification of alkali-resistant glass fibres and carbon fibres for textile reinforced concrete II: Water adsorption and composite interphases. *Composites Science and Technology*, 2009, 69(7-8):905–912

[Schendel 1989] Schendel, U.: *Sparse Matrices: Numerical Aspects with Applications for Scientists and Engineers*. Ellis Horwood Limited: Chichester, 1989

[Schladitz et al. 2009] Schladitz, F.; Lorenz, E.; Jesse, F.; Curbach, M.: Verstärkung einer denkmalgeschützten Tonnenschale mit Textilbeton. *Beton- und Stahlbetonbau*, 2009, 104(7):432–437

[Schorn 2003] Schorn, H.: Ein Verbundmodell für Glasfaserbewehrungen im Beton. *Bautechnik*, 2003, 80(3):174–180

[SFB528 2001] *Sonderforschungsbereich 528 "Textile Bewehrungen zur bautechnischen Verstärkung und Instandsetzung": Arbeits- und Ergebnisbericht für die Periode II/1999 - I/2002* (Technical Report). TU Dresden: Dresden, 2001

[Silva & Wait 2005] Silva, M.; Wait, R.: Sparse Matrix Storage Revisited. In: *Proceedings of the 2nd conference on Computing frontiers*. ACM: Ischia (Italy), 2005, pp. 230-235

[Spanos & Zeldin 1998] Spanos, P.D.; Zeldin, B.A.: Monte Carlo Treatment of Random Fields: A Broad Perspective. *Applied Mechanics Reviews*, 1998, 51(3):219–237

[Spauszus 1974] Spauszus, S.: *Werkstoffkunde - Glas*. VEB Deutscher Verlag der Grundstoffindustrie: Leipzig, 1974

[Stockmann 2002] Stockmann, P.: *Textile Strukturen zur Bewehrung zementgebundener Matrices*. RWTH Aachen: Aachen, 2002 – Dissertation

[Sudret & Der Kiureghian 2000] Sudret, B.; Der Kiureghian, A.: *Stochastic finite element methods and reliability: A state-of-the-art report* (Technical Report UCB/SEMM-2000/08). University of California: Berkeley, 2000

[Vio et al. 2001] Vio, R.; Andreani, P.; Wamsteker, W.: Numerical Simulation of Non-Gaussian Random Fields with Prescribed Correlation Structure. *Publications of the Astronomical Society of the Pacific*, 2001, 113:1009–1020

[Vořechovský 2008] Vořechovský, M.: Simulation of simply cross correlated random fields by series expansion methods. *Structural Safety*, 2008, 30(4):337–363

[Vořechovský & Chudoba 2006] Vořechovský, M.; Chudoba, R.: Stochastic modeling of multi-filament yarns. II. Random properties over the length and size effect. *International Journal of Solids and Structures*, 2006, 43(3-4):435–458

[Warren 1934] Warren, B.E.: X-ray determination of the structure of glass. *Journal of the American Ceramic Society*, 1934, 17:249–254

[Warren & Biscoe 1938] Warren, B.E.; Biscoe, J.: Fourier analysis of x-ray patterns of soda-silica glass. *Journal of the American Ceramic Society*, 1938, 21(7):259–265

[Weibull 1939] Weibull, W. (Ed.): *A Statistical Theory of the Strength of Materials (Ingeniörsvetenskapsakademiens Handlingar Vol. 151)*. Generalstabens Litografiska Anstalts Förlag: Stockholm, 1939

[Weiland 2009] Weiland, S.: *Interaktion von Betonstahl und textiler Bewehrung bei der Biegeverstärkung mit textilbewehrtem Beton*. TU Dresden: Dresden, 2009 – Dissertation

[Weiland et al. 2008] Weiland, S.; Ortlepp, R.; Hauptenbuchner, B.; Curbach, M.: Textile Reinforced Concrete for Flexural Strengthening of RC-Structures - Part 2: Application on a Concrete Shell. In: Aldea, C.M. (Ed.): *ACI SP-251 Design & Applications of Textile-Reinforced Concrete*. ACI: Farmington Hills, 2008, pp. 41–58

[Wolpert & Macready 1997] Wolpert, D.H.; Macready, W.G.: No Free Lunch Theorems for Optimization. *IEEE Transactions on Evolutionary Computation*, 1997, 1(1):67–82

[Wriggers 2001] Wriggers, P.: *Nichtlineare Finite-Element-Methoden*. Springer-Verlag: Berlin, 2001

[Xu et al. 2004] Xu, S.; Krüger, M.; Reinhardt, H.W.; Ožbolt, J.: Bond Characteristics of Carbon, Alkali Resistant Glass, and Aramid Textiles in Mortar. *Journal of Materials in Civil Engineering*, 2004, 16(4):356–364

[Yankelevsky & Reinhardt 1989] Yankelevsky, D.Z.; Reinhardt, H.W.: Uniaxial Behavior of Concrete in Cyclic Tension. *Journal of Structural Engineering*, 1989, 115(1):166–182

[Zachariasen 1932] Zachariasen, W.H.: The atomic arrangement in glass. *Journal of the American Chemical Society*, 1932, 54(10):3841–3851

[Zastrau et al. 2003a] Zastrau, B.; Richter, M.; Lepenies, I.: On the Analytical Solution of Pullout Phenomena in Textile Reinforced Concrete. *Journal of Engineering Materials and Technology*, 2003, 125(1):38–43

[Zastrau et al. 2003b] Zastrau, B.W.; Lepenies, I.; Richter, M.: Zur Entwicklung einer Materialbeschreibung von Textilbeton mit Anwendung repräsentativer Volumenelemente. In: Curbach, M. (Ed.): *Textile Reinforced Structures - Proceedings of the 2nd Colloquium on Textile Reinforced Structures (CTRS2)*. TU Dresden: Dresden, 2003, pp. 387–398

[Zhandarov & Mäder 2003] Zhandarov, S.; Mäder, E.: Characterization of Fiber/Matrix Interface Properties: Applicability of Different Tests, Approaches and

Parameters. In: Curbach, M. (Ed.): *Textile Reinforced Structures - Proceedings of the 2nd Colloquium on Textile Reinforced Structures (CTRS2)*. TU Dresden: Dresden, 2003, pp. 101–120

[Zhandarov & Mäder 2005] Zhandarov, S.; Mäder, E.: Characterization of fiber/matrix interface strength: applicability of different tests, approaches and parameters. *Composites Science and Technology*, 2005, 65(1):149–160

[Zhu & Bartos 1997] Zhu, W.; Bartos, P.J.M.: Assessment of interfacial microstructure and bond properties in aged GRC using a novel microindentation method. *Cement and Concrete Research*, 1997, 27(11):1701–1711

[Zhu & Bartos 2000] Zhu, W.; Bartos, P.J.M.: Application of depth-sensing microindentation testing to study of interfacial transition zone in reinforced concrete. *Cement and Concrete Research*, 2000, 30(8):1299–1304

[Zienkiewicz & Taylor 2000a] Zienkiewicz, O.C.; Taylor, R.L.: *Finite Element Method. Volume 1: The Basis*. Butterworth-Heinemann: Oxford, 5th ed., 2000

[Zienkiewicz & Taylor 2000b] Zienkiewicz, O.C.; Taylor, R.L.: *Finite Element Method. Volume 2: Solid Mechanics*. Butterworth-Heinemann: Oxford, 5th ed., 2000

[Zorn 2003] Zorn, H.: Alkaliresistente Glasfasern - Von der Herstellung bis zur Anwendung. In: Curbach, M. (Ed.): *Textile Reinforced Structures - Proceedings of the 2nd Colloquium on Textile Reinforced Structures (CTRS2)*. TU Dresden: Dresden, 2003, pp. 1–14

A. Selected distribution functions

A.1. Gaussian distribution

The Gaussian distribution also referred to as normal distribution, see e. g. [Rinne 2003], is defined by two parameters $\mu_G \in \mathbb{R}$ and $\sigma_G \in \mathbb{R}$, $\sigma_G > 0$. The probability density function (PDF) is given with

$$f(t) = \frac{1}{\sigma_G\sqrt{2\pi}} \exp\left(-\frac{(t-\mu_G)^2}{2\sigma_G^2}\right) \text{ for } -\infty \leq t \leq +\infty \tag{A.1}$$

The respective cumulative distribution function (CDF) is

$$F(y) = \frac{1}{\sigma_G\sqrt{2\pi}} \int_{-\infty}^{y} \exp\left(-\frac{(t-\mu_G)^2}{2\sigma_G^2}\right) \mathrm{d}t = \frac{1}{2}\left(1 + \mathrm{erf}\left(\frac{y-\mu_G}{\sqrt{2}\sigma_G}\right)\right)$$
$$\text{for } -\infty \leq y \leq +\infty \tag{A.2}$$

where erf(.) is the error function:

$$\mathrm{erf}(x) = \frac{2}{\sqrt{\pi}} \int_0^x \exp\left(-u^2\right) \mathrm{d}u = 2\Phi\left(x\sqrt{2}\right) - 1 \tag{A.3}$$

It can be solved numerically or using tabulated values of the standard Gaussian CDF Φ, e. g. given in [Rinne 2003]. The percent point function (PPF) can be established using the inverse of the error function $\mathrm{erf}(.)^{-1}$, which can be solved numerically:

$$F^{-1}(p) = \mu_G + \sigma_G\sqrt{2}\mathrm{erf}^{-1}(2p-1);\ 0 < p < 1. \tag{A.4}$$

The expected value and standard deviation are given with $E(Y) = \mu_G$ and $D(Y) = \sigma_G$, respectively. The standard Gaussian distribution is defined with $\mu_G = 0$ and $\sigma_G = 1$. The respective CDF, PDF and PPF are given according to Eqs. (4.33-4.35).

A.2. Log-normal distribution

The log-normal distribution, see e. g. [Rinne 2003], is defined by two parameters $\mu_L \in \mathbb{R}$ and $\sigma_L \in \mathbb{R}$, $\sigma_L > 0$. The probability density function (PDF) is given with

$$f(t) = \begin{cases} 0 & \text{for} \quad t \leq 0 \\ \frac{1}{\sigma_L\sqrt{2\pi}} \frac{1}{t} \exp\left(-\frac{(\ln(t)-\mu_L)^2}{2\sigma_L^2}\right) & \text{for} \quad t > 0 \end{cases}. \tag{A.5}$$

The respective cumulative distribution function (CDF) is

$$F(y) = \begin{cases} 0 & \text{for} \quad y \leq 0 \\ \frac{1}{2}\left(1 + \operatorname{erf}\left(\frac{(\ln(y)-\mu_L)}{\sigma_L\sqrt{2}}\right)\right) & \text{for} \quad y > 0 \end{cases}. \tag{A.6}$$

The percent point function (PPF) can be established using the inverse of the error function $\operatorname{erf}(.)^{-1}$:

$$F^{-1}(p) = \exp\left(\sqrt{2}\operatorname{erf}^{-1}(2p-1)\sigma_L + \mu_L\right);\ 0 < p < 1. \tag{A.7}$$

Mean value and variance are according to [Bronstein et al. 2008]:

$$E(Y) = \exp\left(\mu_L + \frac{\sigma_L^2}{2}\right) \tag{A.8}$$

$$D(Y) = \sqrt{(\exp(\sigma_L^2) - 1)\exp(2\mu_L + \sigma_L^2)}. \tag{A.9}$$

A.3. Two-parametric Weibull distribution

The two-parametric Weibull distribution, see e. g. [Rinne 2003], has two parameters $\alpha > 0$ and $\beta > 0$. The parameter α is often denoted by k and called Weibull modulus. The parameter β is often denoted by σ_0 and represents a characteristic failure probability. The probability density function (PDF) is given with

$$f(t) = \begin{cases} 0 & \text{for} \quad t \leq 0 \\ \frac{\alpha}{\beta}\left(\frac{t}{\beta}\right)^{\alpha-1}\exp\left(-\left(\frac{t}{\beta}\right)^{\alpha}\right) = \frac{k}{\sigma_0}\left(\frac{t}{\sigma_0}\right)^{k-1}\exp\left(-\left(\frac{t}{\sigma_0}\right)^{k}\right) & \text{for} \quad t > 0 \end{cases}. \tag{A.10}$$

The respective cumulative distribution function (CDF) is

$$F(y) = \begin{cases} 0 & \text{for} \quad y \leq 0 \\ 1 - \exp\left(-\left(\frac{y}{\beta}\right)^{\alpha}\right) = 1 - \exp\left(-\left(\frac{\sigma}{\sigma_0}\right)^{k}\right) & \text{for} \quad y > 0 \end{cases}. \tag{A.11}$$

The explicit inversion of Eq. (A.11) leading to the percent point function (PPF) is analytically given by

$$F^{-1}(p) = \beta(-\ln(1-p))^{\frac{1}{\alpha}} = \sigma_0\left(-\ln(1-p)\right)^{\frac{1}{k}};\ 0 < p < 1. \tag{A.12}$$

The expected value is given with

$$E(Y) = \beta\Gamma\left(1 + \frac{1}{\alpha}\right) = \sigma_0\Gamma\left(1 + \frac{1}{k}\right) \tag{A.13}$$

where Γ is the Gamma function, which is defined as

$$\Gamma(y) = \int_0^{\infty} \exp(-t)t^{y-1}\mathrm{d}t \quad y > 0, \tag{A.14}$$

see [Bronstein et al. 2008]. The standard deviation is defined as

$$D(Y) = \beta\sqrt{\Gamma\left(1 + \frac{2}{\alpha}\right) - \Gamma^2\left(1 + \frac{1}{\alpha}\right)} = \sigma_0\sqrt{\Gamma\left(1 + \frac{2}{k}\right) - \Gamma^2\left(1 + \frac{1}{k}\right)}. \tag{A.15}$$